MINISTRY OF EDUCATION AND TRAINING
HO CHI MINH CITY UNIVERSITY OF TECHNOLOGY AND EDUCATION

XUAN BACH BUI

DEVELOPMENT OF THE THIN-WALLED COMPOSITE BEAM MODEL UNDER MECHANICAL AND THERMAL LOADS

PH.D THESIS
MAJOR: ENGINEERING MECHANICS

HO CHI MINH CITY, APRIL 2025

MINISTRY OF EDUCATION AND TRAINING
HO CHI MINH CITY UNIVERSITY OF TECHNOLOGY AND EDUCATION

XUAN BACH BUI

DEVELOPMENT OF THE THIN-WALLED COMPOSITE BEAM MODEL UNDER MECHANICAL AND THERMAL LOADS

MAJOR: ENGINEERING MECHANICS - 9520101

SUPERVISOR 1: PROF. TRUNG KIEN NGUYEN
SUPERVISOR 2: DR. DO TIEN THO

HO CHI MINH CITY, APRIL 2025

In memory of my grandmother

ACKNOWLEDGEMENTS

I would like to express my sincere gratitude to the many individuals who been instrumental in the completion of this doctoral thesis. This journey would not have been possible without the support, encouragement, and expertise of these remarkable people.

First and foremost, I am indebted to my advisor, Professor Trung Kien Nguyen, for his guidance, scholarly insight, and patience. His mentorship has been invaluable, providing me with the necessary direction and encouragement to navigate the complexities of my research.

I extend my gratitude to my other mentors, colleagues and seniors, Dr The Truong Phong Nguyen, Dr Phuong Thuc Vo, Dr Ngoc Duong Nguyen, and Dr. Van Hau Nguyen, for their technical resources, supportive endeavours and thoughtful feedback. Their contributions in multiple ways have greatly enhanced the rigor and depth of this work.

To my parents, I owe a debt of gratitude for their unwavering support, love, and understanding. Their sacrifices have allowed me to pursue my academic goals.

Special thanks go to my wife, whose encouragement and sympathy have been a constant source of joy and motivation. Her belief in my abilities has been a driving force during the challenging moments of this journey.

In conclusion, this thesis is a culmination of the collective efforts of those who have touched my academic and personal life. I am profoundly grateful for the contributions of each individual mentioned above.

Xuan Bach Bui

31.12.2023

TABLE OF CONTENTS

LIST OF PUBLICATIONS

[6-13]

ISI papers with peer-reviews:

1. **Bui, X.-B.**, T.-K. Nguyen, N.-D. Nguyen, and T.P. Vo, *A general higher-order shear deformation theory for buckling and free vibration analysis of laminated thin-walled composite I-beams.* Composite Structures, 2022. 295: p. 115775. https://doi.org/10.1016/j.compstruct.2022.115775

2. **Bui, X.-B.**, T.-K. Nguyen, and P.T.T. Nguyen, *Stochastic vibration and buckling analysis of functionally graded sandwich thin-walled beams.* Mechanics Based Design of Structures and Machines, 2023: p. 1-23. https://doi.org/10.1080/15397734.2023.2165101

3. **Bui, X.-B.**, T.-K. Nguyen, A. Karamanli, and T.P. Vo, *Size-dependent behaviours of functionally graded sandwich thin-walled beams based on the modified couple stress theory.* Aerospace Science and Technology, 2023. 142: p. 108664. https://doi.org/10.1016/j.ast.2023.108664

4. **Bui, X.-B** and T.-K. Nguyen, *Deterministic and stochastic flexural behaviors of laminated composite thin-walled I-beams using a sinusoidal higher-order shear deformation theory.* Mechanics Based Design of Structures and Machines, 2023: p. 1-30. https://doi.org/10.1080/15397734.2023.2297840

5. **Bui, X.-B.**, P.T.T. Nguyen, and T.-K. Nguyen, *Spectral projection and linear regression approaches for stochastic flexural and vibration analysis of laminated composite beams.* Archive of Applied Mechanics, 2024 .https://doi.org/10.1007/s00419-024-02565-x

Domestic papers with peer reviews and conference papers:

6. **Bui, X.B**., T.K. Nguyen, Q.C. Le, and T.T.P. Nguyen. *A novel two-variable model for bending analysis of laminated composite beams*. in *2020 5th International Conference on Green Technology and Sustainable Development (GTSD)*. 2020.

7. **Bui, X.-B.,** A.-C. Nguyen, N.-D. Nguyen, T.-T. Do, and T.-K. Nguyen, *Buckling analysis of laminated composite thin-walled I-beam under mechanical and thermal loads.* Vietnam Journal of Mechanics, 2023. 45(1): p. 75-90. https://doi.org/10.15625/0866-7136/17956

8. **Bui, X.-B**., T.-K. Nguyen, T.T.-P. Nguyen, and V.-T. Nguyen. *Stochastic Vibration Responses of Laminated Composite Beams Based on a Quasi-3D Theory*. in *ICSCEA 2021*. 2023. Singapore: Springer Nature Singapore.

List of Tables

List of Figures

NOMENCLATURE

α_z, α_{sz} : thermal expansion coefficients of the fibre materials

b, h, L : Width, height, length of the rectangular solid beam

b_1, b_2, b_3 : the widths of the upper flange, web, and lower flange respectively of the I- or channel thin-walled beams

b_1, b_2, b_3, b_4 : the widths of the left web, lower flange, right web, and upper flange respectively of the thin-walled box beams

β_i : unknown coefficients of the PCE series

c, m : subscripts indicating the ceramic and metal materials in FG beams

δ_{ij} : Knonecker delta

E_1, E_2 : Young's moduli

e_0, e_m : porosity parameters of porous metal foam beams

ε : the beam strain with the subscript indicating the direction

f : external force vector

$F_\omega(s)$: the warping function of thin-walled beams

G_{12}, G_{23}, G_{13} : shear moduli

h_1, h_2, h_3 : the thicknesses of the upper flange, web, and lower flange respectively of the I- or channel thin-walled beams

h_1, h_2, h_3, h_4 : the thicknesses of the left web, lower flange, right web, and upper flange respectively of the thin-walled box beams

K : stiffness matrix

δK : the variation of kinetic energy

l : material length scale parameter in micro-beams

M : mass matrix

m_{ij} : symmetric rotation high-order stress in micro-beams

N_0^t : axial thermal load

$\nu, \nu_{12}, \nu_{13}, \nu_{23}$: Poisson's ratios

p: power law index in FG beams

ρ: mass density

Π_S: strain energy

Π_W: potential energy when the beam is subjected to axial compressive load

Π_K: kinetic energy

$\bar{r}(\mathbf{q})$: beam model response with the input vector $\mathbf{q}$ containing multiple random variables

S_i: first order Sobol index

S_{Ti}: total order Sobol index

σ: the beam stress with the subscript indicating the direction

ΔT: temperature difference

u, w: axial and transverse displacements at any point on the rectangular solid beam

$\bar{u}, \bar{w}$: axial and transverse displacements at mid-plane of rectangular solid beams

δU: the variation of strain energy

V_c: volume fraction of material in FG beams

δV: the variation of external work done

ϕ: rotational angle about the pole axis

χ_{ij}: symmetric rotation strain gradients in micro-beams

Ω_i: multivariate orthogonal basis function for PCE

ABSTRACT

Thin-walled beams are extensively applied in multiple engineering fields such as civil, aerospace or automobile engineering thanks to their advantages in the efficient load-carrying capacity and light weight. The structural responses of various thin-walled beams' cross-section shapes are of interest in this thesis. For the static analysis, the deflection and buckling stability of the beams under different thermal and mechanical loading condition are important in the design process and therefore, requires accurate model prediction. As for the vibration analysis, the free vibration fundamental frequencies and their corresponding mode shapes are scrutinised which are often the cases of torsional modes for the open-section. These analyses provide critical insights that guide the design, optimization, and safety verification of structures utilizing the advanced composite materials. By accurately predicting how these beams will respond to various mechanical and thermal load conditions, material properties' uncertainties, shear strain effects, and size-dependent effects, engineers can design safer, more efficient, and more durable structures capable of exploiting the unique benefits of composite materials.

Past researchers have proposed thin-walled beam models such as the well-known Vlasov's model and first-order shear deformable beam theory for thin-walled beams. This thesis aims to go one step further and propose the high-order shear deformable beam theory for thin-walled composite beam. This beam model is then utilised in the stochastic analysis and size-dependent effects analysis for the laminated composite, functionally graded, and porous thin-walled beams

In the stochastic analysis, the constituent material properties are randomly changed according to the lognormal distributions. These stochastic variabilities are then propagated to the stochastic responses of the thin-walled beam through a new beam solver with hybrid series-type approximation functions. To achieve efficient evaluations for stochastic responses including natural frequencies and critical buckling loads, the polynomial chaos expansion (PCE) based surrogate model and the artificial neural network (ANN) for thin-walled composite beams is developed. The efficiency and accuracy of PCE's and ANN's results are assessed by comparing with those of crude Monte Carlo simulation (MCS).

Sensitivity analysis is carried out to compare the importance of the uncertainty in material properties to stochastic responses. New results reported in this chapter can be interesting benchmarks for scientific and engineering community in the future.

For the size-dependent effects analysis, classical continuum mechanics usually used for macro-beam is replaced by the modified couple stress theory for the ease of theoretical formulation and programming. Numerical results are employed to investigate the effects of material distribution, span-to-height's ratio, material length scale parameters on bending and vibration of microbeams for various boundary conditions.

Before carrying out the aforementioned analyses, the beam theoretical and numerical model are validated with past results. All the studies in this thesis are computed using MATLAB. Besides the accuracy, the efficiency and computing time of the beam model programs are also considered crucial by the PhD candidate.

CHAPTER 1 : INTRODUCTION

This chapter presents a comprehensive overview of composite thin-walled beams, with a particular focus on the quantification of uncertainties inherent in their analysis and design. It begins with an extensive literature review, highlighting key developments and existing gaps in the study of composite beam structures, and proceeds to outline the theoretical foundations underpinning their behavior and modeling. The uncertainty quantification aspect is explored through several probabilistic methods, studying the complexities and variabilities that challenge the predictability of these systems. Following this, the research objectives are clearly defined, aiming to address the identified gaps and contribute novel insights into the understanding and application of composite beams. The methodology section outlines the research approach, detailing the analytical and numerical techniques employed to investigate the behavior of composite and thin-walled beams under various loading and boundary conditions. Finally, the organization of the research is systematically presented, guiding the reader through the subsequent chapters. The chapters in this thesis are structured to sequentially present the theory intricacies, numerical findings, and the implications for analysis practices in engineering.

1.1 Scope

1.1.1 Composite material

Composite materials have emerged as a core element in modern engineering and materials science, revolutionizing the way we design and manufacture a diverse range of structures and products. Unlike homogeneous materials, composites are fabricated by combining two or more distinct materials, each contributing its unique properties to create a synergistic material with enhanced characteristics. This blending of materials enables the development of materials that surpass the limitations of individual constituents, offering a remarkable balance of strength, stiffness, and versatility.

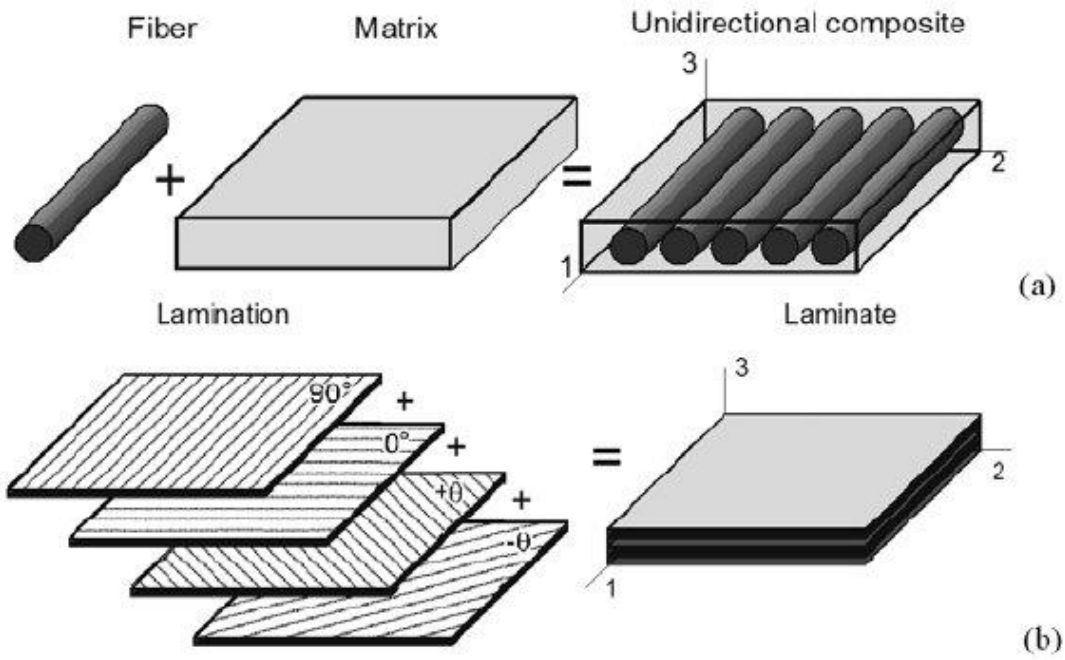

Figure 1-1: Micro- and macroscopic scales of laminated composite material [3]

The state-of-the-art manufacturing techniques enable engineers to fabricate many kinds of composites. In the later sections, functionally graded composite (FGC), laminated composite (LC), and the porous metal foam are deeply analysed and discussed. FG composites are advanced materials designed with spatially varying composition and properties to optimize performance under varying conditions. Unlike traditional composites with uniform properties throughout, FGCs exhibit a gradual transition of material properties, often in the form of a gradient. This gradient can be tailored to achieve specific functional requirements, such as variations in mechanical, thermal, or electrical properties within a single structural component. Laminated composites consist of layers (or laminates) of different materials stacked together to form a unified structure. Each layer, known as a lamina, can be composed of various materials like fibers, fabrics, or sheets, embedded in a matrix material. The arrangement and orientation of these layers contribute to the overall mechanical and physical properties of the composite. Laminated composites are characterized by their layered structure, where each layer has specific material properties. The stacking sequence and orientation of these layers can be tailored to achieve desired

mechanical characteristics, such as stiffness, strength, and durability. Laminated composite also exhibits the anisotropic properties which prove to be advantageous when the applied structural elements require specific material properties along different axes.

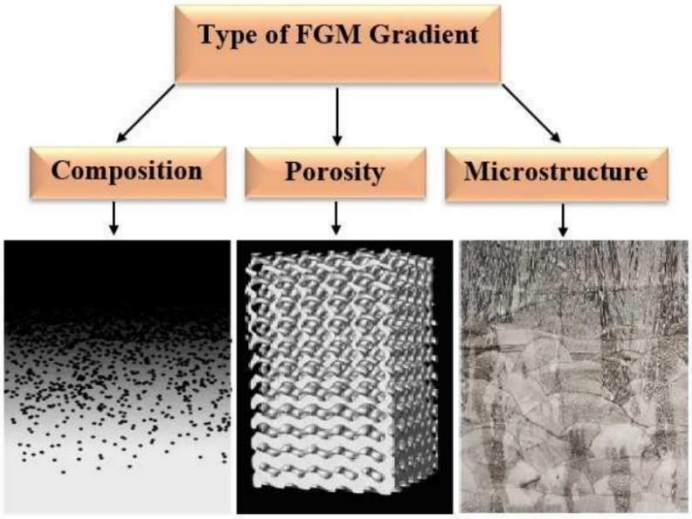

Figure 1-2: Classification of functionally graded composite material [4]

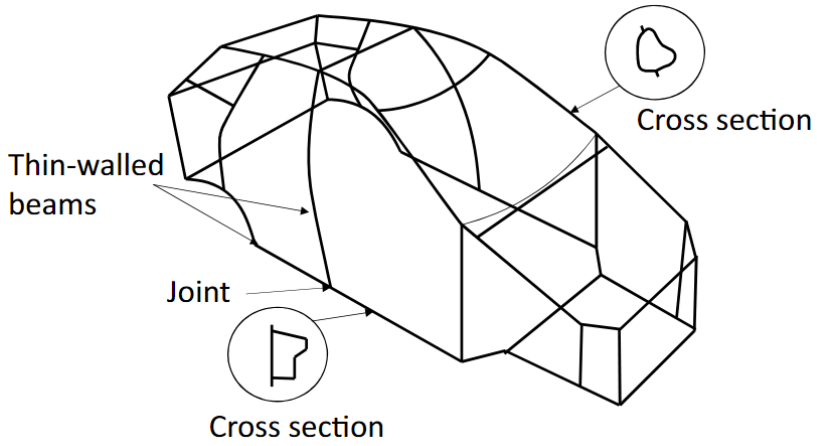

Figure 1-3: Thin-walled beams used in a passenger car [2]

These composites find applications in numerous fields, including aerospace, automotive, sport equipment, and structural engineering. They are particularly beneficial in components

exposed to extreme conditions or varying loads, where a uniform material may not provide optimal performance.

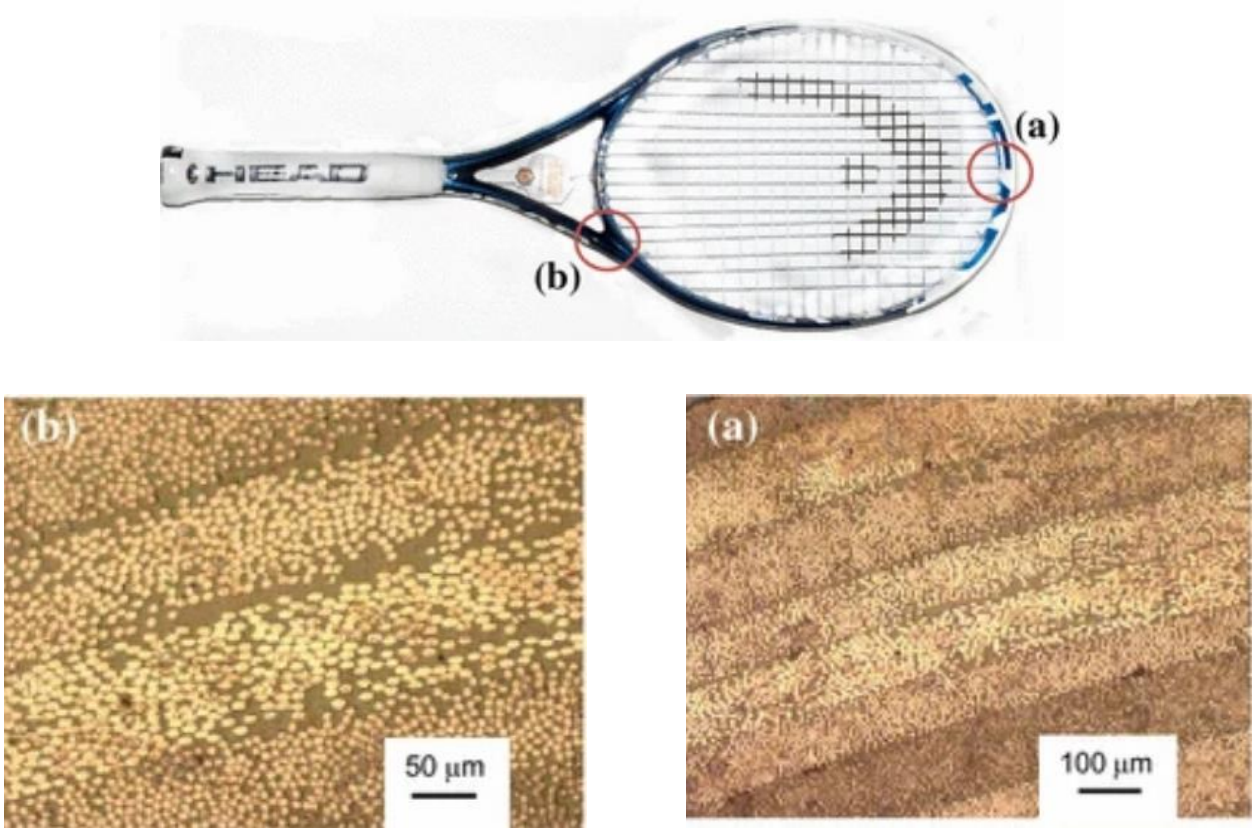

Figure 1-4: The microstructure of a graphene-reinforced tennis racquet made from carbon fibres in an epoxy resin matrix [5]

1.1.2 Thin-walled beams

Thin-walled beams are structural elements characterized by having a relatively small ratio of wall thickness to their other dimensions, such as length and width, distinguishing them with solid or thick-walled counterparts. The use and design of thin-walled beams is always driven by the need for structural efficiency, as the minimal use of material helps reduce weight while maintaining adequate strength and stiffness. For centuries, steel thin-walled beams have been used for building and bridges structures. Their behaviours and design are very well-studied as steel buildings constantly reach new heights and bridges keep increasing their span length. Nonetheless, when the newly introduced composite

material are applied into thin-walled structures and the demand for structural efficiency grows, the research for composite thin-walled structures have a lot more gaps to fill.

Key thin-walled beam sections are widely used in the industry. Closed-sectioned thin-walled beams, such as box beams, tubular sections, find applications in aerospace, automotive, or sport equipment industries as displayed in Fig. 1-4 and 1-5. The geometry of these closed sections allows for effective load distribution and resistance to torsional loads. These sections are optimized to balance between structural efficiency, weight reduction, and overall performance in specific intended structural scenarios. Meanwhile, open-sectioned thin-walled beams shown in Fig. 1-6, including C-channels, Z-channels, I-beams, and H-beams, are widely employed in the construction industry for building frames and support structures. However, they are mostly made from homogeneous material due to the fabrication expense of composites. This study aims to analyse these composite thin-walled beam sections under mechanical and thermal loads.

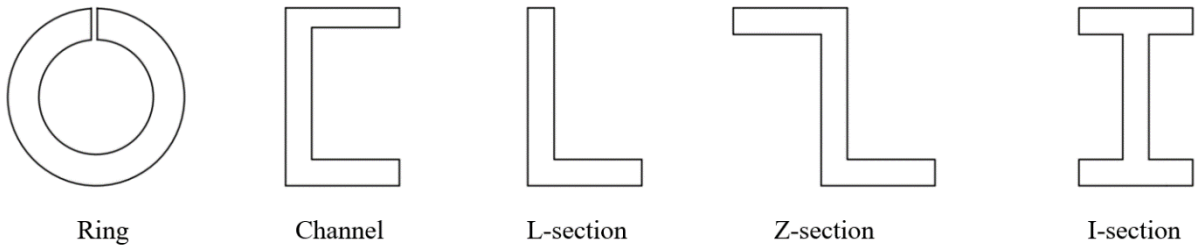

Figure 1-5: Common open thin-walled sections

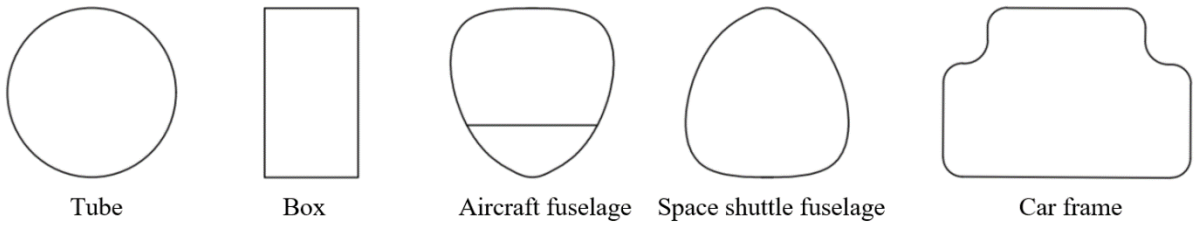

Figure 1-6 : Common closed thin-walled sections and their applications

1.1.3 Uncertainty quantification

In real-world scenarios, the characteristics of component materials unavoidably fluctuate as a result of their production processes or unforeseen elements. Therefore, the need to account for this uncertainty is of utmost importance to enhance the reliability of the beams' response prediction. Uncertainty quantification (UQ) is a multidisciplinary field that addresses the challenges associated with the inherent variability and imprecision present in engineering models. The uncertainties in beam's input parameter are propagated through the beam model and their effects on the output's distribution are quantified. There are three approaches to UQ in this thesis: Monte Carlo Simulation (MCS), Polynomial Chaos Expansion (PCE) and Artificial Neural Network (ANN).

Traditional methods, such as Monte Carlo simulations, have been widely used to address these uncertainties, but their computational expense limits their efficiency for complex systems. Stochastic finite element methods have also been employed, offering a systematic approach to incorporate variability into structural analyses. However, these methods often struggle with high-dimensional parameter spaces or require extensive computational resources. This motivates my research into advanced UQ techniques such as Polynomial Chaos Expansion (PCE) and Artificial Neural Networks (ANNs). PCE provides a highly efficient framework for representing stochastic processes, reducing computational costs while maintaining accuracy. ANNs, with their ability to model nonlinear and complex relationships, are well-suited for surrogate modeling and high-dimensional problems. By integrating these methods into the stochastic and sensitivity analysis of thin-walled composite beams, my work seeks to provide a robust, efficient, and comprehensive framework for addressing uncertainty in modern structural applications.

1.2 Literature review

In the past, numerous research works have been undertaken to study the structural responses of both solid and thin-walled composite beams, as evidenced by existing literature. Different aspects of the beam models such as beam theories, constitutive relations,

and methodologies haven been conducted. This section provides an overview of the available researches on functionally graded and composite beams. Further detailed discussion of the topic is covered in the subsequent chapters.

Regarding beam theories for solid composite beams, there are three main types: Euler-Bernoulli beam theory (EBBT), first-order shear deformation beam theory (FSBT), and higher-order shear deformation beam theory (HSBT). These theories are distinguished by the formulation of transverse shear strain. For regular homogeneous solid beams, this transverse shear strain is not significant and the EBBT is deemed sufficiently accurate in many engineering applications. Carrera et al. [14] described the EBBT and also pointed out its caveat, that is, the EBBT is only suitable for analyzing thin beams as it ignores the effects of transverse shear deformation. To overcome this limitation, the FSBT, or Timoshenko beam theory, accounts for transverse shear deformation effects and can reasonably predict the behavior of thick beams. The theory is named after Timoshenko [15], and have been utilised in many applications, such as tunneling engineering [16], civil engineering [17], micro- and nano-beams [18]. Nonetheless, in this theory, the transverse shear stress gradient is assumed to be constant across the beam's thickness. Therefore, a shear correction factor is necessary to adjust for this assumption. The HSBT was developed to better formulate the axial displacement than FSBT. The axial displacement is assumed to vary with a high-order shear function. Kadoli et al. [19] predicted the static behaviours of functionally graded (FG) beams using higher order shear deformation theory. Ferreira et al. [20] also analysed the laminated composite beams using high-order shear deformation theories. P. Subramanian [21] did the dynamic analysis of the LC beams using HSBT and finite elements. Shao et al. [22] studied the free vibration of refined higher-order shear deformation composite laminated beams with general boundary conditions. Nguyen et al. [23, 24] analysed the responses of functionally graded sandwich beams using FSBT and HSBT. It is without a doubt that HOBT can predict the behavior of beams more accurately than both CBT and FSBT. However, the effect of transverse normal deformation is neglected in this theory. For this reason, the quasi-3D theory was developed based on higher-order changes in both axial and transverse displacements. Vo et al. [23] presented a quasi-3D theory for vibration and

buckling of FG sandwich beams. Nguyen et al. [25] proposed an analytical solution for buckling and vibration analysis of functionally graded sandwich beams using a quasi-3D shear deformation theory.

In the 60s-70s, Tsai and Hahn [26] notably contributed to the fundamentals of composite material science. At the time, the theory mainly revolves around the understanding of composite materials rather than specific applications in composite thin-walled structures. Afterwards, in the 70s-80s, Timoshenko and Vlasov are known to pioneer the theories for thin-walled structures. Vlasov's classical thin-walled beam theory provided a foundation for understanding thin-walled beams. However, it assumes shear deformation is negligible, limiting its applicability for composite materials with complex layups or large deformation scenarios. For decades, many authors have made improvements based on the Vlasov's theory to analyse the behaviours of thin-walled composite beams. Later, the first-order shear deformation thin-walled beam theory extended these concepts by incorporating shear deformation and transverse shear stiffness, improving accuracy for composite beams. Despite its advancements, FSBT assumes a constant shear strain distribution across the thickness, which can be overly simplistic for highly anisotropic materials or thick-walled structures. This motivates my research into higher-order shear deformation thin-walled beam theory, which aims to capture more realistic transverse shear strain distributions and warping effects, providing greater precision for modern applications. The review of laminated composite and functionally graded beams are thoroughly presented by Sayyad and Ghugal [27].

1.3 Theory overview

1.3.1 Solid beam theory

The development of thin-walled beam theories draws significantly from the foundational principles of solid beam theories, including Euler-Bernoulli, Timoshenko, and higher-order shear deformation beam theories (HSBT). The transition involves modifying shear deformation assumptions, incorporating warping effects, and redefining displacement fields to accommodate the multi-dimensional nature of thin-walled geometries. Euler-

Bernoulli theory provides the foundational basis for slender, bending-dominated behaviors, while Timoshenko theory introduces shear deformation and rotational effects. Higher-order shear deformation theories further refine these models by capturing non-linear variations in shear strain across the wall thickness, which is essential for advanced composite materials. This section underscores the basics of solid beam theories that can be transferred to the thin-walled beams.

Composite solid beams have been applied in various engineering fields due to their advantages in versatility, strength and stiffness. Its properties can be engineered to adapt to various requirements for the structure. Many beam models have been developed to accurately predict the behavior of composite beams, which can be distinguished between the following theoretical frameworks: Classical Beam Theory (CBT), First-Order Shear Deformation Theory (FSBT), Higher-Order Shear Deformation Theory with high-order variation of axial displacement (HOBT), and high-order theory approaching three dimensions with high-order changes of both axial and transverse displacements (quasi-3D).

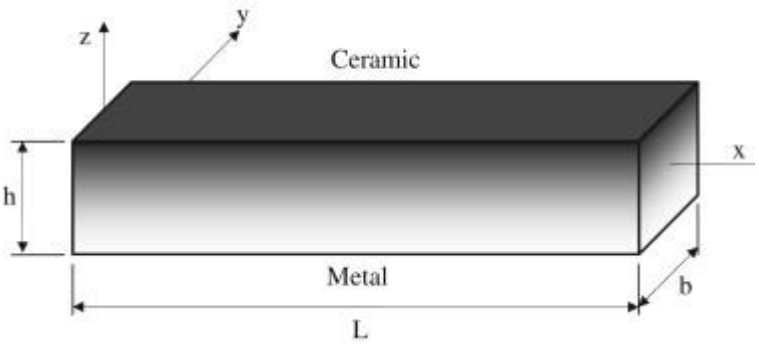

Figure 1-7: FGC solid beam

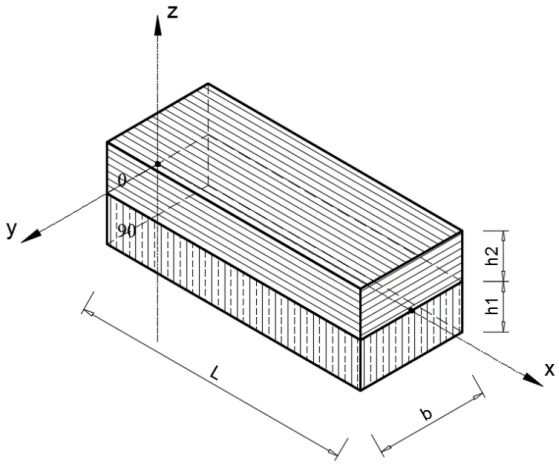

Figure 1-8: LC solid beam

-The Euler-Bernoulli beam theory: also known as the classical beam theory, assumes that the cross-section of the beam remains straight and perpendicular to the neutral axis before and after deformation. Based on this assumption, the displacement field is expressed as follows:

$$u(\mathrm{x},\mathrm{z},\mathrm{t}) = u_0(x,t) - z\mathrm{w}_{0,x} \tag{1-1a}$$

$$w(x,z,t) = w_0(x,t) \tag{1-1b}$$

where $\mathrm{u}_0, \mathrm{w}_0$ are the axial displacement and transverse displacement at the beam's neutral axis. This theory overestimates the stiffness of the beam and its applicability is restricted to slender beams with large length-to-depth ratio.

-The Timoshenko beam theory: addresses some of the limitations inherent in the Euler-Bernoulli beam theory. Timoshenko beam theory takes into account the effects of shear deformation and rotational inertia. This makes it more accurate for a wider range of beams, especially those that are short, thick, or subjected to high-frequency loading. The displacement field is given as:

$$u(\mathrm{x},\mathrm{z},\mathrm{t}) = u_0(x,t) + z\theta_0(x,t) \tag{1-2a}$$

$$w(x,z,t) = w_0(x,t) \tag{1-2b}$$

where ϕ is the rotation angle of the cross-section with respect to the $y-$ axis due to bending and shear. The Timoshenko beam has three variables and accounts for the effect of transverse shear deformation, thus providing a more appropriate prediction of beam behavior compared to the Euler-Bernoulli beam. However, because the transverse shear deformation is constant along the length of the beam, this leads to an unrealistic distribution of shear stress. Therefore, a shear correction factor is added to adjust the calculation of the shear force, and a factor of 5/6 is commonly used. In practice, this beam theory has been applied in the majority of commercial software.

-The Higher-Order shear deformation theory: includes higher-order terms in the displacement field equations, allowing for a more accurate representation of the shear deformation throughout the depth of the beam. This is crucial for accurately predicting the behavior of thick beams, composite beams, and beams made of materials with a low modulus of elasticity. The displacement field is as follows:

$$u(\mathrm{x},\mathrm{z},\mathrm{t}) = u_0(x,t) - \mathrm{z}\,\mathrm{w}_{0.x} + f(z)\theta_0(x,t) \tag{1-3a}$$

$$w(x,z,t) = w_0(x,t) \quad (1\text{-}3b)$$

where $f(z)$ is the high-order shear function. This function has been proposed by many past authors based on the following conditions: $f'(z = \pm h/2) = 0$ and $f(z)$ must be continuous in the z domain.

-The Quasi-3D beam theory: bridge the gap between two-dimensional beam theories and fully three-dimensional elasticity solutions. Unlike the aforementioned beam theories, which simplify the stress and strain within the beam to a one- or two-dimensional problem, quasi-3D beam theory incorporates aspects of three-dimensional stress and strain. This approach allows for a more accurate representation of the physical behavior of beams, including the effects of lateral strains and out-of-plane deformations. The displacement field contains four variables $u_0, \mathrm{w}_0, \theta_0, \mathrm{w}_{z0}$ to be solved:

$$u(\mathrm{x},\mathrm{z},\mathrm{t}) = u_0(x,t) - \mathrm{z}\,\mathrm{w}_{0.x} + f(z)\theta_0(x,t) \quad (1\text{-}4a)$$

$$\mathrm{w}(\mathrm{x},\mathrm{z},\mathrm{t}) = \mathrm{w}_0(x,t) + \mathrm{g}(\mathrm{z})\mathrm{w}_{z0}(x,t) \quad (1\text{-}4b)$$

It is worth noting that the more complex the theory is, the more versatile and accurate the beam analysis becomes. The better accuracy comes with the increased cost of computational resource.

1.3.2 Thin-walled beam theory

In the 2000s-2010s, the researches delved into material optimization and advanced manufacturing techniques for thin-walled composite beams. Thostenson et al. [28] gave a review on advances in the science and technology of carbon nanotubes and their composites. Gay and Suong [29] focused on optimizing the design and manufacturing of thin-walled composite beams to achieve better performance and efficiency. Librescu and Song [30] contributed greatly to the theory and applications of thin-walled composite beams. Vo et al. [31] developed the finite element model for vibration and buckling of functionally graded sandwich beams based on a refined shear deformation theory. Nguyen et al. [32] proposed a new trigonometric-series solution for analysis of laminated composite beams. Lee et al. [33-36] contributed many analyses for thin-walled composite beams This period also saw

advancements in material science, leading to the development of new composite materials with enhanced properties.

In recent years (2020s), research has been exploring more sophisticated areas such as the use of nano-materials in composites, the stochastic behaviours of composites, and smart composite materials that can adapt to changing conditions. For nano- and micro-structures, Ghane et al. [37] studied the vibration of fluid-conveying nanotubes subjected to magnetic field based on the thin-walled Timoshenko beam theory. Xie et al. [38] exprimented and modelled the vibration of multi-scale sandwich micro-beams. ND Nguyen et al. [39] investigated the LC micro-beam based on the modified couple stress theory using a Ritz type solution with exponential trial functions. Roudbari et al. [40] wrote an extensive review of size-dependent continuum mechanics models for micro- and nano-structures. For stochastic analysis and uncertainty quantification of composite beams, several latest researches have been conducted by MC Trinh et al. [41, 42], Sharma et al. [43], and Thuan N. and T. Hien [44]. The responses of thin-walled composite beams when exposed to thermal environment are also paid attention by many researchers. Shen et al. [45] made comparison of various thin-walled composite beams models for thermally induced vibrations of spacecraft boom. Simonetti et al. [46] analysed the thermal buckling of thin-walled closed section FG beams. TK Nguyen et al. [47] researched the hygro-thermal effects on vibration and thermal buckling behaviours of functionally graded beams. These current topics in the researches of composite thin-walled structures are the pillars of this thesis.

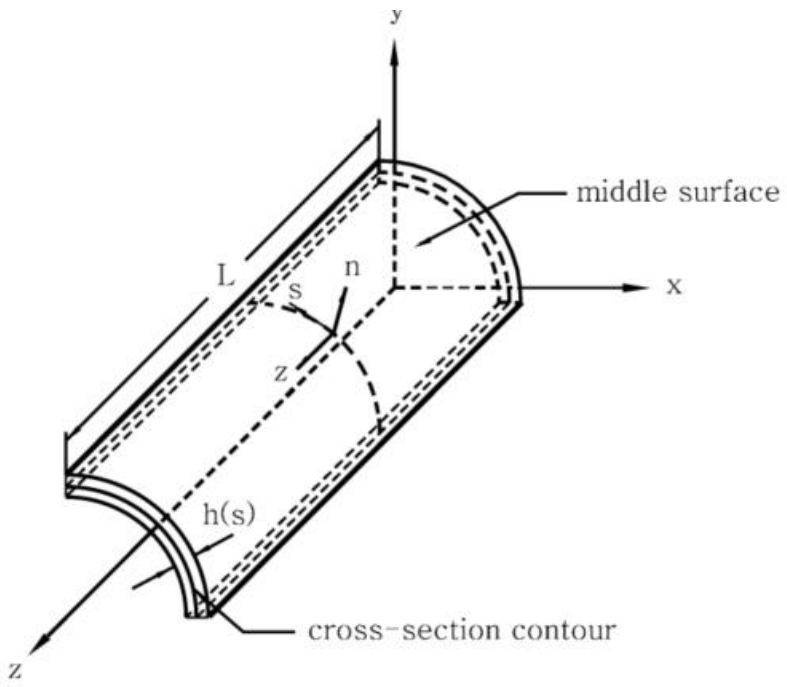

Figure 1-9: Geometry of an arbitary thin-walled beam [48]

Based on the definition of Vlasov [49], thin-walled beams are beams with $\frac{h}{l} \le 0.1$ and $\frac{l}{L} \le 0.1$, where h is the wall thickness, l is any characteristic dimension of the cross-section, and L is the beam length. The wall thickness can only vary along the beam's cross section contour, but remains constant along the beam span.

A same set of coordinates for the analysis of thin-walled beams is used throughout this thesis. Cartesian coordinate system (x, y, z), local plate coordinate system (n, s, z) and contour coordinate s along the profile of the section are considered. It is assumed that θ is an angle of orientation between (n, s, z) and (x, y, z) coordinate systems, the pole P with coordinates (x_P, y_P) is the shear center of the section.

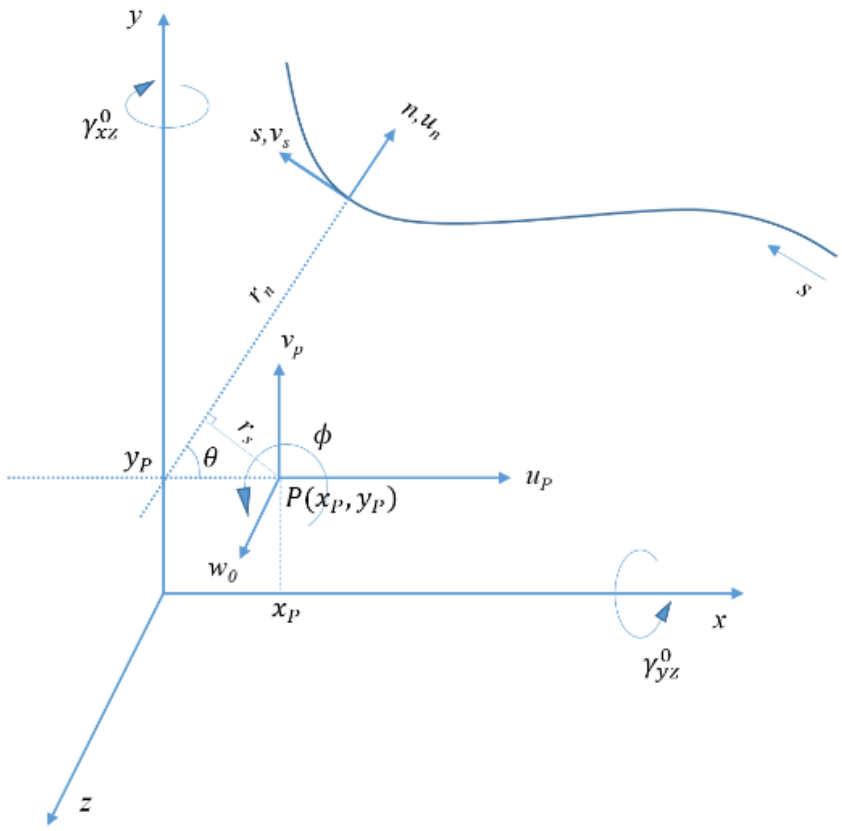

Figure 1-10: Thin-walled coordinate systems

In order to formulate the mathematical model for thin-walled beams, the theory is built upon the following assumptions:

1) The shape and geometry of the beam's cross section remain rigid in its own plane but can warp out of its original planes.

2) The transverse shear strains γ_{yx}^0, γ_{zx}^0, and the warping strain γ_{ω}^0 are uniform over the beam cross-section

3) Local buckling and pre-buckling deformation are neglected

Based on Assumption 1, the section can only displace as a rigid body, which translates to the fact that the displacements of any point on the contour can be expressed in terms of the displacement at an arbitrary point $P(\mathrm{u}_P, \mathrm{v}_P)$. The displacements $u(n,s,z,t)$ and $v(n,s,z,t)$ at any points of the beam cross-section under

a small rotation $\phi(z,t)$ about the pole axis can be expressed in terms of those at the pole $u_P(z,t)$ and $v_P(z,t)$ in $x-$ and $y-$directions, respectively, as follows:

$$u(n,s,z,t) = u_P(z,t) - (y - nx_{,s} - y_P)\phi(z,t) = u_P(z,t) - (Y - y_P)\phi(z,t) \quad (1\text{-}5a)$$

$$v(n,s,z,t) = v_p(z,t) + (x + ny_{,s} - x_P)\phi(z,t) = v_p(z,t) + (X - x_P)\phi(z,t) \quad (1\text{-}5b)$$

where the comma in the subscript is used to indicate the differentiation with respect to the variable that follows, $y_{,s}$ and $x_{,s}$ are the trigonometric functions $\cos\theta$ and $-\sin\theta$ respectively (see Fig. 1-8). X, Y are the coordinates of an arbitrary point along the n axis. Using the transformation rule for the (x, y, z) and (n, s, z) coordinate systems, the membrane shear strain γ_{sz} can be expressed in terms of the transverse shear components γ_{xz} and γ_{yz}:

$$\gamma_{sz} = \gamma_{xz}x_{,s} + \gamma_{yz}y_{,s} + \gamma_t(n,s) = u_{t,s} + w_{,s} \quad (1\text{-}6)$$

where $x_{,s} = -\sin\theta$ and $y_{,s} = \cos\theta$, $\gamma_t(n,s) = 2n\phi_{,z}$ for open section, and $\gamma_t(n,s) = \left(2n + \frac{2\Omega}{\beta}\right)\Phi_{,z}$ for closed section. ϕ is the rotation about point P, Ω is the area enclosed by the contour line of the beam cross-section, β is the contour line's perimeter. By rearranging the Eq. (1-1 to 1-6) to isolate the $w_{,s}$ on one side and integrate both sides with respect to s, the axial displacement $w(n,s,z,t)$ is expressed as:

$$w(n,s,z,t) = w_0(z,t) + (\gamma_{xz} - u_{P,z})\,\mathrm{X(s)} + (\gamma_{yz} - v_{P,z})Y(s) - \phi_{,z}\int \mathrm{R}_n(\mathrm{s})\,\mathrm{ds} \quad (1\text{-}7)$$

$\int \mathrm{R}_n(\mathrm{s})\,\mathrm{ds}$ represents twice the are swept by R_n from point P and along the contour line.

1.3.3 Composite materials' constitutive relations

There are three main types of composote materials used in this thesis: laminated composite material, functionally graded material, and porous metal foam material. The effects of anisotropy in these composite materials allow designer to efficiently aligning the material's structure with the load paths, therefore, reducing structures' weight without compromising strength. These effects are described through the constitutive relation equations shown below.

Based on Hooke's law, the stress-strain relations for anisotropic materials can be expressed in matrix form as follows:

$$\begin{bmatrix} \sigma_{11} \\ \sigma_{22} \\ \sigma_{33} \\ \sigma_{23} \\ \sigma_{13} \\ \sigma_{12} \end{bmatrix} = \begin{bmatrix} C_{11} & C_{12} & C_{13} & C_{14} & C_{15} & C_{16} \\ C_{12} & C_{22} & C_{23} & C_{24} & C_{25} & C_{26} \\ C_{13} & C_{23} & C_{33} & C_{34} & C_{35} & C_{36} \\ C_{14} & C_{24} & C_{34} & C_{44} & C_{45} & C_{46} \\ C_{15} & C_{25} & C_{35} & C_{45} & C_{55} & C_{56} \\ C_{16} & C_{26} & C_{36} & C_{46} & C_{56} & C_{66} \end{bmatrix} \begin{bmatrix} \varepsilon_{11} \\ \varepsilon_{22} \\ \varepsilon_{33} \\ \gamma_{23} \\ \gamma_{13} \\ \gamma_{12} \end{bmatrix} \tag{1-8}$$

where σ_{ij} are the stress components, ε_{ij} are the axial strain components, and γ_{ij} are the shear strain components. The directions of these components can be referred to Fig. 1-11.

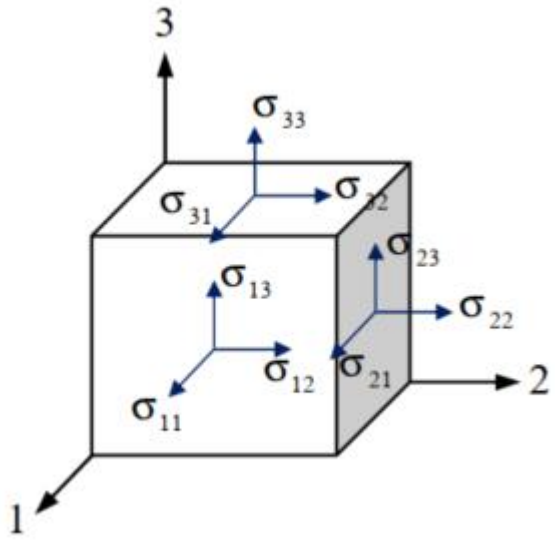

Figure 1-11: Stress and strain component in the coordinate system

-For orthotropic materials, the stress-strain inverse relations can be commonly written as:

$$\begin{bmatrix} \varepsilon_{11} \\ \varepsilon_{22} \\ \varepsilon_{33} \\ \gamma_{23} \\ \gamma_{13} \\ \gamma_{12} \end{bmatrix} = \begin{bmatrix} \frac{1}{E_1} & \frac{-\nu_{12}}{E_1} & \frac{-\nu_{13}}{E_1} & 0 & 0 & 0 \\ \frac{-\nu_{12}}{E_1} & \frac{1}{E_2} & \frac{-\nu_{23}}{E_2} & 0 & 0 & 0 \\ \frac{-\nu_{13}}{E_1} & \frac{-\nu_{23}}{E_2} & \frac{1}{E_3} & 0 & 0 & 0 \\ 0 & 0 & 0 & \frac{1}{G_{23}} & 0 & 0 \\ 0 & 0 & 0 & 0 & \frac{1}{G_{13}} & 0 \\ 0 & 0 & 0 & 0 & 0 & \frac{1}{G_{12}} \end{bmatrix} \begin{bmatrix} \sigma_{11} \\ \sigma_{22} \\ \sigma_{33} \\ \sigma_{23} \\ \sigma_{13} \\ \sigma_{12} \end{bmatrix} \tag{1-9}$$

where E, v, G are the Young's moduli, Poisson ratios, and shear moduli respectively. Under plane stress condition, $\sigma_{23} = \sigma_{33} = \sigma_{13} = 0$, Eq. (1-9) becomes:

$$\begin{bmatrix} \varepsilon_{11} \\ \varepsilon_{22} \\ \gamma_{12} \end{bmatrix} = \begin{bmatrix} \frac{1}{E_1} & \frac{-\nu_{12}}{E_1} & 0 \\ \frac{-\nu_{12}}{E_1} & \frac{1}{E_2} & 0 \\ 0 & 0 & \frac{1}{G_{12}} \end{bmatrix} \begin{bmatrix} \sigma_{11} \\ \sigma_{22} \\ \sigma_{12} \end{bmatrix} \tag{1-10}$$

The stress-strain relations can also inversely deduced:

$$\begin{bmatrix} \sigma_{11} \\ \sigma_{22} \\ \sigma_{12} \end{bmatrix} = \begin{bmatrix} \frac{E_1}{1-\nu_{12}\nu_{21}} & \frac{\nu_{12}E_2}{1-\nu_{12}\nu_{21}} & 0 \\ \frac{\nu_{12}E_2}{1-\nu_{12}\nu_{21}} & \frac{E_2}{1-\nu_{12}\nu_{21}} & 0 \\ 0 & 0 & G_{12} \end{bmatrix} \begin{bmatrix} \varepsilon_{11} \\ \varepsilon_{22} \\ \gamma_{12} \end{bmatrix} = \begin{bmatrix} Q_{11} & Q_{12} & 0 \\ Q_{12} & Q_{22} & 0 \\ 0 & 0 & Q_{66} \end{bmatrix} \begin{bmatrix} \varepsilon_{11} \\ \varepsilon_{22} \\ \gamma_{12} \end{bmatrix} \tag{1-11}$$

For laminated composite material, the fibre angle in each ply can rotate through an angle with respect to the global coordinate system. These transformed stiffness coefficients $\overline{Q}_{ij}$ of each layer can be derived from the reduced stiffness coefficients Q_{ij} as:

$$
\begin{aligned}
\bar{Q}_{11} &= Q_{11}c^4 + Q_{22}s^4 + 2\left(Q_{12} + 2Q_{66}\right)s^2c^2 \\
\bar{Q}_{12} &= \left(Q_{11} + Q_{22} - 4Q_{66}\right)s^2c^2 + Q_{12}\left(s^4 + c^4\right) \\
\bar{Q}_{16} &= \left(Q_{11} - Q_{12} - 2Q_{66}\right)sc^3 + \left(Q_{12} - Q_{22} + 2Q_{66}\right)s^3c \\
\bar{Q}_{22} &= Q_{11}s^4 + Q_{22}c^4 + 2\left(Q_{12} + 2Q_{66}\right)s^2c^2 \\
\bar{Q}_{26} &= \left(Q_{11} - Q_{12} - 2Q_{66}\right)s^3c + \left(Q_{12} - Q_{22} + 2Q_{66}\right)sc^3 \\
\bar{Q}_{66} &= \left[Q_{11} + Q_{22} - 2\left(Q_{12} + Q_{66}\right)\right]s^2c^2 + Q_{66}\left(s^4 + c^4\right)
\end{aligned}
\tag{1-12}
$$

where c and s are $\cos\theta$ and $\sin\theta$, θ is the rotation angle . The reduced constitutive equations at the k^{th} – layer is given by:

$$
\begin{Bmatrix} \sigma_z \\ \sigma_{sz} \\ \sigma_{nz} \end{Bmatrix} = \begin{pmatrix} P_{11} & P_{16} & 0 \\ P_{16} & P_{66} & 0 \\ 0 & 0 & P_{55} \end{pmatrix} \begin{Bmatrix} \varepsilon_z \\ \gamma_{sz} \\ \gamma_{nz} \end{Bmatrix} \tag{1-13}
$$

where $P_{11} = \bar{Q}_{11} - \dfrac{\bar{Q}_{11}^2}{\bar{Q}_{22}}$, $P_{16} = \bar{Q}_{16} - \dfrac{\bar{Q}_{12}\bar{Q}_{26}}{\bar{Q}_{22}}$, $P_{66} = \bar{Q}_{66} - \dfrac{\bar{Q}_{26}^2}{\bar{Q}_{22}}$, $P_{55} = \bar{Q}_{55}$; $\bar{Q}_{ij}$ are the reduced stiffness components of materials (see [50] for more details).

-Functionally graded material:

$$
\begin{Bmatrix} \sigma_z \\ \sigma_{sz} \\ \sigma_{nz} \end{Bmatrix} = \begin{pmatrix} Q_{11} & 0 & 0 \\ 0 & Q_{66} & 0 \\ 0 & 0 & Q_{55} \end{pmatrix} \begin{Bmatrix} \varepsilon_z \\ \gamma_{sz} \\ \gamma_{nz} \end{Bmatrix} \tag{1-14}
$$

where $Q_{11} = E(n)$, $Q_{66} = Q_{55} = \dfrac{E(n)}{2(1+\nu)}$; $E(n)$ is Young's modulus; ν is Poisson's coefficient which is supposed to be constant. The effective mass density ρ and Young's modulus E of the FG sandwich thin-walled beam are approximated by:

$$\rho = \rho_c V_c + \rho_m\left(1 - V_c\right) \tag{1-15a}$$

$$E = E_c V_c + E_m\left(1 - V_c\right) \tag{1-15b}$$

where the subscripts c and m are used to indicate the ceramic and metal constituents, respectively; V_c is the volume fraction of ceramic material.

-Porous metal foam material:

$$\begin{Bmatrix}\sigma_{33}\\ \sigma_{s3}\\ \sigma_{n3}\end{Bmatrix}=\begin{pmatrix}Q_{11} & 0 & 0\\ 0 & Q_{66} & 0\\ 0 & 0 & Q_{55}\end{pmatrix}\begin{Bmatrix}\varepsilon_{33}\\ \gamma_{s3}\\ \gamma_{n3}\end{Bmatrix} \tag{1-16}$$

where $Q_{11}=E(n)$, $Q_{66}=Q_{55}=\dfrac{E(n)}{2(1+\nu)}$; $E(n)$ is Young's modulus; ν is constant Poisson's ratio. Two porosity patterns [51-53] of PMF thin-walled beams are considered:

Symmetric pore distribution:

$$E(n)=E_{\max}\left(1-e_0\cos\left(\frac{\pi n}{h}\right)\right) \tag{1-17a}$$

$$\rho(n)=\rho_{\max}\left(1-e_m\cos\left(\frac{\pi n}{h}\right)\right) \tag{1-17b}$$

Asymmetric pore distribution:

$$E(n)=E_{\max}\left[1-e_0\cos\left(\frac{\pi n}{2h}+\frac{\pi}{4}\right)\right] \tag{1-18a}$$

$$\rho(n)=\rho_{\max}\left[1-e_m\cos\left(\frac{\pi n}{2h}+\frac{\pi}{4}\right)\right] \tag{1-18b}$$

where: $E_{\max}$ and $\rho_{\max}$ are the maximum values of Young's modulus and mass density, respectively; e_0 and $e_m=1-\sqrt{1-e_0}$ are the porosity parameters; $\rho(n)$ is mass density of the PMF thin-walled beams.

1.3.4 Stochastic analysis

Stochastic analysis is a branch of computing science and mathematics that study the randomness in a system or process. It is widely used in many fields such as finance, physics, biology and engineering. The theory foundation of this study branch trace back to Norbert Wiener's work in the 1940s, famously called the Wiener process, that investigate the one-dimensional Brownian motion. This theory introduced the idea that a stochastic process could be decomposed into a series of orthogonal polynomial functions of random variables, and has been deeply discussed by Szabados [54]. With the advances of the computing systems in the 1990s, Ghanem and Spanos presented the use of polynomial chaos for

arbitrary distributions. Andrew and Askey [55] contributed to the polynomial chaos theory by proposing the Askey scheme which organises the orthogonal polynomials and expands the understanding of the stochastic processes. From the 2000s to present, the increasing computational resources and state-of-the-art numerical algorithms have been propelling the use of the polynomial chaos expansion (PCE) across various fields. [56-58]

In this thesis, the stochastic analysis is applied for thin-walled composite beams to study how the random variables of the beam's parameters affect the beam's mechanical responses. These three techniques are depicted briefly below and more detailed in the chapter Four: Monte Carlo Simulation (MCS), Polynomial Chaos Expansion (PCE), and Artificial Neural Network (ANN).

-Monte Carlo Simulation (MCS): the MCS is simply a technique that generate random input samples, and observe how the randomness impacts the outputs. These inputs and outputs can be probabilistic, and are subjected to the physical nature of the variables. The expected value of a random variable can be estimated using Monte Carlo simulation by averaging the outcomes of N simulations:

$$E(X) = \mu \approx \frac{1}{N}\sum_{i=1}^{N} X_i \tag{1-19}$$

where N is the number of simulations, X_i is the output value of the i^{th} simulation. Similarly, other statistical metrics of the output(s), for instance, the variance can be estimated as follows:

$$\sigma^2 \approx \frac{1}{N-1}\sum_{i=1}^{N} (X_i - \mu)^2 \tag{1-20}$$

Among the 3 techniques, MCS is the simplest in term of mathematical formulation, and can give the most accurate representation of the beams' outcomes. However, the accuracy can come with an expensive computing cost, especially when the number of random input variables and samples increases. The PCE and ANN are modern techniques that help overcomes the MCS's problem while achieving the same level of accuracy.

-Polynomial Chaos Expansion (PCE): the PCE represents the uncertain parameters in a system as a series of polynomial of random variables multiplied by respective coefficients.

These polynomials are chosen to be orthogonal with respect to the probability distribution of the inputs.

$$\hat{u} \simeq \hat{u}_{PCE}(\mathbf{x}) = \sum_{i=0}^{P-1} c_i He_i(\mathbf{q}) + \varepsilon \tag{1-21}$$

where responses $\hat{u}$ of FG sandwich thin-walled beams $\hat{u}_{PCE}$ are the responses of interest obtained from PCE; $\mathbf{q}$ is a vector of independent random variables in the PCE space mapped to physical random parameters x; He_i are multivariate orthogonal basis functions, which depends on the probability distribution of the random inputs; c_i are coefficients to be determined so that the residual ε is minimized

In this thesis, the residual ε is minimized by the means of least-square regression and Gaussian quadrature method.

-Artificial Neural Network (ANN): ANNs are computational models inspired by the human brain, used extensively in machine learning. As shown in the Fig. 1-12 below, there are three main types of layers in ANN: Input layer, Hidden layer, and Output layer. The hidden layers are where most of the computation is performed. Each connection between neurons has an associated weight, and each neuron has a bias term. These are the parameters the network learns during training. The blue arrows denote the forward propagation while the red arrows denote the backward propagation.

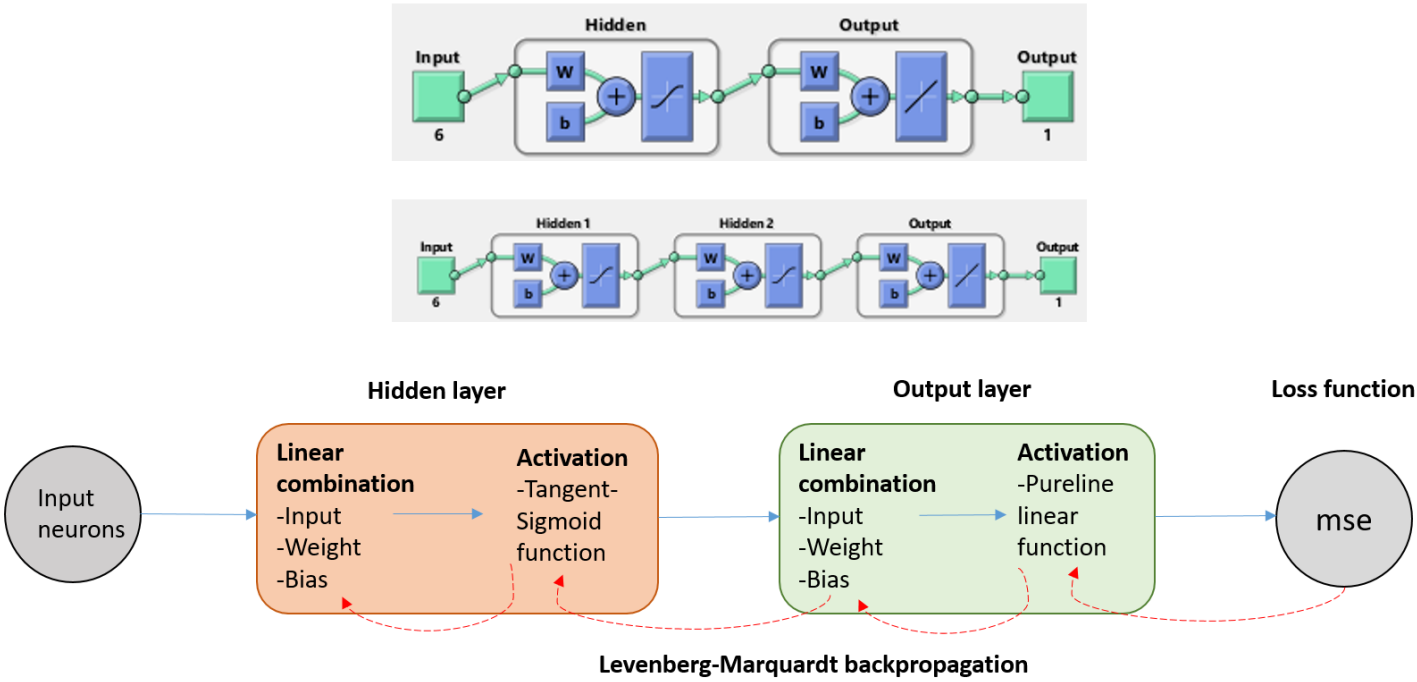

Figure 1-12: Artificial neural network workflow [1]

In each neuron, the input values are multiplied by weights and summed up, then a bias is added:

$$y = w_1 x_1 + w_2 x_2 + \ldots + w_n x_n + b \tag{1-22}$$

where y is the result of the linear combination, w_i are the weights, x_i are the input values, and b is the bias. The result of the linear transformation is passed through an activation function. This function introduces non-linearity, allowing the network to learn complex patterns. Common activation functions are Rectified Linear Unit, Sigmoid, and Tanh functions.

In backward propagation, the loss function measures the difference between the network's prediction and the actual target values. The training loop is stopped when the loss function reaches the required accuracy. The weights and biases are repetitively adjusted to minimize the loss. This involves computing the gradient of the loss function with respect to each weight and bias in the network using partial differentiation. After computing gradients, weights are updated typically using a rule like:

$$w_{new} = w_{old} - \alpha \frac{\partial lossfunction}{\partial w} \tag{1-23}$$

where α is the learning rate, a hyper parameter that controls the step size of the update. It is common to choose the mean square error (MSE) as the loss function for training the ANN. This MSE is expressed as below:

$$MSE = \frac{1}{N_{train}} \sum_{i=1}^{N_{train}} (\mathrm{y}_i - \bar{y}_i)^2 \tag{1-24}$$

where N_{train} is the number of training samples, y_i is the true output data, $\bar{y}_i$ is the predicted output value of the i^{th} sample. Even though the ANN has been recently applied for the behaviour prediction of thin-walled beams [59-61], there is no research that conduct a thorough comparison between MCS, PCE, and ANN for the stochastic analysis of thin-walled composite beams. This gap is considered in the latter chapter of this thesis.

1.4 Research objectives

The research objectives for this PhD thesis are the study of composite thin-walled beams using MATLAB and higher-order shear deformable theory, coupled with the uncertainty quantification, size-dependent effects on micro-beams, and thermal buckling phenomena. This PhD thesis makes significant contributions to the study of composite thin-walled beams by addressing key challenges in their analysis through the development of advanced computational frameworks and methodologies. Specifically, the contributions of this thesis are as follows:

- *Development of a Higher-Order Shear Deformable Computational Framework*: A robust MATLAB-based computational tool is developed and validated to implement higher-order shear deformation theory for composite thin-walled beams, including laminated, functionally graded, and porous metal foam configurations. This framework improves accuracy in predicting mechanical behavior under diverse loading conditions.
- *Investigation of Material Heterogeneity Effects*: The thesis provides a detailed analysis of how material heterogeneity, including variations in composition and

distribution in functionally graded, laminated composite, and porous metal foam beams, affects mechanical properties and structural performance.

- *Quantification of Uncertainties*: A novel integration of probabilistic methods enables the quantification of uncertainties in material properties, geometric imperfections, and loading conditions. The study demonstrates how these uncertainties influence the mechanical response of composite thin-walled beams, paving the way for more reliable designs.
- *Analysis of Size-Dependent Effects on Micro-Beams*: The research delves into the size-dependent behavior of composite micro-beams, contributing to the understanding of scale effects in micro-structural applications, a topic of growing importance in advanced material design.
- *Thermal Buckling Behavior Analysis*: This thesis examines thermal buckling phenomena in composite thin-walled beams under various thermal loading scenarios, providing insights into the effects of temperature gradients and thermal loads on structural stability.
- *Model Validation*: The computational models are rigorously validated through comparative analysis with existing analytical, numerical, and experimental results from the literature, ensuring their accuracy and reliability.
- *Practical Design Guidelines*: The thesis offers comprehensive guidelines for the design and analysis of composite thin-walled beams, integrating the impacts of material heterogeneity, uncertainty, size-dependent effects, and thermal loads to optimize structural performance.

By achieving these objectives, this thesis aims to advance the state of knowledge in the field of composite thin-walled beams, providing a robust computational tool for other researchers, and proposing the optimization approaches for these critical structural elements.

1.5 Research method and Organisation

In each of the following chapters, the data are presented in the order based on the research method. The thin-walled beam models and simulations are verified with multiple

notable articles and experimental results. Subsequently, the parametric studies are conducted with a range of input parameters fed into this thesis's simulation models. This sequence of research method ensures the accuracy and validity of the new contributions.

This thesis consists of seven chapters:

-Chapter 1 gives an introduction to the purpose and scope of this thesis.

-Chapter 2 presents the flexural and vibration analysis of higher-order shear deformable laminated composite solid beam. The cases considered are for the deterministic and random beams' inputs.

-Chapter 3 proposes a general higher-order shear deformation theory for buckling and free vibration analysis of laminated thin-walled composite I-beams. This general theory can be used to model either a CTWBT, FTWBT or HTWBT.

-Chapter 4 incorporates the effects of thermal loads on the composite thin-walled beams

-Chapter 5 presents the stochastic analysis of thin-walled composite beams using PCE and ANN

-Chapter 6 accounts for the size-dependent effects of the micro thin-walled composite beams

-Chapter 7 covers the functionally graded porous thin-walled beams with closed section

-Chapter 8 summarises the key points in this thesis and lists some directions for the future studies.

CHAPTER 2 : FLEXURAL AND VIBRATION ANALYSIS OF LAMINATED COMPOSITE SOLID BEAMS FOR THE DETERMINISTIC AND STOCHASTIC CASES

This chapter lays the groundwork for the subsequent investigation of thin-walled composite beams, highlighting the need for advanced modeling techniques, stochastic analysis, and computational approaches to capture the unique characteristics of composite and functionally graded materials. By bridging classical beam mechanics with modern thin-walled structures, this work provides a unified perspective on the evolution of beam theories and their application in contemporary structural analysis. Uncertainty in material properties and external loads can significantly influence the vibration and static responses of laminated composite beams, making the conventional deterministic beam models insufficient. This chapter addresses this necessity by presenting a novel methodology to efficiently assess these uncertainties using surrogate models based on polynomial chaos expansion (PCE). The approach minimizes computational demands while maintaining high accuracy, leveraging a small training sample size computed via a high-order shear beam model. This deterministic model is rigorously verified and solved using Hamilton's principle and Ritz's method with trigonometric series approximations. The study predicts the statistical moments and probability distributions of key response metrics, including the mid-span displacement and fundamental frequency, and conducts a global sensitivity analysis to evaluate the influence of stochastic variations in material properties and loads. The proposed PCE models, using spectral projection and linear regression techniques, demonstrate a substantial reduction in computational cost compared to Monte Carlo simulations (MCS), with negligible compromise in precision. As most real-world systems are subjected to multiple sources of uncertainty, this chapter provides a state-of-the-art method to quantify such uncertain parameters more efficiently and allow for a better reliability assessment in composite solid beam design.

2.1. Introduction

Composite materials have steadily increased their applications across various engineering disciplines. This can be attributed to their mechanical benefits, including superior strength- and stiffness-to-weight ratios compared to conventional materials. The laminated composite material also enables engineers to control the structures' properties by merely choosing the optimal lamination configuration [62-64]. The static and dynamic behaviors of macro [65-67] and nano [68-70] composite structural elements have captured the attention of numerous researchers, leading to further investigations involving various loading conditions, namely mechanical [71-73], electric, magnet [74-77] and thermal loads [57, 78-80]. Moreover, different methods and solutions such as the finite element method [71, 81-83], Navier's solution [84, 85], or the Ritz-type series solution [39, 86] have been proposed to accurately predict LC structures' responses. Nonetheless, due to the complex fabrication processes and random load fluctuations, these composite structures exhibit inherent variability in their theoretical performance predictions and actual experimental values. The uncertainty sources can be material, geometrical, and loading parameters. These uncertainties significantly influence vibration and static response characteristics such as frequencies and displacements. The deterministic approaches with no uncertainty accounted for are adjusted with a safety factor in design. Meanwhile, the probabilistic modeling approaches study the stochastic responses and assess the structures' performance based on the input uncertainties. Even though there have been many researches concerning stochastic structural mechanics [87-91], the study on stochastic analysis of laminated composite beams is relatively limited.

In order to investigate stochastic behaviors of structures with uncertainties, the most straightforward and intuitive method is the crude Monte Carlo Simulation method (MCS) which simply runs the structural model repetitively to achieve the desired level of accuracy. However, in cases where the physical model is complex, employing MCS becomes impractical for its substantial computational time. Therefore, to overcome this drawback, many numerical methods for stochastic analysis, such as the stochastic finite element method [88, 92], perturbation method [93, 94], support vector machine [95], and polynomial

chaos expansion method [96] have been proposed to reduce the computational cost and maintain accuracy. This chapter particularly examines the use of PCE in the stochastic analysis of laminated composite (LC) beams. The main idea is to approximate the stochastic outputs by representing them as a series in an orthogonal space, including the chosen basis polynomials and their corresponding coefficients. It allows for efficient and accurate calculation of statistics and probability distributions for computational models involving random input parameters.

Herein presents an overview of the previously published works on applying stochastic analysis methods for mechanical systems. Based on the MCS, Nguyen et al. [97] investigated the effects of uncertain material properties on the buckling responses of LC plates based on the isogeometric analysis. Elishakoff and Archaud [98] proposed a modified MCS method that significantly reduces simulation size to analyze the buckling of imperfect beams on softening foundations. Recently, Avíla and Squarcio [99] presented the Neuman-Monte Carlo methodology for the stochastic bending analysis of the Levinson–Bickford beam. Naskar et al. [100] proposed a stochastic approach to study the natural frequencies of thin-walled LC beams with spatially varying matrix cracking damage in a multi-scale framework in which a concept of stochastic representative volume element has been introduced and verified against the traditional MCS. As for the perturbation-based methods, Li et al. [101] analyzed the effect of random system properties on the critical thermal buckling temperature of LC plates with temperature-dependent properties using the perturbation technique. Onkar et al. [102] proposed a stochastic buckling analysis of LC plates with random material properties under uniaxial compressive loading. It is based on the layerwise plate model to solve both pre-buckling and buckling problems, while the stochastic analysis has been done based on the mean-centered first-order perturbation technique.

Meanwhile, PCE has been used extensively for various mechanical problems. Peng et al. [96] presented an uncertainty analysis method for LC plates using a data-driven PCE method under insufficient input data related to uncertain design parameters. Based on this approach,

Verma and Singh [103] studied the thermal buckling responses of LC plates with random geometric and material properties. Chandra et al. [104] presented a stochastic dynamic response analysis of LC plates using generalized polynomial chaos expansion due to random mean temperature increment. Then a stochastic finite element method was developed based on the first-order shear deformation theory (FSBT). Chakraborty et al. [105] presented an improved PCE approach based on a polynomial correlated function expansion for stochastic vibration analysis of LC plates. Bhattacharyya [106] used the Bayesian learning-based PCE to analyze the global reliability sensitivity of a general system. Despite the broad applications of PCE in many areas, its implementation in analyzing the stochastic responses of LC beams under stochastic loads still needs to be explored. Particularly, how material properties variation and load variability influence LC beams' fundamental frequency and mid-span displacement have yet to be sufficiently assessed. For those reasons, it calls for a deeper exploration of future research.

This chapter aims to develop surrogate models using polynomial chaos expansion for uncertainty quantification and sensitivity analysis of LC beams with random material properties and stochastic loads. These input uncertainties are given by defined lognormal distributions. The proposed PCE models consist of multivariate Hermite polynomials and unknown associated coefficients. A set of realizations of random input parameters is generated from which the deterministic beam model gives the corresponding realizations of output responses. These realizations are then used to estimate the PCE coefficients by either the spectral projection using the Gaussian quadrature rule or the ordinary least-square regression approach. The deterministic beam model is derived based on a higher-order shear deformation theory that satisfies the traction-free boundary condition on the top and bottom surfaces of the LC beams. Numerical results are presented to investigate the effects of the stochasticity, fiber angle, span-to-thickness ratio, and boundary conditions on the probabilistic deflection and natural frequencies of the LC beams. Additionally, Sobol's sensitivity indices are computed to rank the most significant random variables affecting both

static and vibration responses of the LC beams. All numerical and statistical results are validated with those obtained from one million samples of Monte Carlo simulation.

2.2. Theoretical formulation

Consider a LC beam with length L and rectangular cross-section $b \times h$ as shown in Fig.2-1. It is made of n plies of orthotropic materials in different fibre angles with respect to the x-axis.

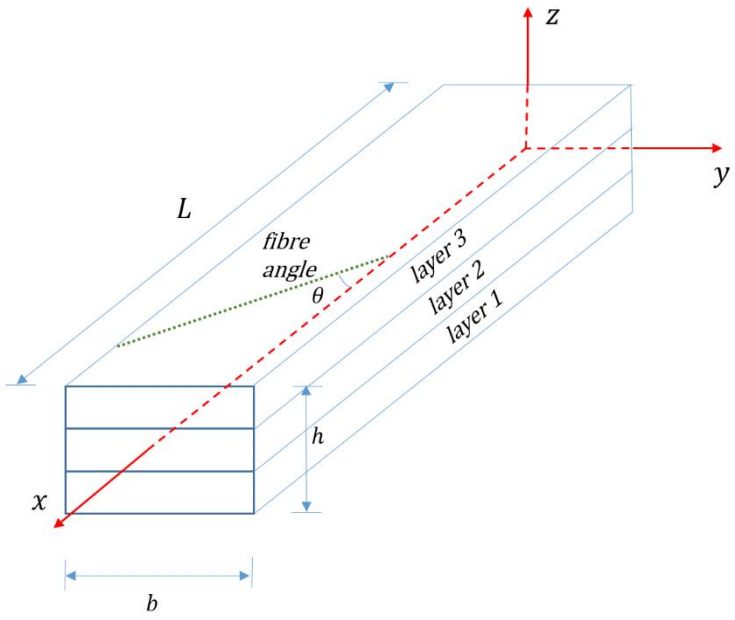

Figure 2-1: Geometry of a laminated composite beam

2.2.1. Kinematic, strain and stress

The displacement field of LC beams based on the higher-order shear deformation theory is given by:

$$u(x,z) = \bar{u}(x) - z\bar{w}_{,x} + \left(\frac{5z}{4} - \frac{5z^3}{3h^2}\right)\bar{\varphi}(x) = \bar{u}(x) - z\bar{w}_{,x} + \psi(z)\bar{\varphi}(x) \tag{2-1a}$$

$$w(x,z) = \bar{w}(z) \tag{2-2b}$$

where $\bar{u}(x), \bar{w}(x)$ are axial and transverse displacements at mid-plane of the LC beams, respectively; $\bar{\varphi}(x)$ is the rotation of a transverse normal about the y-axis; $\psi(z)$ is the shear

function that reveals a higher-order variation of axial displacement; the comma indicates partial differentiation with respect to the coordinate subscript that follows.

The non-zero strains of LC beams are given by:

$$\varepsilon_x = \bar{\varepsilon}_x^{(0)} + z\bar{\varepsilon}_x^{(1)} + \psi\bar{\varepsilon}_x^{(2)} \tag{2-3a}$$

$$\gamma_{xz} = \psi_{,z}\bar{\varphi} \tag{2-4b}$$

where

$$\bar{\varepsilon}_x^{(0)} = \bar{u}_{,x}, \bar{\varepsilon}_x^{(1)} = -\bar{w}_{,xx}, \bar{\varepsilon}_x^{(2)} = \bar{\varphi}_{,x} \tag{2-5}$$

The elastic strain and stress relation of k^{th}-layer in global coordinates is given by:

$$\begin{Bmatrix} \sigma_x \\ \sigma_{xz} \end{Bmatrix}^{(k)} = \begin{pmatrix} \overline{Q}_{11} & 0 \\ 0 & \overline{Q}_{55} \end{pmatrix}^{(k)} \begin{Bmatrix} \varepsilon_x \\ \gamma_{xz} \end{Bmatrix}^{(k)} \tag{2-6}$$

where the $\overline{Q}_{ij}^{(k)}$ are the plane stress-reduced stiffness coefficients in global coordinates (see for details).

2.2.2 Energy formulation

Hamilton's principle is used to derive characteristic equations of the LC beams in which the total potential energy Λ of the LC beams is composed of the strain energy U, work done by external forces V and kinetic energy K.

$$\int_{t_1}^{t_2} \delta\Lambda dt = \int_{t_1}^{t_2} \left(\delta U + \delta V - \delta K\right) dt = 0 \tag{2-7}$$

The variation of strain energy of the LC beams is given by:

$$\begin{aligned} \delta U &= \int_V \left(\sigma_x \delta\varepsilon_x + \sigma_{xz}\delta\gamma_{xz}\right) dV = \int_0^L \left(N_x \delta\bar{\varepsilon}_x^{(0)} + M_x^{(1)}\delta\bar{\varepsilon}_x^{(1)} + M_x^{(2)}\delta\bar{\varepsilon}_x^{(2)} + Q_x\delta\bar{\varphi}\right) dx \\ &= \int_0^L \left(N_x \delta\bar{u}_{,x} - M_x^{(1)}\delta\bar{w}_{,xx} + M_x^{(2)}\delta\bar{\varphi}_{,x} + Q_x\delta\bar{\varphi}\right) dx \end{aligned} \tag{2-8}$$

where the stress resultants $\left(N_x, M_x^{(1)}, M_x^{(2)}, Q_x\right)$ are defined by:

$$N_x = \int_{-h/2}^{h/2} \sigma_x b dz = A\bar{u}_{,x} - B\bar{w}_{,xx} + B^s\bar{\varphi}_{,x} \tag{2-9a}$$

$$M_x^{(1)} = \int_{-h/2}^{h/2} z\sigma_x b dz = B\bar{u}_{,x} - D\bar{w}_{,xx} + D^s\bar{\varphi}_{,x} \tag{2-9b}$$

$$M_x^{(2)} = \int_{-h/2}^{h/2} \psi\sigma_x b dz = B^s\bar{u}_{,x} - D^s\bar{w}_{,xx} + H^s\bar{\varphi}_{,x} \tag{2-9c}$$

$$Q_x = \int_{-h/2}^{h/2} \psi_{,z}\sigma_{xz} b dz = A^s\bar{\varphi} \tag{2-9d}$$

where the stiffness coefficients of the LC beams are determined as follows:

$$\left(A, B, D, B^s, D^s, H^s\right) = \int_{-h/2}^{h/2} \overline{Q}_{11}\left(1, z, z^2, \psi, z\psi, \psi^2\right) b dz \tag{2-10a}$$

$$A^s = \int_{-h/2}^{h/2} \overline{Q}_{55}\psi_{,z}^2 b dz \tag{2-10b}$$

The variation of work done by a transvers distributed force $\bar{f}$ of LC beams is written in the following forms:

$$\delta V = -\int_0^L \bar{f}\delta\bar{w} dx \tag{2-11}$$

The variation of kinetic energy of the LC beams is expressed by:

$$\begin{aligned}\delta K &= \int_V \rho\left(\dot{u}\delta\dot{u} + \dot{w}\delta\dot{w}\right) dV \\ &= \int_0^L \Big[I_0\ddot{\bar{u}}\delta\dot{\bar{u}} - I_1\left(\ddot{\bar{u}}\delta\dot{\bar{w}}_{,x} + \ddot{\bar{w}}_{,x}\delta\dot{\bar{u}}\right) + I_2\ddot{\bar{w}}_{,x}\delta\dot{\bar{w}}_{,x} + J_1\left(\ddot{\bar{u}}\delta\dot{\bar{\varphi}} + \ddot{\bar{\varphi}}\delta\dot{\bar{u}}\right) \\ &\quad - J_2\left(\ddot{\bar{w}}_{,x}\delta\dot{\bar{\varphi}} + \ddot{\bar{\varphi}}\delta\dot{\bar{w}}_{,x}\right) + K_2\ddot{\bar{\varphi}}\delta\dot{\bar{\varphi}} + I_0\ddot{\bar{w}}\delta\dot{\bar{w}} \Big] dx\end{aligned} \tag{2-12}$$

where dot-superscript denotes the differentiation with respect to the time t; ρ is the mass density of each layer, and $I_0, I_1, I_2, J_1, J_2, K_2$ are the inertia coefficients defined by:

$$\left(I_0, I_1, I_2, J_1, J_2, K_2\right) = \int_{-h/2}^{h/2} \rho\left(1, z, z^2, \psi, z\psi, \psi^2\right) b dz \tag{2-13}$$

Substituting Eqs. (2-10), (2-15) and (2-16) into Eq. (2-7) leads to:

$$\begin{aligned}
&\int_{t_1}^{t_2}\int_{0}^{L}\Big[\left(A\bar{u}_{,x} - B\bar{w}_{,xx} + B^s\bar{\varphi}_{,x}\right)\delta\bar{u}_{,x} - \left(B\bar{u}_{,x} - D\bar{w}_{,xx} + D^s\bar{\varphi}_{,x}\right)\delta\bar{w}_{,xx} \\
&+\left(B^s\bar{u}_{,x} - D^s\bar{w}_{,xx} + H^s\bar{\varphi}_{,x}\right)\delta\bar{\varphi}_{,x} + A^s\bar{\varphi}\delta\bar{\varphi}\Big]dx - \int_0^L q\delta\bar{w}dx \\
&-\int_0^L\Big[I_0\ddot{\bar{u}}\delta\dot{\bar{u}} - I_1\left(\ddot{\bar{u}}\delta\dot{\bar{w}}_{,x} + \ddot{\bar{w}}_{,x}\delta\dot{\bar{u}}\right) + I_2\ddot{\bar{w}}_{,x}\delta\dot{\bar{w}}_{,x} + J_1\left(\ddot{\bar{u}}\delta\dot{\bar{\varphi}} + \ddot{\bar{\varphi}}\delta\dot{\bar{u}}\right) \\
&-J_2\left(\ddot{\bar{w}}_{,x}\delta\dot{\bar{\varphi}} + \ddot{\bar{\varphi}}\delta\dot{\bar{w}}_{,x}\right) + K_2\ddot{\bar{\varphi}}\delta\dot{\bar{\varphi}} + I_0\ddot{\bar{w}}\delta\dot{\bar{w}}\Big]dxdt = 0
\end{aligned} \tag{2-14}$$

2.2.3. Ritz method

Based on the Ritz method, the displacement field in Eq. (2-11) is approximated in the following forms:

$$\bar{u}\left(x,t\right) = \sum_{j=1}^{m} N_j^u\left(x\right)u_j e^{i\omega t} \tag{2-15a}$$

$$\bar{w}\left(x,t\right) = \sum_{j=1}^{m} N_j^w\left(x\right)w_j e^{i\omega t} \tag{2-15b}$$

$$\bar{\varphi}\left(x,t\right) = \sum_{j=1}^{m} N_j^\varphi\left(x\right)\varphi_j e^{i\omega t} \tag{2-15c}$$

where ω is the natural frequency, $i^2 = -1$ the imaginary unit; u_j, w_j, φ_j are unknown values to be determined; $N_j^u\left(x\right)$, $N_j^w\left(x\right)$ and $N_j^\varphi\left(x\right)$ are shape functions. It is known that the accuracy and convergence of the Ritz method depend on the choice of these approximate functions ([63, 107]). Trigonometric shape functions which satisfy different boundary

conditions (BCs): simply-supported (S-S), clamped-free (C-F) and clamped-clamped (C-C), are given as follows:

- S-S: $N_u = \cos\dfrac{j\pi x}{L}$, $N_w = \sin\dfrac{j\pi x}{L}$, $N_\varphi = \cos\dfrac{j\pi x}{L}$
- C-F: $N_u = \sin\dfrac{(2j-1)\pi}{2L}x$, $N_w = 1-\cos\dfrac{(2j-1)\pi}{2L}x$, $N_\varphi = \sin\dfrac{(2j-1)\pi}{2L}x$
- C-C: $N_u = \sin\dfrac{2j\pi x}{L}$, $N_w = \sin^2\dfrac{j\pi x}{L}$, $N_\varphi = \sin\dfrac{2j\pi x}{L}$

Substituting Eq. (2-12) into Eq. (2-13) leads to:

$$\left(\begin{bmatrix} \mathbf{K}^{11} & \mathbf{K}^{12} & \mathbf{K}^{13} \\ {}^T\mathbf{K}^{12} & \mathbf{K}^{22} & \mathbf{K}^{23} \\ {}^T\mathbf{K}^{13} & {}^T\mathbf{K}^{23} & \mathbf{K}^{33} \end{bmatrix} - \omega^2 \begin{bmatrix} \mathbf{M}^{11} & \mathbf{M}^{12} & \mathbf{M}^{13} \\ {}^T\mathbf{K}^{12} & \mathbf{M}^{22} & \mathbf{M}^{23} \\ {}^T\mathbf{K}^{13} & {}^T\mathbf{M}^{23} & \mathbf{M}^{33} \end{bmatrix}\right) \begin{Bmatrix} \bar{\mathbf{u}} \\ \bar{\mathbf{w}} \\ \bar{\boldsymbol{\varphi}} \end{Bmatrix} = \begin{Bmatrix} \mathbf{0} \\ \mathbf{f} \\ \mathbf{0} \end{Bmatrix} \tag{2-16}$$

where the components of stiffness matrix $\mathbf{K}$, mass matrix $\mathbf{M}$ and force vector $\mathbf{f}$ are given by:

$$K_{ij}^{11} = A\int_0^L N_{i,x}^u N_{j,x}^u dx \quad K_{ij}^{12} = -B\int_0^L N_{i,x}^u N_{j,xx}^w dx \quad K_{ij}^{13} = B^s\int_0^L N_{i,x}^u N_{j,x}^\varphi dx$$

$$K_{ij}^{22} = D\int_0^L N_{i,xx}^w N_{j,xx}^w dx \quad K_{ij}^{23} = -D^s\int_0^L N_{i,xx}^w N_{j,x}^\varphi dx$$

$$K_{ij}^{33} = -H^s\int_0^L N_{i,x}^\varphi N_{j,x}^\varphi dx + A^s\int_0^L N_i^\varphi N_j^\varphi dx \quad f_i = \int_0^L \bar{f} N_j^\varphi dx$$

$$M_{ij}^{11} = I_0\int_0^L N_i^u N_j^u dx \quad M_{ij}^{12} = -I_1\int_0^L N_i^u N_{j,x}^w dx \quad M_{ij}^{13} = -J_1\int_0^L N_i^u N_j^\varphi dx$$

$$M_{ij}^{22} = I_0\int_0^L N_i^w N_j^w dx + I_2\int_0^L N_{i,x}^w N_{j,x}^w dx,\ M_{ij}^{23} = -J_2\int_0^L N_{i,x}^w N_j^\varphi dx,\ M_{ij}^{33} = K_2\int_0^L N_i^\varphi N_j^\varphi dx$$

(2-17)

2.2.4. Polynomial chaos expansion

For computational models involving random input parameters, the uncertainty in model responses can be characterized by representing them as a series of orthogonal functions as follows:

$$\bar{r}(\mathbf{q}) = \sum_{i=0}^{\infty} \beta_i \Omega_i(\mathbf{q}) \tag{2-18}$$

where $\mathbf{q}$ is a vector of d independent random variables mapped to physical random parameters; Ω_i are multivariate orthogonal basis functions; β_i are coefficients to be determined. In order to determine these components, two main following approaches can be considered: polynomial chaos expansion (PCE) and stochastic collocation, in which the PCE estimates the coefficients in a suitable set of basis functions using either spectral projection or linear regression, whereas the stochastic collocation approach forms the interpolation polynomials for the known coefficients under collocation points ([108]). For the present manuscript, the PCE method with both projection and linear regression methods will be developed. The multivariate Hermite polynomials are used as the basis functions, and $\mathbf{q}$ is used as a vector of standard normal variables.

In practice, Eq. (2-18) is typically truncated using a finite number of terms. If the number of random variables is d and the qualified order of polynomial is p, the number of full polynomial terms N is the permutation of p and $d+p$, determined as follows: $N = \frac{(d+p)!}{d!\,p!}$, Eq. (2-14) therefore becomes:

$$\bar{r}(\mathbf{q}) = \sum_{i=0}^{N-1} \beta_i \Omega_i(\mathbf{q}) + \varepsilon \tag{2-19}$$

in which the basis functions Ω_i are considered under multivariate Hermite polynomials, and their associated coefficients β_i should be determined so that the residual ε is minimized. Among different methods, spectral projection and linear regression approaches are applied in this chapter.

2.2.5. Spectral projection approach

For spectral projection, the residual minimum requires that it must be orthogonal with the projection of response in the selected space or the inner product of the residual and each basis function is zero. From Eq. 2-19, taking the inner product of both sides with respect to Ω_j and enforcing orthogonality yields:

$$\left\langle \bar{r}, \Omega_j \right\rangle = \sum_{i=0}^{N} \beta_i \left\langle \Omega_i, \Omega_j \right\rangle \tag{2-20}$$

Because Ω_j are mutually orthogonal, Eq. 2-20 becomes:

$$\beta_i = \frac{\left\langle \bar{r}, \Omega_i \right\rangle}{\left\langle \Omega_i, \Omega_i \right\rangle} = \frac{1}{\left\langle \Omega_i, \Omega_i \right\rangle} \int \bar{r} \Omega_i \rho_Q(\mathbf{q}) \, d\mathbf{q} \tag{2-21}$$

It is noted that all coefficients can be theoretically obtained by solving Eq. 2-21; however, the random response $\bar{r}$ is unknown. Moreover, Eq. 2-21 involves a multidimensional integral evaluated numerically using either probabilistic techniques (sampling) or deterministic techniques (quadrature rules, sparse grid approaches). In the present chapter, the probabilistic Gauss-Hermite quadrature will be used to compute β_i. Note that the normalization factor $\left\langle \Omega_i, \Omega_i \right\rangle$ in Eq. (2-21) can be analytically estimated. It is worth to noticing that if the order of the output $\bar{r}$ is p, the highest order of the integrands in Eq. (2-21) is at least $2p$, so the minimum number of Gauss point for each dimension is $N_{gp} = p+1$ and the total number of quadrature points is $(p+1)^d$. Hence, if the model response $\bar{r}\left(q_{j_1}^1 ... q_{j_d}^d\right)$ is obtained from the Ritz solution, $(p+1)^d$ deterministic problems need to be solved. In consequence, this method is quite expensive for multidimensional and higher-order problems.

2.2.6. Linear regression approach

Let $\Re = \left\{\mathbf{q}^1,...,\mathbf{q}^{N_s}\right\}$ be a set of $N_s\left(N_s > N\right)$ realizations of input random vector, and $\mathbf{R} = \left\{\overline{r}^1,...,\overline{r}^{N_s}\right\}$ be corresponding output evaluations $\left(\overline{r}^i = \overline{r}\left(\mathbf{q}^i\right), i = 1,...,N_s\right)$. The vector of residuals can be estimated from Eq. (2-17) in the compact form:

$$\Upsilon = \mathbf{R} - \beta^T \mathbf{\Omega} \tag{2-22}$$

where $\mathbf{\Omega}$ is the matrix whose elements are given by $\Omega_{ij} = \Omega_j\left(\mathbf{q}^i\right), i = 1,...,N_s;\ j = 1,...,N$. The coefficients β are estimated by minimizing the L_2-norm (least-square regression) of the residual followed as:

$$\beta = Arg\ \min \left\| \mathbf{R} - \beta^T \mathbf{\Omega} \right\|_2^2 \tag{2-23}$$

Solving Eq. (2-21), the coefficients are given by:

$$\beta = \left(\mathbf{\Omega}^T \mathbf{\Omega}\right)^{-1} \mathbf{\Omega}^T \mathbf{R} \tag{2-24}$$

2.2.7 Sensitivity analysis

Apart from the LC beams' responses concerning the input uncertainty, the degree to which each random variable contributes to the model output uncertainty is of great interest. The sensitivity analysis is a branch of study that quantifies how much the uncertainty of each random input variable, either as an individual or with other variable interaction, contributes to the model output uncertainty. The sensitivity analysis can be carried out effectively by the variance-based method, which has been developed by Sobol [109] and has been further studied by Satelli et al. [110, 111] and Sudret [112]. Sobol's first-order and total-order indices are given by Satelli et al. [110] as follows:

$$\text{First-order Sobol index: } S_i = \frac{Var_{\mathbf{q}^i}\left(E_{q_{\sim i}}\left(\overline{\mathbf{r}} \mid \mathbf{q}^i\right)\right)}{Var\left(\overline{\mathbf{r}}\right)} \mathbf{q}^{k \neq i} \tag{2-25a}$$

$$\text{Total-order Sobol index: } S_{Ti} = 1 - \frac{Var_{\mathbf{q}^{\sim i}}\left(E_{\mathbf{q}^i}\left(\overline{\mathbf{r}} \mid \mathbf{q}^{\sim i}\right)\right)}{Var\left(\overline{\mathbf{r}}\right)} \tag{2-25b}$$

Both kinds of these Sobol indices are normalised by $Var(\bar{r})$ but the difference in meaning is first-order Sobol indices measure only the impact of a sole particular input variable $\mathbf{q}^i$, while total-order Sobol indices also take into account the impact of interactions between $\mathbf{q}^i$ and other variables $\mathbf{q}^{k\neq i}$ .These indices can be computed using crude Monte Carlo simulation with the computational cost of $(d+2)N_s$ or using PCE with no additional cost. The Sobol's first-order and total-order indices can be estimated as follows:

$$S_i = \frac{D_i}{Var(\bar{\mathbf{r}})} \tag{2-26a}$$

$$S_{Ti} = \frac{D_{Ti}}{Var(\bar{\mathbf{r}})} \tag{2-26b}$$

where $D_i = \sum_{j\in\Gamma_i} \beta_j^2 \left\langle \Omega_j(\mathbf{q}^i), \Omega_j(\mathbf{q}^i) \right\rangle j$, Γ_i comprises all indices j such that the multivariate function Ω_j only contains the variable $\mathbf{q}^i$; $D_{Ti} = \sum_{j\in\Gamma_{Ti}} \beta_j^2 \left\langle \Omega_j(\mathrm{q}), \Omega_j(\mathrm{q}) \right\rangle$, Γ_{Ti} comprises all indices j such that the multivariate function Ω_j must contain variable $\mathbf{q}^i$; index j depends on how the list of multivariate functions is sorted.

2.3. Numerical results

Several numerical examples are performed in this section to investigate the accuracy and efficiency of the present theory. The effects of material properties uncertainty on the bending and free vibration behaviors of LC beams are observed with different lay-ups and boundary conditions. Two types of material MAT I [113] and MAT II [97] shown in Table 2-1 are considered for the vibration and bending analysis, respectively. The non-dimensional fundamental frequency and mid-span displacement are given as: $\hat{\omega} = \frac{\omega L^2}{b_3}\sqrt{\frac{\rho}{E_2}}$ and $\hat{w} = \frac{100E_2 bh^3}{qL^4} w$.

Table 2-1: Random input material properties and statistical distribution

Material properties and load	Mean		COV	Distribution
	MAT I [113]	MAT II [32]		
$E_1\ (GPa)$	138	100	0.1	Lognormal
$E_2 = E_3 (GPa)$	6.9	4	0.1	Lognormal
$G_{12} = G_{13} (GPa)$	4.14	2	0.1	Lognormal
$G_{23} (GPa)$	3.45	0.8	0.1	Lognormal
$\nu_{12} = \nu_{13}$	0.25	0.25	0.1	Lognormal
$\rho\ (kg/m^3)$	1550.1	-	0.1	Lognormal
$q\ (N/m)$	-	106	0.1	Lognormal

2.3.1. Convergence study

In order to investigate the convergence of the present solution with an increasing number of series, both non-dimensional first fundamental frequencies (MAT I) and mid-span displacements (MAT II) of $[0^o/90^o/0^o]$ LC beams are computed with increasing Ritz series numbers and different boundary conditions. It can be seen from Table 2-2 that the convergence of the present Ritz-based trigonometric series solution is fairly achieved at $m = 8$. Therefore, $m = 8$ would be used in subsequent calculations.

Table 2-2: Convergence of the non-dimensional fundamental frequency (MAT I) and non-dimensional mid-span displacement (MAT II) of $[0^o/90^o/0^o]$ laminated composite beams

BC	m					
	2	4	6	8	10	12
Non-dimensional fundamental frequency						
S-S	10.76	10.76	10.76	10.76	10.76	10.76
C-C	18.07	17.70	17.59	17.54	17.52	17.51
C-F	4.18	4.15	4.14	4.14	4.14	4.14
Non-dimensional mid-span displacement						
S-S	1.11	1.10	1.10	1.10	1.10	1.10
C-C	0.48	0.52	0.53	0.53	0.53	0.53
C-F	3.13	3.36	3.41	3.43	3.44	3.45

Table 2-3: Convergence of fundamental frequency (*Hz*) of $[0^o/90^o/0^o]$ laminated composite beams with respect to the polynomial order p of the PCE ($L/h=10$, C-C)

Polynomial order p	Properties	LR	SP	MCS
2	μ	1549.373	1549.321	1549.233
	σ	89.566	89.628	89.719
	Kurtosis	3.037	3.045	3.061
	Skewness	0.165	0.176	0.172

3	μ	1549.286	1549.233
	σ	89.656	89.687
	Kurtosis	3.051	3.059
	Skewness	0.172	0.178
4	μ	1549.364	1549.425
	σ	89.565	89.568
	Kurtosis	3.058	3.055
	Skewness	0.176	0.177
5	μ	1549.285	1549.432
	σ	89.595	89.635
	Kurtosis	3.056	3.049
	Skewness	0.175	0.173

Additionally, to verify the convergence of the present solution with respect to the polynomial order p, Table 2-3 introduces fundamental frequencies of $[0^o/90^o/0^o]$ LC beams with MAT I and for the linear regression (LR), spectral projection (SP), and MCS methods. The first fourth statistical moments, including the mean μ, standard deviation σ, kurtosis, and skewness are calculated for C-C boundary conditions. The span-to-depth ratio $L/h=10$ is considered and the order of polynomial p is increased from 2 to 5. In the LR method, a higher-order polynomial gives a higher number of terms N, and the number of simulation runs in the LR method N_s is set to be $3N$. Besides, for the SP method, the number of Gauss quadrature points N_{gp} is equal to the order of polynomial plus one for each variable (i.e., $N_{gp}=p+1$) and the N_s is equal to N_{gp}^d. For both LR and SP, the higher-order

polynomial clearly gives a higher degree of accuracy but also requires more computing time. Based on the results in Table 2-3, this study considers the polynomial order of 3 to be sufficient and will be used in the subsequent sections. The convergence study of the static analysis gives a similar trend and also achieves sufficient accuracy when the polynomial order is 3. As a result, for the LC beam responses of LR, SP and MCS methods in all subsequent Tables, the numbers of simulations are $N_s = 252$, $N_s = 4096$ and $N_s = 10^6$, respectively.

2.3.2. Verification of the model accuracy

Before demonstrating the efficiency of the proposed stochastic analysis for the LC beams, the accuracy of the beam solver model with and without uncertainties in material properties is investigated. Symmetric and asymmetric cross-ply LC beams with different layer-ups of the same thickness are considered. It is noted that the deterministic solution results in Tables 2-4 and 2-5 are derived from the mean values of the input parameters in Table 2-1. To verify the vibration behaviors of the LC beams, Table 2-4 presents the mean, standard deviation, and deterministic fundamental frequencies of $[0^o/90^o/0^o]$ and $[0^o/90^o]$ LC beams with $L = 0.381\text{m}$, $h = 0.0381\text{m}$ and MAT I. The mean values obtained from the MCS, LR and SP are compared with those obtained from previous works of Nguyen et al. [113] and Jun et al. [79]. It can be seen that there are excellent agreements between the models.

Similarly, the reliability of the present theory in predicting static behaviors is carried out in Table 2-5 for both cross-ply $[0^o/90^o/0^o]$ and $[0^o/90^o]$ LC beams made of the MAT II with $L = 0.381\text{m}$, $h = 0.0381\text{m}$. The mean, standard deviation and deterministic results of the transverse mid-span displacement are compared with those derived from Nguyen et al. [32] and Khdeir and Reddy [114] based on the HSBT. In comparison, good agreements with the earlier works are again found. In the following sections, where the uncertainties in material properties are accounted for, the MCS with one million simulation $N_s = 10^6$ is deemed the reference for result verification of the LR and SP methods.

Table 2-4: Mean and standard deviation of fundamental frequency (*Hz*) of $[0^o/90^o/0^o]$ and

$[0^o/90^o]$ laminated composite beams with C-C boundary conditions ($L = 0.381\text{m}$, $h = 0.0381\text{m}$, MAT I)

Theory	$[0^o/90^o/0^o]$		$[0^o/90^o]$	
	μ	σ	μ	σ
Deterministic	1546.8	-	1000.7	-
Nguyen et al. [113]	1552.4	-	1001.2	-
Jun et al. [79]	-	-	999.6	-
Present (LR)	1549.4	89.6	1003.0	58.3
Present (SP)	1549.2	89.5	1002.9	58.2
Present (MCS)	1549.2	89.6	1003.0	58.3

Table 2-5: Mean and standard deviation of mid-span displacement (mm) of $[0^o/90^o/0^o]$ and $[0^o/90^o]$ laminated composite beams with C-C boundary conditions ($L = 0.381\text{m}$, $h = 0.0381\text{m}$, MAT II)

Theory	$[0^o/90^o/0^o]$		$[0^o/90^o]$	
	μ	σ	μ	σ
Deterministic	0.504	-	0.955	-
Nguyen et al. [32]	0.506	-	0.956	-
Khdeir and Reddy [114]	0.507	-	0.957	-
Present (LR)	0.507	0.059	0.961	0.111
Present (SP)	0.507	0.059	0.960	0.111
Present (MC)	0.507	0.059	0.960	0.111

2.3.3. Static analysis

The static behaviors of LC beams with various boundary conditions, span-to-depth ratios, and fiber angles are investigated in this section. These beams are made of MAT II and subjected to a uniformly distributed load. In this stochastic analysis, there are six lognormal-distributed random variables with a coefficient of variation (COV) of 0.1, where COV is the ratio between the standard deviation and mean of an input variable. In order to verify the accuracy of LR and SP methods, as mentioned above, four statistical moments consisting of the mean, standard deviation, skewness, and kurtosis of the mid-span displacement are computed and compared with those of the Monte Carlo simulations. Regarding the computational cost, the MCS, LR, and SP, respectively, require 106, 252 and 4096 simulations of the beam analysis model.

Table 2-6: Mean, standard deviation, kurtosis and skewness of mid-span transverse displacement (mm) for laminated composite beams with different lay-ups (MAT II) and S-S boundary condition

Lay-ups	Statistical moments	$L/h=5$			$L/h=20$		
		LR	SP	MC	LR	SP	MC
$[0^o/90^o]$	Mean	0.573	0.573	0.573	26.228	26.222	26.223
	SD	0.066	0.066	0.066	3.256	3.254	3.255
	Kurtosis	3.219	3.215	3.211	3.248	3.251	3.255
	Skewness	0.351	0.351	0.346	0.370	0.372	0.377
$[45^o/\text{-}45^o]$	Mean	1.671	1.670	1.670	91.799	91.821	91.808
	SD	0.202	0.202	0.202	11.417	11.424	11.413
	Kurtosis	3.244	3.232	3.265	3.260	3.252	3.254
	Skewness	0.372	0.365	0.375	0.380	0.381	0.378
$[0^o/90^o/0^o]$	Mean	0.289	0.289	0.289	5.851	5.852	5.852
	SD	0.034	0.034	0.034	0.773	0.774	0.773
	Kurtosis	3.221	3.223	3.236	3.306	3.301	3.306

	Skewness	0.354	0.350	0.356	0.408	0.411	0.409
$[45^o/-45^o/45^o]$	Mean	1.671	1.670	1.671	91.798	91.798	91.802
	SD	0.202	0.202	0.202	11.407	11.423	11.430
	Kurtosis	3.253	3.247	3.250	3.249	3.255	3.271
	Skewness	0.373	0.371	0.372	0.375	0.381	0.385
Average computing time (s)		0.5	0.8	65.4	0.5	0.8	61.7

Table 2-7: Mean, standard deviation, kurtosis and skewness of mid-span transverse displacement (mm) for laminated composite beams with different lay-ups (MAT II) and C-C boundary condition

Lay-ups	Statistical moments	$L/h=5$			$L/h=20$		
		LR	SP	MC	LR	SP	MC
$[0^o/90^o]$	Mean	0.230	0.230	0.230	5.764	5.766	5.765
	SD	0.026	0.026	0.026	0.696	0.696	0.697
	Kurtosis	3.216	3.213	3.217	3.244	3.236	3.242
	Skewness	0.351	0.346	0.344	0.364	0.362	0.369
$[45^o/\text{-}45^o]$	Mean	0.517	0.517	0.517	19.116	19.112	19.106
	SD	0.061	0.061	0.061	2.356	2.356	2.352
	Kurtosis	3.244	3.221	3.220	3.272	3.256	3.253
	Skewness	0.362	0.356	0.357	0.380	0.379	0.376
$[0^o/90^o/0^o]$	Mean	0.184	0.184	0.184	1.802	1.802	1.802
	SD	0.022	0.022	0.022	0.215	0.215	0.215
	Kurtosis	3.210	3.217	3.222	3.222	3.236	3.230

	Skewness	0.349	0.356	0.354	0.359	0.361	0.364
[45^o/-45^o/45^o]	Mean	0.517	0.517	0.517	19.115	19.115	19.107
	SD	0.061	0.061	0.061	2.357	2.359	2.356
	Kurtosis	3.233	3.227	3.233	3.243	3.263	3.252
	Skewness	0.373	0.379	0.378	0.373	0.379	0.378
Average computing time (s)		0.4	0.9	61.2	0.5	0.9	63.0

Table 2-8: Mean, standard deviation, kurtosis and skewness of mid-span transverse displacement (mm) for laminated composite beams with different lay-ups (MAT II) and C-F boundary condition

Lay-ups	Statistical moment	$L/h=5$			$L/h=20$		
		LR	SP	MC	LR	SP	MC
$[0^o/90^o]$	Mean	1.824	1.825	1.824	88.711	88.719	88.717
	SD	0.214	0.214	0.214	11.004	11.023	11.027
	Kurtosis	3.233	3.226	3.223	3.237	3.244	3.242
	Skewness	0.355	0.355	0.354	0.367	0.370	0.371
$[45^o/\text{-}45^o]$	Mean	5.523	5.522	5.524	311.433	311.427	311.449
	SD	0.671	0.670	0.671	38.729	38.727	38.747
	Kurtosis	3.256	3.253	3.259	3.253	3.253	3.257
	Skewness	0.376	0.375	0.374	0.378	0.377	0.378
$[0^o/90^o/0^o]$	Mean	0.813	0.813	0.813	19.358	19.363	19.360
	SD	0.095	0.095	0.094	2.584	2.585	2.587
	Kurtosis	3.206	3.222	3.202	3.297	3.309	3.302

	Skewness	0.349	0.348	0.344	0.408	0.413	0.414
[45^o/-45^o/45^o]	Mean	5.522	5.522	5.522	311.447	311.381	311.389
	SD	0.671	0.670	0.670	38.707	38.727	38.702
	Kurtosis	3.243	3.261	3.246	3.250	3.265	3.265
	Skewness	0.371	0.373	0.371	0.375	0.380	0.379
Average computing time (s)		0.4	0.9	62.4	0.5	0.8	59.4

It can be seen from Tables 2-6 to 2-8 that the results obtained from LR and SP agree well with the MCS. Although the SP method runs 16 times more simulations than the LR, the improvement in accuracy is only noticeable in a few cases of thin beam $\left(L/h=20\right)$ where the lay-ups are $[45^o/-45^o]$ and $[-45^o/45^o/-45^o]$. These results ascertain the accuracy of the LR and SP methods. Furthermore, the average computing time is also displayed for each method. The time taken to pre-compute the integrals of stiffness and mass matrices is excluded. Even though this recorded time can vary considerably depending on the computer specifications or programming languages, the ratios between the run-time of MCS and PCE methods are evaluated. Both LR and SP approaches for the PCE method take the authors' computer less than a second, while the MCS requires slightly over a minute. This remark demonstrates the efficiency of the current PCE method. In addition, the LC beam deflections under various boundary conditions are plotted in Figs. 2-3 shows the probability density function (PDF) and probability of exceedance (PoE) curves of the mid-span displacements. The PDF graph shows identical data distribution across three methods, whereas in the PoE figures, all three methods only give the matching results up to $P\left(X>10^{-4}\right)$. This discrepancy is due to the lack of samples whose probability of occurrence is less than 10^{-4}. In Fig. 2-4,

the PoE curves of the output distribution computed by MCS, SP and LR are plotted 10 times and all of them show visible variation pass the point where $P\left(X<10^{-4}\right)$.

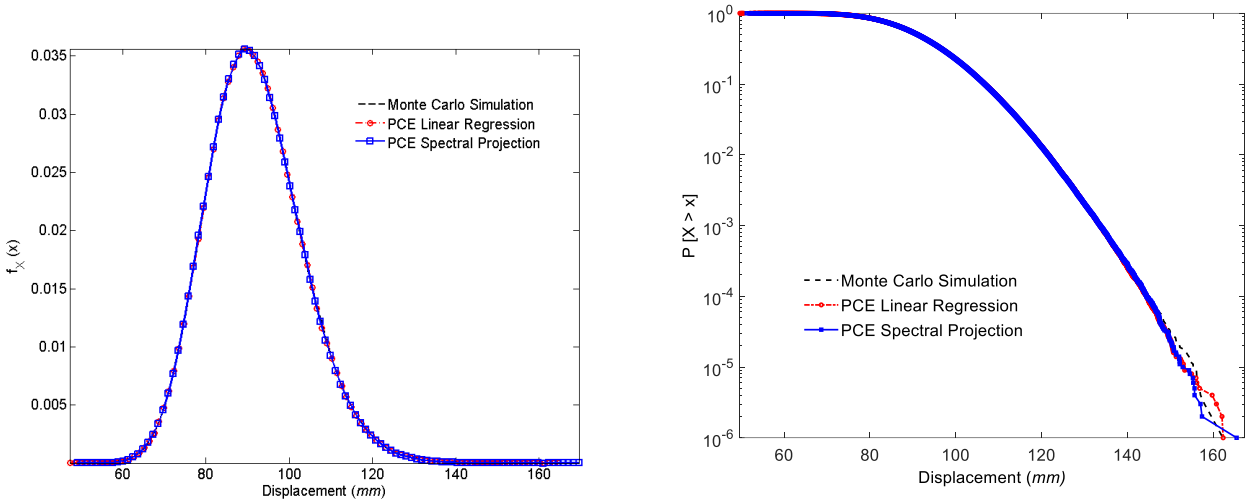

Figure 2-2: Probability density function (PDF) and Probability of exceedance (PoE) of three numerical methods (MCS, LR, SP) of the mid-span displacement (mm) for laminated composite beam (L/h = 20, S-S boundary condition)

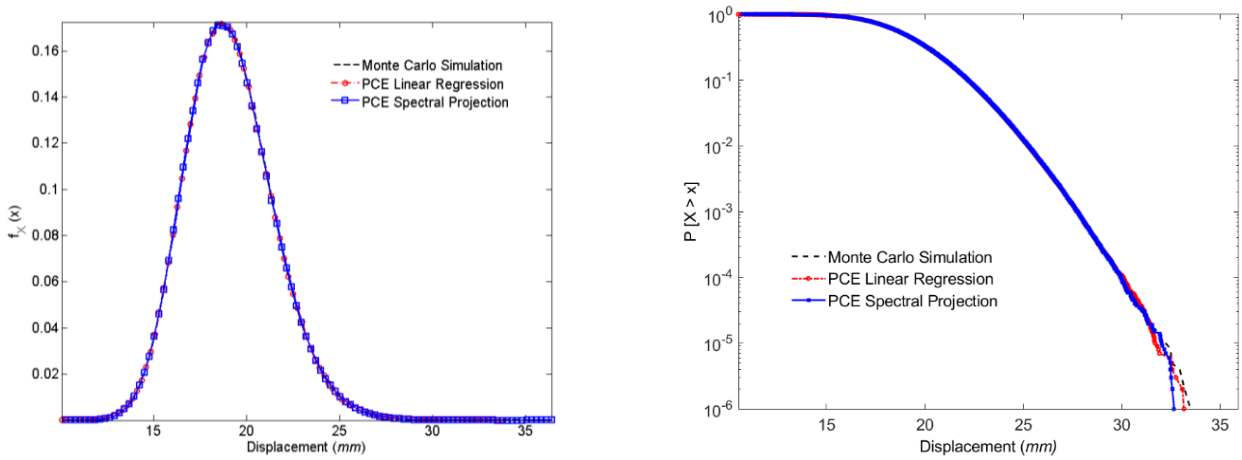

Figure 2-3: Probability density function (PDF) and Probability of exceedance (PoE) of three numerical methods (MCS, LR, SP) of the mid-span displacement (mm) for $[45^o/\text{-}45^o/45^o]$ laminated composite beam (L/h = 20, C-C boundary condition

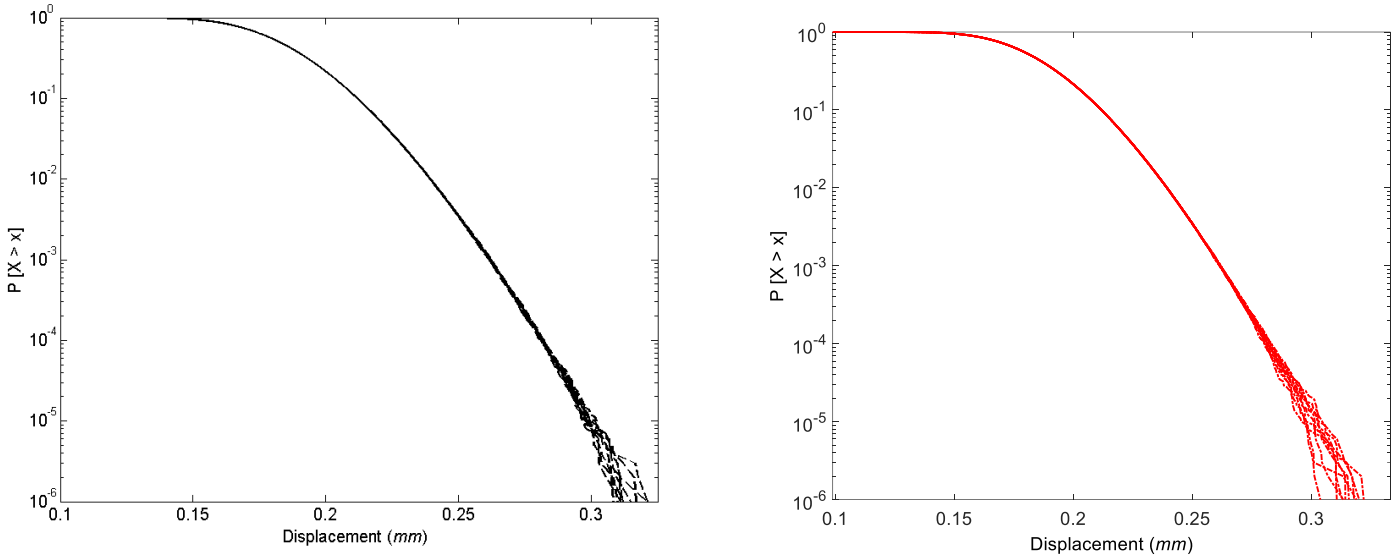

(a) MCS (b) LR

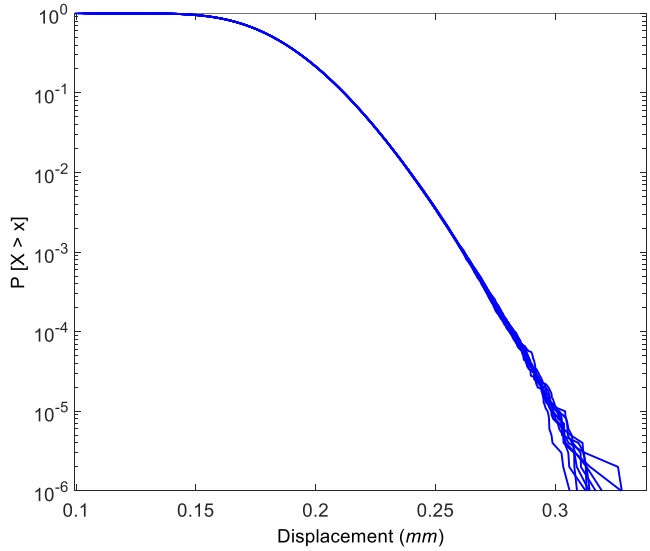

(c) SP

Figure 2-4: Variation in probability of exceedance (PoE) of mid-span displacement (mm) for the laminated composite beam (L/h=5, C-C boundary condition)

Table 2-9: Mean, standard deviation, kurtosis and skewness of fundamental frequency (Hz) of laminated composite beams with different lay-ups (MAT I) and S-S boundary condition

Lay-ups	Statistical moments	$L/h=5$			$L/h=20$		
		LR	SP	MC	LR	SP	MC
$[0^o/90^o]$	Mean	891.230	891.265	891.345	251.138	251.107	251.122
	SD	52.197	52.210	52.186	15.478	15.465	15.436
	Kurtosis	3.046	3.054	3.054	2.942	3.072	3.057
	Skewness	0.170	0.176	0.174	0.222	0.187	0.185
$[45^o/\text{-}45^o]$	Mean	574.380	574.405	574.391	152.486	152.481	152.472
	SD	34.893	34.908	34.892	9.380	9.374	9.389
	Kurtosis	3.061	3.056	3.060	2.887	3.058	3.065
	Skewness	0.180	0.177	0.179	0.207	0.183	0.185
$[0^o/90^o/0^o]$	Mean	1433.000	1433.202	1433.094	529.764	529.855	529.840
	SD	83.171	83.156	83.169	35.966	35.948	35.927
	Kurtosis	3.059	3.060	3.054	3.070	3.075	3.068

	Skewness	0.169	0.175	0.170	0.201	0.202	0.191
[45^o/-45^o/45^o]	Mean	574.429	574.418	574.417	152.500	152.484	152.484
	SD	34.925	34.890	34.910	9.391	9.387	9.371
	Kurtosis	3.056	3.064	3.059	3.063	3.057	3.073
	Skewness	0.179	0.181	0.180	0.182	0.187	0.183
Average computing time (s)		1.4	1.9	117.5	1.3	2.5	120.3

Table 2-10: Mean, standard deviation, kurtosis and skewness of fundamental frequency (Hz) of laminated composite beams with different lay-ups (MAT I) and C-C boundary condition

Lay-ups	Statistical moments	$L/h=5$			$L/h=20$		
		LR	SP	MC	LR	SP	MC
$[0^o/90^o]$	Mean	1558.420	1558.239	1558.318	552.984	552.986	552.989
	SD	87.957	87.872	87.812	33.448	33.478	33.501
	Kurtosis	3.042	3.055	3.053	2.668	3.057	3.056
	Skewness	0.171	0.171	0.169	0.185	0.183	0.180
$[45^o/\text{-}45^o]$	Mean	1119.291	1119.101	1119.239	341.336	341.318	341.307
	SD	66.516	66.533	66.471	20.931	20.892	20.888
	Kurtosis	3.044	3.047	3.059	2.937	3.058	3.052
	Skewness	0.170	0.175	0.175	0.120	0.178	0.176
$[0^o/90^o/0^o]$	Mean	1903.023	1902.896	1903.137	1052.855	1053.112	1053.129
	SD	110.435	110.430	110.547	65.283	65.372	65.372
	Kurtosis	3.056	3.058	3.061	3.063	3.065	3.056

	Skewness	0.173	0.171	0.179	0.181	0.178	0.178
[45^o/-45^o/45^o]	Mean	1119.214	1119.171	1119.285	341.353	341.308	341.353
	SD	66.382	66.429	66.480	20.911	20.920	20.945
	Kurtosis	3.053	3.043	3.055	3.061	3.049	3.058
	Skewness	0.170	0.173	0.173	0.181	0.177	0.181
Average computing time (s)		1.3	3.5	114.2	0.8	1.2	117.1

Table 2-11: Mean, standard deviation, kurtosis and skewness of fundamental frequency (*Hz*) of laminated composite beams with different lay-ups (MAT I) and C-F boundary condition

Lay-ups	Statistical moments	$L/h=5$			$L/h=20$		
		LR	SP	MC	LR	SP	MC
$[0^o/90^o]$	Mean	338.969	338.930	338.967	89.918	89.933	89.922
	SD	20.346	20.336	20.345	5.548	5.553	5.558
	Kurtosis	3.061	3.057	3.049	2.724	3.073	3.071
	Skewness	0.180	0.181	0.177	0.045	0.190	0.191
$[45^o/\text{-}45^o]$	Mean	211.651	211.635	211.629	54.453	54.456	54.458
	SD	12.952	12.956	12.939	3.351	3.354	3.353
	Kurtosis	3.049	3.062	3.063	2.770	3.049	3.062
	Skewness	0.178	0.181	0.185	0.032	0.178	0.183
$[0^o/90^o/0^o]$	Mean	617.404	617.420	617.421	193.115	193.109	193.121
	SD	37.323	37.290	37.282	13.374	13.389	13.375
	Kurtosis	3.055	3.056	3.060	3.069	3.077	3.080

	Skewness	0.172	0.175	0.175	0.203	0.207	0.206
[45^o/-45^o/45^o]	Mean	211.646	211.644	211.633	54.454	54.461	54.460
	SD	12.955	12.942	12.944	3.353	3.354	3.353
	Kurtosis	3.043	3.047	3.047	3.062	3.051	3.059
	Skewness	0.179	0.180	0.177	0.182	0.182	0.179
Average computing time (s)		0.4	1.0	112.0	0.5	1.1	119.8

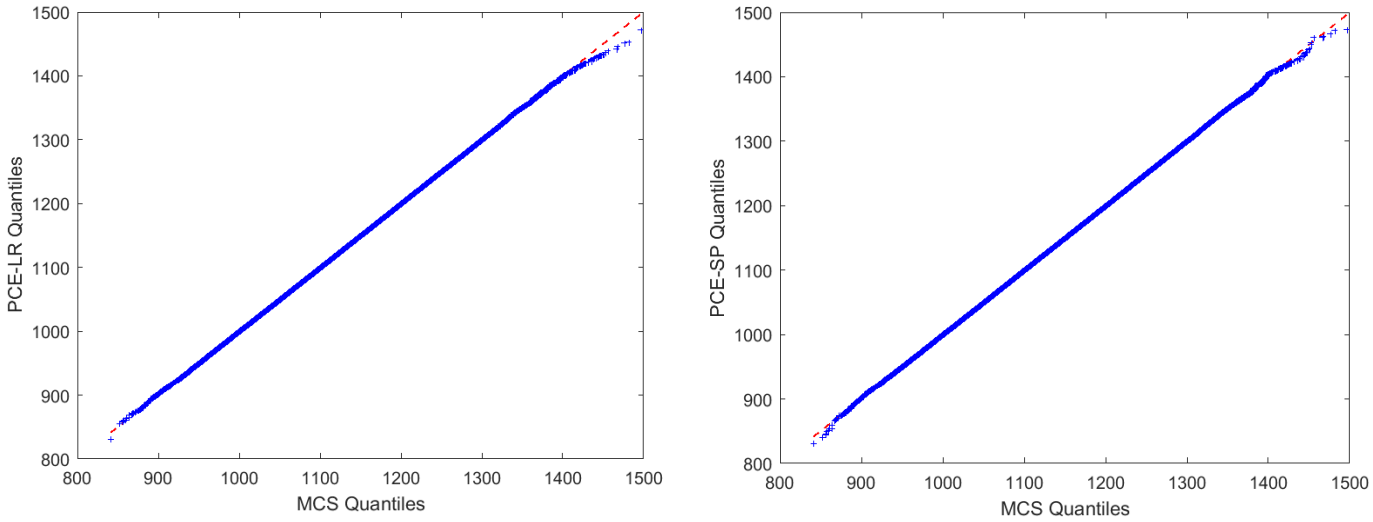

Figure 2-5: Quantile-quantile plot of Linear regression (LR) and Spectral projection (SP) methods with respect to the Monte Carlo Simulation (MCS) for the fundamental frequencies of $[45^o/\text{-}45^o]$ laminated composite beam (L/h=5, C-C boundary condition)

2.3.4. Vibration analysis

In this section, the fundamental frequencies (Hz) of LC beams with various boundary conditions, span-to-depth ratio, and fiber angles are given in Tables 2-9 to 2-11. These beams made of the MAT I have six lognormal-distributed random variables with a COV of 0.1. Similar to the static analysis, four statistical moments of mean, standard deviation, skewness, and kurtosis of the fundamental frequency (Hz) are computed and verified with those of the Monte Carlo simulations. While both the LR and SP methods give matching results for the mean and standard deviation, there is an apparent discrepancy of the skewness and kurtosis between the LR method and the other two. Tables 2-9 to 2-11 show that the kurtosis and skewness obtained from the LR method in the cases of $45^o/\text{-}45^o$ and $0^o/90^o$ beams differ from the kurtosis and skewness of the SP and MCS methods. This difference in the skewness and kurtosis does not mean the whole output distributions from these methods differ. Concerning efficiency, like the static analysis section above, the PCE methods show considerable improvement in the average computing time compared to the MCS for all cases of the LC beams.

Instead of comparing the PDF and PoE as above, Fig. 2-5 shows the quantile-quantile plots of 106 sample outputs obtained from MCS compared with the outputs of LR and SP methods in each of the two graphs. In a quantile-quantile plot, the two samples plotted have the same distribution when the plot is linear and lies along the 45-degree reference line. The straight lines shown in Fig. 2-5 further confirm that compared with the computationally-expensive MCS, the output distribution of LR and SP methods are accurate despite the much fewer simulations. In addition, the PoE curves of the output from all three methods are plotted ten times in Fig. 2-6 to demonstrate how the lack of samples pass the point $P\left(X<10^{-4}\right)$ causes the variation in the vibration output distribution. This also explains the deviation of data points from the 45-degree reference line at the lower- and upper-extreme quantiles in Fig. 2-5.

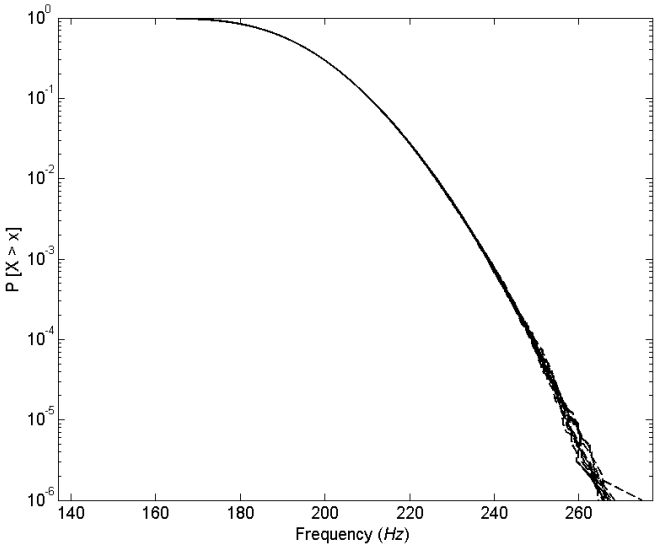

(a) MCS

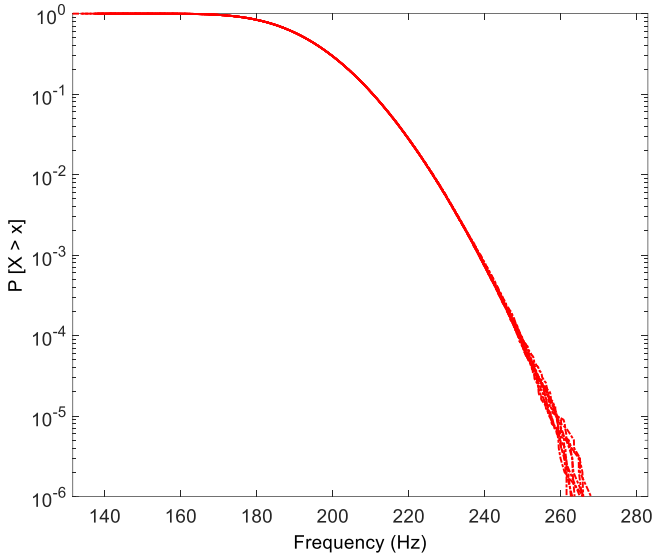

(b) LR

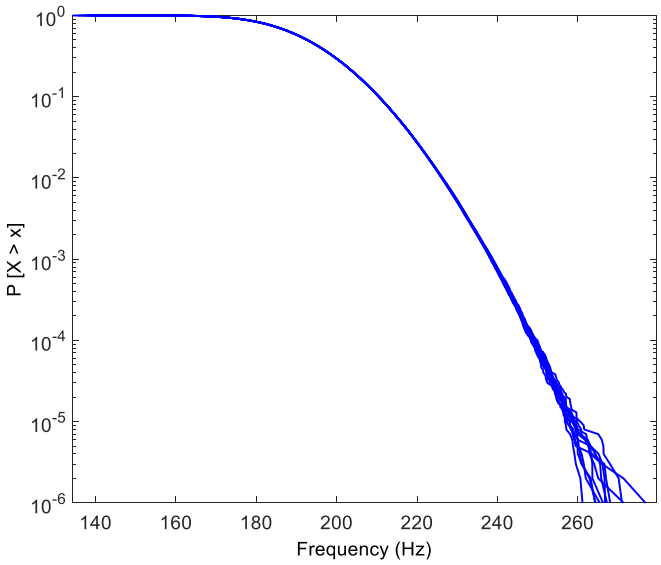

(c) SP

Figure 2-6: Variation in probability of exceedance (PoE) of fundamental frequencies (Hz) for the laminated composite beam (*L/h*=20, C-F boundary condition)

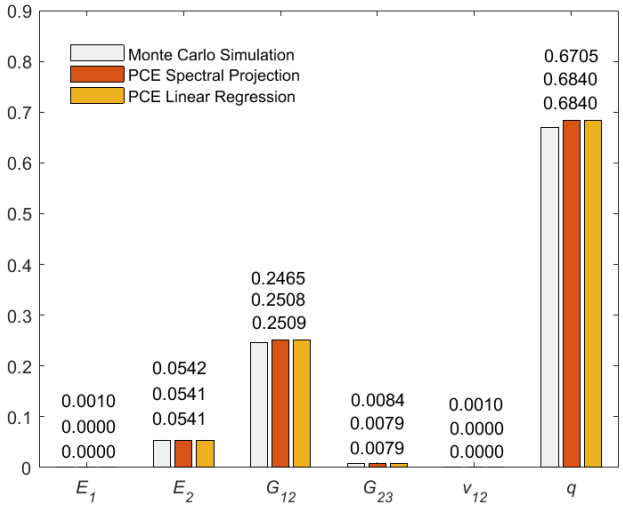

(a) $[45^o / -45^o]$

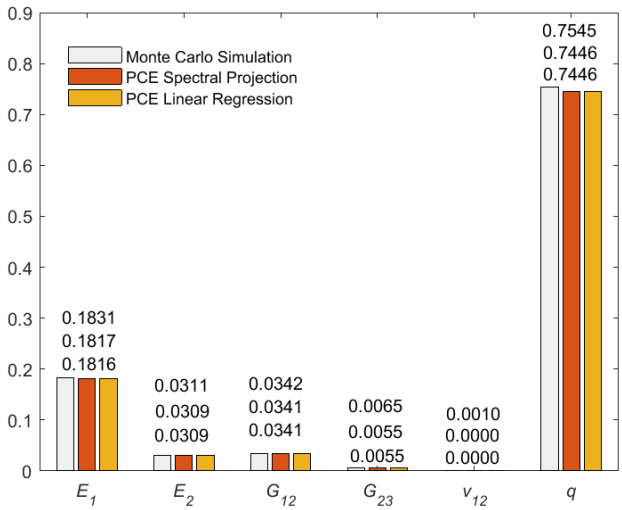

(b) $[0^o / 90^o]$

Figure 2-7: First-order Sobol indices of the random input variables with respect to the mid-span displacement (mm) of the LC beam model obtained from MCS and PCE (*L*/*h*=5, S-S boundary condition)

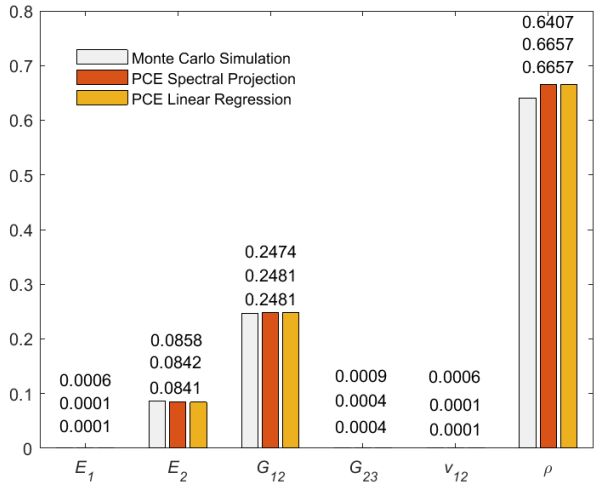

$[45^o / -45^o / 45^o]$

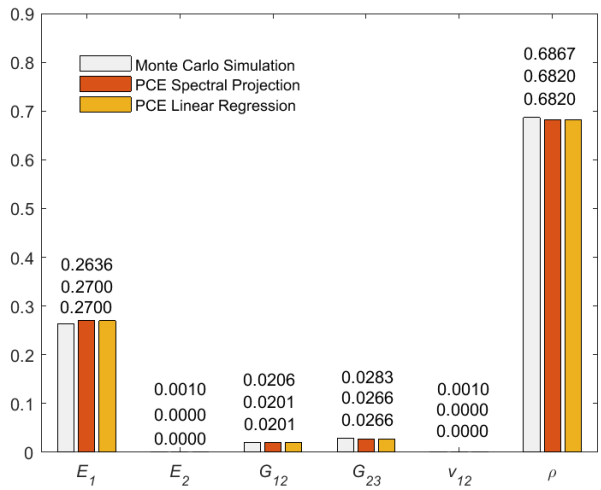

$[0^o / 90^o / 0^o]$

Figure 2-8: First-order Sobol indices of the random input variables with respect to the first fundamental frequency (Hz) of the LC beam model obtained from MCS and PCE (*L*/*h*=5, C-F boundary condition)

2.3.5 Sensitivity analysis

This section discusses the impact of each random input variable on the beam's deflection and fundamental frequency. In all cases, total-order Sobol indices computed are very similar to the first-order Sobol indices which infer that there is almost no interaction between the random input variables. Therefore, only the first-order Sobol indices are presented in Figs. 2-7 and 2-8. While these Sobol indices can be derived effortlessly from the PCE coefficients, they theoretically require two nested loops of N_s^2 beam solver runs in the crude MCS method. Several improved MCS algorithms proposed [110] can reduce the complexity to $(N_{rv}+2)N_s$ which is still nowhere near the efficiency of the PCE method presented in this chapter. In both figures, the three bars represent the first-order Sobol indices of the variable underneath computed using the MCS, PCE-SP and PCE-LR methods. The values above each group of bars are, respectively, for the MCS, PCE-SP and PCE-LR from top to bottom. It can be seen from both Figs. 2-7 and 2-8 that the PCE-SP and PCE-LR methods give the same results, all of which agree well with the MCS. Fig. 2-7 indicates the variation of applied distributed load q affects the beam's deflection the most.

Interestingly, to a lesser extent, the variation of the material's shear modulus G_{12} also influences the model outputs in the case of $[45^o/-45^o]$ lay-up while in the case of $[0^o/90^o]$ lay-up, the second most impactful variable is E_1. All the other four variables in both cases of lay-ups are considered insignificant and can be ignored to reduce the computational cost. Fig. 2-8 shows a similar pattern for the vibration analysis of the beam. For both $[45^o/-45^o/45^o]$ and $[0^o/90^o/0^o]$ lay-ups, the material mass density ρ affects the fundamental frequencies the most. The second most important variable is G_{12} for $[45^o/-45^o/45^o]$ lay-up and E_1 for $[0^o/90^o/0^o]$ lay-up. There is a small difference compared to the static analysis that in the case of $[45^o/-45^o/45^o]$ lay-up, E_2 plays a minor role in altering the beam's vibration responses. Knowing the lay-up arrangement, the sensitivity analysis is thus valuable for filtering the critical variables in a beam model, reducing the size of the random input vector and saving computing time.

2.4. Conclusion

This chapter investigated the stochastic static and vibration characteristics of laminated composite beams considering the uncertainty in material properties and applied loads. The random input parameters are modeled within a given range of the lognormal distributions. A metamodel-based polynomial chaos expansion with spectral projection and linear regression approaches was constructed using a few training samples simulated from the deterministic beam model. The higher-order shear deformation theory and Hamilton's principle are employed to derive the beam's governing equations which are then solved by Ritz's method. The results from PCE are validated against the crude Monte Carlo simulation regarding different statistical metrics and input parameters' sensitivity. The following conclusions could be drawn from the observations of the numerical results:

- The proposed PCE method has been demonstrated to accurately capture the stochastic output distribution while significantly reducing the number of required simulations and substantially reducing computing expenses.
- The linear regression approach requires fewer simulations than the spectral projection approach.
- The proposed methods can estimate Sobol's indices in global sensitivity analysis without incurring additional computing costs beyond those necessary for constructing the PCE model.
- The variability in the applied load influences the mid-span displacement most, while mass density variation significantly affects the vibration characteristics of LC beams.

The proposed use of PCE in this chapter for laminated composite beams can be extended to stochastic analysis of other composite structures. This approach is particularly valuable in cases where the complexity of calculations or the cost of practical experiments hinder efficient data collection.

CHAPTER 3 : A GENERAL HIGHER-ORDER SHEAR DEFORMATION THEORY FOR BUCKLING AND FREE VIBRATION ANALYSIS OF LAMINATED THIN-WALLED COMPOSITE I-BEAMS

This chapter extends the discussion to thin-walled structures, focusing on an advanced deterministic modeling approach. A general higher-order shear deformation thin-walled beam theory (HTWBT) is proposed to improve the accuracy of buckling and free vibration analyses for laminated thin-walled composite I-beams. The theory incorporates a unified nonlinear variation of shear strains across the wall thickness, offering a generalized formulation capable of recovering previous conventional beam theories as special cases. Series-type solutions with hybrid shape functions are developed for different boundary conditions. Numerical examples are performed on laminated thin-walled composite I-beams with arbitrary lay-ups. Effects of transverse shear strains, fiber angles and slenderness ratio on the critical buckling loads and natural frequencies of the beams are reported.

3.1. Introduction

It is known that the classical thin-walled beam theory (CTWBT), which neglects shear effects, by Vlasov [115] is the simplest one to analyse LC thin-walled beams [34, 116-118]. It underestimates the deflection and overestimates the natural frequencies/critical buckling loads. Latalski [119] developed a generalised beam theory for the semi-angular cross section based on Vlasov's work but added the effects of cross-section distortion. Yu and Hodges [120] developed a generalised Vlasov theory for composite beams using the finite element method. In order to account for effects of transverse shear strains, the first-order thin-walled beam theory (FTWBT) with the linear variation of the displacement in the wall thickness, which provides more accurate results than the CTWBT, has been employed [33, 121-128]. However, this theory requires a shear correction factor to rectify the stress-free boundary conditions. To solve this problem, the higher-order thin-walled beam theory (HTWBT), in which the axial displacement is nonlinearly approximated in the wall thickness, is proposed.

It should be highlighted the work of Carrera and colleagues [129-143], who invented the Carrera Unified Formulation (CUF) by using Taylor expansion and Lagrange expansion in displacement fields to obtain any refined theories on the basis of known fundamental nuclei. This approach has been successfully employed for many problems such as plates [129, 131, 132, 134, 136, 141, 143], shells [130, 133] and thin-walled composite beams sections such as C, box, I-section and wing structures [135, 137-140, 142]. It should be mentioned that the mathematic formulation from CUF is complicated with many variables in displacement fields. Chandiramani et al. [144] investigated free, forced and geometrically nonlinear vibration responses of LC composite box beams based on the assumption of a parabolic distribution of the transverse shear strains through the wall thickness. Literature review shows that the study on behaviours of thin-walled I-beams based on the general HTWBT, which can recover conventional theories such as CTWBT and FTWBT, is very limited. This intriguing topic therefore needs to be study further.

The objective of this Chapter is to develop a general higher-order shear deformation theory for buckling and free vibration analysis of LC thin-walled beams. The transverse shear strains are assumed to be nonlinearly variation by a shear function, and the axial displacement is obtained with a higher-order variation in the wall thickness. A hybrid series solution is developed for solving equations of motion with different boundary conditions and various theories including CTWBT, FTWBT and HTWBT. Numerical examples are performed to investigate the effects of lay-ups, fiber angle and shear deformation on the natural frequencies and critical buckling loads of the LC thin-walled I-section beams.

3.2. Theoretical formulation

In order to investigate theoretical formulation, three coordinate systems, namely, Cartesian coordinate system (x, y, z), local plate coordinate system (n, s, z) and contour coordinate s along the profile of the section are considered and illustrated in Fig. 3-1. It is assumed that θ is an angle of orientation between (n, s, z) and (x, y, z) coordinate systems, the pole P

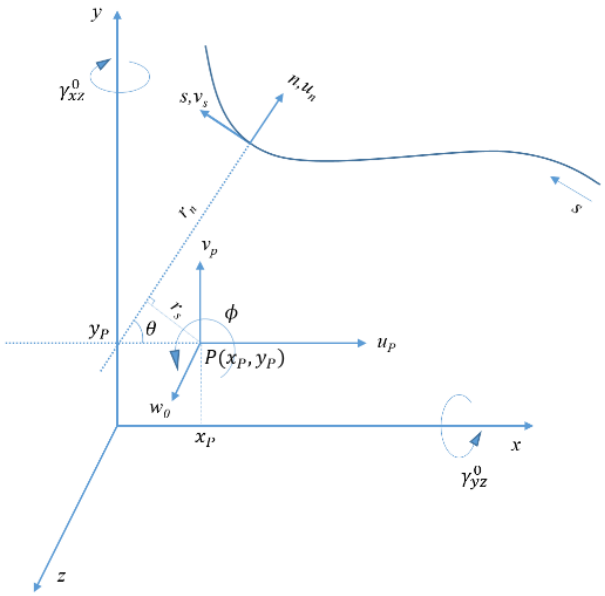

Figure 3-2: Thin-walled coordinate systems

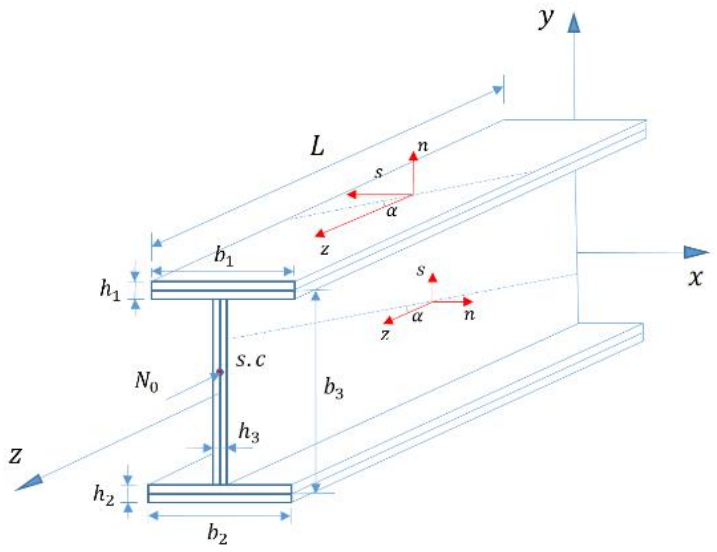

Figure 3-1: Geometry of laminated composite thin-walled I-beams

with coordinates (x_P, y_P) is the shear centre of the section.

For simplicity purpose, the following assumptions are employed: the displacements are small so that the geometrically nonlinear behaviours are neglected, the section contour does not deform in its own plane and the transverse shear strains vary nonlinearly in the wall thickness. The geometry of the thin-walled I-beam is shown in Fig. 3-2 with b_1, b_2, b_3 denote the widths and h_1, h_2, h_3 denote the thicknesses of top, bottom flange, and web, respectively.

3.2.1. Kinematics

The displacements $u(n, s, z, t)$ and $v(n, s, z, t)$ at any points of the beam cross-section under

a small rotation $\phi(z,t)$ about the pole axis can be expressed in terms of those at the pole $u_P(z,t)$ and $v_P(z,t)$ in $x-$ and $y-$directions, respectively, as follows ([145]):

$$u(n,s,z,t) = u_P(z,t) - (y - nx_{,s} - y_P)\phi(z,t) = u_P(z,t) - (Y - y_P)\phi(z,t) \tag{3-1a}$$

$$v(n,s,z,t) = v_P(z,t) + (x + ny_{,s} - x_P)\phi(z,t) = v_P(z,t) + (X - x_P)\phi(z,t) \tag{3-1b}$$

where the comma in the subscript is used to indicate the differentiation with respect to the variable that follows, $y_{,s}$ and $x_{,s}$ are the trigonometric functions $\cos\theta$ and $-\sin\theta$ respectively (see Fig. 3-1). X, Y are the coordinates of an arbitrary point along the n axis. It can be seen that the displacements in Eq. (3-1) satisfy the non-deformability conditions of cross-section. The displacements in the contour lines $u_n(n,s,z,t)$, $v_s(n,s,z,t)$ can be hence derived from the displacements in Eq. (3-1) as follows:

$$u_n(n,s,z,t) = u_P(z,t)y_{,s} - v_P(z,t)x_{,s} - R_s(n,s)\phi(z,t) \tag{3-2a}$$

$$v_s(n,s,z,t) = u_P(z,t)x_{,s} + v_P(z,t)y_{,s} + R_n(n,s)\phi(z,t) \tag{3-2b}$$

where $R_s(n,s) = r_s(s)$, $R_n(n,s) = r_n(n,s) + n$ in which $r_s(s), r_n(s)$ are the lengths of the perpendiculars from P to the tangent and normal of the profile line center (see Figure 3-1). Moreover, the shear strains $(\gamma_{sz}, \gamma_{nz})$ in the contour of thin-walled beams with open sections can be written in terms of the transverse shear strains $(\gamma_{xz}, \gamma_{yz})$ and a direct shear strain caused by the change rate of twist angle $\phi_{,z}$ ([146]) as follows:

$$\begin{aligned}\gamma_{sz}(n,s,z,t) &= \gamma_{xz}(n,z,t)X_{,s} + \gamma_{yz}(n,z,t)Y_{,s} + 2n\phi_{,z}(z,t) \\ &= v_{s,z} + w_{,s}\end{aligned} \tag{3-3a}$$

$$\begin{aligned}\gamma_{nz}(n,s,z,t) &= \gamma_{xz}(n,z,t)Y_{,s} - \gamma_{yz}(n,z,t)X_{,s} \\ &= u_{n,z} + w_{,n}\end{aligned} \tag{3-3b}$$

where w is the axial displacement at any point of the beam cross-section. It is assumed that the transverse shear strains $(\gamma_{xz}, \gamma_{yz})$ vary nonlinearly through the wall thickness as follows:

$$\gamma_{xz}(n,z,t) = g(n)\gamma_{xz}^{(0)}(z,t) \tag{3-4a}$$

$$\gamma_{yz}(n,z,t) = g(n)\gamma_{yz}^{(0)}(z,t) \tag{3-4b}$$

where $\gamma_{xz}^{(0)}, \gamma_{yz}^{(0)}$ are mid-surface transverse shear strains; $g(n)$ is a general higher-order shear function which satisfies the stress-free boundary conditions, i.e. $g(n = \pm h/2) = 0$ where h is the wall thickness.

$$\gamma_{xz}^{(0)} = \psi_y + \frac{\partial u_P}{\partial z} \tag{3-5a}$$

$$\gamma_{yz}^{(0)} = \psi_x + \frac{\partial v_P}{\partial z} \tag{3-5b}$$

where ψ_x, ψ_y are the rotations of the cross-section with respect to x and y

Substituting Eq. (3-2) and (3-4) into Eq. (3-3) and then integrating the subsequent results with respect to s and n lead to the expression of the axial displacement as follows:

$$\begin{aligned} &w(n,s,z,t) = w_0(z,t) + \gamma_{xz}^{(0)}(z,t)\left(g_0 x + f y_{,s}\right) + \gamma_{yz}^{(0)}(z,t)\left(g_0 y - f x_{,s}\right) \\ &-u_{P,z}(z,t)\left(x + n y_{,s}\right) - v_{P,z}(z,t)\left(y - n x_{,s}\right) - \phi_{,z}(z,t)\left(\bar{F}_\omega - n r_s\right) \end{aligned} \tag{3-6}$$

where $g_0 = g(n=0)$, $g = f_{,n}$; $\bar{F}_\omega(s)$ is a warping function which is defined by:

$$\bar{F}_\omega(s) = \int_{s_0}^{s} r_n(s) ds \tag{3-7}$$

A general higher-order shear deformation kinematics at any points of the LC thin-walled beam can be expressed as follows:

$$u(n,s,z,t) = u_P(z,t) - \left(y - n x_{,s} - y_P\right)\phi(z,t) \tag{3-8a}$$

$$v(n,s,z,t) = v_p(z,t) + \left(x + n y_{,s} - x_P\right)\phi(z,t) \tag{3-8b}$$

$$\begin{aligned} &w(n,s,z,t) = w_0(z,t) + \gamma_{xz}^{(0)}(z,t)\left(g_0 x + f y_{,s}\right) + \gamma_{yz}^{(0)}(z,t)\left(g_0 y - f x_{,s}\right) \\ &-u_{P,z}(z,t)\left(x + n y_{,s}\right) - v_{P,z}(z,t)\left(y - n x_{,s}\right) - \phi_{,z}(z,t)\left(\bar{F}_\omega - n r_s\right) \end{aligned} \tag{3-8c}$$

In this chapter, $f = n - \frac{4n^3}{3h^2}$ and $g = 1 - \frac{4n^2}{h^2}$ will be selected. It is worth noticing that the CTWBT can be found by setting $\gamma_{xz}^{(0)} = 0, \gamma_{yz}^{(0)} = 0$, while the FTWBT is recovered by putting $g = g_0 = 1, f = n$.

3.2.2. Strains

The linear non-zero strains related to the displacement in Eq. (3-8) are given by:

$$\varepsilon_z\left(n,s,z,t\right)=\varepsilon_z^{(0)}+n\varepsilon_z^{(1)}+f\varepsilon_z^{(2)} \tag{3-9a}$$

$$\gamma_{sz}\left(n,s,z,t\right)=n\gamma_{sz}^{(1)}+g\gamma_{sz}^{(2)} \tag{3-9b}$$

$$\gamma_{nz}\left(n,s,z,t\right)=g\gamma_{nz}^{(0)} \tag{3-9c}$$

where

$$\varepsilon_z^{(0)}\left(s,z,t\right)=w_{0,z}+\left(g_0\gamma_{xz,z}^{(0)}-u_{P,zz}\right)x+\left(g_0\gamma_{yz,z}^{(0)}-v_{P,zz}\right)y-\phi_{,zz}\bar{F}_\omega \tag{3-10a}$$

$$\varepsilon_z^{(1)}\left(s,z,t\right)=v_{P,zz}x_{,s}-u_{P,zz}y_{,s}+\phi_{,zz}r_s \tag{3-10b}$$

$$\varepsilon_z^{(2)}\left(s,z,t\right)=\gamma_{xz,z}^{(0)}y_{,s}-\gamma_{yz,z}^{(0)}x_{,s} \tag{3-10c}$$

$$\gamma_{sz}^{(1)}\left(s,z,t\right)=2\phi_{,z} \tag{3-10d}$$

$$\gamma_{sz}^{(2)}\left(s,z,t\right)=\gamma_{xz}^{(0)}x_{,s}+\gamma_{yz}^{(0)}y_{,s} \tag{3-10e}$$

$$\gamma_{nz}^{(0)}\left(s,z,t\right)=\gamma_{xz}^{(0)}y_{,s}-\gamma_{yz}^{(0)}x_{,s} \tag{3-10f}$$

3.2.3. Stresses

For LC thin-walled beams, it is supposed to be constituted by a number of orthotropic material layers with the same thickness. The reduced constitutive equations at the k^{th} – layer is given by:

$$\begin{Bmatrix}\sigma_z\\ \sigma_{sz}\\ \sigma_{nz}\end{Bmatrix}=\begin{pmatrix}P_{11} & P_{16} & 0\\ P_{16} & P_{66} & 0\\ 0 & 0 & P_{55}\end{pmatrix}\begin{Bmatrix}\varepsilon_z\\ \gamma_{sz}\\ \gamma_{nz}\end{Bmatrix} \tag{3-11}$$

where $P_{11}=\bar{Q}_{11}-\dfrac{\bar{Q}_{11}^2}{\bar{Q}_{22}}$, $P_{16}=\bar{Q}_{16}-\dfrac{\bar{Q}_{12}\bar{Q}_{26}}{\bar{Q}_{22}}$, $P_{66}=\bar{Q}_{66}-\dfrac{\bar{Q}_{26}^2}{\bar{Q}_{22}}$, $P_{55}=\bar{Q}_{55}$; $\bar{Q}_{ij}$ are the reduced stiffness components of materials (see [50] for more details).

3.2.4. Variational formulation

The characteristic equations of the LC thin-walled beams can be derived by Hamilton's equations in which the total energy of the system Π is composed of the strain energy Π_S,

work done by external force Π_W and kinetic energy Π_K as follows:

$$\int_{t_1}^{t_2} \left(\delta\Pi_S + \delta\Pi_W - \delta\Pi_K \right) dt = 0 \tag{3-12}$$

The variation of strain energy Π_S is defined by:

$$\delta\Pi_S = \int_\Omega \left(\sigma_z \delta\varepsilon_z + \sigma_{sz} \delta\gamma_{sz} + \sigma_{nz} \delta\gamma_{nz} \right) d\Omega \tag{3-13}$$

Substituting Eqs. (9) and (11) into Eq. (3-13) leads to:

$$\begin{aligned} \delta\Pi_S = \int_0^L \Big[& T_z \delta w_{0,z} + M_y \delta\gamma_{xz,z}^{(0)} + M_x \delta\gamma_{yz}^{(0)} + M_{ya} \delta u_{P,zz} + M_{xa} \delta v_{P,zz} \\ & + M_\omega \delta\phi_{,zz} + Q_x \delta\delta\gamma_{xz}^{(0)} + Q_y \delta\delta\gamma_{yz}^{(0)} + M_z \delta\phi_{,z} \Big] dz \end{aligned} \tag{3-14}$$

where the stress resultants $\left(T_z, M_y, M_x, M_{ya}, M_{xa}, M_\omega, Q_x, Q_y, M_z \right)$ are defined as follows:

$$\left(T_z, M_y, M_x \right) = \int_A \sigma_z \left(1, g_0 x + f y_{,s}, g_0 y - f x_{,s} \right) ds dn \tag{3-15a}$$

$$\left(M_{ya}, M_{xa}, M_\omega \right) = \int_A \sigma_z \left[-\left(x + n y_{,s} \right), -y + n x_{,s}, -\bar{F}_\omega + n r_s \right] ds dn \tag{3-15b}$$

$$Q_x = \int_A g \left(\sigma_{sz} x_{,s} + \sigma_{nz} y_{,s} \right) ds dn \tag{3-15c}$$

$$Q_y = \int_A g \left(\sigma_{sz} y_{,s} - \sigma_{nz} x_{,s} \right) ds dn \tag{3-15d}$$

$$M_z = \int_A 2n\sigma_{sz} ds dn \tag{3-15e}$$

These stress resultants are related to the displacement gradients as follows:

$$\begin{Bmatrix} T_z \\ M_y \\ M_x \\ Q_x \\ Q_y \\ M_{ya} \\ M_{xa} \\ M_\omega \\ M_z \end{Bmatrix} = \begin{bmatrix} L_{11} & L_{12} & L_{13} & L_{14} & L_{15} & L_{16} & L_{17} & L_{18} & L_{19} \\ L_{12} & L_{22} & L_{23} & L_{24} & L_{25} & L_{26} & L_{27} & L_{28} & L_{29} \\ L_{13} & L_{23} & L_{33} & L_{34} & L_{35} & L_{36} & L_{37} & L_{38} & L_{39} \\ L_{14} & L_{24} & L_{34} & L_{44} & L_{45} & L_{46} & L_{47} & L_{48} & L_{49} \\ L_{15} & L_{25} & L_{35} & L_{45} & L_{55} & L_{56} & L_{57} & L_{58} & L_{59} \\ L_{16} & L_{26} & L_{36} & L_{46} & L_{56} & L_{66} & L_{67} & L_{68} & L_{69} \\ L_{17} & L_{27} & L_{37} & L_{47} & L_{57} & L_{67} & L_{77} & L_{78} & L_{79} \\ L_{18} & L_{28} & L_{38} & L_{48} & L_{58} & L_{68} & L_{78} & L_{88} & L_{89} \\ L_{19} & L_{29} & L_{39} & L_{49} & L_{59} & L_{69} & L_{79} & L_{89} & L_{99} \end{bmatrix} \begin{Bmatrix} w_{0,z} \\ \gamma_{xz,z}^{(0)} \\ \gamma_{yz,z}^{(0)} \\ \gamma_{xz}^{(0)} \\ \gamma_{yz}^{(0)} \\ u_{P,zz} \\ v_{P,zz} \\ \phi_{,zz} \\ \phi_{,z} \end{Bmatrix} \tag{3-16}$$

where the stiffness components of the LC thin-walled beams L_{ij} $(i, j = 1,...,9)$ are defined by:

$$L_{11} = \int_s A_{11} ds \, , L_{12} = \int_s \left(A_{11} g_0 x + E_{11} y_{,s} \right) ds \, , L_{13} = \int_s \left(A_{11} g_0 y - E_{11} x_{,s} \right) ds \tag{3-17a}$$

$$L_{14} = \int_s A_{s16} x_{,s} ds \, , L_{15} = \int_s A_{s16} y_{,s} ds \, , L_{16} = -\int_s \left(A_{11} x + B_{11} y_{,s} \right) ds \tag{3-17b}$$

$$L_{17} = \int_s \left(-A_{11} y + B_{11} x_{,s} \right) ds \, , L_{18} = \int_s \left(-A_{11} \bar{F}_{\omega} + B_{11} r_s \right) ds \, , L_{19} = \int_s 2 B_{16} ds \tag{3-17c}$$

$$L_{22} = \int_s \left[g_0 x \left(A_{11} g_0 x + 2 E_{11} y_{,s} \right) + H_{11} y_{,s}^2 \right] ds \tag{3-17d}$$

$$L_{23} = \int_s \left[g_0 x \left(A_{11} g_0 y - E_{11} x_{,s} \right) + y_{,s} \left(E_{11} g_0 y - H_{11} x_{,s} \right) \right] ds \tag{3-17e}$$

$$L_{24} = \int_s \left(A_{s16} x g_0 + D_{s16} y_{,s} \right) x_{,s} ds \, , L_{25} = \int_s \left(A_{s16} x g_0 + D_{s16} y_{,s} \right) y_{,s} ds \tag{3-17f}$$

$$L_{26} = -\int_s \left[g_0 x \left(A_{11} x + B_{11} y_{,s} \right) + y_{,s} \left(E_{11} x + F_{11} y_{,s} \right) \right] ds \tag{3-17g}$$

$$L_{27} = \int_s \left[g_0 x \left(-A_{11} y + B_{11} x_{,s} \right) + y_{,s} \left(-E_{11} y + F_{11} x_{,s} \right) \right] ds \tag{3-17h}$$

$$L_{28} = \int_s g_0 x \left(-A_{11} \bar{F}_{\omega} + B_{11} r_s \right) + y_{,s} \left(-E_{11} \bar{F}_{\omega} + F_{11} r_s \right) ds \tag{3-17i}$$

$$L_{29} = \int_s 2 \left(B_{16} x g_0 + F_{16} y_{,s} \right) ds \tag{3-17j}$$

$$L_{33} = \int_s \left[g_0 y \left(A_{11} g_0 y - E_{11} x_{,s} \right) - x_{,s} \left(E_{11} g_0 y - H_{11} x_{,s} \right) \right] ds \tag{3-17k}$$

$$L_{34} = \int_s \left(A_{s16} y g_0 - D_{s16} x_{,s} \right) x_{,s} ds \, , L_{35} = \int_s \left(A_{s16} y g_0 - D_{s16} x_{,s} \right) y_{,s} ds \tag{3-17l}$$

$$L_{36} = -\int_s \left[x \left(A_{11} g_0 y - E_{11} x_{,s} \right) + y_{,s} \left(B_{11} g_0 y - F_{11} x_{,s} \right) \right] ds \tag{3-17m}$$

$$L_{37} = \int_s \left[-y \left(A_{11} g_0 y - E_{11} x_{,s} \right) + x_{,s} \left(B_{11} g_0 y - F_{11} x_{,s} \right) \right] ds \tag{3-17n}$$

$$L_{38} = \int_s \left[-\bar{F}_{\omega} \left(A_{11} g_0 y - E_{11} x_{,s} \right) + r_s \left(B_{11} g_0 y - F_{11} x_{,s} \right) \right] ds \tag{3-17o}$$

$$L_{39} = \int_s 2 \left(B_{16} y g_0 - F_{16} x_{,s} \right) ds \tag{3-17p}$$

$$L_{44}=\int_s\left(H_{s66}x_{,s}^2+H_{s44}y_{,s}^2\right)ds\,,\,L_{45}=\int_s x_{,s}y_{,s}\left(H_{s66}-H_{s44}\right)ds \tag{3-17q}$$

$$L_{46}=-\int_s\left(A_{s16}x+B_{s16}y_{,s}\right)x_{,s}ds\,,\,L_{47}=\int_s\left(-A_{s16}y+B_{s16}x_{,s}\right)x_{,s}ds \tag{3-17r}$$

$$L_{48}=\int_s\left(-A_{s16}\bar{F}_{\omega}+B_{s16}r_s\right)x_{,s}ds\,,\,L_{49}=\int_s 2x_{,s}B_{s66}ds \tag{3-17s}$$

$$L_{55}=\int_s\left(H_{s66}y_{,s}^2+H_{s44}x_{,s}^2\right)ds\,,\,L_{56}=-\int_s\left(A_{s16}x+B_{s16}y_{,s}\right)y_{,s}ds \tag{3-17t}$$

$$L_{57}=\int_s\left(-A_{s16}y+B_{s16}x_{,s}\right)y_{,s}ds\,,\,L_{58}=\int_s\left(-A_{s16}\bar{F}_{\omega}+B_{s16}r_s\right)y_{,s}ds \tag{3-17u}$$

$$L_{59}=\int_s 2y_{,s}B_{s66}ds\,,\,L_{66}=-\int_s\left[x\left(A_{11}x+B_{11}y_{,s}\right)+y_{,s}\left(B_{11}x+D_{11}y_{,s}\right)\right]ds \tag{3-17v}$$

$$L_{67}=\int_s\left[-y\left(A_{11}x+B_{11}y_{,s}\right)+x_{,s}\left(B_{11}x+D_{11}y_{,s}\right)\right]ds \tag{3-17w}$$

$$L_{68}=\int_s\left[-\bar{F}_{\omega}\left(A_{11}x+B_{11}y_{,s}\right)+r_s\left(B_{11}x+D_{11}y_{,s}\right)\right]ds \tag{3-17x}$$

$$L_{69}=\int_s 2\left(B_{16}x+D_{16}y_{,s}\right)ds\,,\,L_{77}=\int_s\left[y\left(A_{11}y-B_{11}x_{,s}\right)+x_{,s}\left(-B_{11}y+D_{11}x_{,s}\right)\right]ds \tag{3-17y}$$

$$L_{78}=\int_s\left[\bar{F}_{\omega}\left(A_{11}y-B_{11}x_{,s}\right)+r_s\left(-B_{11}y+D_{11}x_{,s}\right)\right]ds \tag{3-17z}$$

$$L_{79}=\int_s 2\left(-B_{16}y+D_{16}x_{,s}\right)ds \tag{3-17aa}$$

$$L_{88}=\int_s\left[-\bar{F}_{\omega}\left(-\bar{F}_{\omega}A_{11}+B_{11}r_s\right)+r_s\left(-B_{11}\bar{F}_{\omega}+D_{11}r_s\right)\right]ds \tag{3-17ab}$$

$$L_{89}=\int_s 2\left(-B_{16}\bar{F}_{\omega}+D_{16}r_s\right)ds\,,\,L_{99}=\int_s 4D_{66}ds \tag{3-17ac}$$

$$\left(A_{ij},B_{ij},D_{ij},E_{ij},F_{ij},H_{ij},B_{sij},H_{sij}\right)=\sum_{k=1}^{nl}\left(\int_{n_k}^{n_{k+1}}\left(1,n,n^2,f,nf,f^2,ng,g^2\right)Q_{ij}dn\right) \tag{3-18}$$

where nl is the number of layers and k is the layer index

The variation of potential energy Π_W of the LC thin-walled beams subjected to axial compressive load N_0 can be expressed as:

$$\begin{aligned}
&\delta\Pi_W = \int_\Omega \sigma_z^0 \left(u_{,z}\delta u_{,z} + v_{,z}\delta v_{,z}\right) d\Omega \\
&= \int_0^L N_0 \left[\delta u_{P,z}\left(u_{P,z} - J_P\phi_{,z}\right) + \delta v_{P,z}\left(v_{P,z} + I_P\phi_{,z}\right) + \delta\phi_{,z}\left(I_P v_{P,z} + K_P\phi_{,z} - J_P u_{P,z}\right)\right] dz
\end{aligned} \tag{3-19}$$

where $\sigma_z^0 = N^0 / A$ is averaged axial stress; A is the cross-sectional area; $\left(I_P, J_P, K_P\right)$ are moments of inertia of the cross-section about the centroid defined by:

$$\left\{I_P, J_P, K_P\right\} = \frac{1}{A}\int_{-h/2}^{h/2}\int_s \left\{X - x_P, Y - y_P, \left(Y - y_P\right)^2 + \left(X - x_P\right)^2\right\} dsdn \tag{3-20}$$

The variation of kinetic energy Π_K of the LC thin-walled beams is given by:

$$\begin{aligned}
&\delta\Pi_K = \int_\Omega \rho(n)\left(\dot{u}\delta\dot{u} + \dot{v}\delta\dot{v} + \dot{w}\delta\dot{w}\right) d\Omega \\
&= \int_0^L \left\{\delta\dot{u}_P\left(m_1\dot{u}_P - m_2\dot{\phi}\right) + \delta\dot{v}_P\left(m_1\dot{v}_P - m_3\dot{\phi}\right) + \delta\dot{\phi}\left[-m_2\dot{u}_P + \left(m_4 + m_5\right)\dot{\phi} - m_3\dot{v}_P\right]\right. \\
&+\delta\dot{w}_0\left(m_1\dot{w}_0 + m_{17}\dot{\gamma}_{xz}^{(0)} + m_{21}\dot{\gamma}_{yz}^{(0)} - m_6\dot{u}_{P,z} - m_{13}\dot{v}_{P,z} - m_{24}\dot{\phi}_{,z}\right) \\
&+\delta\dot{\gamma}_{xz}^{(0)}\left(m_{17}\dot{w}_0 + m_{18}\dot{\gamma}_{xz}^{(0)} + m_{19}\dot{\gamma}_{yz}^{(0)} - m_9\dot{u}_{P,z} - m_{14}\dot{v}_{P,z} - m_{20}\dot{\phi}_{,z}\right) \\
&+\delta\dot{\gamma}_{yz}^{(0)}\left(m_{21}\dot{w}_0 + m_{19}\dot{\gamma}_{xz}^{(0)} + m_{22}\dot{\gamma}_{yz}^{(0)} - m_{10}\dot{u}_{P,z} - m_{15}\dot{v}_{P,z} - m_{23}\dot{\phi}_{,z}\right) \\
&-\delta\dot{u}_{P,z}\left(m_6\dot{w}_0 + m_9\dot{\gamma}_{xz}^{(0)} + m_{10}\dot{\gamma}_{yz}^{(0)} - m_7\dot{u}_{P,z} - m_8\dot{v}_{P,z} - m_{11}\dot{\phi}_{,z}\right) \\
&-\delta\dot{v}_{P,z}\left(m_{12}\dot{w}_0 + m_{14}\dot{\gamma}_{xz}^{(0)} + m_{15}\dot{\gamma}_{yz}^{(0)} - m_8\dot{u}_{P,z} - m_{13}\dot{v}_{P,z} - m_{16}\dot{\phi}_{,z}\right) \\
&\left.-\delta\dot{\phi}_{,z}\left(m_{24}\dot{w}_0 + m_{20}\dot{\gamma}_{xz}^{(0)} + m_{23}\dot{\gamma}_{yz}^{(0)} - m_{11}\dot{u}_{P,z} - m_{16}\dot{v}_{P,z} - m_{25}\dot{\phi}_{,z}\right)\right\} dz
\end{aligned} \tag{3-21}$$

where the following relations have been used: $X_1 = g_0 x + f y_{,s}$, $Y_1 = g_0 y - f x_{,s}$; $F = \bar{F}_\omega - n r_s$; the dot-superscript is used to denote the differentiation with respect to the time t; $\rho(n)$ is the mass density and the inertia coefficients are given as follows:

$$\left\{m_1, m_2, m_3, m_4, m_5\right\} = \int_{-h/2}^{h/2}\int_s \rho\left\{1, Y - y_P, X - x_P, \left(Y - y_P\right)^2, \left(X - x_P\right)^2\right\} dsdn \tag{3-22a}$$

$$\left\{m_6, m_7, m_8, m_9, m_{10}, m_{11}\right\} = \int_{-h/2}^{h/2}\int_s \rho X\left\{1, X, Y, X_1, Y_1, F\right\} dsdn \tag{3-22b}$$

$$\left\{m_{12}, m_{13}, m_{14}, m_{15}, m_{16}\right\} = \int_{-h/2}^{h/2}\int_s \rho Y\left\{1, Y, X_1, Y_1, F\right\} dsdn \tag{3-22c}$$

$$\left\{m_{17}, m_{18}, m_{19}, m_{20}\right\} = \int_{-h/2}^{h/2} \int_{s} \rho X_1 \left\{1, X_1, Y_1, F\right\} dsdn \tag{3-22d}$$

$$\left\{m_{21}, m_{22}, m_{23}, m_{24}, m_{25}\right\} = \int_{-h/2}^{h/2} \int_{s} \rho \left\{Y_1, Y_1^2, Y_1 F, F, F^2\right\} dsdn \tag{3-22e}$$

3.2.5. Hybrid series solution

The displacement field is approximated as follows:

$$\left\{u_P, v_P, \phi\right\}(z,t) = \sum_{j=1}^{m} \varphi_j(z) \left\{u_{Pj}, v_{Pj}, \phi_j\right\}(t) \tag{3-23a}$$

$$\left\{w_0, \gamma_{xz}^{(0)}, \gamma_{yz}^{(0)}\right\}(z,t) = \sum_{j=1}^{m} \varphi_{j,z}(z) \left\{w_j, \xi_j, \eta_j\right\}(t) \tag{3-23b}$$

where $w_j(t), u_{Pj}(t), v_{Pj}(t), \xi_j(t), \eta_j(t)$ and $\phi_j(t)$ are six unknowns to be determined; $\varphi_j(z)$ are shape functions. It is noted that the approximations in Eq. (3-22) are known as Ritz-type series ones whose functions of approximation should be constructed to satisfy the specified essential boundary conditions (BCs). For the present chapter, shape functions are proposed in Table 3-1 and these functions must satisfy various BCs such as simply-supported (SS), clamped-free (CF) and clamped-clamped (CC).

Table 3-1. Shape functions and essential BCs of LC thin-walled I-beams

BC	$\varphi_j(z)$	$z=0$	$z=L$
SS	$\frac{z}{L}\left(1-\frac{z}{L}\right)e^{\frac{-jz}{L}}$	$u_P=v_P=\phi=0$	$u_P=v_P=\phi=0$
CF	$\left(\frac{z}{L}\right)^2 e^{\frac{-jz}{L}}$	$u_P=v_P=\phi=0$ $u_{P,z}=v_{P,z}=\phi_{,z}=0$ $w_0=\gamma_{xz}^{(0)}=\gamma_{yz}^{(0)}=0$	
CC	$\left(\frac{z}{L}\right)^2\left(1-\frac{z}{L}\right)^2 e^{\frac{-jz}{L}}$	$u_P=v_P=\phi=0$ $u_{P,z}=v_{P,z}=\phi_{,z}=0$ $w_0=\gamma_{xz}^{(0)}=\gamma_{yz}^{(0)}=0$	$u_P=v_P=\phi=0$ $u_{P,z}=v_{P,z}=\phi_{,z}=0$ $w_0=\gamma_{xz}^{(0)}=\gamma_{yz}^{(0)}=0$

Substituting Eq. (3-22) into Eq. (3-12) accounting for Eq. (3-14), (3-18), (3-20), and then using Lagrange's equations lead to the characteristic equations for vibration and buckling analysis of LC thin-walled beams as follows:

$$\mathbf{Kd}+\mathbf{M}\ddot{\mathbf{d}}=\mathbf{0} \tag{3-24}$$

where $\mathbf{K},\mathbf{M}$ are the stiffness and mass matrix, respectively; $\mathbf{d}=\begin{bmatrix}\mathbf{w} & \mathbf{u} & \mathbf{v} & \boldsymbol{\xi} & \boldsymbol{\eta} & \boldsymbol{\Phi}\end{bmatrix}^T$ is the displacement vector. The components of the stiffness matrix $\mathbf{K}$ are expressed by:

$$\mathbf{K}=\begin{bmatrix} \mathbf{K}^{11} & \mathbf{K}^{12} & \mathbf{K}^{13} & \mathbf{K}^{14} & \mathbf{K}^{15} & \mathbf{K}^{16} \\ {}^T\mathbf{K}^{12} & \mathbf{K}^{22} & \mathbf{K}^{23} & \mathbf{K}^{24} & \mathbf{K}^{25} & \mathbf{K}^{26} \\ {}^T\mathbf{K}^{13} & {}^T\mathbf{K}^{23} & \mathbf{K}^{33} & \mathbf{K}^{34} & \mathbf{K}^{35} & \mathbf{K}^{36} \\ {}^T\mathbf{K}^{14} & {}^T\mathbf{K}^{24} & {}^T\mathbf{K}^{34} & \mathbf{K}^{44} & \mathbf{K}^{45} & \mathbf{K}^{46} \\ {}^T\mathbf{K}^{15} & {}^T\mathbf{K}^{25} & {}^T\mathbf{K}^{35} & {}^T\mathbf{K}^{45} & \mathbf{K}^{55} & \mathbf{K}^{56} \\ {}^T\mathbf{K}^{16} & {}^T\mathbf{K}^{26} & {}^T\mathbf{K}^{36} & {}^T\mathbf{K}^{46} & {}^T\mathbf{K}^{56} & \mathbf{K}^{66} \end{bmatrix} \tag{3-25}$$

where

$$K_{ij}^{11}=L_{11}S_{ij}^{22},\ K_{ij}^{12}=L_{16}S_{ij}^{22},\ K_{ij}^{13}=L_{17}S_{ij}^{22},\ K_{ij}^{14}=L_{12}S_{ij}^{22}+L_{14}S_{ij}^{12}$$

$$K_{ij}^{15}=L_{13}S_{ij}^{22}+L_{15}S_{ij}^{12},\ K_{ij}^{16}=L_{18}S_{ij}^{22}+L_{19}S_{ij}^{12},\ K_{ij}^{22}=L_{66}S_{ij}^{22}+N_0S_{ij}^{11},\ K_{ij}^{23}=L_{67}S_{ij}^{22}$$

$$K_{ij}^{24}=L_{26}S_{ij}^{22}+L_{46}S_{ij}^{12},K_{ij}^{25}=L_{36}S_{ij}^{22}+L_{56}S_{ij}^{12},K_{ij}^{26}=L_{68}S_{ij}^{22}+L_{69}S_{ij}^{12}-N_0J_PS_{ij}^{11}$$

$$K_{ij}^{33}=L_{77}S_{ij}^{22}+N_0S_{ij}^{11},K_{ij}^{34}=L_{27}S_{ij}^{22}+L_{47}S_{ij}^{12},K_{ij}^{35}=L_{37}S_{ij}^{22}+L_{57}S_{ij}^{12}$$

$$K_{ij}^{36}=L_{78}S_{ij}^{22}+L_{79}S_{ij}^{12}+N_0I_PS_{ij}^{11},K_{ij}^{44}=L_{22}S_{ij}^{22}+L_{24}\left(S_{ij}^{12}+S_{ij}^{21}\right)+L_{44}S_{ij}^{11}$$

$$K_{ij}^{45}=L_{23}S_{ij}^{22}+L_{25}S_{ij}^{12}+L_{34}S_{ij}^{21}+L_{45}S_{ij}^{11},K_{ij}^{46}=L_{28}S_{ij}^{22}+L_{29}S_{ij}^{12}+L_{48}S_{ij}^{21}+L_{49}S_{ij}^{11}$$

$$K_{ij}^{55}=L_{33}S_{ij}^{22}+L_{35}\left(S_{ij}^{12}+S_{ij}^{21}\right)+L_{55}S_{ij}^{11},K_{ij}^{56}=L_{38}S_{ij}^{22}+L_{39}S_{ij}^{12}+L_{58}S_{ij}^{21}+L_{59}S_{ij}^{11}$$

$$K_{ij}^{66}=L_{88}S_{ij}^{22}+L_{89}\left(S_{ij}^{12}+S_{ij}^{21}\right)+L_{99}S_{ij}^{11}+N_0K_PS_{ij}^{11}$$

$$S_{ij}^{rs}=\int_0^L\frac{\partial^r\varphi_i}{\partial z^r}\frac{\partial^s\varphi_j}{\partial z^s}dz \tag{3-26}$$

The components of mass matrix $\mathbf{M}$ are given by:

$$\mathbf{M}=\begin{bmatrix}\mathbf{M}^{11}&\mathbf{M}^{12}&\mathbf{M}^{13}&\mathbf{M}^{14}&\mathbf{M}^{15}&\mathbf{M}^{16}\\{}^T\mathbf{M}^{12}&\mathbf{M}^{22}&\mathbf{M}^{23}&\mathbf{M}^{24}&\mathbf{M}^{25}&\mathbf{M}^{26}\\{}^T\mathbf{M}^{13}&{}^T\mathbf{M}^{23}&\mathbf{M}^{33}&\mathbf{M}^{34}&\mathbf{M}^{35}&\mathbf{M}^{36}\\{}^T\mathbf{M}^{14}&{}^T\mathbf{M}^{24}&{}^T\mathbf{M}^{34}&\mathbf{M}^{44}&\mathbf{M}^{45}&\mathbf{M}^{46}\\{}^T\mathbf{M}^{15}&{}^T\mathbf{M}^{25}&{}^T\mathbf{M}^{35}&{}^T\mathbf{M}^{45}&\mathbf{M}^{55}&\mathbf{M}^{56}\\{}^T\mathbf{M}^{16}&{}^T\mathbf{M}^{26}&{}^T\mathbf{M}^{36}&{}^T\mathbf{M}^{46}&{}^T\mathbf{M}^{56}&\mathbf{M}^{66}\end{bmatrix} \tag{3-27}$$

where

$$M_{ij}^{11}=m_1S_{ij}^{11},M_{ij}^{12}=-m_6S_{ij}^{11},M_{ij}^{13}=-m_{12}S_{ij}^{11},M_{ij}^{14}=m_{17}S_{ij}^{11},M_{ij}^{15}=m_{21}S_{ij}^{11}$$

$$M_{ij}^{16}=-m_{24}S_{ij}^{11},M_{ij}^{22}=m_7S_{ij}^{11}+m_1S_{ij}^{00},M_{ij}^{23}=m_8S_{ij}^{11},M_{ij}^{24}=-m_9S_{ij}^{11}$$

$$M_{ij}^{25}=-m_{10}S_{ij}^{11},M_{ij}^{26}=m_{11}S_{ij}^{11}-m_2S_{ij}^{00},M_{ij}^{33}=m_{13}S_{ij}^{11}+m_1S_{ij}^{00}$$

$$M_{ij}^{34}=-m_{14}S_{ij}^{11},M_{ij}^{35}=-m_{15}S_{ij}^{11},M_{ij}^{36}=m_{16}S_{ij}^{11}+m_3S_{ij}^{00},M_{ij}^{44}=m_{18}S_{ij}^{11},M_{ij}^{45}=m_{19}S_{ij}^{11}$$

$$M_{ij}^{46}=-m_{20}S_{ij}^{11},M_{ij}^{55}=m_{22}S_{ij}^{11},\ M_{ij}^{56}=-m_{23}S_{ij}^{11},\ M_{ij}^{66}=m_{25}S_{ij}^{11}+\left(m_4+m_5\right)S_{ij}^{00} \tag{3-28}$$

It is noted that the buckling responses of the LC thin-walled beams can be derived from Eq. (3-24) by solving $\left|\mathbf{K}-\lambda\mathbf{K_g}\right|=\mathbf{0}$, whereas the free vibration behaviours are obtained by setting $\mathbf{d}\left(t\right)=\mathbf{d}e^{i\omega t}$ where ω is the natural frequency, $i^2=-1$ the imaginary unit, and then solving the subsequent result $\left(\mathbf{K}-\omega^2\mathbf{M}\right)\mathbf{d}=\mathbf{0}$.

3.3. Numerical results

The material properties of the beams analysed in this section are shown in Table 3-2 below.

Table 3-2: Material properties of LC thin-walled I-beams

Material properties	MAT I [147]	MAT II [148]	MAT III [149]	MAT IV [147]
$E_1\ (GPa)$	53.78	144	144	25
$E_2\ (GPa)$	17.93	9.65	9.68	1
$G_{12} = G_{13}\ (GPa)$	8.96	4.14	4.14	0.6
$G_{23}\ (GPa)$	3.45	3.45	3.45	0.6
ν	0.25	0.3	0.3	0.25
$\rho\ (kg/m^3)$	1968.90	1389	-	1

3.3.1 Convergence study

This section conducts convergence study of the present solution for vibration and buckling analysis of composite I-beams (MAT I, $b_1 = b_2 = b_3 = 5\times10^{-2}\,\text{m}$, $h_1 = h_2 = h_3 = 2.08\times10^{-3}\,\text{m}$ and $L = 2\,\text{m}$) with various boundary conditions, namely, SS, CF and CC . For lay-up, all the flanges and web are angle-ply $[45^o/-45^o]_{4s}$ with 16 plies and uniform thickness. Their natural frequencies (*Hz*) and critical buckling loads (*kN*) are given in Table 3-3.

Table 3-3. Convergence of fundamental frequencies (*Hz*) and critical buckling loads (*kN*) for the LC thin-walled I-beam with different boundary conditions

BC	m					
	2	4	6	8	10	12
Fundamental frequency (*Hz*)						
SS	16.7573	16.5382	16.4762	16.4753	16.4753	16.4753
CC	37.3798	37.2488	37.2435	37.2409	37.2374	37.2272
CF	5.9567	5.877	5.8723	5.8721	5.8721	5.8722
Critical buckling load (*kN*)						
SS	2.7505	2.6880	2.6691	2.6688	2.6688	2.6688
CC	10.7671	10.6489	10.6281	10.6281	10.6281	10.6281
CF	0.7060	0.6680	0.6679	0.6679	0.6679	0.6679

It can be observed that the convergence speed of the buckling analysis is quicker than the vibration one. The proposed solutions converge with series number $m=10$ for natural frequencies and $m=6$ for buckling loads. These series numbers are therefore applied in the subsequent analyses.

3.3.2 Verification and parametric study

Example 1: For verification purpose, composite I-beams (MAT I, $b_1=b_2=b_3=0.05\text{m}$, $h_1=h_2=h_3=h=0.00208\text{m}$) and symmetrical lay-up $[\alpha^o/-\alpha^o]_{4s}$ in both flanges and web are studied. Tables 3-4 and 3-5 show the fundamental frequencies and critical buckling loads with various BCs. It is clear that the present solutions for FTWBT are in excellent agreement with those from previous studies [124, 147, 150, 151]. Due to the additional shear effect, the results from HTWBT are slightly different. These tables also present some new results for thicker beams ($L/b_3=5$ and 10), which can be useful for future reference. Fig. 3-3 displays the variation of the fundamental frequencies and critical buckling loads with respect to fiber angle change for various theories. It can be observed that the results from HTWBT

are slightly lower than those from FTWBT and those from CBWBT are noticeably higher than the HTWBT and FTWBT in all fiber angles.

Table 3-4. Fundamental frequency (*Hz*) of LC thin-walled I-beams with different boundary conditions and span-to-height ratios

BC	Reference	Lay-up						
		$[0]_{4s}$	$[15/-15]_{4s}$	$[30/-30]_{4s}$	$[45/-45]_{4s}$	$[60/-60]_{4s}$	$[75/-75]_{4s}$	$[90/-90]_{4s}$
L/b_3=40								
SS	Present (HTWBT)	24.135	22.954	19.794	16.475	14.657	14.068	13.538
	Present (FTWBT)	24.163	22.974	19.805	16.481	14.661	14.072	13.965
	Nguyen et al. [147] (FTWBT)	24.169	22.977	19.806	16.481	14.660	14.071	13.964
	Nguyen et al. [147] (CTWBT)	24.198	23.001	19.820	16.490	14.668	14.079	13.972
	Vo and Lee [124] (FTWBT)	24.150	22.955	19.776	16.446	14.627	14.042	13.937
	Kim et al. [150] (CTWBT)	24.194	22.997	19.816	16.487	14.666	14.077	13.970
L/b_3=20								
CF	Present (HTWBT)	26.436	25.143	21.685	18.050	16.058	15.413	15.296
	Present (FTWBT)	26.470	25.168	21.698	18.057	16.063	15.418	15.301
	Kim and Lee [151] (FTWBT)	26.460	25.160	21.700	18.060	16.060	15.420	15.300
	Nguyen et al. [147] (FTWBT)	26.479	25.174	21.699	18.057	16.063	15.417	15.299
	Nguyen et al. [147] (CTWBT)	26.514	25.202	21.717	18.069	16.072	15.427	15.309
L/b_3=40								
CC	Present (HTWBT)	54.198	51.655	44.677	37.237	33.142	31.811	31.568
	Present (FTWBT)	54.499	51.876	44.790	37.302	33.1897	31.856	31.613
L/b_3=10								
SS	Present (HTWBT)	372.076	356.585	310.809	260.096	231.742	222.431	220.705
	Present (FTWBT)	378.427	361.331	313.311	261.494	232.810	223.457	221.739
CF	Present (HTWBT)	104.813	99.874	86.359	71.977	64.058	61.487	61.018
	Present (FTWBT)	105.351	100.271	86.564	72.090	64.143	61.567	61.099
CC	Present (HTWBT)	745.489	731.822	661.601	564.603	506.049	485.710	481.698
	Present (FTWBT)	798.300	773.783	685.611	578.677	516.922	496.144	492.167
L/b_3=5								
SS	Present (HTWBT)	1344.158	1312.736	1176.720	999.590	894.553	858.598	851.566

	Present (FTWBT)	1422.882	1374.247	1211.303	1019.590	909.980	873.414	866.491
CF	Present (HTWBT)	405.333	388.894	339.562	284.438	253.531	243.382	241.503
	Present (FTWBT)	413.280	394.858	342.708	286.182	254.845	244.626	242.751
CC	Present (HTWBT)	2200.409	2252.548	2193.488	1964.319	1787.989	1715.788	1698.878
	Present (FTWBT)	2594.384	2600.996	2434.795	2123.285	1915.436	1838.472	1822.071

Table 3-5. Critical buckling load (N) of LC thin-walled I-beams with different boundary conditions and span-to-height ratios

BC	Reference	Lay-up						
		[0]4s	$[15/-15]_{4s}$	$[30/-30]_{4s}$	$[45/-45]_{4s}$	$[60/-60]_{4s}$	$[75/-75]_{4s}$	$[90/-90]_{4s}$
L/b_3=80								
SS	Present	1437.0	1298.7	964.7	667.9	528.5	486.9	958.6
	Present	1438.0	1299.4	965.1	668.1	528.7	487.0	959.0
	Nguyen et. al	1438.1	1299.4	965.0	668.1	528.6	487.0	959.0
	Nguyen et. al	1438.8	1300.0	965.2	668.2	528.7	487.1	959.3
	Kim et al. [152]	1438.8	1300.0	965.2	668.2	528.7	487.1	964.4
L/b_3=20								
CF	Present	5727.4	5180.3	3852.4	2668.8	2112.1	1945.8	3826.0
	Present	5740.3	5189.3	3856.4	2670.6	2113.3	1946.9	3831.1
	Nguyen et. al	5743.3	5191.0	3856.8	2670.6	2113.2	1946.7	3831.4
	Nguyen et. al	5755.2	5199.7	3861.0	2672.7	2114.7	1948.3	3837.3
	Kim et al. [152]	5755.2	5199.8	3861.0	2672.7	2114.7	1948.3	3837.8
	Vo and Lee	5741.5	5189.0	3854.5	2668.4	2111.3	1945.1	3829.8
L/b_3=80								
CC	Present	5727.4	5180.3	3852.4	2668.8	2112.1	1945.8	3826.0
	Present	5740.3	5189.3	3856.4	2670.6	2113.3	1946.9	3831.1
L/b_3=10								
SS	Present	85.45	78.50	59.65	41.78	33.17	30.56	58.70
	Present	88.43	80.63	60.63	42.24	33.48	30.84	59.93
CF	Present	22.58	20.49	15.31	10.63	8.42	7.75	15.17
	Present	22.78	20.63	15.37	10.66	8.44	7.77	15.25
CC	Present	281.03	268.44	216.23	156.26	125.21	115.34	207.48
	Present	315.97	295.06	229.62	162.83	129.74	119.52	223.67
L/b_3=5								
SS	Present	281.05	268.47	216.25	156.28	125.22	115.35	207.49
	Present	316.00	295.08	229.64	162.85	129.75	119.54	223.69
CF	Present	85.45	78.49	59.65	41.77	33.16	30.55	58.69
	Present	88.42	80.62	60.62	42.23	33.47	30.84	59.93
CC	Present	657.01	679.58	629.11	496.32	408.95	376.70	566.53
	Present	885.99	880.70	757.62	569.25	461.62	425.24	705.90

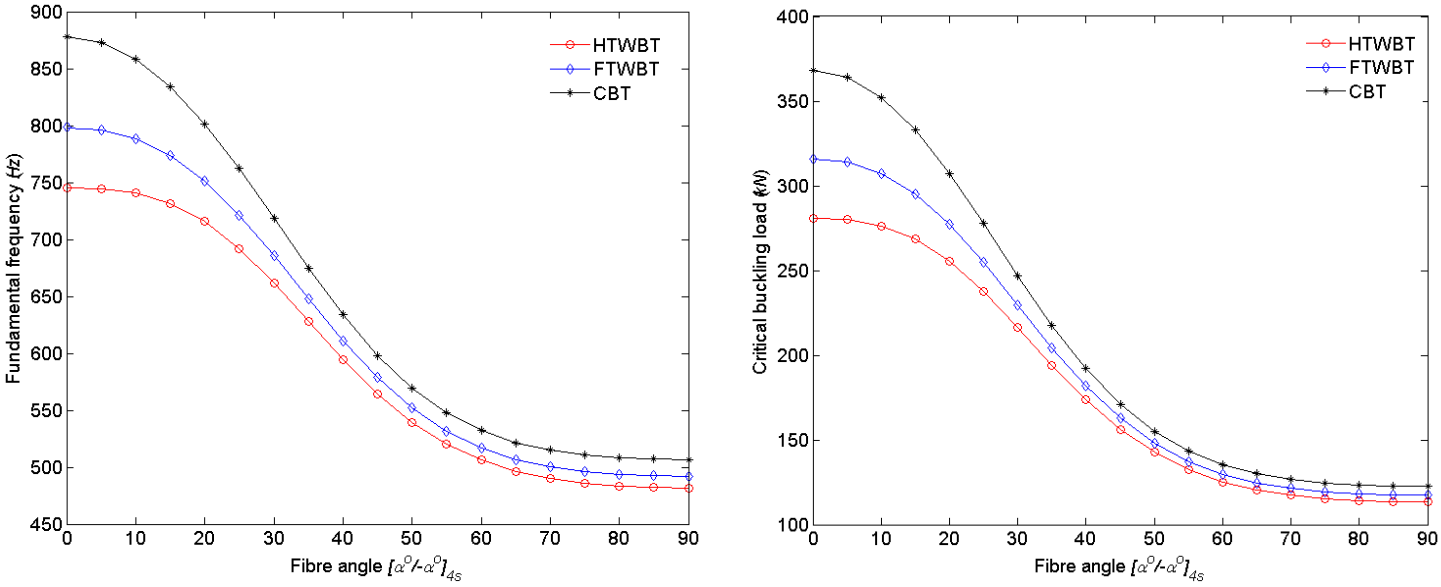

a) Fundamental frequencies b) Critical buckling loads

Figure 3-3: Variation of the fundamental frequencies (Hz) and critical buckling loads of LC thin-walled I-beam with respect to fiber angle change (CC boundary condition,)

Example 2: Two composite I-beams with three different lay-ups $[0^o/0^o/0^o/0^o]$, $[0^o/90^o/90^o/0^o]$, $[45^o/-45^o/-45^o/45^o]$ in both flanges and web are considered, the first one for torsional frequencies (MAT II, $h_1 = h_2 = h_3 = h = 0.03\text{m}$, $b_1 = b_2 = b_3 = 0.6\text{m}$) and the second one for critical buckling loads (MAT III, $h_1 = h_2 = h_3 = h = 0.01\text{m}$, $b_1 = b_2 = 0.05\text{m}$, $b_3 = 0.1m$). The present solutions of torsional frequencies in Table 3-6 for both FTWBT and HTWBT, match with those without shear effect [148] but differ from the results accounting for the shear effect. The discrepancy in transverse shear effect in the FTWBT and HTWBT model does not have much impact on the torsional frequencies. On the other hand, the critical buckling loads in Table 3-7 show good agreement with those from Piovan and Cortinez [149]. It is worth noting that the critical buckling loads from HTWBT model are slightly less than those from FTWBT in the cases of $[0^o/0^o/0^o/0^o]$ and $[0^o/90^o/90^o/0^o]$ lay-ups but are almost the same for $[45^o/-45^o/-45^o/45^o]$.

Table 3-6. Torsional frequencies (*Hz*) of LC thin-walled I-beams with various fibre lay-up and slenderness span-to-height ratios

Lay-up	b_3/L	Theory	ω_1	ω_2	ω_3	ω_4
[0°/0°/0°/0°]	0.05	Present (FTWBT)	16.24	63.22	141.08	249.51
		Present (HTWBT)	16.24	63.22	141.09	249.56
		Cortinez and Piovan (CTWBT) [148]	16.24	63.35	141.86	251.76
		Cortinez and Piovan (FTWBT) [148]	15.64	55.00	107.55	165.41
	0.10	Present (FTWBT)	63.22	249.20	552.69	966.04
		Present (HTWBT)	63.22	249.20	552.69	966.01
		Cortinez and Piovan (CTWBT) [148]	63.35	251.76	565.78	1005.4
		Cortinez and Piovan (FTWBT) [148]	55.00	165.41	284.29	401.86
	0.15	Present (FTWBT)	141.08	552.65	1207.87	2070.50
		Present (HTWBT)	141.07	552.65	1207.81	2069.76
		Cortinez and Piovan (CTWBT) [148]	141.86	565.78	1272.31	2261.46
		Cortinez and Piovan (FTWBT) [148]	107.55	284.29	459.86	631.49
[0°/90°/90°/0°]	0.05	Present (FTWBT)	12.20	46.54	103.44	182.69
		Present (HTWBT)	12.20	46.54	103.44	182.72
		Cortinez and Piovan (CTWBT) [148]	12.19	46.61	103.95	184.21
		Cortinez and Piovan (FTWBT) [148]	11.96	43.02	87.94	140.98
	0.10	Present (FTWBT)	46.54	182.44	404.19	706.08
		Present (HTWBT)	46.54	182.44	404.18	705.98
		Cortinez and Piovan (CTWBT) [148]	46.61	184.21	413.54	734.59
		Cortinez and Piovan (FTWBT) [148]	43.02	140.98	257.02	375.94
	0.15	Present (FTWBT)	103.43	404.18	882.88	1511.93
		Present (HTWBT)	103.43	404.17	882.91	1512.98
		Cortinez and Piovan (CTWBT) [148]	103.95	413.54	929.52	1651.89
		Cortinez and Piovan (FTWBT) [148]	87.94	257.02	435.12	610.43

	0.05	Present (FTWBT)	8.54	24.45	49.80	84.88
		Present (HTWBT)	8.54	24.45	49.80	84.82
		Cortinez and Piovan (CTWBT) [148]	10.98	28.11	54.18	89.99
		Cortinez and Piovan (FTWBT) [148]	10.96	27.98	53.61	88.35
[45º/-45º/ -45º/45º]	0.10	Present (FTWBT)	24.45	84.78	182.77	316.11
		Present (HTWBT)	24.45	84.78	182.77	316.10
		Cortinez and Piovan (CTWBT) [148]	28.11	89.99	191.65	333.74
		Cortinez and Piovan (FTWBT) [148]	27.98	88.34	184.14	311.75
	0.15	Present (FTWBT)	49.80	182.76	394.21	672.39
		Present (HTWBT)	49.80	182.76	394.20	672.38
		Cortinez and Piovan (CTWBT) [148]	54.18	191.65	419.94	739.46
		Cortinez and Piovan (FTWBT) [148]	53.61	184.14	386.03	644.07

Table 3-7. Critical buckling load (N) of LC cantilever I-beam with various lay-ups and span-to-height ratios

Lay-up		L/b_3=20	L/b_3=10
[0°/0°/0°/0°]	Present (HTWBT)	19144	75403
	Present (FTWBT)	19179	75951
	Piovan and Cortinez (FTWBT) [149]	19175	75559
[0°/90°/90°/0°]	COSMOS/M [149]	19058	73564
	Present (HTWBT)	10495	41591
	Present (FTWBT)	10501	41683
	Piovan and Cortinez (FTWBT) [149]	10561	41861
	COSMOS/M [149]	10350	40698
[45°/-45 °/-45°/4 °]	Present (HTWBT)	1935	7846
	Present (FTWBT)	1935	7848
	Piovan and Cortinez (FTWBT) [149]	2003	8012
	COSMOS/M [149]	2033	7958

Example 3: This example further confirms the accuracy of the present solution and investigates the effects of additional shear deformation with respect to fiber angle change. Tables 3-8 to 3-10 present the first three natural frequencies and critical buckling loads of composite I-beams (MAT IV, $h_1 = h_2 = h_3 = h = 0.01\text{m}$, $b_1 = b_2 = 0.2\text{m}$, $b_3 = 0.3\text{m}$) with angle-ply lay-up $[\alpha^o / -\alpha^o]$ in both flanges and unidirectional in the web. The following non-dimensional terms are used $\bar{\omega} = \dfrac{\omega L^2}{b_3}\sqrt{\dfrac{\rho}{E_2}}$ and $\bar{N}_{cr} = N_{cr}\dfrac{L^2}{E_2 h b_3^{\,3}}$. Again, the present results for both HTWBT and FTWBT are in excellent match with those from Nguyen et al. [147] and Vo and Lee [124]. Some new results for thick beams $L/b_3 = 5$ and 10 are also given for future benchmark.

Table 3-8. Non-dimensional fundamental frequency of LC thin-walled I-beams with different boundary conditions and span-to-height ratios

BC	Reference	Frequency	Lay-up						
			[0]	[15/-15]	[30/-30]	[45/-45]	[60/-60]	[75/-75]	[90/-90]
SS	Present (HTWBT)	ω_1	7.042	6.305	3.751	2.150	1.627	1.492	1.468
		ω_2	8.300	7.737	5.356	3.663	2.975	2.715	2.647
		ω_3	17.967	16.676	12.574	8.567	6.485	5.949	5.851
	Present (FTWBT)	ω_1	7.107	6.326	3.755	2.150	1.625	1.490	1.465
		ω_2	8.300	7.737	5.357	3.665	2.979	2.720	2.652
		ω_3	19.140	17.583	12.943	8.569	6.469	5.925	5.824
	Nguyen et al. [147] (FTWBT)	ω_1	7.107	6.327	3.755	2.151	1.627	1.493	1.468
		ω_2	8.189	7.528	5.137	3.610	2.967	2.713	2.645
		ω_3	19.140	17.594	12.904	8.538	6.495	5.985	5.860
CF	Present (HTWBT)	ω_1	2.536	2.255	1.338	0.767	0.580	0.532	0.523
		ω_2	3.197	3.247	2.612	1.915	1.577	1.439	1.401
		ω_3	6.886	6.327	4.642	3.778	3.565	3.323	3.268
	Present (FTWBT)	ω_1	2.547	2.259	1.339	0.766	0.580	0.532	0.523
		ω_2	3.197	3.247	2.612	1.915	1.578	1.440	1.402
		ω_3	7.123	6.502	4.708	3.814	3.596	3.318	3.263
	Nguyen et al. [147] (FTWBT)	ω_1	2.547	2.259	1.339	0.767	0.580	0.532	0.523
		ω_2	3.174	3.057	2.423	1.877	1.572	1.438	1.400
		ω_3	7.123	6.538	4.746	3.821	3.597	3.327	3.272
CC	Present (HTWBT)	ω_1	14.867	13.907	8.432	4.854	3.675	3.373	3.316
		ω_2	18.354	16.434	10.190	6.233	4.853	4.436	4.344
		ω_3	28.752	27.689	23.010	13.310	10.088	9.261	9.099
	Present (FTWBT)	ω_1	15.481	14.129	8.472	4.857	3.667	3.358	3.301
		ω_2	18.354	16.434	10.192	6.243	4.873	4.462	4.372
		ω_3	34.230	32.473	23.215	13.337	10.060	9.205	9.046
	Nguyen et al. [147] (FTWBT)	ω_1	15.480	14.129	8.474	4.865	3.682	3.378	3.322
		ω_2	17.239	16.086	10.104	6.206	4.839	4.423	4.332
		ω_3	34.221	32.379	23.221	13.368	10.121	9.285	9.131
		ω_1	15.460	14.122	8.471	4.862	3.678	3.374	3.319
		ω_2	17.211	16.064	10.092	6.202	4.836	4.421	4.330

Vo and Lee [124] (FTWBT)	ω_3	33.996	32.174	23.209	13.392	10.147	9.308	9.152

Table 3-9. Non-dimensional fundamental frequency of LC thin-walled I-beams with different boundary conditions and span-to-height ratios

BC	Reference	Frequency	Lay-up [0]	[15/-15]	[30/-30]	[45/-45]	[60/-60]	[75/-75]	[90/-90]
L/b_3=10									
SS	Present (HTWBT)	ω_1	6.657	6.168	3.724	2.140	1.617	1.482	1.457
		ω_2	8.091	7.257	4.510	2.764	2.157	1.974	1.934
		ω_3	13.506	12.932	10.697	8.424	6.373	5.834	5.733
	Present (FTWBT)	ω_1	6.886	6.250	3.739	2.146	1.624	1.490	1.465
		ω_2	8.091	7.257	4.510	2.762	2.152	1.967	1.926
		ω_3	15.790	14.874	11.714	8.501	6.442	5.909	5.810
CF	Present (HTWBT)	ω_1	2.466	2.232	1.333	0.765	0.578	0.530	0.521
		ω_2	2.949	2.730	1.863	1.251	1.007	0.920	0.898
		ω_3	5.756	5.418	4.244	3.552	3.373	3.274	3.218
	Present (FTWBT)	ω_1	2.508	2.246	1.336	0.766	0.579	0.531	0.523
		ω_2	2.949	2.729	1.863	1.251	1.006	0.919	0.897
		ω_3	6.382	5.923	4.470	3.681	3.483	3.305	3.250
CC	Present (HTWBT)	ω_1	12.121	12.681	8.170	4.770	3.612	3.306	3.249
		ω_2	16.777	16.158	9.676	5.638	4.302	3.944	3.874
		ω_3	18.220	16.651	15.560	12.891	9.797	8.959	8.801
	Present (FTWBT)	ω_1	13.621	13.395	8.325	4.822	3.655	3.353	3.297
		ω_2	18.220	16.158	9.674	5.628	4.280	3.916	3.845
		ω_3	21.931	21.449	19.233	13.125	9.969	9.144	8.990
L/b_3=5									
SS	Present (HTWBT)	ω_1	5.580	5.701	3.621	2.106	1.593	1.459	1.433
		ω_2	8.009	7.106	4.258	2.482	1.894	1.736	1.705
		ω_3	8.169	8.033	7.393	6.833	6.086	5.570	5.469
	Present (FTWBT)	ω_1	6.173	5.969	3.678	2.125	1.610	1.477	1.453
		ω_2	8.009	7.106	4.257	2.477	1.884	1.724	1.693
		ω_3	10.486	10.201	8.960	8.006	6.245	5.727	5.628
CF	Present	ω_1	2.234	2.144	1.316	0.759	0.574	0.526	0.517

	(HTWBT)	ω_2	2.877	2.576	1.594	0.972	0.756	0.692	0.678
		ω_3	3.858	3.749	3.289	2.928	2.828	3.143	2.808
	Present (FTWBT)	ω_1	2.369	2.196	1.326	0.762	0.577	0.529	0.521
		ω_2	2.877	2.576	1.594	0.971	0.754	0.690	0.676
		ω_3	4.756	4.554	3.778	3.261	3.119	3.085	3.081
CC	Present (HTWBT)	ω_1	7.913	8.858	7.327	4.504	3.447	3.155	3.097
		ω_2	8.875	9.778	8.660	5.449	4.125	3.782	3.718
		ω_3	16.826	16.016	9.499	8.616	8.411	8.232	8.046
	Present (FTWBT)	ω_1	9.860	11.306	7.802	4.647	3.525	3.221	3.163
		ω_2	12.082	11.912	9.500	5.456	4.141	3.802	3.739
		ω_3	18.104	16.016	11.369	11.006	9.371	8.559	8.401

Table 3-10. Non-dimensional critical buckling load of LC thin-walled I-beams with different boundary conditions and span-to-height ratios

BC	Reference	Lay-up						
		[0]	[15/-15]	[30/-30]	[45/-45]	[60/-60]	[75/-75]	[90/-90]
L/b_3=20								
SS	Present (HTWBT)	11.730	9.405	3.329	1.094	0.626	0.527	0.509
	Present (FTWBT)	11.948	9.469	3.336	1.095	0.626	0.527	0.510
	Nguyen et al. [147]	11.947	9.468	3.336	1.094	0.626	0.527	0.510
CF	Present (HTWBT)	3.021	2.377	0.835	0.274	0.157	0.132	0.128
	Present (FTWBT)	3.035	2.381	0.835	0.274	0.157	0.132	0.128
	Nguyen et al. [147]	3.035	2.381	0.835	0.274	0.157	0.132	0.128
CC	Present (HTWBT)	41.973	36.051	13.143	4.347	2.491	2.096	2.027
	Present (FTWBT)	44.914	37.007	13.249	4.363	2.498	2.103	2.034
	Nguyen et al. [147]	44.914	37.007	13.249	4.363	2.498	2.102	2.034
L/b_3=10								
SS	Present (HTWBT)	10.494	9.014	3.286	1.087	0.623	0.524	0.507

	Present (FTWBT)	11.230	9.253	3.313	1.091	0.625	0.526	0.508
CF	Present (HTWBT)	2.932	2.351	0.832	0.273	0.156	0.132	0.127
	Present (FTWBT)	2.987	2.367	0.834	0.274	0.157	0.132	0.127
CC	Present (HTWBT)	29.532	30.909	12.494	4.242	2.444	2.056	1.988
	Present (FTWBT)	36.203	33.915	12.889	4.306	2.473	2.080	2.012
L/b_3=5								
SS	Present (HTWBT)	7.384	7.728	3.124	1.061	0.611	0.514	0.497
	Present (FTWBT)	9.052	8.480	3.223	1.077	0.618	0.520	0.503
CF	Present (HTWBT)	2.623	2.253	0.821	0.272	0.156	0.131	0.127
	Present (FTWBT)	2.807	2.313	0.828	0.273	0.156	0.131	0.127
CC	Present (HTWBT)	13.514	17.699	10.435	3.870	2.272	1.910	1.843
	Present (FTWBT)	20.387	25.420	11.623	4.091	2.374	1.997	1.929

The additional shear effect of HTWBT when compared to FTWBT for fundamental frequencies and buckling loads is investigated. The shear effect percentage is defined as $S.E(\%) = \frac{\bar{\omega}_{FTWBT} - \bar{\omega}_{HTWBT}}{\bar{\omega}_{FTWBT}} \times 100\%$ or $S.E(\%) = \frac{\bar{N}_{cr-FTWBT} - \bar{N}_{cr-HTWBT}}{\bar{N}_{cr-FTWBT}} \times 100\%$. As expected, the shear effect is particularly significant for thick beam where L/b_3 is small in Figs. 3-4 and 3-5. For lay-up $[15^o/-15^o]$ and $L/b_3 = 5$, the maximum shear effect on the critical buckling load of C-C beams is 30%, which is higher than that of fundamental frequency (21%). The increase in the fiber angle drastically reduces the shear effect from more than 18% for

unidirectional lay-up $[0^o/0^o]$ to 2% one with lay-up with fiber angle greater than 60^o (Fig. 3-6b). The shear effect of CC beams is much higher than that of SS and CF ones even though these differences become lower as the L/b_3 ratio and the fiber angle increases (Figs. 3-5 and 3-6).

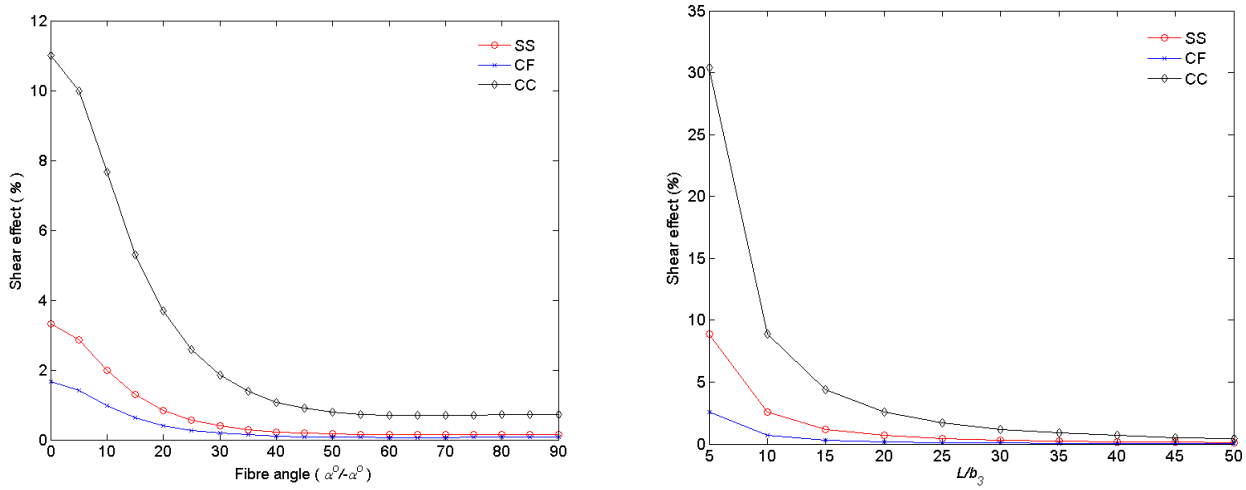

a) Fundamental frequencies b) Critical buckling loads

Figure 3-4: Shear effect (%) on the fundamental frequencies and critical buckling loads for various span-to-height ratios with lay-up (SS, CC, CF boundary conditions)

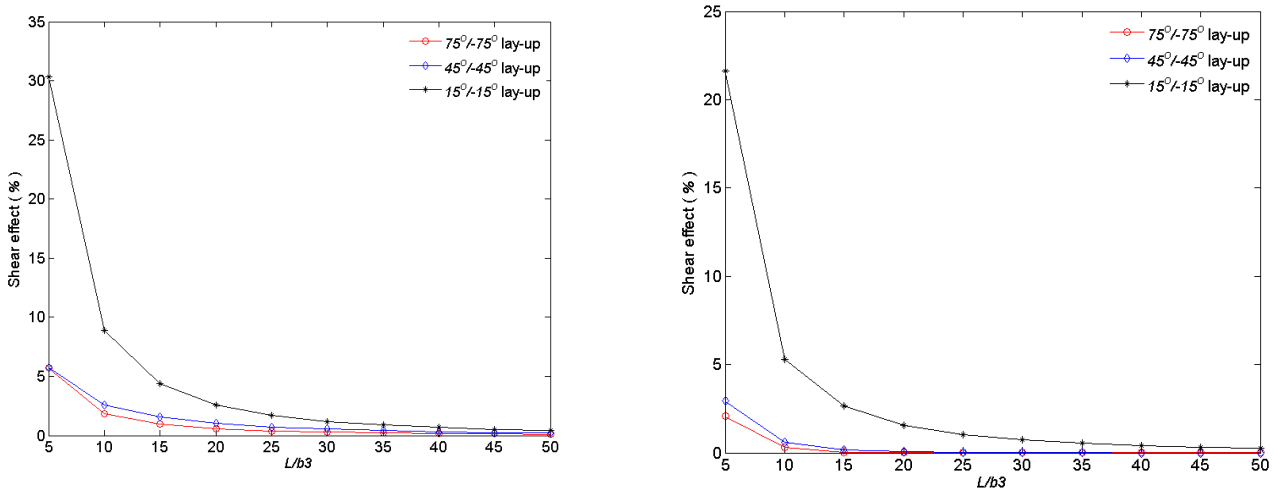

a) Fundamental frequencies b) Critical buckling load

Figure 3-5: Shear effect (%) on the fundamental frequencies and critical buckling loads of LC thin-walled I-beam for various span-to-height ratios with lay-ups , and (CC boundary condition

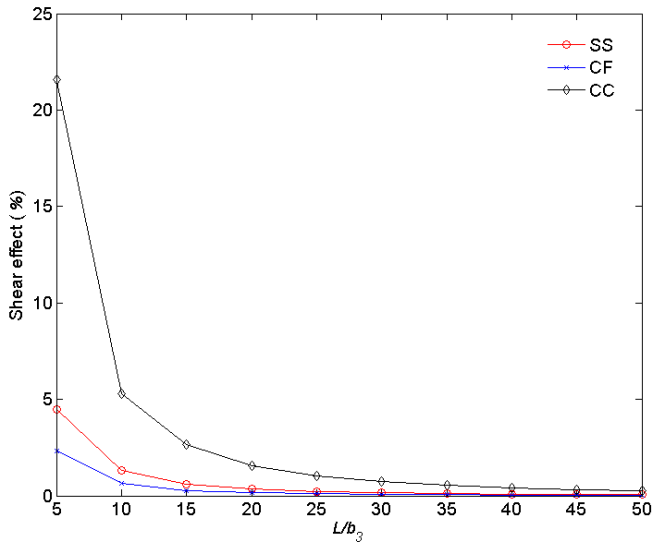

a) Fundamental frequencies

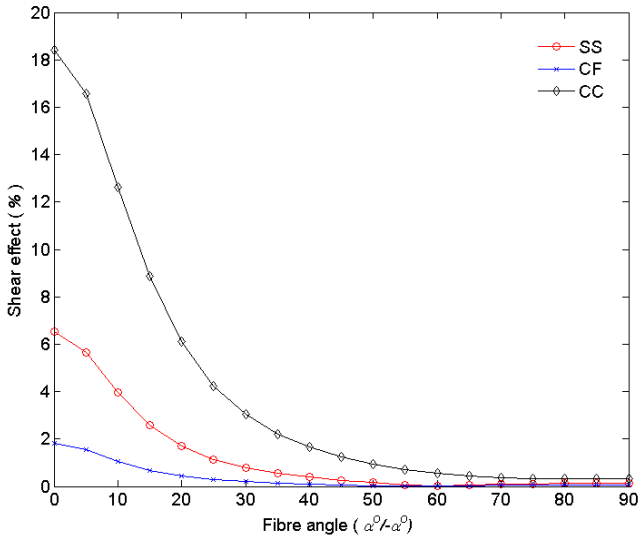

b) Critical buckling load

Figure 3-6: Variation of shear effect (%) on the fundamental frequencies and critical buckling loads with respect to fiber angle change and boundary conditions ()

Figs. 3-7 to 3-9 present the first three vibration mode shapes, which are plotted from the FTWBT and HTWBT, of C-C beam with lay-up $[45^{\circ}/\text{-}45^{\circ}]$. There is no visible difference in Fig. 3-8 between two models as expected since the beam is in torsion mode and the transverse shear strain γ_{xz}^{0} and γ_{yz}^{0} are zero along the beam length. This explains the torsional frequencies of two models in Table 3-6 are almost identical. Nonetheless, the transverse shear strains γ_{xz}^{0} and γ_{yz}^{0} in Figs. 3-7 and 3-9 are different and more apparent at the beam ends.

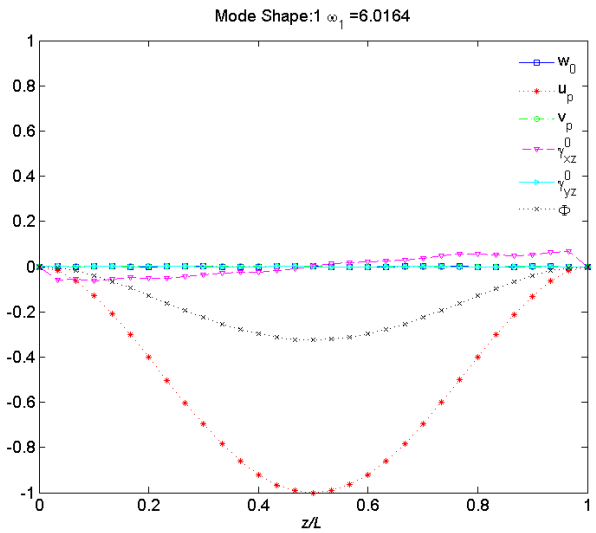

a) FTWBT

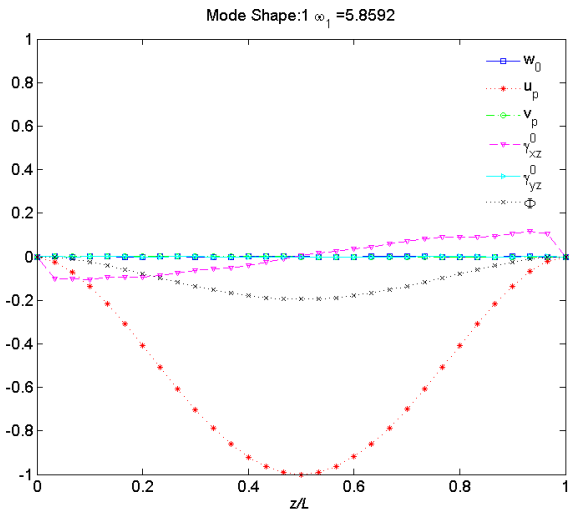

b) HTWBT

Figure 3-7: The first mode shape of LC thin-walled I-beams with lay-up $[45^o/\text{-}45^o]$

(CC boundary condition, $L/b_3 = 10$)

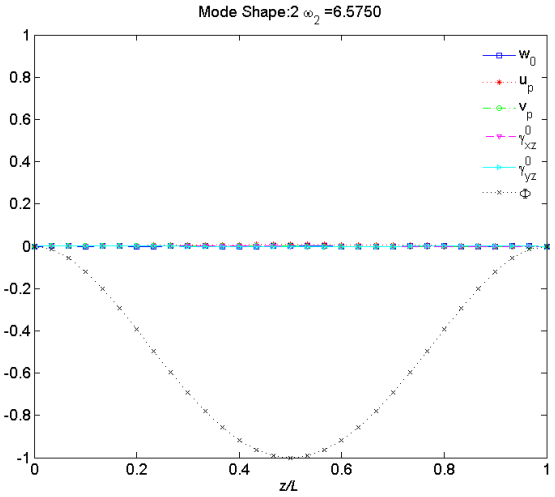

a) FTWBT

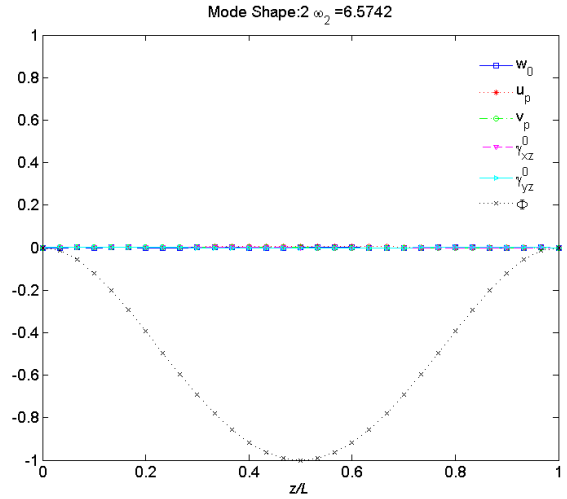

b) HTWBT

Figure 3-8: Second mode shape of LC thin-walled I-beams with lay-up $[45^o/\text{-}45^o]$

(CC boundary condition and $L/b_3 = 10$)

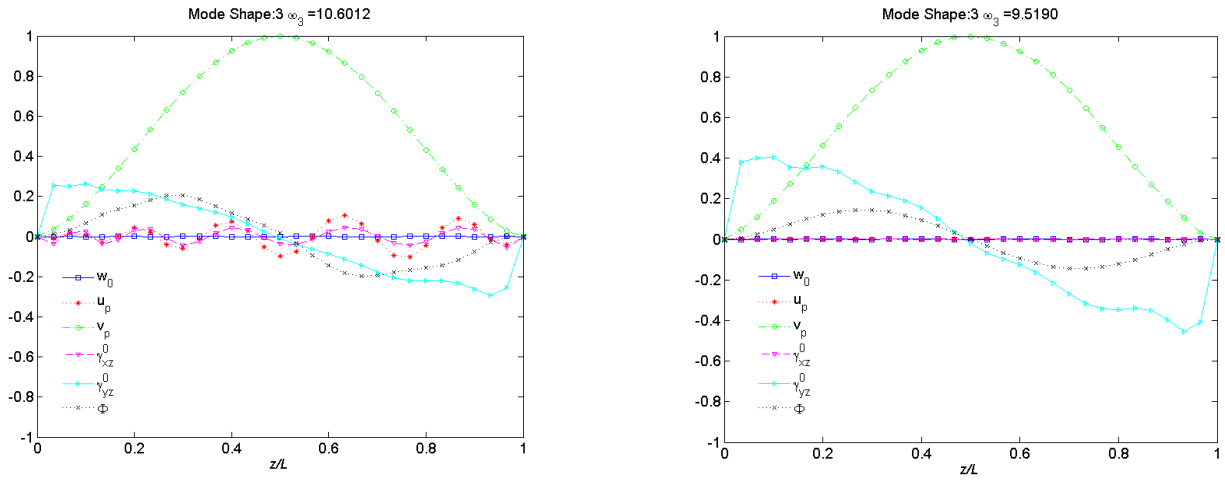

a) FTWBT b) HTWBT

Figure 3-9: Third mode shape of LC thin-walled I-beams with lay-up $[45^{o}/\text{-}45^{o}]$ (CC boundary condition and $L/b_3 = 10$)

3.4. Conclusion

A general higher-order shear deformation theory for thin-walled composite I-beams is proposed in this chapter. Theoretical formulation is derived in the general form which can recover the previous conventional theories. A hybrid series solution is developed to solve equations of motion for various theories including CTWBT, FTWBT and HTWBT of thin-walled composite I-beams with different boundary conditions. Numerical examples are performed to investigate the effects of lay-ups, fiber angle and shear deformation on the natural frequencies and critical buckling loads of the thin-walled I-section beams. Some new results for thick-beams are provided for future reference. Due to the additional shear effects, the results from the HTWBT are slightly lower than those from the CTWBT and FTWBT. They become particularly significant for low span-to-high ratio and small fiber angle of angle-ply lay-up. The present model has proved to be reliable in analysing laminated composite thin-walled beams.

CHAPTER 4 : BUCKLING ANALYSIS OF LAMINATED COMPOSITE THIN-WALLED COMPOSITE I-BEAM UNDER MECHANICAL AND THERMAL LOADS

Expanding upon the deterministic modeling of thin-walled composite I-beams in Chapter 3, this chapter focuses on the buckling behavior of these structures under combined mechanical and thermal loads. The theory is based on the first-order shear deformation beam theory with linear variation of displacements in the wall thickness. The governing equations of motion are derived from Hamilton's principle and are solved by series-type solutions with hybrid shape functions. Numerical results are presented to investigate the effects of fibre angle, material distribution, span-to-height's ratio and shear deformation on critical buckling load and temperature rise. These results for several cases are verified with available references to demonstrate the present beam model’s accuracy. This integration of mechanical and thermal considerations enhances the applicability of the research to real-world engineering scenarios.

4.1. Introduction

In practical engineering contexts, thin-walled beams are exposed to high-temperature environments. Therefore, the predictions of the thin-walled beams’ responses to the thermal load in such contexts are of utmost importance. Many models and approaches on this matter have been studied in recent years for solid beams with rectangle sections, some representative references are herein cited. Trinh et al. [153] presented an analytical method for the vibration and buckling of functionally graded beams under mechanical and thermal loads. Nguyen et al. [47] investigated the hygro-thermal effects on vibration and thermal buckling behaviours of functionally graded beams. Li et al. [154] studied the free vibration characteristics of a spinning composite thin-walled beam under hygrothermal environment. Sun et al. [155] investigated the buckling and post-buckling behaviors of functionally graded Timoshenko beams on non-linear elastic foundation. A brief literature study shows that

although many researches on thermal responses of laminated composite and functionally graded beams with rectangle sections have been performed, thermal buckling behaviors of thin-walled beams are extremely limited, Simonetti et al. [46] recently presented the thermal buckling analysis of thin-walled closed section functionally graded beam-type structures [46]. Pantousa [156] conducted a numerical study on thermal buckling of empty thin-walled steel tanks under multiple pool-fire scenarios.

This Chapter aims to investigate the elastic buckling of laminated composite thin-walled beams with I-section in thermo-mechanical environments. It is based on the FTWBT with a uniform temperature rise. The characteristic equations are derived from Hamilton's principle and solved by Ritz method with hybrid shape functions. Numerical results are presented for the laminated composite I-beams with various boundary conditions, fibre angles and length-to-height ratios.

4.2. Theoretical formulation

To analyse the thin-walled beam, the variables are defined in three set of coordinate systems as displayed in Fig. 3-1. The assumptions made in this beam model are : the effects

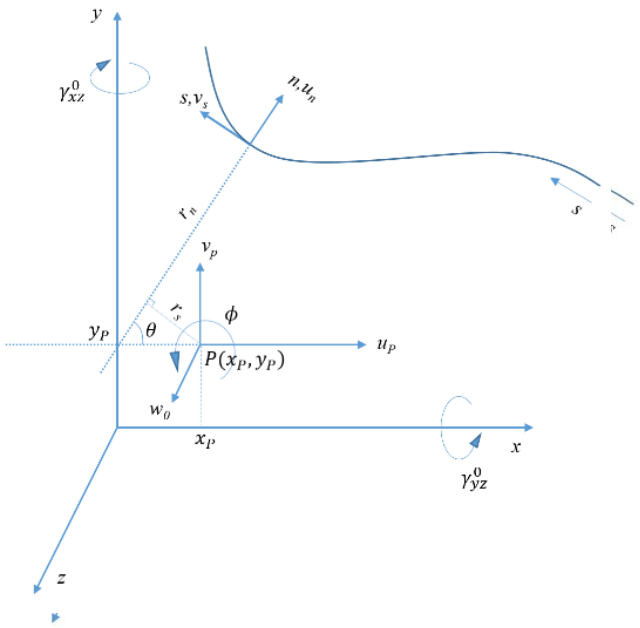

of geometrical nonlinearity are ignored, the section contour remains undeformed in its own

Figure 4-1: Coordinate systems of a thin-walled beam

plane and the transverse shear strains are constant in the wall thickness. Fig. 4-2 shows how the aforementioned coordinate systems fit in to the thin-walled I-beam in this chapter. The widths (b_1, b_2, b_3) and the thicknesses (h_1, h_2, h_3) with lower index 1, 2, 3 are for the beam's top, bottom flange, and web, respectively.

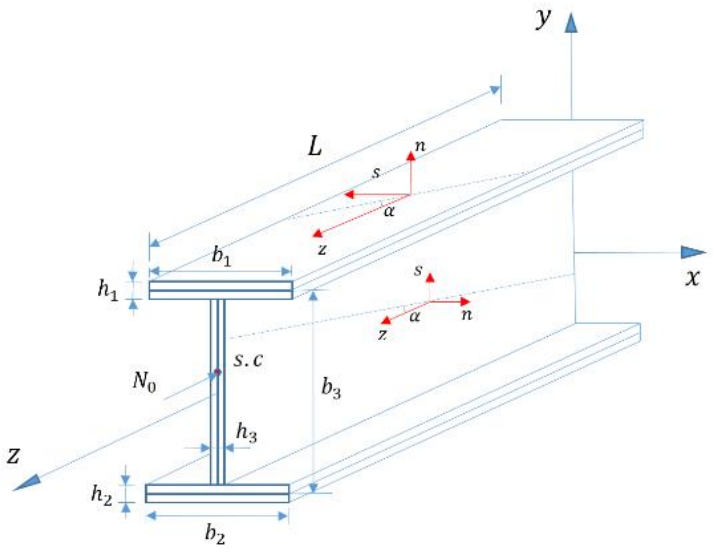

Figure 4-2: Geometry of a thin-walled I-beam

4.2.1. Kinematics

The displacements $(\bar{u}, \bar{v}, \bar{w})$ at any point on the midsurface of the laminated composite thin-walled beams under a small rotation ϕ about the pole axis can be expressed in terms of those at the pole (u_P, v_P, w_P) as follows:

$$\bar{u}(s,z) = u_P(z)\sin\theta(s) - v_P(z)\cos\theta(s) - \phi(z) r_s(s) \tag{4-1a}$$

$$\bar{v}(s,z) = u_P(z)\cos\theta(s) + v_P(z)\sin\theta(s) - \phi(z) r_n(s) \tag{4-1b}$$

$$\bar{w}(s,z) = w_P(z) + \varsigma_y(z) x(s) + \varsigma_x(z) y(s) + \varsigma_\omega(z)\omega(s) \tag{4-1c}$$

where $\varsigma_x, \varsigma_y, \varsigma_\omega$ are the rotations of the cross-section with respect to x, y and ω, respectively, which are defined by:

$$\varsigma_y = \gamma_{xz}^0 - u_{P,z}, \ \varsigma_x = \gamma_{yz}^0 - v_{P,z}, \ \varsigma_\omega = \gamma_\omega^0 - \phi_{,z} \tag{4-2}$$

The warping function ω is given by:

$$\omega(s) = \int_{s_0}^{s} r_n(s) ds \tag{4-3}$$

Moreover, the displacements (u, v, w) at a point on the beam section are expressed in term of the mid-surface displacements $(\bar{u}, \bar{v}, \bar{w})$ as follows:

$$u(n, s, z) = \bar{u}(s, z) \tag{4-4a}$$

$$v(n, s, z) = \bar{v}(s, z) + n\bar{\varsigma}_s(s, z) \tag{4-4b}$$

$$w(n, s, z) = \bar{w}(s, z) + n\bar{\varsigma}_z(s, z) \tag{4-4c}$$

where $\bar{\varsigma}_s$ and $\bar{\varsigma}_z$ are expressed as follows:

$$\bar{\varsigma}_Z = \varsigma_y \sin\theta - \varsigma_X \cos\theta - \varsigma_\omega q\,,\ \bar{\psi}_S(s, z, t) = -\frac{\partial u}{\partial s} \tag{4-5}$$

4.2.2. Strains

From the displacements defined in Eq. (4-4), the strain field can be written as:

$$\varepsilon_S(n, s, z) = \bar{\varepsilon}_S(s,z) + n\bar{\kappa}_S(s,z) \tag{4-6a}$$

$$\varepsilon_Z(n,s,z) = \bar{\varepsilon}_Z(s,z) + n\bar{\kappa}_Z(s,z) \tag{4-6b}$$

$$\gamma_{SZ}(n,s,z) = \bar{\gamma}_{SZ}(s,z) + n\bar{\kappa}_{SZ}(s,z) \tag{4-6c}$$

$$\gamma_{nz}(n,s,z) = \bar{\gamma}_{nZ}(s,z) + n\bar{\kappa}_{nZ}(s,z) \tag{4-6d}$$

where

$$\bar{\varepsilon}_s = 0\,,\ \bar{\varepsilon}_z = \frac{\partial \bar{w}}{\partial z} = \varepsilon_z^0 + x\kappa_y + y\kappa_x + \omega\kappa_\omega\,,\ \bar{\kappa}_s = 0 \tag{4-7a}$$

$$\bar{\kappa}_z = \frac{\partial \bar{\varsigma}_z}{\partial z} = \kappa_y \sin\theta - \kappa_x \cos\theta - \kappa_\omega q\,,\ \bar{\kappa}_{sz} = \kappa_{sz}\,,\ \bar{\kappa}_{nz} = 0 \tag{4-7b}$$

$$\varepsilon_z^0 = W'\,,\ \kappa_x = \varsigma_x'\,,\ \kappa_y = \varsigma_y'\,,\ \kappa_\omega = \varsigma_\omega'\,,\ \kappa_{sz} = \phi' - \varsigma_\omega \tag{4-7c}$$

$$\varepsilon_z = \varepsilon_0^z + (x + n\sin\theta)\kappa_y + (y - n\cos\theta)\kappa_x + (\omega - nq)\kappa_\omega \tag{4-7d}$$

$$\gamma_{sz} = \gamma_{xz}^0 \cos\theta + \gamma_{yz}^0 \sin\theta + \gamma_\omega^0 r + n\kappa_{sz}\,,\ \gamma_{nz} = \gamma_{xz}^0 \sin\theta - \gamma_{yz}^0 \cos\theta - \gamma_\omega^0 q \tag{4-7e}$$

4.2.3. Stress-strains relation

For laminated composite thin-walled beams, it is supposed to be constituted by a number of orthotropic material layers with the same thickness. The reduced constitutive equations at the k^{th} – layer is given by:

$$\begin{Bmatrix} \sigma_z \\ \sigma_{sz} \\ \sigma_{nz} \end{Bmatrix} = \begin{pmatrix} P_{11} & P_{16} & 0 \\ P_{16} & P_{66} & 0 \\ 0 & 0 & P_{55} \end{pmatrix} \begin{Bmatrix} \varepsilon_z \\ \gamma_{sz} \\ \gamma_{nz} \end{Bmatrix} \tag{4-8a}$$

where $P_{11} = \bar{Q}_{11} - \frac{\bar{Q}_{12}^2}{\bar{Q}_{22}}$, $P_{16} = \bar{Q}_{16} - \frac{\bar{Q}_{12}\bar{Q}_{26}}{\bar{Q}_{22}}$, $P_{66} = \bar{Q}_{66} - \frac{\bar{Q}_{26}^2}{\bar{Q}_{22}}$, $P_{55} = \bar{Q}_{55}$; $\bar{Q}_{ij}$ are the transformed reduced stiffness matrix elements which can be computed based on the fibre lay-up as follows:

$$\bar{Q}_{11} = Q_{11}c^4 + Q_{22}s^4 + 2(Q_{12} + 2Q_{66})\mathrm{s}^2 c^2 \tag{4-8b}$$

$$\bar{Q}_{12} = (Q_{11} + Q_{22} - 4Q_{66})\mathrm{s}^2 c^2 + Q_{12}(s^4 + c^4) \tag{4-8c}$$

$$\bar{Q}_{22} = Q_{11}s^4 + 2(Q_{12} + 2Q_{66})\mathrm{s}^2 c^2 + Q_{22}c^4 \tag{4-8d}$$

$$\bar{Q}_{16} = (Q_{11} - Q_{12} - 2Q_{66})\mathrm{s}\, c^3 + (Q_{12} - Q_{22} + 2Q_{66})\mathrm{s}^3 c \tag{4-8e}$$

$$\bar{Q}_{26} = (Q_{12} - Q_{22} + 2Q_{66})\mathrm{s}\, c^3 + (Q_{11} - Q_{12} - 2Q_{66})\mathrm{s}^3 c \tag{4-8f}$$

$$\bar{Q}_{55} = Q_{55}c^2 + Q_{44}\mathrm{s}^2 \tag{4-8g}$$

$$\bar{Q}_{66} = (Q_{11} + Q_{22} - 2Q_{12} - 2Q_{66})\mathrm{s}^2 c^2 + Q_{66}(s^4 + c^4) \tag{4-8h}$$

$$Q_{11} = E_1 / (1 - \nu_{12}\nu_{21}),\ Q_{22} = E_2 / (1 - \nu_{12}\nu_{21}),\ Q_{12} = \nu_{12}Q_{22} \tag{4-8i}$$

$$Q_{44} = G_{23},\ Q_{55} = G_{13},\ Q_{66} = G_{12},\ s = \sin\theta,\ c = \cos\theta \tag{4-8j}$$

where θ is the fibre orientation angle of the current laminated layer, E_1 and E_2 are the Young's moduli, ν_{12} and ν_{21} are the Poisson's ratio values, G_{12}, G_{13} and G_{23} are the shear moduli of the laminated composite material.

4.2.4. Variational formulation

The characteristic equations of the laminated composite thin-walled beams can be derived by Hamilton's principle in which the total energy of the system Π is composed of

the strain energy Π_S and work done by external force Π_W. The strain energy Π_S of the laminated composite thin-walled beam is expressed by:

$$\Pi_S = \frac{1}{2}\int_\Omega \left(\sigma_z \varepsilon_z + \sigma_{sz}\gamma_{sz} + \sigma_{nz}\gamma_{nz}\right) d\Omega \tag{4-9}$$

where Ω is the beam volume.

where E_{ij} are the stiffness coefficients of the laminated composite thin-walled composite beams ([147]).

The work done by the external mechanical axial load N_0^m and thermal load N_0^t is defined as:

$$\begin{aligned}\Pi_W &= \frac{1}{2}\int_\Omega \frac{\left(N_0^m + N_0^t\right)}{A}\left(u'^2 + v'^2\right) d\Omega \\ &= \frac{1}{2}\int_0^L \left(N_0^m + N_0^t\right)\left(U_x'^2 + U_y'^2 + 2y_p U_x'\phi' - 2x_p U_y'\phi' + \frac{I_p}{A}\phi'^2\right) dz\end{aligned} \tag{4-11}$$

where A is the cross-sectional area; I_p is the polar moment of inertia about the centroid given by:

$$I_p = I_x + I_y \tag{4-12}$$

where I_x and I_y are the second moment of inertia with respect to the $x-$ and $y-$axes, respectively:

$$I_x = \int_A y^2 dA,\ I_y = \int_A x^2 dA \tag{4-13}$$

The axial thermal load is given as:

$$N_0^t = \int_n \left(\alpha_z P_{11} + 2\alpha_{sz} P_{16}\right)\Delta T dn \tag{4-14}$$

where $\Delta T = T - T_0$ is the temperature difference; T_0 is the initial temperature; α_z, α_{sz} are the thermal expansion coefficients in the (n,s,z) coordinate system. The components (α_z, α_{sz}) are derived from the thermal expansion coefficients of the studied fibre materials (α_1, α_2) as follows:

$$\alpha_z = \alpha_1 \cos^2\theta + \alpha_2 \sin^2\theta \tag{4-15a}$$

$$\alpha_{sz} = (\alpha_1 - \alpha_2)\sin\theta\cos\theta \tag{4-15b}$$

4.2.5. Hybrid series solution

Based on the Ritz method, the displacement field can be approximated as follows:

$$\{U_x, U_y, \phi\}(z) = \sum_{j=1}^{m} \varphi_j(z)\{U_{xj}, U_{yj}, \phi_j\} \tag{4-16a}$$

$$\{U_z, \varsigma_y, \varsigma_x, \varsigma_\omega\}(z) = \sum_{j=1}^{m} \varphi_{j,z}(z)\{U_{zj}, \varsigma_{yj}, \varsigma_{xj}, \varsigma_{\omega j}\} \tag{4-16b}$$

where $U_{xj}, U_{yj}, \phi_j, U_{zj}, \varsigma_{yj}, \varsigma_{xj}, \varsigma_{\omega j}$ are the unknowns to be computed; $\varphi_j(z)$ is the shape functions which satisfy the boundary conditions (BCs) (Table 4-1).

Table 4-1: Shape functions and essential BCs of laminated composite thin-walled I-beams

BC	$\varphi_j(x)/\mathrm{e}^{\frac{-jx}{L}}$	$x=0$	$x=L$
S-S	$\sin\left(\frac{\pi x}{L}\right)$	$U_x = U_y = \phi = 0$	$U = V = \phi = 0$
C-F	$\sin^2\left(\frac{\pi x}{2L}\right)$	$U_x = U_y = \phi = 0$ $U_x' = U_y' = \phi' = 0$ $U_z = \varsigma_y = \varsigma_x = \varsigma_\varpi = 0$	
C-C	$\sin^2\left(\frac{\pi x}{L}\right)$	$U_x = U_y = \phi = 0$ $U_x' = U_y' = \phi' = 0$ $U_z = \varsigma_y = \varsigma_x = \varsigma_\varpi = 0$	$U_x = U_y = \phi = 0$ $U_x' = U_y' = \phi' = 0$ $U_z = \varsigma_y = \varsigma_x = \varsigma_\varpi = 0$

Substituting Eq. (4-16) in to Eq. (4-10) and (4-11), and then applying Hamilton's principle lead to the characteristic equation for the buckling analysis of the laminated composite thin-walled beams as follows:

$$\mathbf{Kp} = \mathbf{0} \tag{4-17}$$

where $\mathbf{p} = \left[\mathbf{U_z} \quad \mathbf{U_x} \quad \mathbf{U_y} \quad \mathbf{\Phi} \quad \boldsymbol{\varsigma}_\mathbf{x} \quad \boldsymbol{\varsigma}_\mathbf{y} \quad \boldsymbol{\varsigma}_{\boldsymbol{\omega}}\right]^T$ is the displacement vector; $\mathbf{K}$ is the stiffness matrix and is given as:

$$\mathbf{K}=\begin{bmatrix} \mathbf{K}^{11} & \mathbf{K}^{12} & \mathbf{K}^{13} & \mathbf{K}^{14} & \mathbf{K}^{15} & \mathbf{K}^{16} & \mathbf{K}^{17} \\ {}^{T}\mathbf{K}^{12} & \mathbf{K}^{22} & \mathbf{K}^{23} & \mathbf{K}^{24} & \mathbf{K}^{25} & \mathbf{K}^{26} & \mathbf{K}^{27} \\ {}^{T}\mathbf{K}^{13} & {}^{T}\mathbf{K}^{23} & \mathbf{K}^{33} & \mathbf{K}^{34} & \mathbf{K}^{35} & \mathbf{K}^{36} & \mathbf{K}^{37} \\ {}^{T}\mathbf{K}^{14} & {}^{T}\mathbf{K}^{24} & {}^{T}\mathbf{K}^{34} & \mathbf{K}^{44} & \mathbf{K}^{45} & \mathbf{K}^{46} & \mathbf{K}^{47} \\ {}^{T}\mathbf{K}^{15} & {}^{T}\mathbf{K}^{25} & {}^{T}\mathbf{K}^{35} & {}^{T}\mathbf{K}^{45} & \mathbf{K}^{55} & \mathbf{K}^{56} & \mathbf{K}^{57} \\ {}^{T}\mathbf{K}^{16} & {}^{T}\mathbf{K}^{26} & {}^{T}\mathbf{K}^{36} & {}^{T}\mathbf{K}^{46} & {}^{T}\mathbf{K}^{56} & \mathbf{K}^{66} & \mathbf{K}^{67} \\ {}^{T}\mathbf{K}^{17} & {}^{T}\mathbf{K}^{27} & {}^{T}\mathbf{K}^{37} & {}^{T}\mathbf{K}^{47} & {}^{T}\mathbf{K}^{57} & {}^{T}\mathbf{K}^{67} & \mathbf{K}^{77} \end{bmatrix} \tag{4-18}$$

with the following matrix elements:

$$K_{ij}^{11}=E_{11}\int_0^L\varphi_i''\varphi_j''dz,K_{ij}^{12}=E_{16}\int_0^L\varphi_i''\varphi_j'dz,K_{ij}^{13}=E_{17}\int_0^L\varphi_i''\varphi_j'dz$$

$$K_{ij}^{14}=\left(E_{15}+E_{18}\right)\int_0^L\varphi_i''\varphi_j'dz,K_{ij}^{15}=E_{12}\int_0^L\varphi_i''\varphi_j''dz+E_{16}\int_0^L\varphi_i'\varphi_jdz$$

$$K_{ij}^{16}=E_{13}\int_0^L\varphi_i''\varphi_j''dz+E_{17}\int_0^L\varphi_i''\varphi_j'dz,K_{ij}^{17}=E_{14}\int_0^L\varphi_i''\varphi_j''dz+\left(E_{18}-E_{15}\right)\int_0^L\varphi_i''\varphi_j'dz$$

$$K_{ij}^{22}=E_{66}\int_0^L\varphi_i'\varphi_j'dz+\left(N_0^m+N_0^t\right)\int_0^L\varphi_i'\varphi_j'dz,K_{ij}^{23}=E_{67}\int_0^L\varphi_i'\varphi_j'dz$$

$$K_{ij}^{24}=\left(E_{56}+E_{68}\right)\int_0^L\varphi_i'\varphi_j'dz+\left(N_0^m+N_0^t\right)y_p\int_0^L\varphi_i'\varphi_j'dz$$

$$K_{ij}^{25}=E_{26}\int_0^L\varphi_i'\varphi_j''dz+E_{66}\int_0^L\varphi_i'\varphi_j'dz,K_{ij}^{26}=E_{36}\int_0^L\varphi_i'\varphi_j'dz+E_{67}\int_0^L\varphi_i'\varphi_j'dz$$

$$K_{ij}^{27}=E_{46}\int_0^L\varphi_i'\varphi_j''dz+\left(E_{68}-E_{56}\right)\int_0^L\varphi_i'\varphi_j'dz,K_{ij}^{33}=E_{77}\int_0^L\varphi_i'\varphi_j'dz+\left(N_0^m+N_0^t\right)\int_0^L\varphi_i'\varphi_j'dz$$

$$K_{ij}^{34}=\left(E_{57}+E_{78}\right)\int_0^L\varphi_i'\varphi_j'dz-\left(N_0^m+N_0^t\right)x_p\int_0^L\varphi_i'\varphi_j'dz,K_{ij}^{35}=E_{27}\int_0^L\varphi_i'\varphi_j''dz+E_{67}\int_0^L\varphi_i'\varphi_j'dz$$

$$K_{ij}^{36}=E_{37}\int_0^L\varphi_i'\varphi_j''dz+E_{77}\int_0^L\varphi_i'\varphi_j'dz,K_{ij}^{37}=E_{47}\int_0^L\varphi_i'\varphi_j''dz+\left(E_{78}-E_{57}\right)\int_0^L\varphi_i'\varphi_j'dz$$

$$K_{ij}^{44}=\left(E_{55}+2E_{58}+E_{88}\right)\int_0^L\varphi_i'\varphi_j'dz+\frac{\left(N_0^m+N_0^t\right)I_p}{A}\int_0^L\varphi_i'\varphi_j'dz$$

$$
\begin{aligned}
K_{ij}^{45} &= \left(E_{25}+E_{28}\right)\int_0^L \varphi_i'\varphi_j''dz + \left(E_{56}+E_{68}\right)\int_0^L \varphi_i'\varphi_j'dz \\
K_{ij}^{46} &= \left(E_{35}+E_{38}\right)\int_0^L \varphi_i'\varphi_j''dz + \left(E_{57}+E_{78}\right)\int_0^L \varphi_i'\varphi_j'dz \\
K_{ij}^{47} &= \left(E_{45}+E_{48}\right)\int_0^L \varphi_i'\varphi_j''dz + \left(E_{88}-E_{55}\right)\int_0^L \varphi_i'\varphi_j'dz \\
K_{ij}^{55} &= E_{22}\int_0^L \varphi_i''\varphi_j''dz + E_{26}\int_0^L \left(\varphi_i''\varphi_j' + \varphi_i'\varphi_j''\right)dz + E_{66}\int_0^L \varphi_i'\varphi_j'dz \\
K_{ij}^{56} &= E_{23}\int_0^L \varphi_i''\varphi_j''dz + E_{27}\int_0^L \varphi_i''\varphi_j'dz + E_{36}\int_0^L \varphi_i'\varphi_j''dz + E_{67}\int_0^L \varphi_i'\varphi_j'dz \\
K_{ij}^{57} &= E_{24}\int_0^L \varphi_i''\varphi_j''dz + \left(E_{28}-E_{25}\right)\int_0^L \varphi_i''\varphi_j'dz + E_{46}\int_0^L \varphi_i'\varphi_j''dz + \left(E_{68}-E_{56}\right)\int_0^L \varphi_i'\varphi_j'dz \\
K_{ij}^{66} &= E_{33}\int_0^L \varphi_i''\varphi_j''dz + E_{37}\int_0^L \left(\varphi_i''\varphi_j' + \varphi_i'\varphi_j''\right)dz + E_{77}\int_0^L \varphi_i'\varphi_j'dz, \\
K_{ij}^{67} &= E_{34}\int_0^L \varphi_i''\varphi_j''dz + \left(E_{38}-E_{35}\right)\int_0^L \varphi_i''\varphi_j'dz + E_{47}\int_0^L \varphi_i'\varphi_j''dz + \left(E_{78}-E_{57}\right)\int_0^L \varphi_i'\varphi_j'dz, \\
K_{ij}^{77} &= E_{44}\int_0^L \varphi_i''\varphi_j''dz + \left(E_{48}-E_{45}\right)\int_0^L \left(\varphi_i''\varphi_j' + \varphi_i'\varphi_j''\right)dz + \left(E_{88}-2E_{58}+E_{55}\right)\int_0^L \varphi_i'\varphi_j'dz
\end{aligned}
\tag{4-19}
$$

The buckling responses of the laminated composite thin-walled beam can be obtained by solving $\left|\mathbf{K}-\lambda\mathbf{K}_\mathbf{g}\right|=\mathbf{0}$.

4.3. Numerical results

The laminated composite thin-walled I-beam in this numerical study is made of glass-epoxy materials with the following properties: $E_1 = 53.78\text{GPa}$, $E_2 = 17.93\text{GPa}$, $G_{12} = G_{13} = 8.96\text{GPa}$, $G_{23} = 3.45\text{GPa}$, $\nu_{12} = 0.25$. The thermal expansion coefficients of glass and epoxy are $\alpha_1 = 6.7\times10^{-7}K^{-1}$ and $\alpha_2 = 3.6\times10^{-6}K^{-1}$ respectively. The geometry of the laminated composite thin-walled I-beam is shown in Fig. 4-2 with $b_1 = b_2 = b_3 = 0.05\text{m}$, $h_1 = h_2 = h_3 = 0.00208\text{m}$.

4.3.1. Convergence and verification study

This section conducts a convergence study of the present solution for buckling analysis of laminated composite thin-walled I-beams under mechanical loads. For Table 4-2, the laminated composite I-beam's length is expressed as $L/b_3 = 40$. The laminated angle-ply for all the flanges and web is $[45^o/-45^o]_{4s}$. It can be observed in Table 4-2 that the results of this chapter's approach achieve numerical convergence at $m = 8$ and agree with the results of Nguyen et al. [147]. Therefore, the series number $m = 8$ is applied in subsequent analyses.

To further verify the current solution in mechanical environment, Table 4-3 presents the effects of the various fibre angle lay-ups, boundary conditions and the length-to-depth ratio on the laminated composite I-beam's critical buckling loads. It can be seen that in both cases of $L/b_3 = 20$ and $L/b_3 = 80$, the critical buckling loads decrease with the increasing fibre angle θ^o of the $[\theta^o, -\theta^o]_{4s}$ lay-up. The buckling results of the laminated composite I-beam with S-S boundary condition and $L/b_3 = 80$, C-F boundary condition and $L/b_3 = 20$ show good agreements with past researches from Kim et al. [152] and Vo and Lee [124]. More results are computed for the laminated composite I-beam set-up in Table 4-3 but with more cases of fibre angle θ^o. These results are plotted for $L/b_3 = 20$ and $L/b_3 = 80$ in Fig.4-3.

Table 4-2: Convergence of critical buckling loads (*kN*) for the laminated composite thin-walled I-beams under mechanical load

BCs	Reference	m					
		2	4	6	8	10	12
S-S	Present	2.931	2.679	2.671	2.671	2.671	2.671
	Nguyen et al. (Shear) [147]	2.752	2.690	2.671	2.671	2.671	2.671
	Nguyen et al. (No shear) [147]	2.755	2.692	2.673	2.673	2.673	2.673
C-F	Present	3.852	1.564	0.738	0.671	0.668	0.669
	Nguyen et al. (Shear) [147]	0.706	0.668	0.668	0.668	0.668	0.668
	Nguyen et al. (No shear) [147]	0.706	0.668	0.668	0.668	0.668	0.668
C-C	Present	10.76	10.65	10.65	10.65	10.65	10.65
	Nguyen et al. (Shear) [147]	10.79	10.67	10.65	10.65	10.65	10.65
	Nguyen et al. (No shear) [147]	10.83	10.71	10.69	10.69	10.69	10.69

Table 4-3: Comparison of critical buckling loads (N) of the thin-walled composite I-beams under mechanical loads

BC	Reference	Fibre angle							
		$[0]_{16}$	$[15/-15]_{4s}$	$[30/-30]_{4s}$	$[45/-45]_{4s}$	$[60/-60]_{4s}$	$[75/-75]_{4s}$	$[90/-90]_{4s}$	$[0/90]_{4s}$
L/b_3=80									
S-S	Present	1438.1	1299.4	965.0	668.1	528.6	487.0	479.6	959.0
	Kim et al. (No shear) [152]	1438.8	1300.0	965.2	668.2	528.7	487.1	-	959.3
C-F	Present	361.2	326.4	242.4	167.8	132.7	122.3	120.4	240.9
C-C	Present	5743.3	5191.0	3856.8	2670.6	2113.2	1946.7	1917.1	3831.4
L/b_3=20									
S-S	Present	22832.7	20660.1	15376.7	10657.3	8433.9	7767.7	7648.6	15255.8
C-F	Present	5768.6	5213.8	3873.7	2682.4	2122.5	1955.2	1925.5	3848.3
	Vo and Lee (Shear) [124]	5741.5	5189.0	3854.5	2668.4	2111.3	1945.1	-	3829.8
	Kim et al. (No shear)[152]	5755.2	5199.8	3861.0	2672.7	2114.7	1948.3	-	3857.8
C-C	Present	77772.9	72116.0	57102.8	42069.5	33438.5	30632.4	29873.	53993.2

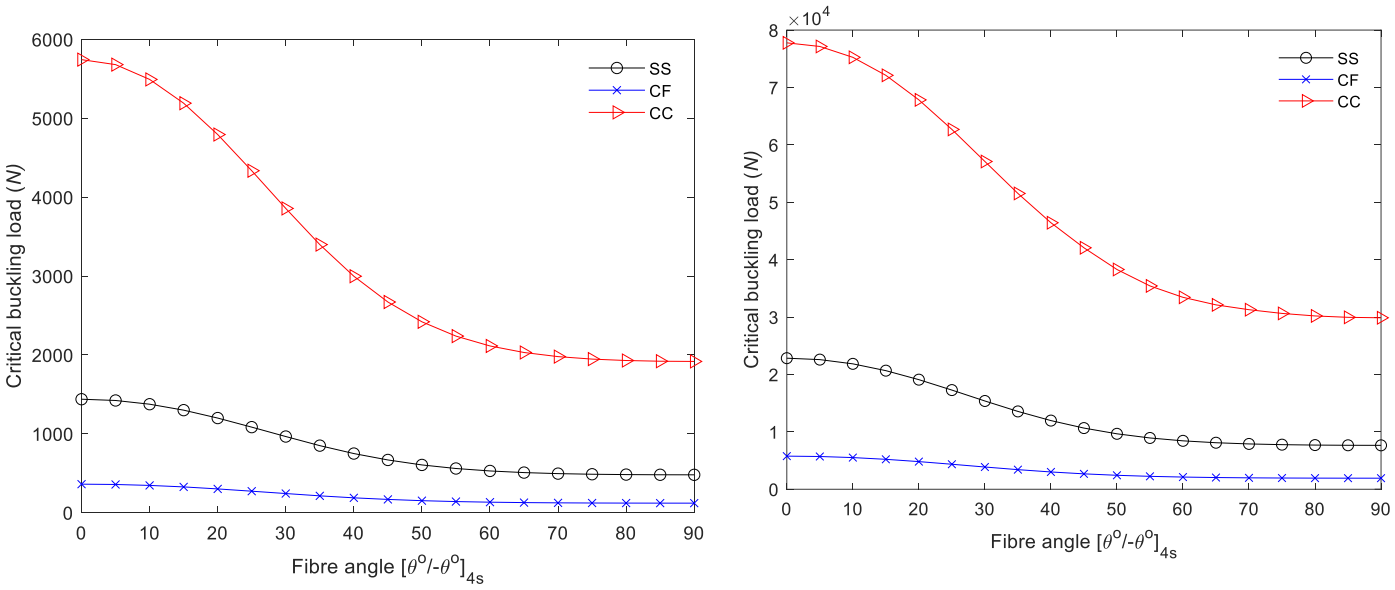

a) $L/b_3 = 80$ b) $L/b_3 = 20$

Figure 4-3: Critical buckling loads (N) for the glass-epoxy composite I-beam with respect to fibre angle for different boundary conditions

4.3.2 Thermal buckling stability

This section aims to study the effect of fibre angle, length-to-depth ratio and boundary conditions on the thermal buckling stability of the laminated composite thin-walled I-beams. The critical buckling temperature for various fibre angle lay-ups, boundary conditions and length-to-depth ratios are plotted in Fig.4-4 and 4-5. It can be seen that the critical buckling temperature slightly increases when θ^o goes from 0° to 20° and drop sharply when θ^o is in the range of 20°-70° before plateauing afterwards. This trend is particularly clearer when the beam is under C-C boundary condition.

Moreover, the laminated composite I-beam can withstand much more temperature rise and thermal load with $L/b_3 = 20$ compared to $L/b_3 = 80$. Fig.4-5 demonstrates better the effects of length-to-depth ratios on the thermal buckling stability of the laminated composite I-beams. The thin-walled beam is drastically more stable at low L/b_3 and the L/b_3 becomes

less significant when $L/b_3 > 30$.

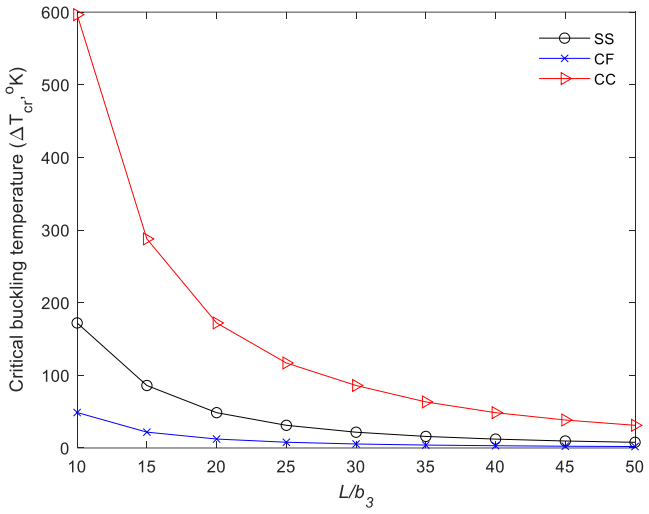

Figure 4-4: Critical buckling temperature (^oK) for the laminated composite I-beam with various length-to-depth ratios L/b_3

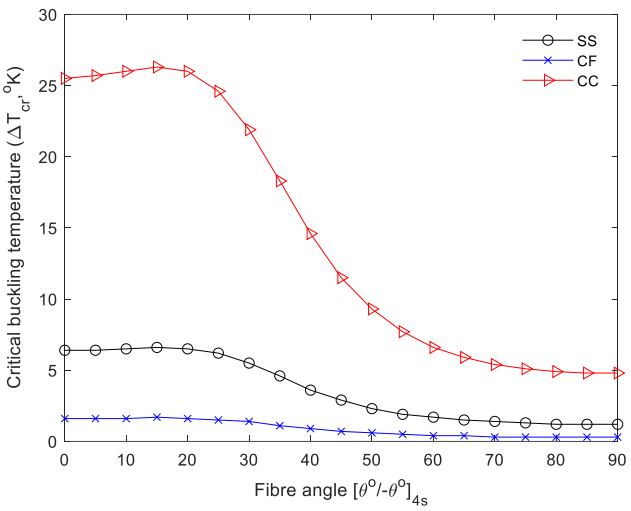

a) $L/b_3 = 80$

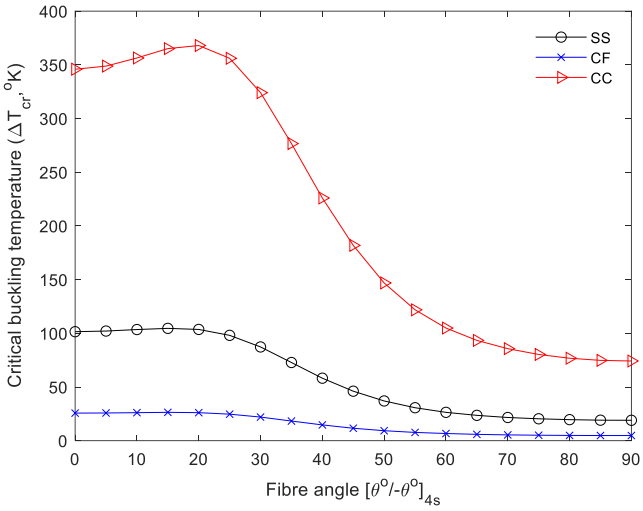

b) $L/b_3 = 20$

Figure 4-5: Critical buckling temperature ΔT_{cr} (^oK) for the glass-epoxy composite I-beam

4. Conclusion

A shear-deformable thin-walled beam model and a hybrid series solution are presented in this study. The glass-epoxy composite I-beam is investigated for its mechanical and thermal buckling stability. This model can predict accurately the critical buckling loads and critical

buckling temperature for different beam configurations. The effects of fibre angle lay-up, boundary conditions and length-to-depth ratios are shown in the numerical results. The beam's buckling capacity is higher for low fibre angle, low length-to-depth ratios and clamped-clamped boundary condition. The present model is shown to be valid for buckling analysis of laminated composite I-beam under mechanical and thermal loads.

CHAPTER 5 : STOCHASTIC ANALYSIS OF THE THIN-WALLED COMPOSITE BEAMS USING MONTE CARLO SIMULATION, POLYNOMIAL CHAOS EXPANSION AND ARTIFICIAL NEURAL NETWORK

Building on the deterministic and stochastic analyses of solid and thin-walled beams in previous chapters, this chapter introduces a novel sinusoidal higher-order shear deformation theory for stochastic analysis of laminated composite thin-walled beams with open sections. The deterministic solution framework, developed using Hamilton's principle and Ritz-type exponential shape functions, serves as the foundation for exploring the effects of uncertainties in material properties and external loads on the beams' static responses. Several mechanical parameters of laminated composite materials are randomised and plugged into the beam solver to investigate the beam's stochastic flexural behaviors. The computational cost and accuracy of the polynomial chaos expansion (PCE) method with both projection and linear regression approaches are presented and evaluated by comparing its results with crude Monte Carlo simulation (MCS). This comparison allows for a thorough assessment of the PCE method's performance. Additionally, a sensitivity analysis is conducted to compare the relative significance of the uncertainty in material properties and loads on the stochastic responses. The supervised training of the artificial neural network (ANN) based on the MCS beam data is also conducted. The findings about the stochastic outputs are introduced in various statistical metrics and illustrations to demonstrate the influences of material properties' randomness on different laminated composite thin-walled beam configurations. This chapter integrates advanced deterministic and stochastic approaches, culminating in a comprehensive framework for uncertainty quantification in thin-walled composite structures.

5.1. Introduction

A literature survey reveals that though many researches have been performed in examining stochastic responses of laminated composite plates with different approaches [42, 96, 97, 105, 157-163], the number of studies on stochastic behaviors of laminated composite thin-

walled beams is extremely limited. To compute the stochastic responses of the beam, the crude Monte Carlo Simulation (MCS) is the simplest. However, when the beam's outcome of interest takes minutes or hours to compute, the surrogate model is preferred. This surrogate model can save computational cost by learning patterns from much fewer data points and provide the highly similar outputs of MCS with a higher number of simulations. In recent years, the artificial neural network (ANNs) based surrogate modeling has seen a growing trend and has been applied to many engineering problems involving uncertainties. [164] proposed a deep collocation method that is based on the feedforward deep neural network (DNN) to study the bending of Kirchoff plates. [165] opted for the DNN to approximate the solution of the partial differential equations of a mechanical system. [166] used an improved DNN method based on a deep autoencoder to minimise the total potential energy and thus, compute the bending, vibration and buckling behaviours of Kirchoff plates. [167] made use of the ANN and the balancing composite motion optimization algorithm to study the functionally graded porous plates with uncertainties in material properties. Despite its ease of implementation, the ANN-based surrogate model requires further steps to compute sensitivity indices of the input variables. This drawback is not the case with the polynomial chaos expansion (PCE) method [168]. Besides, when the size of the random input vector is reasonably small, the PCE method is more efficient in providing the stochastic responses of a mechanical system [169]. Recent researches have paid attention to the application of PCE in mechanical systems. Bui et al. [11], [170] investigated stochastic buckling and free vibration behaviors of functionally graded sandwich thin-walled beams based on the FTWT and PCE with spectral projection approach. The effects of transverse shear strains and uncertainty of mechanical loads and materials properties on flexural behaviors of laminated composite thin-walled beams using the sinusoidal HTWT have not been carried out, this gap needs to be considered further.

5.2. Theoretical formulation

Consider a laminated composite thin-walled I-section beam with widths (b_1, b_2, b_3) and thicknesses (h_1, h_2, h_3) as in Fig. 5-1 in which Cartesian coordinate system (x, y, z), local

coordinate system (n,s,z) and contour coordinate s along the profile of the section are used for the theoretical formulation. The angle of orientation between (n,s,z) and (x,y,z) coordinate systems is namely θ, the pole point P with coordinates (x_P, x_P) is considered as the shear center of the section. Moreover, it is assumed that the displacements are small, the section contour does not deform in its own plane, and the transverse shear strains vary nonlinearly under a sinusoidal function in the wall thickness.

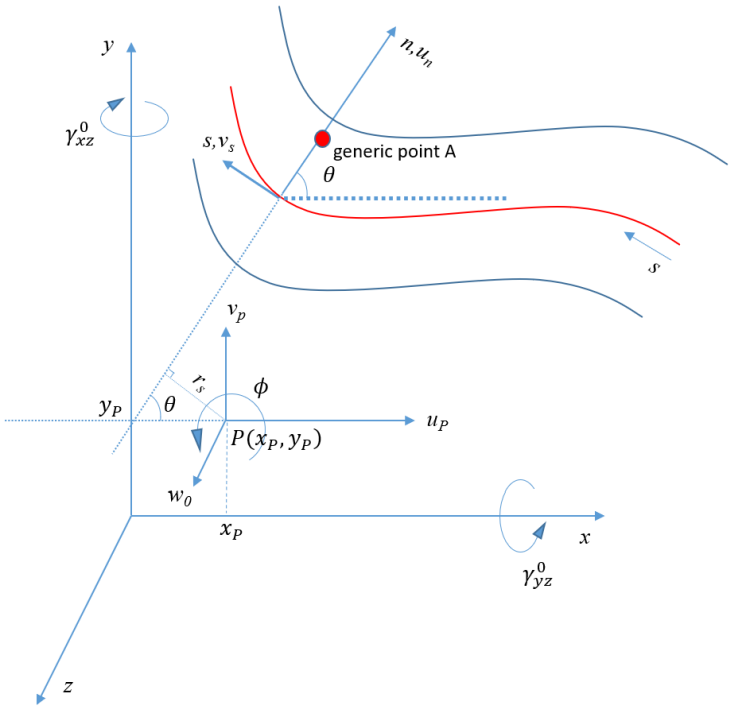

Figure 5-1: Thin-walled coordinate systems

The thin-walled beam theory in this Chapter is similar to the one presented in Chapter II, apart from the fact that the shear function describing transverse shear strains is a sinusoidal function. The geometry and dimension notations of the I-beam in this Chapter are shown in Fig. 5-2.

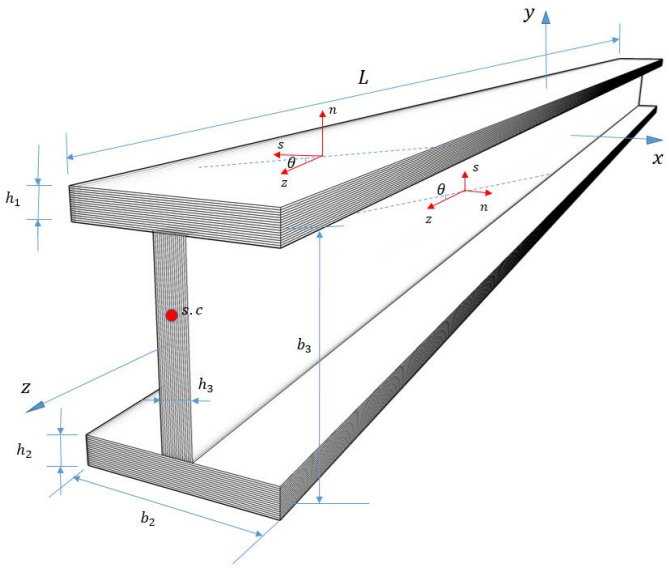

Figure 5-2: Geometry of laminated composite thin-walled I-beams

5.2.1. Polynomial chaos expansion

The responses for computational models with input uncertainties can be approximated by using a series of orthogonal functions as follows:

$$\bar{r}\left(\mathbf{q}\right)=\sum_{i=0}^{\infty}\beta_i\Omega_i\left(\mathbf{q}\right) \tag{5-1}$$

where $\mathbf{q}$ is a vector of d independent random variables mapped to physical random parameters; Ω_i are multivariate orthogonal basis functions; β_i are the unknown coefficients. In order to determine these coefficients β_i, two main following approaches could be considered: polynomial chaos expansion (PCE) and stochastic collocation. In the PCE approach, the coefficients are estimated by fitting a suitable set of basis functions using either a projection approach or least-square regression. Meanwhile, the stochastic collocation approach constructs interpolation polynomials for known coefficients at specific collocation points [108]. In this manuscript, the PCE method is developed using multivariate Hermite polynomials as basis functions and standard normal variables $\mathbf{q}$ as inputs [171].

In practice, the number of series terms in Eq. (5-1) is reduced to a carefully chosen finite

number, so that the model responses are sufficiently accurate while using a minimal computing resource. Given N_{rv} random variables and polynomial order p, the number of polynomial terms N is the permutation of p and N_{rv}, which can be expressed as: $N = \frac{(N_{rv}+p)!}{N_{rv}!\,p!}$, Eq. (5-1) therefore becomes:

$$\bar{r}(\mathbf{q}) = \sum_{i=0}^{N-1} \beta_i \Omega_i(\mathbf{q}) + \varepsilon \tag{5-2}$$

where the basis functions Ω_i are multivariate Hermite polynomials and the associated coefficients β_i need to be determined to minimize the residual term.

5.2.2. Spectral projection approach

In the spectral projection approach, the residual term must be orthogonal to the projection of the response in the selected space. Therefore, the inner product of the residual and each basis function is zero. By taking the inner product of both sides of Eq. (5-2) with Ω_j and enforcing orthogonality:

$$\left\langle \bar{r}, \Omega_j \right\rangle = \sum_{i=0}^{N} \beta_i \left\langle \Omega_i, \Omega_j \right\rangle \tag{5-3}$$

Because Ω_j are mutually orthogonal, Eq. (5-3) becomes:

$$\beta_i = \frac{\left\langle \bar{r}, \Omega_i \right\rangle}{\left\langle \Omega_i, \Omega_i \right\rangle} = \frac{1}{\left\langle \Omega_i, \Omega_i \right\rangle} \int \bar{r} \Omega_i \rho_Q(\mathbf{q})\, d\mathbf{q} \tag{5-4}$$

In order to solve for β_i in Eq. (5-4), a number of sampling responses $\bar{r}$ is required. The multidimensional integral representing the inner product of beam responses $\bar{r}$ and the basis function Ω are calculated using the Gaussian quadrature numerical method. The order p of the basis function and the number or quadrature points n_s are chosen based on the stochastic model precision requirement. For a beam model with N_{rv} random input variables and p^{th} order Hermite basis functions, the number of quadrature points are given as $n_s = (p+1)^{N_{rv}}$. This also means n_s samples of beam model need to be generated and solved. On the account of this n_s formula, the computational cost of this spectral projection

approach does not scale up well with a high order basis function and large number of random input parameters.

5.2.3. Least-square regression approach

Let $\Re = \left\{\mathbf{q}^1,...,\mathbf{q}^{N_s}\right\}$ be a set of $N_s\left(N_s > N\right)$ realizations of input random vector, and $\mathbf{R} = \left\{\bar{r}^1,...,\bar{r}^{N_s}\right\}$ be corresponding output evaluations $\left(\bar{r}^i = \bar{r}\left(\mathbf{q}^i\right), i = 1,...,N_s\right)$. The vector of residuals can be estimated from Eq. (5-2) in the compact form:

$$\Upsilon = \mathbf{R} - \beta^T \mathbf{\Omega} \tag{5-5}$$

where $\mathbf{\Omega}$ is the matrix whose elements are given by $\Omega_{ij} = \Omega_j\left(\mathbf{q}^i\right), i = 1,...,N_s;\ j = 1,...,N$. The coefficients β are estimated by minimizing the L_2-norm (least-square regression) of the residual followed as:

$$\beta = Arg\ \min \left\|\mathbf{R} - \beta^T \mathbf{\Omega}\right\|_2^2 \tag{5-6}$$

Solving Eq. (5-6), the coefficients are given by:

$$\beta = \left(\mathbf{\Omega}^T \mathbf{\Omega}\right)^{-1} \mathbf{\Omega}^T \mathbf{R} \tag{5-7}$$

5.2.4 Sensitivity analysis

In addition to the mere stochastic output of the beam model, the variance-based quantification of each random input parameter's influence on the model output is also discussed in this chapter. The sources of variance in the model output can be attributed to individual inputs, and thus, the importance of each input can be ranked accordingly. Among various sensitivity analysis methods, the Sobol indices [109] are the most widely used one. The Sobol's first-order and total-order indices are given by Saltelli et al. [110] as follows:

First-order Sobol index: $S_i = \dfrac{Var_{\mathbf{q}^i}(E_{q_{\sim i}}(\bar{r} \mid \mathbf{q}^i))}{Var(\bar{r})}\mathbf{q}^{k \neq i}$ (5-8)

Total-order Sobol index: $S_{Ti} = 1 - \dfrac{Var_{\mathbf{q}^{\sim i}}(E_{\mathbf{q}^i}(\bar{r} \mid \mathbf{q}^{\sim i}))}{Var(\bar{r})}$ (5-9)

Both kinds of these Sobol indices are normalised by $Var(\bar{r})$ but the difference in meaning

is first-order Sobol indices measure only the impact of a sole particular input variable $\mathbf{q}^i$, while total-order Sobol indices also take into account the impact of interactions between $\mathbf{q}^i$ and other variables $\mathbf{q}^{k\neq i}$ .These indices can be computed using crude Monte Carlo simulation with the computational cost of $(N_{rv}+2)\times N_s$ or using PCE with no additional cost. The Sobol's first-order and total-order indices can be estimated as follows:

$$S_i = \frac{D_i}{Var(\bar{r})} \tag{5-10}$$

$$S_{Ti} = \frac{D_{Ti}}{Var(\bar{r})} \tag{5-11}$$

where $D_i = \sum_{j\in\Gamma_i} \beta_j^2 \left\langle \Omega_j(\mathbf{q}^i), \Omega_j(\mathbf{q}^i) \right\rangle j$, Γ_i comprises all indices j such that the multivariate function Ω_j only contains the variable $\mathbf{q}^i$; $D_{Ti} = \sum_{j\in\Gamma_{Ti}} \beta_j^2 \left\langle \Omega_j(\mathrm{q}), \Omega_j(\mathrm{q}) \right\rangle$, Γ_{Ti} comprises all indices j such that the multivariate function Ω_j must contain variable $\mathbf{q}^i$; index j depends on how the list of multivariate functions is sorted.

5.2.5 Artificial neural network (ANN)

The Artificial Neural Networks (ANNs) in this chapter consist of layers of interconnected neurons organized into three main layers: the input layer, hidden layer(s), and the output layer. This architecture is shown in Fig.5-2. The input layer receives the raw input data whose each variable is assigned into a node. Each connection between an input node and a neuron in the hidden layer contributes to the weighted sum of inputs for that neuron. The initial weight values are random to avoid identical and redundant neurons in the network. The weighted sum is then passed through an activation function. Activation functions are preferably non-linear so that the neural network can learn complex models and their data relationship better. The weighted sum and activation function steps are repeated for the output layer, producing the final output of the neural network. The difference between this predicted output and the true output obtained from the beam model are assessed using a loss (or cost) function. Usually, further training iterations or epochs are needed to adjust the

weight and minimise the loss function. In the present study, the mean square error (MSE) is used as the loss function. The root mean square error (RMSE) of the test set is also computed in this chapter for future references.

The network uses the computed loss to update its weights and bias through a process known as backpropagation. This involves calculating the gradient of the loss with respect to the weights and adjusting the weights in the opposite direction of the gradient to minimize the loss. This chapter applies the Levenberg-Marquardt backpropagation algorithm to train the ANN from the stochastic thin-walled beam data. The predicted output data of ANN and PCE are compared in terms of computing performance and accuracy.

5.3. Numerical results

The numerical studies in this section can be separated into two parts. Firstly, the present thin-walled I-beam model with fixed material properties are analysed and verified with other previous works. In the second part, the chosen beam's material properties are randomly generated to be the stochastic input variables for the Monte Carlo Simulation (MCS) and Polynomial Chaos Expansion (PCE) numerical analysis.

The beams studied throughout this section are laminated composite thin-walled I-beams composed of 16 angle plies with uniform thickness. Unless stated otherwise, these are made from glass-epoxy material whose mechanical properties are as follows: $E_1 = 53.78GPa$, $E_2 = E_3 = 17.93GPa$, $G_{12} = G_{13} = 8.96GPa$, $G_{23} = 3.45GPa$, $\nu_{12} = \nu_{13} = 0.25$. These material properties along with the applied uniformly distributed load (UDL) q are the six stochastic input parameters that are randomised based on the lognormal distribution and the coefficient of variation $CoV = 0.1$. This CoV is the ratio between the sample's standard deviation and mean. Referring to Fig. 5-3, the dimensions of the top flange, bottom flange and the web are $h_1 = h_2 = h_3 = 0.00208m$ and $b_1 = b_2 = b_3 = 0.05m$. The beam's length-to-depth ratio varies between the forthcoming examples and can be from $L/b_3 = 5$ to $L/b_3 = 50$.

5.3.1 Deterministic beam model

Example 1: Convergence study

This example examines the convergence of the current solution for analyzing the displacement of composite I-beams under different boundary conditions, namely, simply supported (S-S), clamped-free (C-F), and clamped-clamped (C-C). The angle-ply stacking sequence for the I-beams' flanges and web is $[45^o/-45^o]_{4s}$, and these 16 laminate plies have a uniform thickness. The beam is under a UDL $q=1kN/m$. The results presented in Table 5-1 reveal that the proposed solutions converge with series number $m=10$ for S-S and C-F boundary conditions and $m=8$ for C-C boundary condition. These series numbers will be employed in subsequent analyses accordingly.

Table 5-1: Convergence of deterministic mid-span displacement for laminated composite thin-walled I-beam with different boundary conditions

BC	m					
	2	4	6	8	10	12
S-S	13.000	13.398	13.484	13.478	13.479	13.479
C-C	2.744	2.735	2.738	2.740	2.740	2.739
C-F	44.312	45.679	45.806	45.799	45.802	45.802

Example 2: Verification and parametric study

For the purpose of verification, this section compare the predictions made by the present beam model with the past experimental test [172] and other authors' results [33, 36]. The following tables and figures describe the static behavior of isotropic steel beam and composite I-beams with different symmetrical lay-up $[\theta^o/-\theta^o]_{4s}$ in both flanges and the web.

Fig. 5-3 manifests the accuracy of the present thin-walled beam model in the matching of mid-span deflections with the test results conducted by [172]. According to Colombi and Poggi, standard hot rolled carbon steel profiles HEA 140 of quality Fe E 275 were used for the experiments. There is no definite specifications of the carbon steel used and its material properties can vary based on several factors such as heat treatment, manufacturing process and steel alloy composition. Therefore, the predictions computed in Fig.5-4 are for the

isotropic steel beams with the following assumed properties: $E = 190GPa$, $G = 73GPa$ and $v = 0.3$.

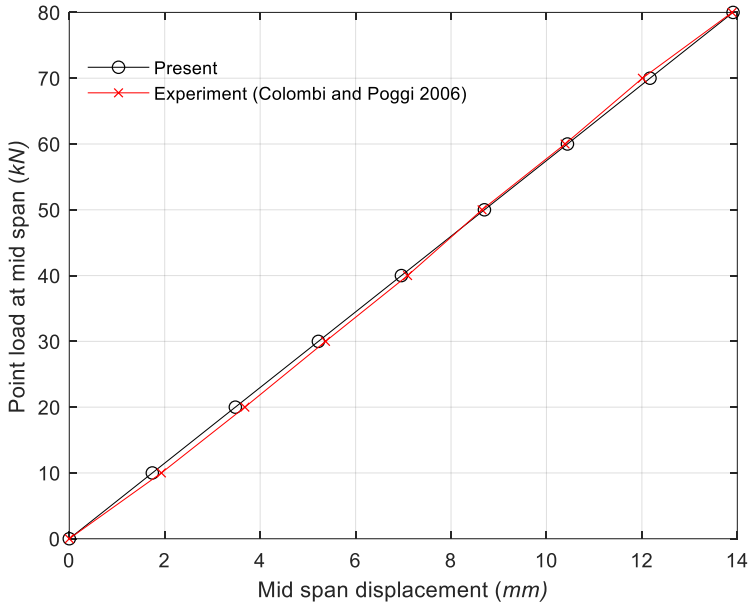

Figure 5-3: Verification with experimental static test of the HEA 140 carbon steel beam (.., $G = 73GPa$, $v = 0.3$)

Table 5-2 presents the simply supported laminated composite thin-walled beam's mid-span deflection under a UDL $q = 1kN/m$. It is evident that the current solutions for FTWT align exceptionally well with the findings of previous studies and the ABAQUS software [33, 36]. Moreover, Table 5-3 further confirms the accuracy of the present deterministic beam model under C-C and C-F BCs by demonstrating that the present FTWT results are highly consistent with earlier study by Nguyen and Nguyen [173]. It can also be seen that the beam deflections increase as the ply angles increase, and the deflection of the $[0^o/90^o]_{4s}$ beam is similar to that of the $[30^o/-30^o]_{4s}$. However, due to the additional shear effect, the results for STWT in both Tables 5-2 and 5-3 are slightly higher than FTWT and CTWT. The discrepancies due to this shear effect particularly grow wider as the beam becomes thicker. To demonstrate this remark, Table 5-4 compares the FTWT and the STWT for the laminated

composite thin-walled beams with $L/b_3 = 5$ and $L/b_3 = 10$ under all boundary conditions. The beam's mid-span displacements computed using STWT are considerably higher than when using FTWT. Furthermore, the higher-order shear effect on the laminated composite thin-walled beam's mid-span displacement is computed for many cases of the beam's lay-up and length-to-height ratios L/b_3. This so-called higher-order shear effect is defined as the percentage difference between the beam responses yielded from the STWT and FTWT. It is observed from Fig.5-5 that the shear effect is the highest at $L/b_3 = 5$ and drastically drops as the L/b_3 increases to 10 and subsequently, 15. After the point where $L/b_3 = 15$, the plots for all cases of beam lay-ups reach a plateau with the increasing value of the abscissa. Apart from the aforementioned pattern, it is clear that the shear effect on the beam under C-C boundary condition is roughly more than double the shear effect on the cantilever beam. These findings are beneficial in accurately predicting the laminated composite thick thin-walled beam's behaviors under extremely high loads. These results indicate that thick and short beams in bending are more likely to fail due to the transverse shear stress.

Table 5-2: Verification of deterministic mid-span displacements for laminated composite thin-walled I-beam under a uniformly distributed load (cm, $L/b_3 = 50$, S-S BC)

Lay-ups	References				
	CTWT	FTWT [33]	ABAQUS	Present	Present
$[0]_{16}$	6.233	6.259	6.340	6.280	6.327
$[15/-15]_{4s}$	6.899	6.923	6.989	6.940	6.981
$[30/-30]_{4s}$	9.290	9.314	9.360	9.323	9.356
$[45/-45]_{4s}$	13.421	13.446	13.479	13.450	13.480
$[60/-60]_{4s}$	16.962	16.992	17.023	16.990	17.019
$[75/-75]_{4s}$	18.411	18.449	18.490	18.440	18.468
$[0/90]_{4s}$	9.299	9.381	9.400	9.383	9.416

Table 5-3: Verification of deterministic mid-span displacements for laminated composite thin-walled I-beam under a uniformly distributed load (cm, $L/b_3 = 50$, C-F and C-C BCs)

Lay-ups	C-F			C-C		
	Present (FTWT)	Present (STWT)	Nguyen and Nguyen [173]	Present (FTWT)	Present (STWT)	Nguyen and Nguyen [173]
$[0]_{16}$	21.332	21.472	21.274	1.292	1.344	1.274
$[15/-15]_{4s}$	23.577	23.699	23.535	1.420	1.459	1.406
$[30/-30]_{4s}$	31.685	31.783	31.666	1.890	1.922	1.884
$[45/-45]_{4s}$	45.718	45.805	45.718	2.712	2.741	2.713
$[60/-60]_{4s}$	57.755	57.839	57.777	3.420	3.447	3.427
$[75/-75]_{4s}$	62.682	62.765	62.728	3.709	3.737	3.724
$[0/90]_{4s}$	31.888	31.986	31.889	1.904	1.935	1.904

5.3.2 Stochastic analysis

The procedures for the stochastic analysis is presented in the Fig.5-4 flowchart. While Section 3.1 emphasizes the accuracy of the sinusoidal thin-walled beam model, this section aims to maximise the efficiency of the computational model and thus, reduce the computing

time. On average, it takes authors' computer 100 seconds to run a case of thin-walled beam analysis. Most of this computing time is attributed to the evaluation of many integrals for the material coefficients and stiffness matrix. In order to make the MCS with 10^6 samples feasible, all these integrals are pre-computed and then later assembled every time a set of stochastic inputs is generated. The computing time displayed in Tables 5-5 to 5-7 are measured from the moment that the aforementioned integrals have been pre-computed to when all the desired outputs have been found. Apparently, the time measured here are subjected to the researchers' computer system but it should provide a good reference for comparing the methods' efficiency. The applied UDL q in this section are $q = 10kN/m$ for

C-C boundary condition and $q = 1kN/m$ for S-S and C-F boundary conditions.

Example 3: Statistics of the laminated composite thin-walled beam outputs

The accuracy and efficiency of the Polynomial Chaos Expansion (PCE) surrogate model are

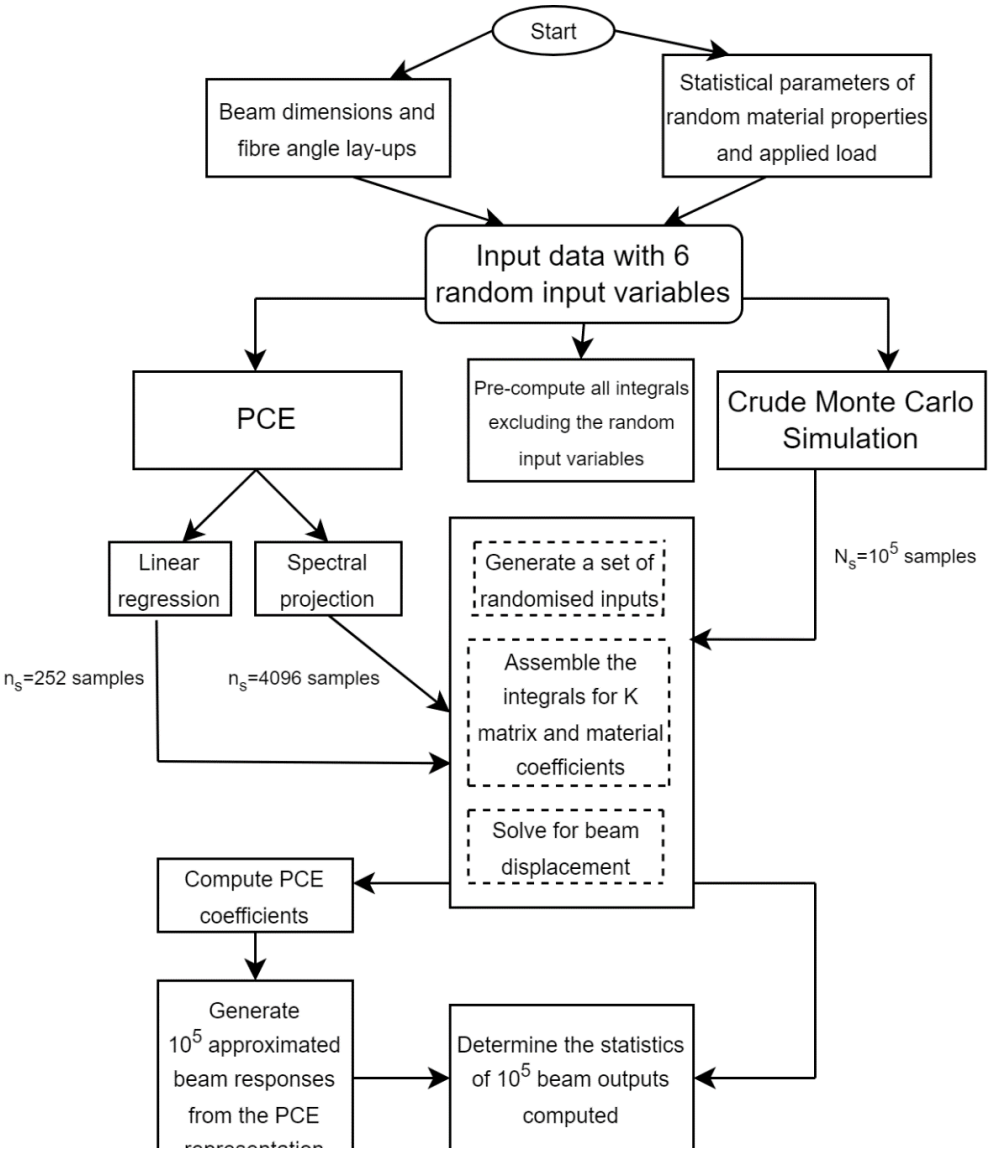

Figure 5-4: Flowchart for the stochastic static analysis of thin-walled I-beams using Polynomial Chaos expansion and Monte Carlo Simulation

verified through Monte Carlo Simulation (MCS) with $N_s = 100,000$ samples (S-S and CF boundary conditions) and $N_s = 1,000,000$ samples (C-C boundary condition). It would have taken days to compute the 100,000 outputs for a case of beam using MCS, but in this chapter,

the time-consuming integrals of material coefficients and stiffness matrix are pre-computed. This leads to a great reduction in computing time, as shown in Table 5-5 to 5-7 but this workaround might not be possible for other stochastic mechanical models. For the PCE method, the third-order Hermite polynomials with six variables are employed. These polynomials are presented in the Appendix. To construct the PCE model, 252 and 4,096 output samples from the beam solver are needed for the Least-square regression [162] approach and Spectral projection (SP) approaches, respectively. Tables 5-5 to 5-7 compare the four first statistical moments (mean, standard deviation, skewness, and kurtosis) of the mid-span and end-span displacements obtained from the MCS and PCE models.

The mean and standard deviation of the fundamental frequencies from both the MCS and PCE models show excellent agreements in all cases. Most of the skewness and kurtosis values also closely match, with only a few cases showing slight differences in these higher-order statistical moments. Both the LR and SP approaches using the PCE method prove to be far more efficient than the MCS by reducing the computing time significantly while possessing closely similar key statistical metrics.

T

able 5-4: Mean, standard deviation, kurtosis and skewness of mid-span transverse displacement (mm) for laminated composite thin-walled beams with different lay-ups and S-S boundary condition

Lay-ups	Statistical moments	$L/b_3 = 20$			$L/b_3 = 50$		
		LR	SP	MC	LR	SP	MC
$[0/90]_{4s}$	Mean	1.76	1.76	1.77	63.87	63.94	63.93
	SD	0.24	0.24	0.24	9.00	8.99	9.04
	Kurtosis	3.33	3.32	3.31	3.29	3.32	3.34
	Skewness	0.42	0.42	0.42	0.42	0.42	0.43
Computing time (s)		0.58	3.95	73.72	0.77	3.10	81.27
$[15/-15]_{4s}$	Mean	1.91	1.91	1.91	70.41	70.41	70.41
	SD	0.26	0.25	0.26	9.54	9.56	9.55
	Kurtosis	3.30	3.24	3.28	3.31	3.29	3.27
	Skewness	0.40	0.39	0.40	0.41	0.41	0.40
Computing time (s)		0.46	3.60	89.91	0.46	3.40	96.35
$[30/-30]_{4s}$	Mean	2.50	2.50	2.50	94.20	94.28	94.31
	SD	0.31	0.31	0.31	11.62	11.60	11.66
	Kurtosis	3.28	3.28	3.25	3.23	3.21	3.22
	Skewness	0.38	0.38	0.38	0.37	0.36	0.36
Computing time (s)		0.36	3.20	88.50	0.41	3.14	98.31
$[45/-45]_{4s}$	Mean	3.55	3.56	3.56	136.05	135.92	136.01
	SD	0.44	0.44	0.44	16.96	16.84	17.00
	Kurtosis	3.29	3.23	3.31	3.35	3.26	3.29
	Skewness	0.39	0.37	0.39	0.42	0.38	0.39
Computing time (s)		0.39	2.90	92.68	0.38	3.19	98.40

Table 5-5: Mean, standard deviation, kurtosis and skewness of mid-span transverse displacement (*mm*) for laminated composite beams with different lay-ups and C-F boundary condition

Lay-ups	Statistical moments	$L/b_3=10$			$L/b_3=20$		
		LR	SP	MC	LR	SP	MC
$[0/90]_{4s}$	Mean	1.12	1.12	1.12	16.07	16.08	16.08
	SD	0.15	0.15	0.15	2.24	2.24	2.23
	Kurtosis	3.29	3.32	3.31	33.14	3.34	3.36
	Skewness	0.40	0.42	0.41	4.19	0.43	0.43
Computing time (s)		0.79	3.84	79.19	1.10	3.30	79.62
$[15/-15]_{4s}$	Mean	1.20	1.20	1.20	17.62	17.63	17.62
	SD	0.16	0.16	0.16	2.37	2.38	2.36
	Kurtosis	3.31	3.28	3.28	32.70	3.27	3.29
	Skewness	0.41	0.40	0.39	3.99	0.40	0.40
Computing time (s)		0.50	3.01	88.34	0.90	3.15	87.62
$[30/-30]_{4s}$	Mean	1.54	1.54	1.54	23.42	23.41	23.39
	SD	0.19	0.19	0.19	2.88	2.89	2.88
	Kurtosis	3.27	3.21	3.26	32.38	3.26	3.22
	Skewness	0.37	0.37	0.38	3.68	0.39	0.38
Computing time (s)		0.43	2.80	89.26	0.80	3.02	103.35
$[45/-45]_{4s}$	Mean	2.17	2.17	2.17	33.63	33.65	33.64
	SD	0.27	0.27	0.27	4.17	4.18	4.16
	Kurtosis	3.26	3.24	3.28	32.61	3.26	3.30
	Skewness	0.37	0.37	0.38	3.82	0.38	0.39
Computing time (s)		0.48	2.78	88.30	0.92	3.38	100.93

Table 5-6: Mean, standard deviation, kurtosis and skewness of mid-span transverse displacement (mm) for laminated composite beams with different lay-ups and C-C boundary condition

Lay-ups	Statistical moments	$L/b_3 = 20$			$L/b_3 = 50$		
		LR	SP	MC	LR	SP	MC
$[0/90]_{4s}$	Mean	4.69	4.69	4.69	135.07	135.09	135.09
	SD	0.58	0.58	0.58	18.52	18.51	18.53
	Kurtosis	3.24	3.26	3.25	3.31	3.32	3.33
	Skewness	0.39	0.38	0.38	0.42	0.42	0.42
Computing time (s)		0.71	3.59	521.79	1.04	4.00	521.69
$[15/-15]_{4s}$	Mean	4.83	4.84	4.84	147.12	147.11	147.13
	SD	0.60	0.60	0.61	19.64	19.68	19.66
	Kurtosis	3.22	3.26	3.27	3.29	3.28	3.29
	Skewness	0.37	0.38	0.38	0.41	0.40	0.41
Computing time (s)		0.48	3.57	574.66	0.94	3.93	590.87
$[30/-30]_{4s}$	Mean	5.81	5.81	5.81	193.60	193.49	193.50
	SD	0.70	0.70	0.70	23.76	23.73	23.78
	Kurtosis	3.21	3.25	3.22	3.18	3.24	3.24
	Skewness	0.37	0.36	0.36	0.35	0.37	0.37
Computing time (s)		0.31	3.08	582.50	0.88	3.78	590.42
$[45/-45]_{4s}$	Mean	7.83	7.84	7.84	276.39	276.40	276.35
	SD	0.95	0.96	0.96	34.30	34.26	34.29
	Kurtosis	3.40	3.24	3.26	3.27	3.27	3.26
	Skewness	0.40	0.37	0.38	0.38	0.39	0.38
Computing time (s)		0.33	3.25	582.67	0.91	3.15	590.90

To better visualise the output data, Fig. 5-5 and 5-6 show the probability density function (PDF) and cumulative distribution function (CDF) plots produced from the MCS and PCE methods for the quantity of interest (QoI). The PDF and CDF graphs for outputs from MCS and PCE are coincident in most beam displacement values. The only differences are at the peaks of the graphs for PDF and below the part where $P(X \le x) < 10^{-3}$ for CDF. This is due to the lack of samples at those certain points in the output data distribution.

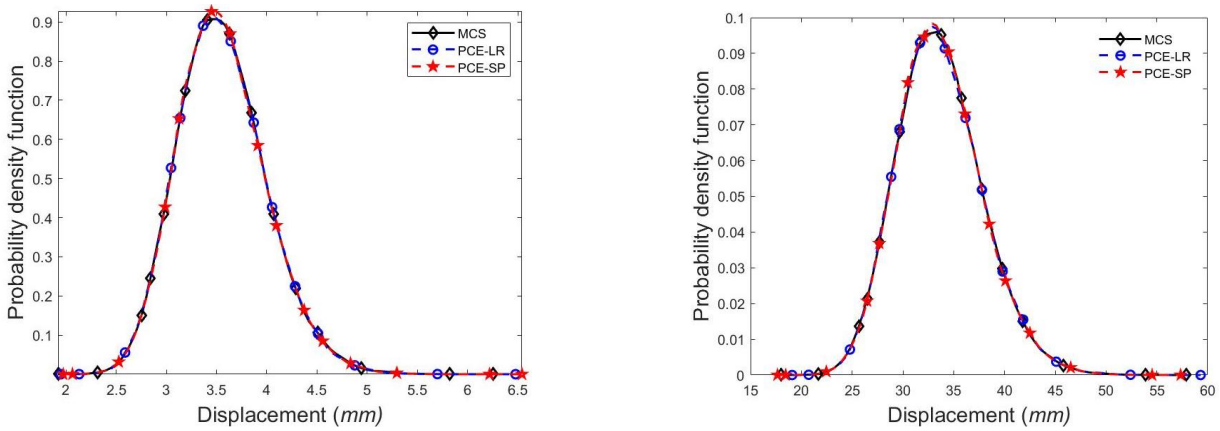

a) S-S boundary condition

b. C-C boundary condition

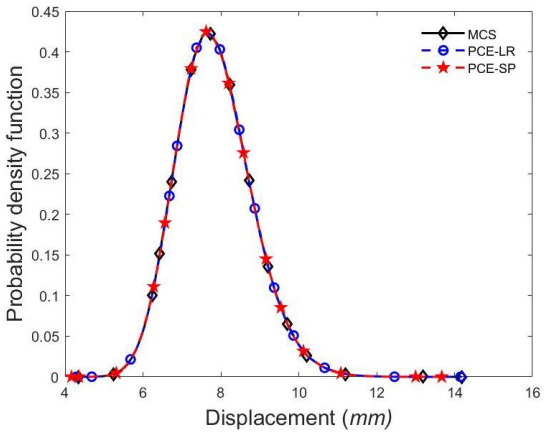

c) C-F boundary condition

Figure 5-5: Probability density function (PDF) of the MCS and PCE methods for the laminated composite thin-walled glass-epoxy beams' displacement (mm) with S-S, C-F ($N_s = 10^5$) boundary conditions ($N_s = 10^6$)

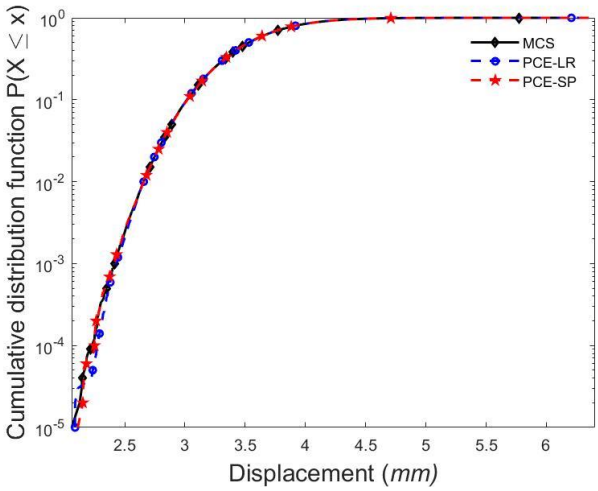

a) S-S

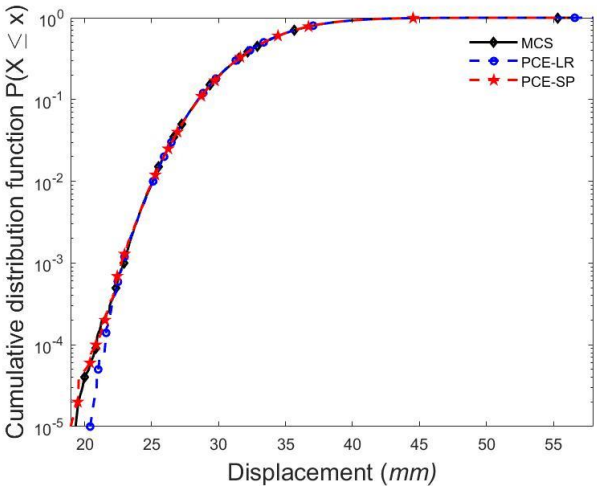

b) C-C

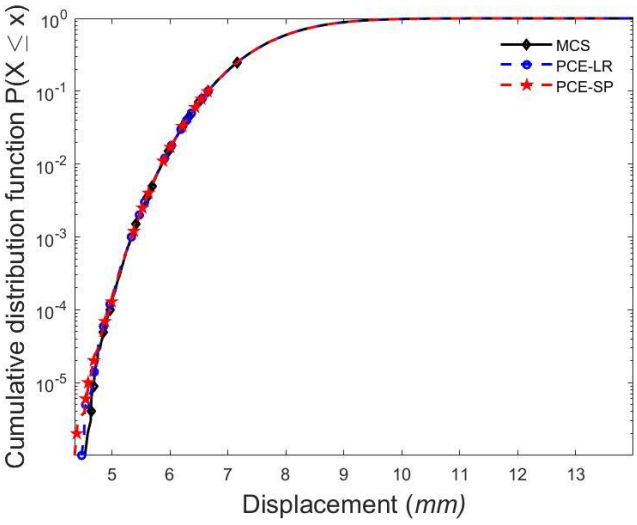

c) C-F

Figure 5-6: Cumulative distribution function (CDF) of the MCS and PCE methods for the laminated composite glass-epoxy thin-walled beam displacement (mm) with S-S, C-F ($N_s = 10^5$) boundary conditions ($N_s = 10^6$)

Zooming in the sample output data, Fig. 5-7 to 5-9 show the percentage difference between the MCS outputs and PCE-LR or SP outputs simulation-by-simulation. For every simulation, the random input parameters for both MCS and PCE methods are identical. For the S-S and C-F boundary conditions with $N_s = 100,000$, the error percentage are mostly from 0% to -0.2% with some outliers from +1.5% to -1.0%. For the C-C boundary conditions with a bigger sample size $N_s = 10^6$, the percentage error points tend to be on the negative side, most being less than -0.2%.

It is not feasible for the structural designer to guarantee the absolute safety of the beam due to countless sources of uncertainties. Design calculations are based on the characteristic load and characteristic strength which have a reasonably low probability of nonconforming. For instance, the characteristic yield stress of steel is typically defined as the yield stress threshold below which no more than 5% of the test values are anticipated to fall. It is resource-intensive to conduct the beam's mechanical testing and produce the probability distribution of the load applied and the beam's strength. Therefore, the PCE method presented in this chapter helps save time and cost by significantly reducing the number of test samples, but still give a comparable results to the crude MCS testing.

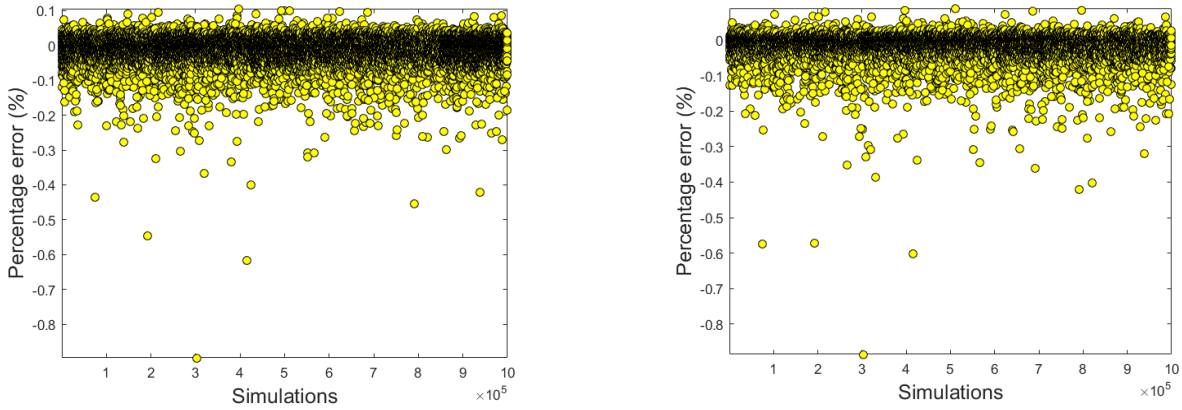

a. MCS vs PCE-LR b. MCS vs PCE-SP

Figure 5-7: Percentage error in each simulation between the PCE surrogate responses and the deterministic glass-epoxy beam model responses computed from the same input parameters ($N_s = 10^5$, $[45^o/-45^o]_{4s}$, C-F boundary condition, $L/b_3 = 20$)

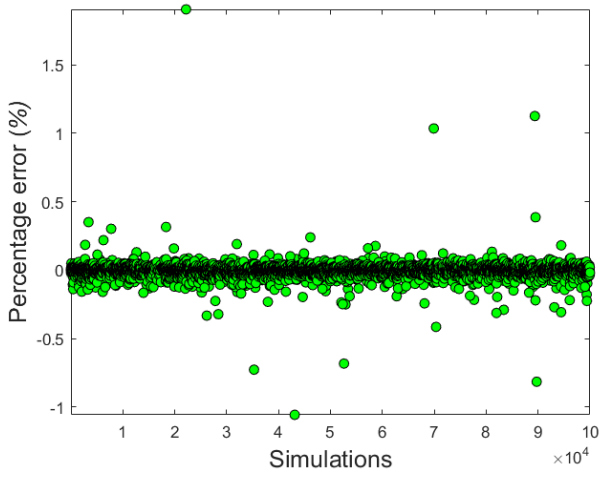

a. MCS vs PCE-LR

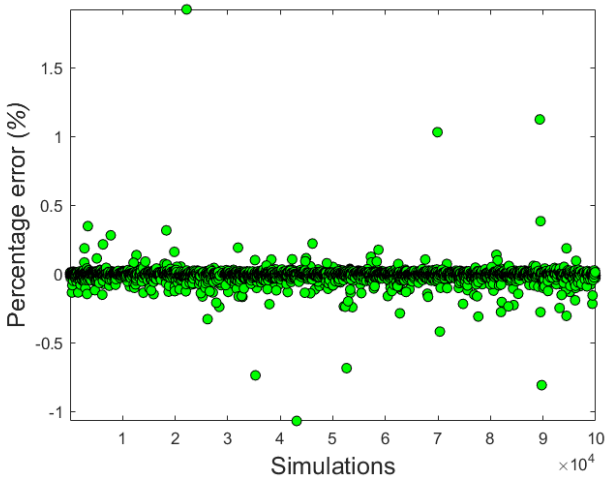

b. MCS vs PCE-SP

Figure 5-8: Percentage error in each simulation between the PCE surrogate responses and the deterministic glass-epoxy beam model responses computed from the same input parameters ($N_s = 10^5$, $[45^o / -45^o]_{4s}$, S-S boundary condition, $L/b_3 = 20$)

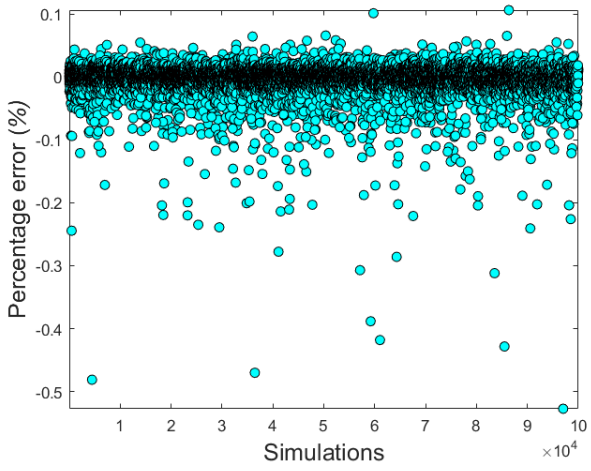

a. MCS vs PCE-LR

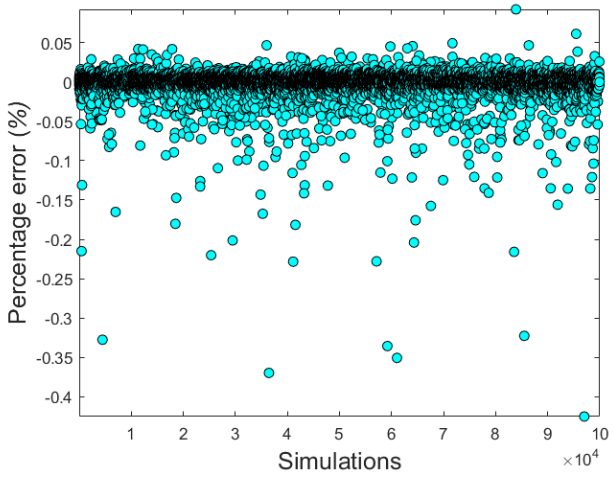

b. MCS vs PCE-SP

Figure 5-9: Percentage error in each simulation between the PCE surrogate responses and the deterministic beam model responses computed from the same input parameters ($N_s = 10^6$, $[45^o / -45^o]_{4s}$, C-C boundary condition, $L/b_3 = 20$)

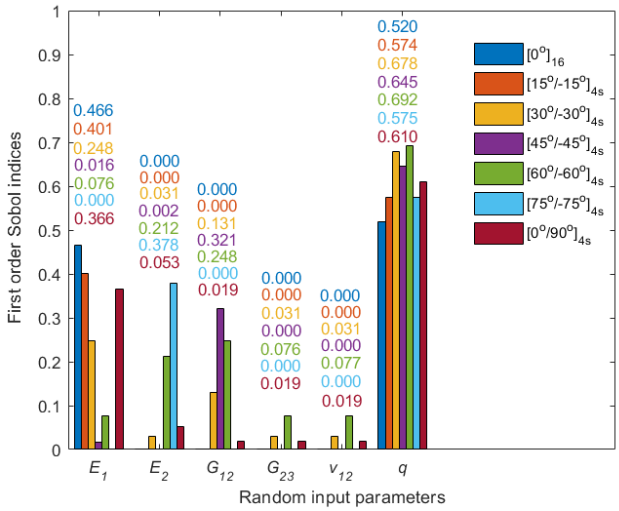

Figure 5-10: First order Sobol indices for six random input parameters of different thin-walled glass-epoxy beam lay-ups (C-F boundary condition,)

Example 4: Sensitivity analysis

The study also examines the influence of each random input on the variation of the model responses. The first-order Sobol index is used to measure the parameters' influence on the variance of the model output without considering the effect of parameters' interaction. Since the Sobol indices are not affected by the boundary conditions, only Sobol indices for cantilever beams are shown. Fig. 5-10 compares the first-order Sobol indices for static analysis using the MCS and PCE methods across all beam lay-ups. It is evident that the Sobol indices computed from the polynomial expansion coefficients closely match those calculated from the MCS. The sensitivity study reveals that the PCE method is significantly more efficient than the MCS. While the PCE method can compute the Sobol indices with no extra computing cost, the MCS demands at least $(\mathrm{N}_{rv}+2)\times N_s$ simulations based on several efficient algorithm proposed by Saltelli et al. [110] and N_s^2 simulations based on the raw mathematical definition of Sobol indices. Fig. 5-11 presents the total Sobol indices bar graphs with the same settings and beam configurations as Fig. 5-10. It is observed that the differences between the first- and total Sobol sensitivity indices are small for all variables.

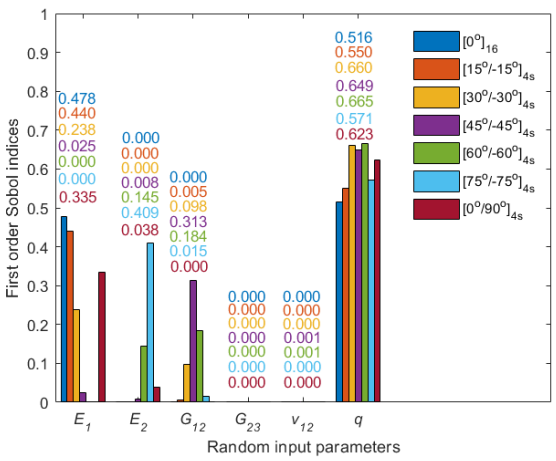

a. MCS

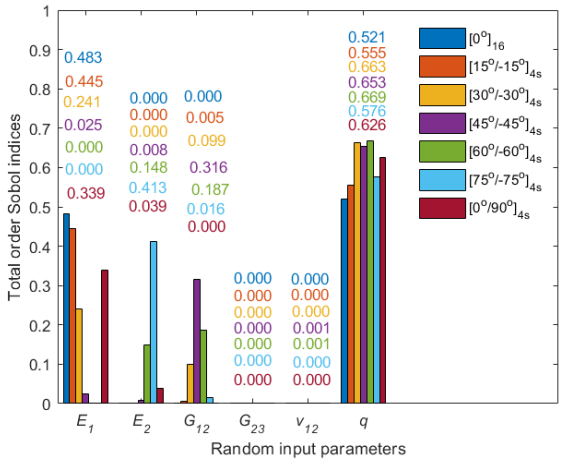

b. PCE

Figure 5-11: Total order Sobol indices for six random input parameters of different thin-walled beam lay-ups (C-F boundary condition,)

Comparing the influences of the input variables, G_{23} and ν_{12} play an insignificant role in the beam static responses with the Sobol indices equal to zero. The influence of E_1, E_2 and G_{12} change with the beam fibre-angle lay-ups and this information can be useful in the composite structure design. It is apparent that the variation in the applied UDL contributes the most to the beam's displacement, but the fluctuation of the Sobol indices for q as the fibre angle increases is interesting to see. These findings allow the structural designer to determine the most influential material properties on the static behaviour of various thin-walled composite beams' configurations. Thus, fewer mechanical testing is required to ensure the beams' quality.

5.3.3 Artificial neural network (ANN)

Example 5: Compare ANN with PCE and MCS

This example makes a comparison between ANN, PCE, and MCS's accuracy and learning capability. The MCS with $N_S = 100,000$ samples are the input training data and test data for the predictions of PCE and ANN. Table 5-8 presents the statistical moments, computing time, and the mean square error of the three methods with various attributes. The ANN is computed using the MATLAB "nntool" and setting the number of epochs equal to 300. The

hyperparameters, such as the number of of hidden layers and the number of neurons, are calibrated so that the MSE and RMSE are close to the results of PCE. The ANN with 1 hidden layer and 8 neurons is sufficient compared to PCE. Even though the mean, standard deviation (SD), kurtosis and skewness of the output distribution for ANN and PCE are almost the same as the MCS, the ANN method takes much more time than the PCE. The PCE's advantage over ANN has been shown in Example 4, where Sobol's sensitivity indices can be computed from the coefficients for free of computing cost..

While the ANN can produce much faster predictions than the MCS, it does requires $(\mathrm{N}_{rv}+2)\times N_s$ more output data for the Sobol indices. Nonetheless, the PCE method suffers when the beam model contains a higher number of random input variables, which translates to a higher dimensional PCE model. The ANN otherwise can be conveniently tuned by changing many hyperparameters. Fig. 5-12 displays the quantile-quantile plot between the outputs of MCS and ANN with different layer sizes. The output points in Fig. 5-12a, 5-12b, and 5-12d create a thick line around the ANN=MCS line, which means the errors are high, especially at the upper part of the tenth deciles. The accuracy is observably improved in Fig. 5-12c, 5-12e, and 5-12f when the number of neurons increases.

Table 5-7: Comparison between the ANN, PCE and MCS for $N_S = 100,000$ samples of laminated composite beams with $L/b_3 = 20$, $[45^o/\text{-}45^o]_{4S}$ lay-ups and C-F boundary condition

Method	Attribute	Training	Mean	SD	Kurto	Skew-	Time	MSE	RMSE
ANN	1 hidden	252	33.612	4.169	3.283	0.390	26.5	1.05E-5	3.24E-3
	1 hidden	4096	33.604	4.166	3.259	0.381	25.2	8.76E-6	2.96E-3
	2 hidden	252	33.611	4.170	3.266	0.384	40.1	5.62E-5	7.49E-3
	2 hidden	4096	33.613	4.172	3.271	0.385	32.8	5.31E-5	7.29E-3
PCE	Least-	252	33.635	4.185	3.283	0.388	1.8	7.99E-06	2.80E-3
	Spectral	4096	33.635	4.186	3.287	0.389	2.6	4.32E-06	2.10E-3
MCS	Ns=100,000	-	33.644	4.171	3.285	0.390	100.	-	-

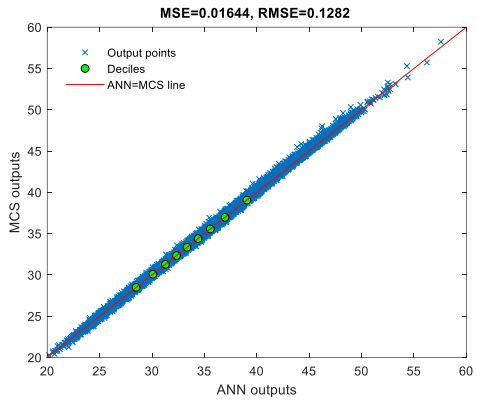

a) 1 hidden layers, 2 neurons

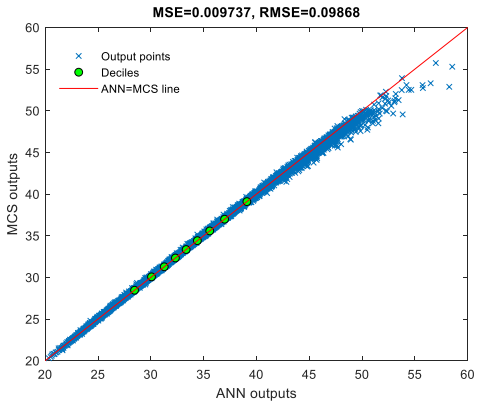

b) 1 hidden layers, 3 neurons

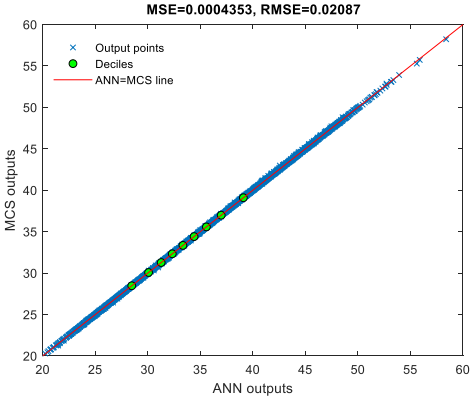

c) 1 hidden layers, 4 neurons

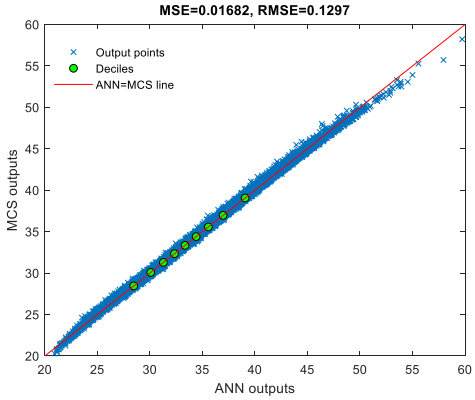

d) 2 hidden layers, 2 neurons each

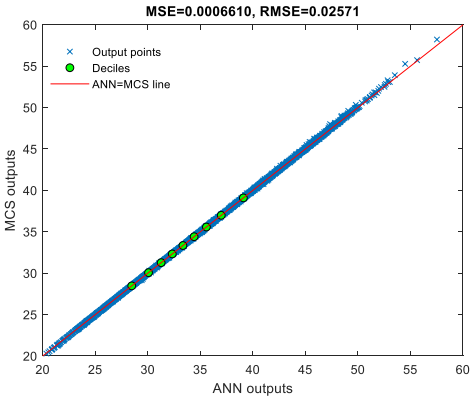

e) 2 hidden layers, 3 neurons each

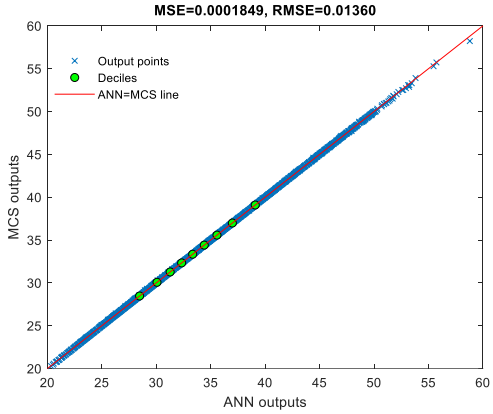

f) 2 hidden layers, 4 neurons each

Figure 5-12: Quantile-quantile plot for comparing the 100,000 test outputs of MCS and ANN with different hidden layers' size ($L/b_3 = 20$, $[45^o/\text{-}45^o]_{4S}$, C-F boundary condition)

5.4. Conclusion

This chapter presented a stochastic model for analyzing the static behavior of laminated composite thin-walled beams with an I-section based on a novel sinusoidal higher-order shear deformation thin-walled beam theory. The material properties of the laminated composite material are assumed to follow lognormal distributions, and their uncertainty is fed into a beam solver for the computation of sample stochastic outputs. The surrogate models based on Polynomial Chaos Expansion (PCE) and Artificial Neural Network (ANN) are developed to evaluate the stochastic responses efficiently. The benchmarks for accuracy and efficiency are the stochastic responses obtained from crude Monte Carlo simulation. The study also includes a sensitivity analysis to compare the importance of uncertainty in material properties to the stochastic responses. In conclusion, the present work's findings can be distilled into the following points:

- The proposed STWT is found to be efficient and accurate in predicting flexural behaviors of laminated composite thin-walled beams with open sections. The laminated composite thin-walled I-beam's displacements are higher than those from the CTWT and FTWT theories.
- The higher-order shear deformation effect on the displacement of thin-walled laminated composite beams is significant for thick beams $(L/b_3 < 15)$.
- The PCE method has been shown to be able to preserve the stochastic output distribution with a considerably fewer required number of simulations, thus with much lower computing expense in which the LR and SP approaches only required 252 and 4,096 samples, respectively, in comparison with 100,000 samples from the MCS.
- The PCE method requires no extra computing cost to determine the Sobol indices, while the MCS, in the best case, demands more sample runs proportional to the number of random input parameters N_{rv} and the chosen base number of samples N_s ($(N_{rv}+2)\times N_s$).

- The sensitivity analysis helps detect and eliminate insignificant variables, which in turn speeds up the stochastic model even more. The numerical results showed that the applied external load is the most critical variable affecting the flexural behaviors of the laminated composite thin-walled beams.
- Both supervised-learning ANN and PCE can accurately predict a high number of composite I-beams' outputs.
    - ANN costs more computational time than PCE with a low number of random input variables.
    - ANN can only prove its superiority over PCE when the dimensionality is high (large number of random input variables). Since PCE faces the curse of dimensionality severely, ANNs handle high-dimensional problems better due to their ability to learn complex nonlinear mappings using various activation functions.

CHAPTER 6 : SIZE-DEPENDENT BEHAVIOURS OF FUNCTIONALLY GRADED SANDWICH THIN-WALLED BEAMS BASED ON THE MODIFIED COUPLE STRESS THEORY

Expanding the scope of the macro thin-walled composite beams discussed in earlier chapters, this chapter examines the static and vibration analysis of functionally graded sandwich thin-walled microbeams using the modified couple stress theory. The material properties in both web and flanges are varied continuously through their thickness. The equations of motion are derived and solved by the Ritz method. Numerical results are computed to investigate the effects of material distribution, span-to-height's ratio, and material length scale parameters on the deflections and natural frequencies of microbeams for various boundary conditions. The microbeams with the size effect are predicted to be much stiffer than their macro counterparts. The results of the analysis indicate that bending and vibration of functionally graded sandwich thin-walled microbeams are greatly influenced by the variations of parameters mentioned earlier. The results offer benchmark data for future research in microstructure engineering.

6.1. Introduction

Owing to the high weight-to-stiffness ratio and performance of electro-thermo-mechanical properties, laminated composite and functionally graded (FG) structures have been employed in many engineering fields such as aerospace, automotive engineering, construction and many others. In the aerospace sector where the materials must undergo intense mechanical and thermal conditions, FG materials have proven to be applicable in numerous components. To name a few, some examples are the rocket nozzle, the spacecraft truss structure, the heat exchange panels, the reflector, the rocket engine and various micro-electro-mechanical systems [174-176]. The recent developments in the FG materials promise its important applications for thin-walled beams. Literature review shows that although considerable number of studies have been carried out on static and dynamic

responses of FG thin-walled beams, there is a limited number of works on their size-dependent behaviours. In order to take the size effects into account, advanced theories with material length scale parameters (MLSPs), in which the modified coupled stress theory (MCT) is the most popular one, have been proposed. The MCT initiated by Yang et al. [177] accounts for the size effects with only one MLSP. Thanks to its simplicity, many size-dependent FG microbeam and microplate models based on the MCT have been developed [178-187]. Although many chapters have been devoted for analysis of FG microplates/microbeams, there are very few studies for FG thin-walled nanobeams. Soltani et al. [188-190] used CTWBT and non-local elasticity theory of Eringen to study the stability of FG nano I-beams. However, there is no other investigation for FG thin-walled microbeams, this interesting and complicated topic needs to be studied further.

This Chapter employs the FTWBT and MCT to investigate the static and vibration analysis of the FG sandwich thin-walled microbeams. The governing equations of motion are derived and then a hybrid series solution is developed. Verification studies are performed on the bending and vibration responses of FG sandwich thin-walled beams. Parametric study is carried out to depict the effects of material distribution and MLSP on their deflections and natural frequencies.

6.2. Theoretical formulation

Considering a FG sandwich thin-walled microbeam with length L and open sections. As shown in Fig. 5-1, three sets of coordinate systems are examined. The following assumptions are made: the strains are small, the section contour does not deform in its own plane, the shear and warping strains are uniform and local buckling and pre-buckling deformations are negligible.

6.2.1. Modified couple stress theory (MCT)

The total energy of system is composed of the strain energy Π_S, potential energy Π_W and kinetic energy Π_K as follows:

$$\Pi = \Pi_S + \Pi_W - \Pi_K \tag{6-1}$$

Based on the MCT, the strain energy of the system Π_S is given by:

$$\Pi_U = \int_V \left(\sigma_{ij} \varepsilon_{ij} + m_{ij} \chi_{ij} \right) dV \tag{6-2}$$

where $\varepsilon_{ij}, \chi_{ij}$ are strains and symmetric rotation gradients; σ_{ij} is Cauchy stress; m_{ij} is the high-order stress corresponding with strain gradients χ_{ij}. The components of strain ε_{ij} and strain gradients χ_{ij} are expressed in terms of the displacements u_i as follows:

$$\varepsilon_{ij} = \frac{1}{2}\left(u_{i,j} + u_{j,i} \right) \tag{6-3a}$$

$$\chi_{ij} = \frac{1}{4}\left(u_{n,mj} e_{imn} + u_{n,mi} e_{jmn} \right) \tag{6-3b}$$

where e_{imn} is the permutation symbol; the comma in the subscript indicates the differentiation with respect to the variable that follows.

The stress components σ_{ij} and m_{ij} are computed from constitutive equations as follows:

$$\sigma_{ij} = \lambda \varepsilon_{kk} \delta_{ij} + 2\mu \varepsilon_{ij} \tag{6-4a}$$

$$m_{ij} = 2\mu l^2 \chi_{ij} \tag{6-4b}$$

where λ, μ are Lamé constants; δ_{ij} is the Knonecker delta; l is the MLSP which can be determined by experimental works [191].

The potential energy of the system Π_W subjected to a transverse load q can be expressed as:

$$\Pi_W = -\int_0^L q v_P dz \tag{6-5}$$

where v_P is the transverse displacement at P.

The kinetic energy of the system Π_K is expressed by:

$$\Pi_K = \frac{1}{2}\int_V \rho(z)\left(\dot{u}^2 + \dot{v}^2 + \dot{w}^2\right)dV \tag{6-6}$$

where $\rho(z)$ is the mass density; $\dot{u} = u_{,t}$, $\dot{v} = v_{,t}$, $\dot{w} = w_{,t}$ are the velocities in the $x-$, $y-$ and $z-$directions, respectively.

6.2.2. Kinematics

In this chapter, the kinematics of the FTWBT at any points of the section can be derived from section 3.2.1 of Chapter 3 by setting $g = g_0 = 1, f = n$. These displacements are expressed by:

$$u(n,s,z) = u_P(z) - \left(y - nx_{,s} - y_P\right)\phi(z) \tag{6-12a}$$

$$v(n,s,z) = v_P(z) + \left(x + ny_{,s} - x_P\right)\phi(z) \tag{6-12b}$$

$$\begin{aligned} w(n,s,z) &= w_0(z) + \gamma_{xz}^{(0)}(z)\left(x + ny_{,s}\right) + \gamma_{yz}^{(0)}(z)\left(y - nx_{,s}\right) \\ &-\phi_{,z}(z)(F_\omega - nr_{,s}) - u_{P,z}(z)\left(x + ny_{,s}\right) - v_{P,z}\left(y - nx_{,s}\right) \end{aligned} \tag{6-12c}$$

6.2.3. Strains

Using the displacements in Eq. (6-12), the non-zero linear strains are given by:

$$\varepsilon_z(n,s,z) = \varepsilon_z^{(0)} + n\varepsilon_z^{(1)} \tag{6-13a}$$

$$\gamma_{sz}(n,s,z) = \gamma_{sz}^{(0)} + n\gamma_{sz}^{(1)} \tag{6-13b}$$

$$\gamma_{nz}(n,s,z) = \gamma_{nz}^{(0)} \tag{6-13c}$$

where

$$\varepsilon_z^{(0)}(s,z) = w_{0,z} + \left(\gamma_{xz,z}^{(0)} - u_{P,zz}\right)x + \left(\gamma_{yz,z}^{(0)} - v_{P,zz}\right)y - \phi_{,zz}(F_\omega - nr_s) \tag{6-14a}$$

$$\varepsilon_z^{(1)}(s,z) = (v_{P,zz} - \gamma_{yz,z}^{(0)})x_{,s} - (u_{P,zz} - \gamma_{xz,z}^{(0)})y_{,s} + \phi_{,zz} r_s \tag{6-14b}$$

$$\gamma_{sz}^{(0)}(s,z) = \gamma_{xz}^{(0)} x_{,s} + \gamma_{yz}^{(0)} y_{,s} \tag{6-14c}$$

$$\gamma_{sz}^{(1)}(s,z) = 2\phi_{,z} \tag{6-14d}$$

$$\gamma_{nz}^{(0)}(s,z) = \gamma_{xz}^{(0)} y_{,s} - \gamma_{yz}^{(0)} x_{,s} \tag{6-14e}$$

Moreover, the symmetric rotation gradients can be calculated by:

$$\chi_{ij} = \frac{1}{2}\left(\bar{\theta}_{i,j} + \bar{\theta}_{j,i}\right) \tag{6-15}$$

where $\bar{\theta}_i$ is defined as:

$$\bar{\theta}_x = \frac{1}{2}\left(w_{,y} - v_{,z}\right) = \frac{1}{2}\left[(\gamma_{yz}^{(0)} - v_{P,z}) - v_{P,z} - \left(X_1 - u_P\right)\phi_{,z}\right] \tag{6-16a}$$

$$\bar{\theta}_y = \frac{1}{2}\left(u_{,z} - w_{,x}\right) = \frac{1}{2}\left[u_{P,z} - (\gamma_{xz}^{(0)} - u_{P,z}) - \left(X_2 - v_P\right)\phi_{,z}\right] \tag{6-16b}$$

$$\bar{\theta}_z = \frac{1}{2}\left(v_{,x} - u_{,y}\right) = \phi \tag{6-16c}$$

Substituting Eq. (6-16) into Eq. (6-15), the non-zero rotation gradients are expressed as follows:

$$\chi_{xx} = -\frac{1}{2}\phi_{,z} \tag{6-17a}$$

$$\chi_{yy} = -\frac{1}{2}\phi_{,z} \tag{6-17b}$$

$$\chi_{zz} = \phi_{,z} \tag{6-17c}$$

$$\chi_{xz} = \frac{1}{4}\left[(\gamma_{yz}^{(0)} - v_{P,z})_{,z} - v_{P,zz} - \left(X_1 - x_P\right)\phi_{,zz}\right] \tag{6-17d}$$

$$\chi_{yz} = \frac{1}{4}\left[u_{P,zz} - (\gamma_{xz}^{(0)} - u_{P,z})_{,z} - \left(X_2 - y_P\right)\phi_{,zz}\right] \tag{6-17e}$$

6.2.4. Stresses

The constitutive equations can be written as:

$$\begin{Bmatrix} \sigma_z \\ \sigma_{sz} \\ \sigma_{nz} \end{Bmatrix} = \begin{bmatrix} Q_{11} & 0 & 0 \\ 0 & Q_{66} & 0 \\ 0 & 0 & Q_{55} \end{bmatrix} \begin{Bmatrix} \varepsilon_z \\ \gamma_{sz} \\ \gamma_{nz} \end{Bmatrix} \tag{6-18a}$$

$$\begin{Bmatrix} m_{xx} \\ m_{yy} \\ m_{zz} \\ m_{yz} \\ m_{xz} \end{Bmatrix} = 2\mu l^2 \begin{bmatrix} 1 & 0 & 0 & 0 & 0 \\ 0 & 1 & 0 & 0 & 0 \\ 0 & 0 & 1 & 0 & 0 \\ 0 & 0 & 0 & 1 & 0 \\ 0 & 0 & 0 & 0 & 1 \end{bmatrix} \begin{Bmatrix} \chi_{xx} \\ \chi_{yy} \\ \chi_{zz} \\ \chi_{yz} \\ \chi_{xz} \end{Bmatrix} \tag{6-18b}$$

where $Q_{11} = E(n)$, $Q_{66} = Q_{55} = \mu = \dfrac{E(n)}{2(1+\nu)}$; $E(n)$ is the Young's modulus; ν is the Poisson's ratio, which is assumed to be constant. The effective mass density ρ and E are expressed by:

$$\rho = \rho_c V_c + \rho_m (1 - V_c) \tag{6-19a}$$

$$E = E_c V_c + E_m (1 - V_c) \tag{6-19b}$$

where the subscripts c and m indicate the ceramic and metal, V_c is the volume fraction of ceramic for I- and C-sections which are given as follows:

- For C1 section (FG):

$$V_c = \left[\frac{n}{h_j} + 0.5\right]^p, \; -0.5h_j \le n \le 0.5h_j \tag{6-20}$$

- For C2, I2 sections and I1 section's web (FG sandwich):

$$V_c = \left[\frac{-|n| + 0.5h_j}{0.5(1-\alpha_j)h_j} \right]^p, \quad -0.5h_j \le n \le -0.5\alpha_j h_j \text{ or } 0.5\alpha_j h_j \le n \le 0.5h_j \tag{6-21a}$$

$$V_c = 1, \quad -0.5\alpha_j h_j \le n \le 0.5\alpha_j h_j \tag{6-21b}$$

- For I1-section's flanges (FG sandwich):

$$V_c = \left[\frac{n + 0.5h_j}{(1-\alpha_j)h_j} \right]^p, \quad -0.5h_j \le n \le (0.5-\alpha_j)h_j \tag{6-22a}$$

$$V_c = 1, \quad -0.5h_j \le n \le (0.5-\alpha_j)h_j, \quad (0.5-\alpha_j)h_j \le n \le 0.5h_j \tag{6-22b}$$

where p is the power-law index, h_j (j = 1, 2, 3) are the thicknesses of the top flange, bottom flange and web; α_j ($j = 1, 2, 3$) are the thickness ratio of the ceramic for the top flange, bottom flange and web, respectively. The notations of $h_1, h_2, h_3, \alpha_1, \alpha_2, \alpha_3$ in various sections are shown in Fig. 6-2 and Fig. 6-3.

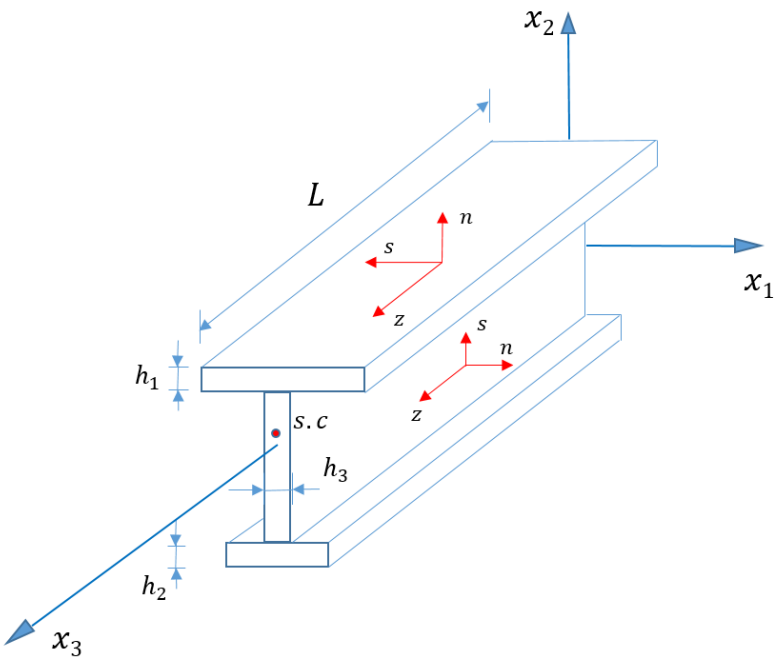

a) I-section

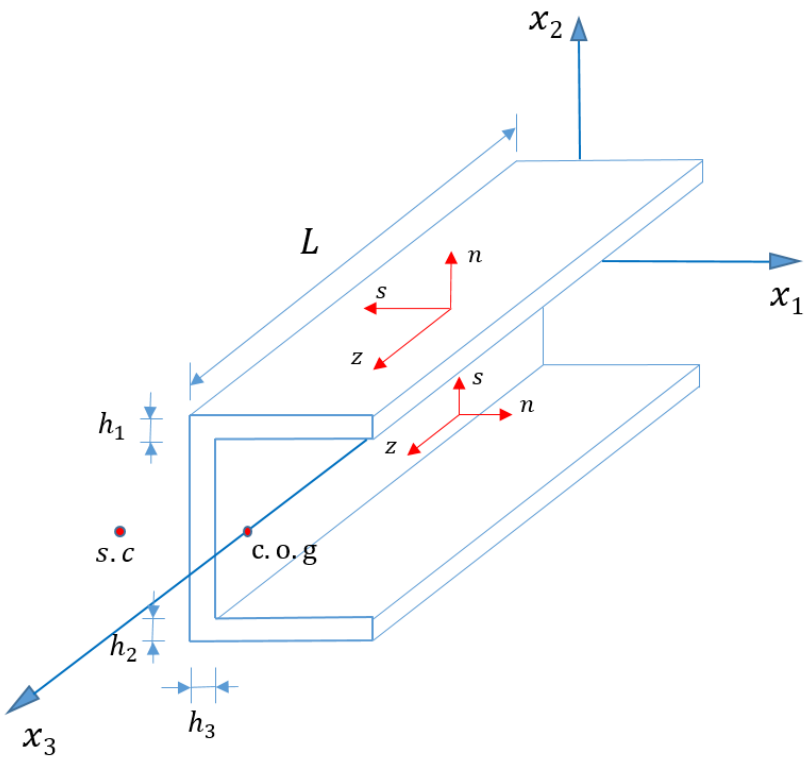

b) Channel section

Figure 6-1: Geometry of FG thin-walled beams.

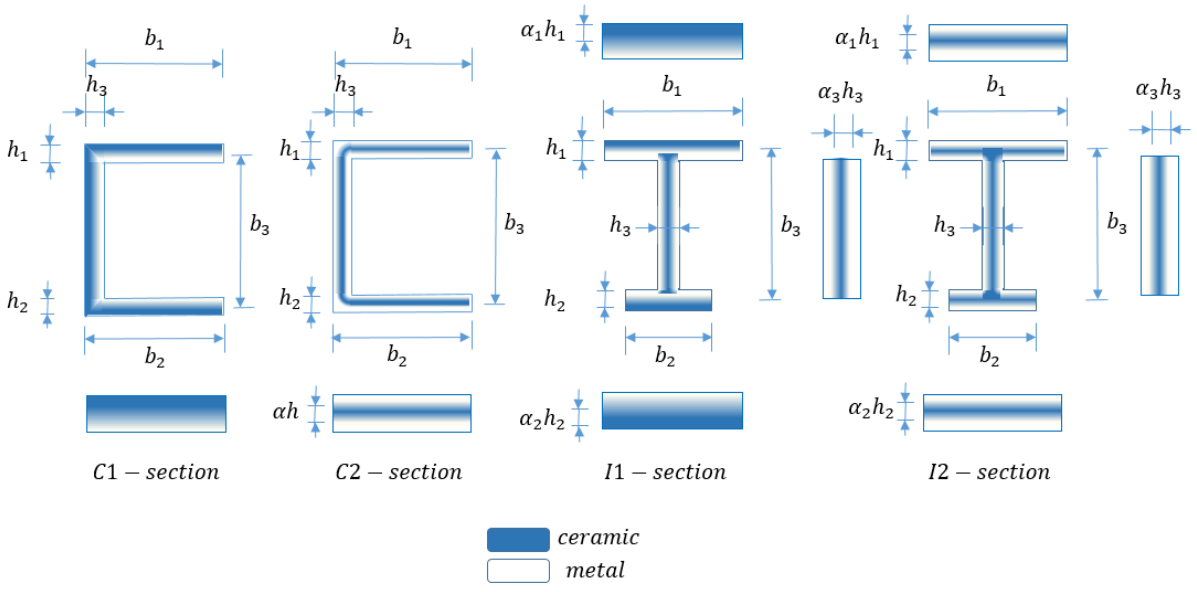

Figure 6-2: Material distribution of thin-walled FG sandwich microbeams

6.2.5. Variational formulation

The characteristic equations of the system can be derived from Eq. (6-1) based on Hamilton's principle as follows:

$$\int_{t_1}^{t_2}\left(\delta\Pi_S+\delta\Pi_W-\delta\Pi_K\right)dt=0 \tag{6-23}$$

The variation of the strain energy $\delta\Pi_S$ of the system is defined by:

$$\begin{aligned}\delta\Pi_S&=\int_V\left(\sigma_z\delta\varepsilon_z+\sigma_{sz}\delta\gamma_{sz}+\sigma_{nz}\delta\gamma_{nz}\right)dV\\&+\int_V\left(m_{xx}\delta\chi_{xx}+m_{yy}\delta\chi_{yy}+m_{zz}\delta\chi_{zz}+2m_{xz}\delta\chi_{xz}+2m_{yz}\delta\chi_{yz}\right)dV\end{aligned} \tag{6-24}$$

where the shear correction coefficient is assumed to be unity. Substituting Eqs. (13) and (17) into Eq. (6-24) leads to have:

$$\begin{aligned}\delta\Pi_S&=\int_0^L\Big[T_{zz}\delta w_{,z}^{(0)}+M_{yy}\delta\theta_{y,z}+M_{xx}\delta\theta_{x,z}+M_{\varpi}\delta\phi_{,zz}\\&+V_{xx}\delta\left(u_{P,z}+\theta_y\right)+V_{yy}\delta\left(v_{P,z}+\theta_x\right)+M_{zz}\delta\phi_{,z}\Big]dx_z\\&+\int_0^L\Big[M_{zz}^{\chi}\delta\phi_{,z}+V_{xx}^{\chi}\delta\left(u_{P,zz}-\theta_{y,z}\right)+V_{yy}^{\chi}\delta\left(\theta_{x,z}-v_{P,zz}\right)+M_{\varpi}^{\chi}\delta\phi_{,zz}\Big]dz\end{aligned} \tag{6-25}$$

where the stress resultants $\left(T_{zz},M_{yy},M_{xx},M_{\varpi},V_{xx},V_{yy},M_{zz}\right)$ and $\left(M_{zz}^{\chi},M_{\varpi}^{\chi},V_{xx}^{\chi},V_{yy}^{\chi}\right)$ are defined as follows:

$$\left(T_{zz},M_{yy},M_{xx},M_{\varpi}\right)=\int_A\left(1,X_1,X_2,nr_s-F_{\omega}\right)\sigma_z dsdn \tag{6-26a}$$

$$\left(V_{xx},V_{yy},M_{zz}\right)=\int_A\left(\sigma_{sz}x_{,s}+\sigma_{nz}y_{,s},\sigma_{sz}y_{,s}-\sigma_{nz}x_{,s},2n\sigma_{sz}\right)dsdn \tag{6-26b}$$

$$\left(M_{zz}^{\chi},V_{xx}^{\chi},V_{yy}^{\chi}\right)=\int_A\left(m_{zz}-\frac{m_{xx}}{2}-\frac{m_{yy}}{2},\frac{m_{yz}}{2},\frac{m_{xz}}{2}\right)dsdn \tag{6-26c}$$

$$M_{\varpi}^{\chi}=-\int_A\Big[m_{xz}\left(X_1-x_P\right)+m_{yz}\left(X_2-y_P\right)\Big]dsdn \tag{6-26d}$$

The rotation angles around the $x-$ and $y-$ axes are denoted as:

$$\theta_x=\gamma_{yz}^{(0)}-v_{P,z} \tag{6-26e}$$

$$\theta_y=\gamma_{xz}^{(0)}-u_{P,z} \tag{6-26f}$$

The stress resultants given above are related to the displacement as follows:

$$\begin{Bmatrix} T_{zz} \\ M_{yy} \\ M_{xx} \\ V_{xx} \\ V_{yy} \\ M_{zz} \\ M_{\varpi} \end{Bmatrix} = \begin{bmatrix} L_{11} & L_{12} & L_{13} & 0 & 0 & 0 & L_{17} \\ L_{12} & L_{22} & L_{23} & 0 & 0 & 0 & L_{27} \\ L_{13} & L_{23} & L_{33} & 0 & 0 & 0 & L_{37} \\ 0 & 0 & 0 & L_{44} & L_{45} & L_{46} & 0 \\ 0 & 0 & 0 & L_{45} & L_{55} & L_{56} & 0 \\ 0 & 0 & 0 & L_{46} & L_{56} & L_{66} & 0 \\ 0 & 0 & 0 & 0 & 0 & 0 & L_{77} \end{bmatrix} \begin{Bmatrix} w_{,z}^{(0)} \\ \theta_{y,z} \\ \theta_{x,z} \\ u_{P,z} + \theta_y \\ v_{P,3} + \theta_x \\ \phi_{,z} \\ \phi_{,zz} \end{Bmatrix} \tag{6-27a}$$

$$\begin{Bmatrix} M_{zz}^{\chi} \\ V_{xx}^{\chi} \\ V_{yy}^{\chi} \\ M_{\varpi}^{\chi} \end{Bmatrix} = \begin{bmatrix} H_{11} & 0 & 0 & 0 \\ 0 & H_{22} & 0 & H_{24} \\ 0 & 0 & H_{33} & H_{34} \\ 0 & H_{24} & H_{34} & H_{44} \end{bmatrix} \begin{Bmatrix} \phi_{,z} \\ u_{P,zz} - \theta_{y,z} \\ \theta_{x,z} - v_{P,zz} \\ \phi_{,zz} \end{Bmatrix} \tag{6-27b}$$

where the stiffness components are defined by:

$$L_{11} = \int_s A_{11} ds, L_{12} = \int_s \left(A_{11} x + B_{11} y_{,s} \right) ds, L_{13} = \int_s \left(A_{11} y - B_{11} x_{,s} \right) ds$$

$$L_{17} = \int_s \left(B_{11} r_s - A_{11} F_{\omega} \right) ds \, , L_{22} = \int_s \left(A_{11} x^2 + 2 B_{11} x y_{,s} + D_{11} y_{,s}^2 \right) ds$$

$$L_{23} = \int_s \left[A_{11} xy + B_{11} \left(y y_{,s} - x x_{,s} \right) - D_{11} x_{,s} y_{,s} \right] ds$$

$$L_{27} = \int_s \left[-A_{11} x F_{\omega} + B_{11} \left(x r_s - y_{,s} F_{\omega} \right) + D_{11} r_s y_{,s} \right] ds$$

$$L_{33} = \int_s \left(A_{11} y^2 - 2 B_{11} x_{,s} y + D_{11} x_{,s}^2 \right) ds$$

$$L_{37} = \int_s \left[-A_{11} y F_{\omega} + B_{11} \left(y r_s + x_{,s} F_{\omega} \right) - D_{11} r_s x_{,s} \right] ds$$

$$L_{44} = \int_s \left(A_{66} x_{,s}^2 + A_{55} y_{,s}^2 \right) ds \, , \; L_{45} = \int_s \left(A_{66} - A_{55} \right) x_{,s} y_{,s} ds, L_{46} = \int_s 2 B_{66} x_{,s} ds$$

$$L_{55} = \int_s \left(A_{66} y_{,s}^2 + A_{55} x_{,s}^2 \right) ds \, , \; L_{56} = \int_s 2 B_{66} y_{,s} ds \, , \; L_{66} = \int_s 4 D_{66} ds$$

$$L_{77} = \int_s \left(A_{11} F_{\omega}^2 - 2 B_{11} r_s F_{\omega} + D_{11} r_s^2 \right) ds$$

$$H_{11} = 3 l^2 \int_A \mu dn ds \, , \; H_{22} = \frac{l^2}{4} \int_A \mu dn ds \, , \; H_{24} = -\frac{l^2}{4} \int_A \mu \left(y - n x_{,s} - y_P \right) dn ds$$

$$H_{33}=\frac{l^2}{4}\int_A \mu dnds\,,\ H_{34}=-\frac{l^2}{4}\int_A \mu\left(x+ny_{,s}-x_P\right)dnds$$

$$H_{44}=\frac{l^2}{4}\int_A \mu\left[\left(x+ny_{,s}-x_P\right)^2+\left(y-nx_{,s}-y_P\right)^2\right]dnds$$

$$\left(A_{ij},B_{ij},D_{ij}\right)=\int_s\left(1,n,n^2\right)Q_{ij}ds \tag{6-28}$$

The variation of potential energy Π_W of the system subjected to a transverse load q can be expressed as:

$$\delta\Pi_W=-\int_0^L q\delta y_P dz \tag{6-29}$$

The variation of kinetic energy Π_K of the system is given by:

$$\begin{aligned}
&\delta\Pi_K=\int_\Omega \rho(n)\left(\dot{u}\delta\dot{u}+\dot{v}\delta\dot{v}+\dot{w}\delta\dot{w}\right)d\Omega\\
&=\int_0^L\Big\{\delta\dot{u}_P\left(m_1\dot{u}_P-m_2\dot{\phi}\right)+\delta\dot{v}_P\left(m_1\dot{v}_P+m_3\dot{\phi}\right)+\delta\dot{w}^{(0)}\left(m_1\dot{w}^{(0)}+m_6\dot{\theta}_y+m_{10}\dot{\theta}_x-m_{13}\dot{\phi}_{,z}\right)\\
&+\delta\dot{\theta}_y\left(m_6\dot{w}^{(0)}+m_7\dot{\theta}_y+m_8\dot{\theta}_x-m_9\dot{\phi}_{,z}\right)+\delta\dot{\theta}_x\left(m_{10}\dot{w}^{(0)}+m_8\dot{\theta}_y+m_{11}\dot{\theta}_x-m_{12}\dot{\phi}_{,z}\right)\\
&+\delta\dot{\phi}\left[-m_2\dot{u}_P+m_3\dot{v}_P+\left(m_4+m_5\right)\dot{\phi}\right]+\delta\dot{\phi}_{,z}\left[-m_{13}\dot{w}^{(0)}-m_9\dot{\theta}_y-m_{12}\dot{\theta}_x+m_{14}\dot{\phi}_{,z}\right]\Big\}dz
\end{aligned} \tag{6-30}$$

where the terms of mass m_i are given as follows:

$$\left\{m_1,m_2,m_3,m_4,m_5\right\}=\int_A \rho\begin{Bmatrix}1,\ y-nx_{,s}-y_P,\ x+ny_{,s}-x_P,\\ \left(y-nx_{,s}-y_P\right)^2,\left(x+ny_{,s}-x_P\right)^2\end{Bmatrix}dnds \tag{6-31a}$$

$$\left\{m_6,m_7,m_8,m_9\right\}=\int_A \rho(x+ny_{,s})\left\{1,x+ny_{,s},y-nx_{,s},\bar{F}_\omega\right\}dnds \tag{6-31b}$$

$$\left\{m_{10},m_{11},m_{12}\right\}=\int_A \rho(y-nx_{,s})\left\{1,y-nx_{,s},\bar{F}_\omega\right\}dnds \tag{6-31c}$$

$$\left\{m_{13},m_{14}\right\}=\int_A \rho\left\{\bar{F}_\omega,\bar{F}_\omega^2\right\}dnds \tag{6-31d}$$

6.2.6. Hybrid series solution

The displacement field is approximated via unknowns ($u_{Pj}(t),v_{Pj}(t),\ w_j(t),\ \theta_{yj}(t),\ \theta_{xj}(t)$ and $\phi_j(t)$) and shape functions ($\psi_j(x_3)$) as follows:

$$\left\{u_1^P, u_2^P, \phi\right\}(z,t) = \sum_{j=1}^{m} \psi_j(x_3)\left\{u_{Pj}, v_{Pj}, \phi_j\right\}(t) \tag{6-32a}$$

$$\left\{w^{(0)}, \theta_x, \theta_y\right\}(z,t) = \sum_{j=1}^{m} \psi_{j,z}(z)\left\{w_j, \theta_{xj}, \theta_{yj}\right\}(t) \tag{6-32b}$$

It should be noted that hybrid shape functions are proposed in Table 6-1 by a combination of exponential and admissible trigonometric functions to satisfy various BCs such as simply-supported (S-S), clamped-free (C-F) and clamped-clamped (C-C).

Table 6-1. Shape functions and essential BCs

BC	$\varphi_j(x_3)$	$x_3 = 0$	$x_3 = L$
S-S	$\frac{z}{L}\left(1-\frac{z}{L}\right)e^{\frac{-jz}{L}}$	$u_1^P = u_2^P = \phi = 0$	$u_1^P = u_2^P = \phi = 0$
C-F	$\left(\frac{z}{L}\right)^2 e^{\frac{-jz}{L}}$	$u_1^P = u_2^P = \phi = 0$ $u_{1,3}^P = u_{2,3}^P = \phi_{,3} = 0$	
C-C	$\left(\frac{z}{L}\right)^2\left(1-\frac{z}{L}\right)^2 e^{\frac{-jz}{L}}$	$u_1^P = u_2^P = \phi = 0$ $u_{1,3}^P = u_{2,3}^P = \phi_{,3} = 0$	$u_1^P = u_2^P = \phi = 0$ $u_{1,3}^P = u_{2,3}^P = \phi_{,3} = 0$

Substituting Eq. (6-32) into Eq. (6-25), (6-29) and (6-30), and then plugging the subsequent results into Eq. (6-23) leads to the characteristic equations for bending and vibration analysis of FG sandwich thin-walled microbeams as follows:

$$\mathbf{Kd} + \mathbf{M}\ddot{\mathbf{d}} = \mathbf{F} \tag{6-33}$$

where $\mathbf{K}, \mathbf{M}, \mathbf{F}$ are the stiffness matrix, the mass matrix and the force vector, respectively; $\mathbf{d} = \left[\mathbf{u_1^P} \quad \mathbf{u_2^P} \quad \mathbf{u_3} \quad \boldsymbol{\theta}_\mathbf{2} \quad \boldsymbol{\theta}_\mathbf{1} \quad \boldsymbol{\Phi}\right]^T$ is the displacement vector. It is noted that the stiffness matrix $\mathbf{K}$ can be divided into that of strain part $\mathbf{K}^\varepsilon$ and that of strain gradient $\mathbf{K}^\chi$, i.e. $\mathbf{K} = \mathbf{K}^\varepsilon + \mathbf{K}^\chi$ as follows:

$$\mathbf{K}^\varepsilon = \begin{bmatrix} \mathbf{K}^{\varepsilon 11} & \mathbf{K}^{\varepsilon 12} & \mathbf{0} & \mathbf{K}^{\varepsilon 14} & \mathbf{K}^{\varepsilon 15} & \mathbf{K}^{\varepsilon 16} \\ \mathbf{K}^{\varepsilon 12} & \mathbf{K}^{\varepsilon 22} & \mathbf{0} & \mathbf{K}^{\varepsilon 24} & \mathbf{K}^{\varepsilon 25} & \mathbf{K}^{\varepsilon 26} \\ \mathbf{K}^{\varepsilon 13} & \mathbf{K}^{\varepsilon 23} & \mathbf{K}^{\varepsilon 33} & \mathbf{K}^{\varepsilon 34} & \mathbf{K}^{\varepsilon 35} & \mathbf{K}^{\varepsilon 36} \\ \mathbf{K}^{\varepsilon 14} & \mathbf{K}^{\varepsilon 24} & \mathbf{K}^{\varepsilon 34} & \mathbf{K}^{\varepsilon 44} & \mathbf{K}^{\varepsilon 45} & \mathbf{K}^{\varepsilon 46} \\ \mathbf{K}^{\varepsilon 15} & \mathbf{K}^{\varepsilon 25} & \mathbf{K}^{\varepsilon 35} & \mathbf{K}^{\varepsilon 45} & \mathbf{K}^{\varepsilon 55} & \mathbf{K}^{\varepsilon 56} \\ \mathbf{K}^{\varepsilon 16} & \mathbf{K}^{\varepsilon 26} & \mathbf{K}^{\varepsilon 36} & \mathbf{K}^{\varepsilon 46} & \mathbf{K}^{\varepsilon 56} & \mathbf{K}^{\varepsilon 66} \end{bmatrix} \tag{6-34a}$$

$$\mathbf{K}^{\chi} = \begin{bmatrix} \mathbf{K}^{\chi 11} & \mathbf{0} & \mathbf{0} & \mathbf{K}^{\chi 14} & \mathbf{0} & \mathbf{K}^{\chi 16} \\ \mathbf{K}^{\chi 12} & \mathbf{K}^{\chi 22} & \mathbf{0} & \mathbf{0} & \mathbf{K}^{\chi 25} & \mathbf{K}^{\chi 26} \\ \mathbf{0} & \mathbf{0} & \mathbf{0} & \mathbf{0} & \mathbf{0} & \mathbf{0} \\ \mathbf{K}^{\chi 14} & \mathbf{0} & \mathbf{0} & \mathbf{K}^{\chi 44} & \mathbf{0} & \mathbf{K}^{\chi 46} \\ \mathbf{0} & \mathbf{K}^{\chi 25} & \mathbf{0} & \mathbf{0} & \mathbf{K}^{\chi 55} & \mathbf{K}^{\chi 56} \\ \mathbf{K}^{\chi 16} & \mathbf{K}^{\chi 26} & \mathbf{0} & \mathbf{K}^{\chi 46} & \mathbf{K}^{\chi 56} & \mathbf{K}^{\chi 66} \end{bmatrix} \tag{6-34b}$$

where

$$K_{ij}^{\varepsilon 11} = L_{44} S_{ij}^{11}, K_{ij}^{\varepsilon 12} = L_{45} S_{ij}^{11}, K_{ij}^{\varepsilon 14} = L_{44} S_{ij}^{11}, K_{ij}^{\varepsilon 15} = L_{45} S_{ij}^{11}, K_{ij}^{\varepsilon 16} = L_{46} S_{ij}^{11}$$

$$K_{ij}^{\varepsilon 22} = L_{55} S_{ij}^{11}, K_{ij}^{\varepsilon 24} = L_{45} S_{ij}^{11}, K_{ij}^{\varepsilon 25} = L_{55} S_{ij}^{11}, K_{ij}^{\varepsilon 26} = L_{56} S_{ij}^{11}$$

$$K_{ij}^{\varepsilon 33} = L_{11} S_{ij}^{22}, K_{ij}^{\varepsilon 34} = L_{12} S_{ij}^{22}, K_{ij}^{\varepsilon 35} = L_{13} S_{ij}^{22}, K_{ij}^{\varepsilon 36} = L_{17} S_{ij}^{22}$$

$$K_{ij}^{\varepsilon 44} = L_{22} S_{ij}^{22} + L_{44} S_{ij}^{11}, K_{ij}^{\varepsilon 45} = L_{23} S_{ij}^{22} + L_{45} S_{ij}^{11}$$

$$K_{ij}^{\varepsilon 46} = L_{27} S_{ij}^{22} + L_{46} S_{ij}^{11}, K_{ij}^{\varepsilon 55} = L_{33} S_{ij}^{22} + L_{55} S_{ij}^{11}$$

$$K_{ij}^{\varepsilon 56} = L_{37} S_{ij}^{22} + L_{56} S_{ij}^{11}, K_{ij}^{\varepsilon 66} = L_{77} S_{ij}^{22} + L_{66} S_{ij}^{11}$$

$$K_{ij}^{\chi 11} = H_{22} S_{ij}^{22}, K_{ij}^{\chi 14} = -H_{22} S_{ij}^{22}, K_{ij}^{\chi 16} = H_{24} S_{ij}^{22}$$

$$K_{ij}^{\chi 22} = H_{23} S_{ij}^{22}, \; K_{ij}^{\chi 25} = -H_{23} S_{ij}^{22}, \; K_{ij}^{\chi 26} = -H_{34} S_{ij}^{22}$$

$$K_{ij}^{\chi 44} = H_{22} S_{ij}^{22}, \; K_{ij}^{\chi 46} = -H_{24} S_{ij}^{22}, \; K_{ij}^{\chi 55} = H_{23} S_{ij}^{22}$$

$$K_{ij}^{\chi 55} = H_{23} S_{ij}^{22}, \; K_{ij}^{\chi 56} = H_{34} S_{ij}^{22}, \; K_{ij}^{\chi 66} = H_{11} S_{ij}^{11} + H_{44} S_{ij}^{22}$$

$$S_{ij}^{rs} = \int_0^L \frac{\partial^r \psi_i}{\partial^r z} \frac{\partial^s \psi_j}{\partial^s z} dz \tag{6-35}$$

The components of mass matrix $\mathbf{M}$ are given by:

$$\mathbf{M} = \begin{bmatrix} \mathbf{M}^{11} & \mathbf{0} & \mathbf{0} & \mathbf{0} & \mathbf{0} & \mathbf{M}^{16} \\ \mathbf{0} & \mathbf{M}^{22} & \mathbf{0} & \mathbf{0} & \mathbf{0} & \mathbf{M}^{26} \\ \mathbf{0} & \mathbf{0} & {}^{T}\mathbf{M}^{33} & \mathbf{M}^{34} & \mathbf{M}^{35} & \mathbf{M}^{36} \\ \mathbf{0} & \mathbf{0} & {}^{T}\mathbf{M}^{34} & \mathbf{M}^{44} & \mathbf{M}^{45} & \mathbf{M}^{46} \\ \mathbf{0} & \mathbf{0} & {}^{T}\mathbf{M}^{35} & {}^{T}\mathbf{M}^{45} & \mathbf{M}^{55} & \mathbf{M}^{56} \\ {}^{T}\mathbf{M}^{16} & {}^{T}\mathbf{M}^{26} & {}^{T}\mathbf{M}^{36} & {}^{T}\mathbf{M}^{46} & {}^{T}\mathbf{M}^{56} & \mathbf{M}^{66} \end{bmatrix} \tag{6-36}$$

where

$$M_{ij}^{11} = m_1 S_{ij}^{00}, M_{ij}^{16} = -m_2 S_{ij}^{00}, M_{ij}^{22} = m_1 S_{ij}^{00}, M_{ij}^{26} = m_3 S_{ij}^{00}, M_{ij}^{33} = m_1 S_{ij}^{11}$$

$$M_{ij}^{34} = m_6 S_{ij}^{11}, M_{ij}^{35} = M_{10} S_{ij}^{11}, M_{ij}^{36} = -m_{13} S_{ij}^{11}, M_{ij}^{44} = m_7 S_{ij}^{11}, M_{ij}^{45} = m_8 S_{ij}^{11}$$

$$M_{ij}^{46} = -m_9 S_{ij}^{11}, M_{ij}^{55} = m_{11} S_{ij}^{11}, M_{ij}^{56} = -m_{12} S_{ij}^{11}, M_{ij}^{66} = m_{14} S_{ij}^{11} + \left(m_4 + m_5\right) S_{ij}^{00} \quad (6\text{-}37)$$

The non-zero components of load vector $\mathbf{F} = \begin{bmatrix} 0 & \mathbf{f} & 0 & 0 & 0 & 0 \end{bmatrix}^T$ are given by:

$$f_i = \int_0^L q\psi_i dz \quad (6\text{-}38)$$

6.3. Numerical results

In this section, several numerical examples for FG thin-walled sandwich microbeams with and without the size-effect are presented. The geometries of I- and C-sections are given in Fig. 6-3 by $h = h_1 = h_2 = h_3, b_3 = 40h$. For C1 and C2-section, $b_1 = b_2 = 20h$ while for I1 and I2-section, $b_1 = 20h, b_2 = 10h$. Unless stated otherwise, the thickness ratios of ceramic material are given as: for I1, $\alpha_1 = 0.9, \alpha_2 = 0.1, \alpha_3 = 0.4$; for I2, $\alpha_1 = \alpha_2 = \alpha_3 = 0.1$ and for C2, $\alpha_1 = \alpha_2 = \alpha_3 = 0.3$. The following material properties are used for the static analysis: $E_c = 320.7GPa$, $E_m = 105.69GPa$, $\nu = \nu_c = \nu_m = 0.3$ and the vibration analysis: $E_c = 380GPa$, $E_m = 70GPa$, $\rho_c = 3960kg/m^3$, $\rho_m = 2702kg/m^3$, $\nu = \nu_c = \nu_m = 0.3$. The MLSP is assumed to be $l = 15\mu m$ for the analysis of all subsequent sections. The non-dimensional deflections and frequencies of microbeams are revealed as follows.

Non-dimensional deflection under point load (P):

$$\bar{u}_2^P = 1000 \frac{E_c h b^3}{PL^3} u_2^P \quad (6\text{-}39)$$

Non-dimensional deflection under uniform distributed load (q):

$$\bar{u}_2^P = 1000 \frac{E_c h b^3}{qL^4} u_2^P \quad (6\text{-}40)$$

Non-dimensional frequency:

$$\bar{\omega} = \frac{L^2}{b_3} \sqrt{\frac{\rho_m}{E_m}} \omega \quad (6\text{-}41)$$

6.3.1 Convergence study

FG thin-walled C1-beams ($p=5$, $L/b_3=20$ and 40) under uniformly distributed load q with various BCs are analysed. Their fundamental frequencies and mid-span deflections are presented in Table 6-2. The beam height-to-material length scale ratio $b_3/l=0$ refers to macrobeam while $b_3/l=1$ is for microbeam. It can be seen that in all cases, the series number $m=10$ ensures the convergence of the present solution. For that reason, $m=10$ will be used in the subsequent sections.

Table 6-2: Convergence of fundamental frequencies and mid-span deflections of FG sandwich thin-walled C1-beams ($p=5$)

b_3/l	BC	m					
		2	4	6	8	10	12
Non-dimensional fundamental frequency							
1	S-S	8.157	8.051	8.020	8.020	8.020	8.020
	C-F	2.900	2.861	2.859	2.859	2.859	2.859
	C-C	18.186	18.121	18.118	18.116	18.115	18.115
0	S-S	2.039	2.012	2.005	2.005	2.005	2.005
	C-F	0.725	0.715	0.714	0.714	0.714	0.714
	C-C	4.546	4.529	4.529	4.529	4.529	4.529
Non-dimensional mid-span displacement							
1	S-S	26.205	26.993	27.164	27.151	27.153	27.153
	C-F	89.072	91.847	92.131	92.115	92.123	92.122
	C-C	5.704	5.696	5.714	5.722	5.723	5.722
0	S-S	86.280	88.895	89.461	89.418	89.424	89.423
	C-F	293.611	302.730	303.642	303.599	303.640	303.635
	C-C	18.550	18.514	18.561	18.589	18.589	18.590

6.3.2 Verification studies

Since there is no available results on the FG sandwich thin-walled microbeams, the

verification is carried out with those of macrobeams ($b_3 / l = 0$).

Example 1: FG thin-walled C1- and C2-beams are considered. Tables 6-3 and 6-4 display the mid-span deflection (*mm*) under a uniformly distributed load $q = 500N/m$ and fundamental frequencies of the C1-beam. The first four natural frequencies of the C2-beam with various material power index p are given in Table 6-5. In Table 6-3, the bending results show good agreements with those given by Nguyen et al. [192] for both cases of $L/b_3 = 20$ and $L/b_3 = 50$. As predicted, the deflections increase with the increase of the power index p. In Tables 6-4 and 6-5, the fundamental frequencies are compared with the results from Nguyen et al. [193] and Nguyen et al. [192]. It can be seen that the results align well with those from previous studies, especially the one using shear deformable theory.

Table 6-3: Verification on the mid-span deflections (mm) of FG sandwich C1- beams

BC	Theory	p					
		0	0.5	1	2	5	10
$L/b_3 = 20$, Uniformly distributed load $q = 500N/m$							
S-S	Present	0.394	0.507	0.592	0.712	0.892	1.008
	Nguyen et al. (Shear) [192]	0.396	0.510	0.596	0.716	0.897	1.014
	Nguyen et al. (No shear)	0.390	0.502	0.586	0.705	0.883	0.998
C-F	Present	1.337	1.722	2.011	2.418	3.030	3.424
	Nguyen et al. (Shear) [192]]	1.343	1.730	2.021	2.429	3.044	3.440
	Nguyen et al. (No shear)	1.325	1.706	1.993	2.396	3.003	3.393
C-C	Present	0.082	0.105	0.123	0.148	0.185	0.210
	Nguyen et al. (Shear) [192]]	0.084	0.108	0.126	0.152	0.190	0.215
	Nguyen et al. (No shear)	0.078	0.100	0.117	0.141	0.177	0.200
$L/b_3 = 50$, Uniformly distributed load $q = 500N/m$							
S-S	Present	15.249	19.637	22.939	27.572	34.554	39.047
	Nguyen et al. (Shear) [192]	15.261	19.654	22.958	27.596	34.583	39.080
	Nguyen et al. (No shear) [192]	15.223	19.605	22.900	27.527	34.496	38.982
C-F	Present	51.834	66.752	77.972	93.726	117.455	132.731
	Nguyen et al. (Shear) [192]	51.872	66.802	78.030	93.796	117.543	132.829

	Nguyen et al. (No shear) [192]	51.759	66.655	77.859	93.590	117.285	132.539
C-C	Present	3.069	3.952	4.617	5.550	6.955	7.859
	Nguyen et al. (Shear) [192]	3.082	3.969	4.637	5.573	6.984	7.893
	Nguyen et al. (No shear) [192]	3.045	3.921	4.580	5.505	6.899	7.797

Table 6-4: Verification on the fundamental frequencies of FG thin-walled S-S C1-beams ($L/b_3 = 40$)

Theory	$\bar{\omega}$	p					
		0	0.5	1	2	5	10
Present	$\bar{\omega}_1$	3.0659	2.7541	2.5543	2.3112	2.0047	1.8348
	$\bar{\omega}_2$	4.3456	3.8292	3.5581	3.2963	3.0128	2.8087
	$\bar{\omega}_3$	10.2076	9.1571	8.5057	7.7367	6.7841	6.2312
	$\bar{\omega}_4$	12.0947	10.7398	9.9695	9.1286	7.9979	7.3273
Nguyen et al. [193]	$\bar{\omega}_1$	3.0668	2.7612	2.5642	2.3227	2.0148	1.8421
	$\bar{\omega}_2$	4.3475	3.8641	3.6385	3.4141	3.1054	2.8575
	$\bar{\omega}_3$	10.2254	9.2060	8.5828	7.8407	6.8811	6.2951
	$\bar{\omega}_4$	12.1029	10.8223	10.1441	9.2903	8.0589	7.3684
Nguyen et al. [192] (Shear)	$\bar{\omega}_1$	3.0659	2.7541	2.5544	2.3114	2.0048	1.8349
	$\bar{\omega}_2$	4.3462	3.8270	3.5533	3.2895	3.0075	2.8059
	$\bar{\omega}_3$	10.1965	9.1416	8.4879	7.7173	6.7663	6.2169
	$\bar{\omega}_4$	12.0939	10.7356	9.9661	9.1447	8.0110	7.3327
Nguyen et al. [192] (No shear)	$\bar{\omega}_1$	3.0668	2.7549	2.5551	2.3119	2.0054	1.8354
	$\bar{\omega}_2$	4.3475	3.8653	3.6402	3.4168	3.1088	2.8599
	$\bar{\omega}_3$	10.2254	9.2126	8.5910	7.8480	6.8848	6.2971
	$\bar{\omega}_4$	12.1028	10.7996	10.1011	9.2302	8.0168	7.3391

Table 6-5: Verification on fundamental frequencies of FG thin-walled S-S C2- beams ($L/b_3 = 40$)

Theory	$\bar{\omega}$	p					
		0	0.5	1	2	5	10

Present	$\bar{\omega}_1$	3.0659	2.8667	2.7484	2.6137	2.4585	2.3796
	$\bar{\omega}_2$	4.3456	3.7623	3.4420	3.1188	2.8245	2.7139
	$\bar{\omega}_3$	10.2076	9.4192	8.9713	8.4818	7.9459	7.6852
	$\bar{\omega}_4$	12.0947	10.8030	10.0971	9.3697	8.6553	8.3493
Nguyen et al. [193]	$\bar{\omega}_1$	3.0668	2.8676	2.7492	2.6145	2.4592	2.3803
	$\bar{\omega}_2$	4.3475	3.7636	3.4431	3.1197	2.8252	2.7146
	$\bar{\omega}_3$	10.2254	9.4364	8.9881	8.4980	7.9612	7.7001
	$\bar{\omega}_4$	12.1029	10.8096	10.1029	9.3747	8.6598	8.3535

Example 2: FG thin-walled sandwich I1- and I2-beams with $L/b_3 = 10$ and 20 are considered. The mid-span displacements are presented in Table 6-6 and 6-7 for the I1- and I2-beams subjected to a concentrated load at mid span. Good agreement is observed between the present results and those accounting for shear effect given by Kim and Lee [194] and Nguyen et al. [195]. Furthermore, Table 6-6 to 6-8 compares the fundamental frequencies between the present model and those from Nguyen et al. [193]. Again, excellent agreement between these results is found for different values of ceramic thickness ratio α_j and power index p.

Table 6-6: Verification on the mid-span deflections of FG thin-walled I2-beams under concentrated load at mid-span with different boundary conditions

BC	Reference	$L/b_3 = 10$				$L/b_3 = 20$			
		p=0	1	2	5	p=0	1	2	5
S-S	Present	82.963	118.814	138.803	166.876	80.347	115.064	134.430	161.615
	Nguyen et al. (Shear) [195]	82.965	118.813	138.799	166.879	80.346	115.064	134.424	161.614
	Nguyen et al. (No shear) [195]	79.476	113.816	132.962	159.863	79.473	113.815	132.964	159.859
C-F	Present	166.157	237.953	277.989	334.219	160.796	230.275	269.020	323.436
	Nguyen et al. (Shear) [195]	166.026	237.761	277.765	333.951	160.761	230.227	268.963	323.367
	Nguyen et al. (No shear) [195]	159.009	227.716	266.027	319.841	159.007	227.715	266.028	319.839
C-C	Present	23.321	33.365	38.974	46.851	20.717	29.659	34.650	41.658
	Nguyen et al. (Shear) [195]	23.251	33.212	38.689	46.655	20.663	29.603	34.589	41.588
	Nguyen et al. (No shear) [195]	19.871	28.363	33.039	39.844	19.8169	24.1543	26.1739	28.7235

Table 6-7: Verification on the non-dimensional fundamental frequencies of FG thin-walled S-S I1- beams ($L/b_3 = 40$)

Section	Theory	p	α_3					
			0	0.2	0.4	0.6	0.8	1
M1 [193] ($\alpha_1 = 0.9$, $\alpha_2 = 0.1$)	Present	1	1.516	1.504	1.493	1.485	1.478	1.471
		5	1.511	1.486	1.468	1.455	1.446	1.438
	Nguyen et al. [193]	1	1.530	1.515	1.503	1.491	1.482	1.475
		5	1.559	1.522	1.493	1.472	1.456	1.444
M2 [193] ($\alpha_1 = 0.1$, $\alpha_2 = 0.9$)	Present	1	1.334	1.322	1.311	1.301	1.292	1.284
		5	1.165	1.144	1.125	1.108	1.093	1.079
	Nguyen et al. [193]	1	1.327	1.316	1.306	1.297	1.288	1.281
		5	1.153	1.133	1.116	1.101	1.087	1.074

6.3.3 Parametric study

In this section, the results are computed for the FG thin-walled microbeams with various $b_3/l = 1, 2, 4$ along with those from macrobeam $b_3/l = 0$ to investigate the size effect.

Example 3: The mid-span deflections and fundamental frequencies of FG thin-walled C1-beams are shown in Tables 6-9 and 6-10. As seen in Table 6-8, in the cases where $b_3/l = 1, 2, 4$, the size-dependent effect is significant. The size effect makes the beam stiffer which results in a smaller mid-span deflection and larger frequencies.

Table 6-8: Size effects on the mid-span deflections of FG thin-walled C1-section microbeams under uniformly distributed load

BC	b_3/l	$L/b_3=10$				$L/b_3=20$			
		p=0	1	2	5	p=0	1	2	5
SS	0	40.682	61.198	73.563	92.187	39.463	59.364	71.358	89.424
	1	12.501	18.805	22.604	28.327	11.983	18.025	21.667	27.153
	2	25.858	38.898	46.756	58.595	25.042	37.670	45.281	56.745
	4	35.563	53.497	64.305	80.586	34.492	51.885	62.367	78.158
CF	0	137.612	207.009	248.835	311.834	133.997	201.570	242.296	303.640
	1	42.090	63.315	76.107	95.377	40.654	61.154	73.510	92.123
	2	87.326	131.362	157.903	197.883	85.012	127.882	153.719	192.639
	4	120.218	180.842	217.380	272.417	117.110	176.165	211.757	265.371
CC	0	9.383	14.117	16.965	21.483	8.209	12.341	14.834	18.592
	1	2.982	4.485	5.392	6.758	2.526	3.799	4.566	5.723
	2	5.965	8.963	10.774	13.507	5.214	7.843	9.426	11.815
	4	8.182	12.309	14.788	18.540	7.163	10.786	12.965	16.249

Table 6-9: Size effects on the lowest frequencies of FG thin-walled S-S C1-section microbeams ($L/b_3 = 10$)

b_3/l	$\bar{\omega}$	p					
		0	0.5	1	2	5	10
0	$\bar{\omega}_1$	2.530	2.267	2.106	1.917	1.685	1.549
	$\bar{\omega}_2$	3.053	2.743	2.544	2.302	1.997	1.828
	$\bar{\omega}_3$	9.406	8.475	7.874	7.136	6.193	5.661
	$\bar{\omega}_4$	9.509	8.553	7.944	7.207	6.275	5.746
1	$\bar{\omega}_1$	11.982	10.809	10.049	9.110	7.903	7.219
	$\bar{\omega}_2$	13.597	12.269	11.408	10.343	8.972	8.195
	$\bar{\omega}_3$	45.890	41.402	38.490	34.896	30.270	27.651
	$\bar{\omega}_4$	49.831	44.968	41.810	37.910	32.886	30.037
2	$\bar{\omega}_1$	6.595	5.945	5.525	5.007	4.344	3.969
	$\bar{\omega}_2$	9.432	8.511	7.914	7.175	6.224	5.685
	$\bar{\omega}_3$	25.859	23.315	21.667	19.638	17.035	15.565
	$\bar{\omega}_4$	34.818	31.422	29.216	26.492	22.980	20.989
4	$\bar{\omega}_1$	4.231	3.809	3.537	3.204	2.779	2.541
	$\bar{\omega}_2$	7.977	7.199	6.694	6.070	5.265	4.809
	$\bar{\omega}_3$	16.682	15.020	13.948	12.634	10.959	10.020
	$\bar{\omega}_4$	28.861	26.050	24.224	21.968	19.057	17.404

It can also be seen from Figs. 6-4 and 6-5 that under all boundary conditions, the beam's bending and vibration responses experience a drastic change from $b_3/l = 1$ to $b_3/l = 2$ but the slope quickly becomes less steep when $b_3/l > 2$. To better understand the the influences of the flange-width-to –MLSP ratio (b_1/l) on the dynamic behaviours of these C1 FG microbeams, the first three natural frequencies are shown in Fig. 6-6. Since the microbeam's geometrical shape is preserved and is set with $b_3 = 2b_1$, the b_1/l ratio's effects on the frequencies at all modes are proportional to the b_3/l ratio, which can be deduced by comparing Figs. 6-5 and 6-6. Additionally, it is interesting to see the very sharp drop of the frequencies in the third mode compared to first one in all boundary conditions when $b_1/l < 5$. Besides, the second frequencies converge to the macro beam value when $b_1/l = 20$, which is much quicker than the other two modes.

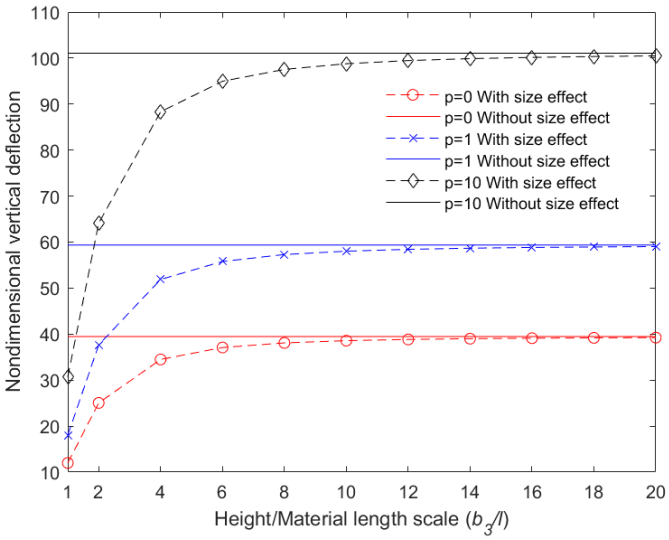

a) S-S

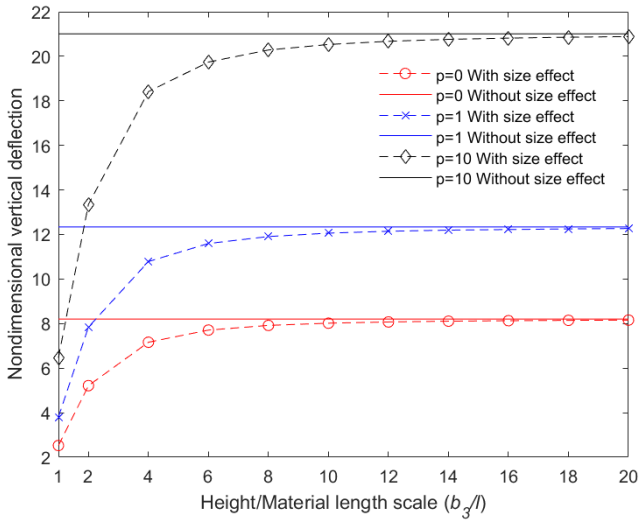

b) C-C

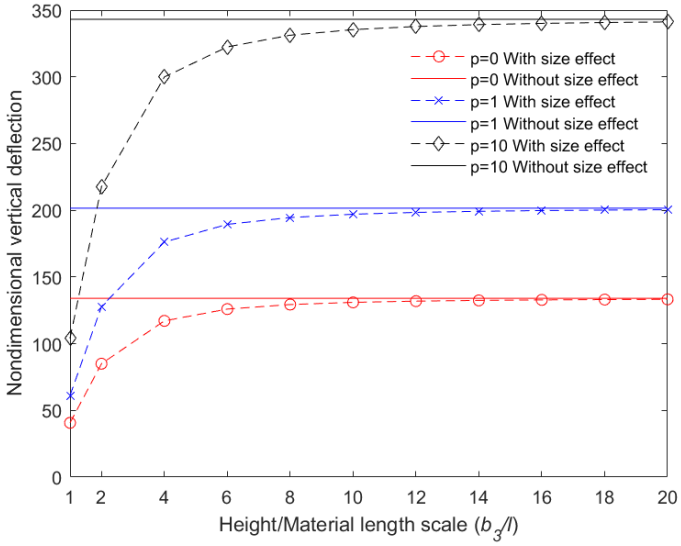

c) C-F

Figure 6-3: Effects of on the mid-span deflections of FG thin-walled C1-beams under uniformly distributed load

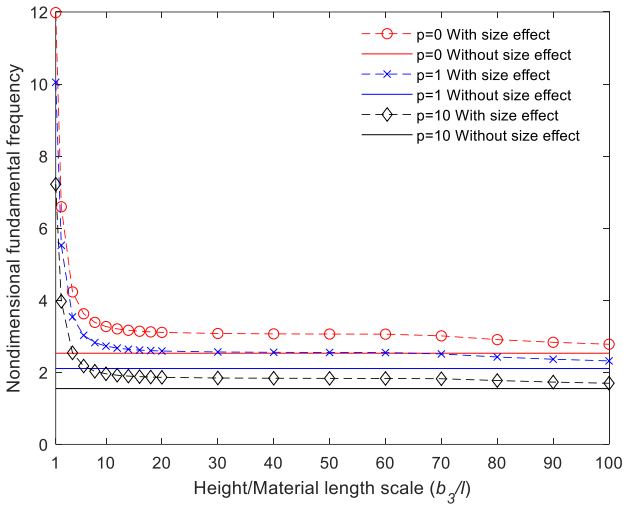

a) S-S

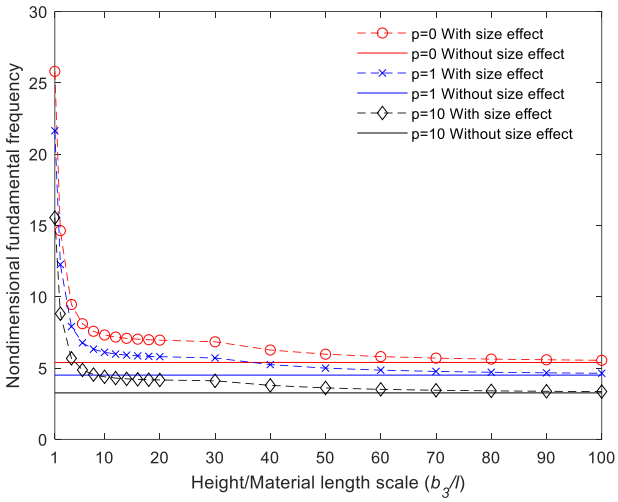

b) C-C

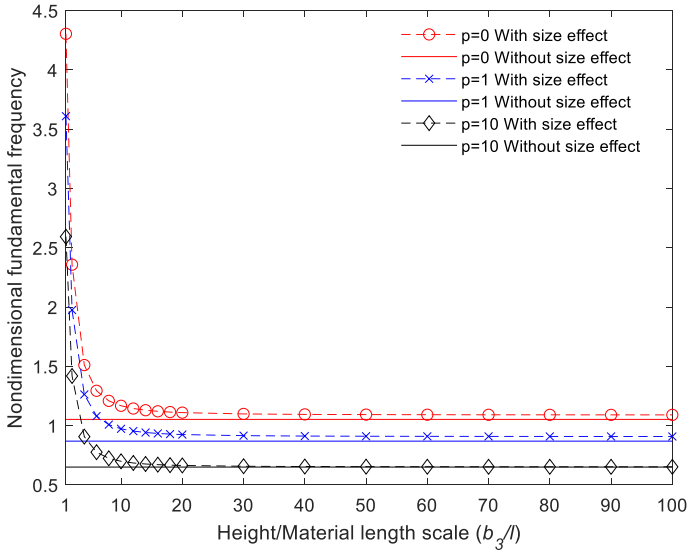

c) C-F

Figure 6-4: Effects of b_3 / l on the fundamental frequency of FG thin-walled C1-beams $\left(L / b_3 = 10\right)$

Example 4: This example investigates the vibration of FG thin-walled C2-beam. The

present solution in Table 6-10 shows that when taking the size-dependent effect into account, the fundamental frequencies at $b_3/l=1$ are more than 4 times greater than at $b_3/l=0$. As b_3/l ratio increases, the vibration responses decrease and become closer to those of the macrobeam model. This pattern applies for all values of power index p and all three boundary conditions as can be seen in Table 6-10 and Fig. 6-6. It is also worth pointing out that in Fig. 6-6, at $b_3/l=0$, there is only a slight decrease in fundamental frequency when the power index p changes from 0 to 1. Nonetheless, at $b_3/l=1$, a big difference in the fundamental frequencies compared between the microbeam and macrobeam model can be observed. Figure 6-8 shows the first two mode shapes when $b_3/l=0$ and $b_3/l=1$. It is noticeable that the first mode of the macrobeam is torsion mode. The second mode of marcobeam can be observed to be very similar to the first one of microbeams which are bending mode. The second mode of microbeam is also bending mode. The understanding of the beam vibrational mode can help detect defects and prevent structural failures.

Table 6-10: Size effects on the lowest frequencies of FG thin-walled S-S C1-section microbeams ($L/b_3=10$)

b_3/l	$\bar{\omega}$	p					
		0	0.5	1	2	5	10
0	$\bar{\omega}_1$	2.530	2.267	2.106	1.917	1.685	1.549
	$\bar{\omega}_2$	3.053	2.743	2.544	2.302	1.997	1.828
	$\bar{\omega}_3$	9.406	8.475	7.874	7.136	6.193	5.661
	$\bar{\omega}_4$	9.509	8.553	7.944	7.207	6.275	5.746
1	$\bar{\omega}_1$	11.982	10.809	10.049	9.110	7.903	7.219
	$\bar{\omega}_2$	13.597	12.269	11.408	10.343	8.972	8.195
	$\bar{\omega}_3$	45.890	41.402	38.490	34.896	30.270	27.651
	$\bar{\omega}_4$	49.831	44.968	41.810	37.910	32.886	30.037
2	$\bar{\omega}_1$	6.595	5.945	5.525	5.007	4.344	3.969
	$\bar{\omega}_2$	9.432	8.511	7.914	7.175	6.224	5.685
	$\bar{\omega}_3$	25.859	23.315	21.667	19.638	17.035	15.565
	$\bar{\omega}_4$	34.818	31.422	29.216	26.492	22.980	20.989

4	$\bar{\omega}_1$	4.231	3.809	3.537	3.204	2.779	2.541
	$\bar{\omega}_2$	7.977	7.199	6.694	6.070	5.265	4.809
	$\bar{\omega}_3$	16.682	15.020	13.948	12.634	10.959	10.020
	$\bar{\omega}_4$	28.861	26.050	24.224	21.968	19.057	17.404

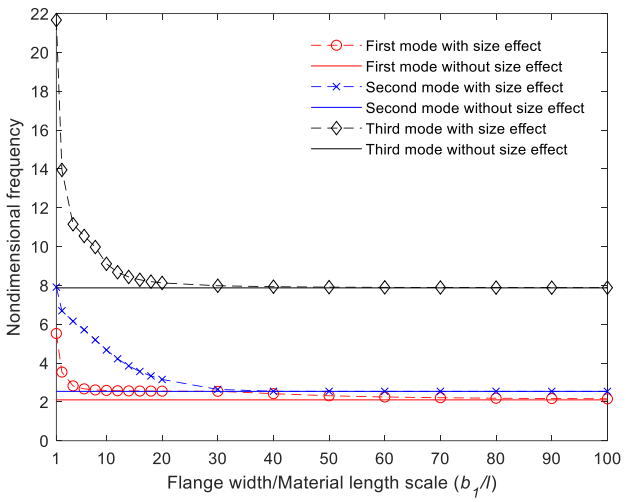

a) S-S

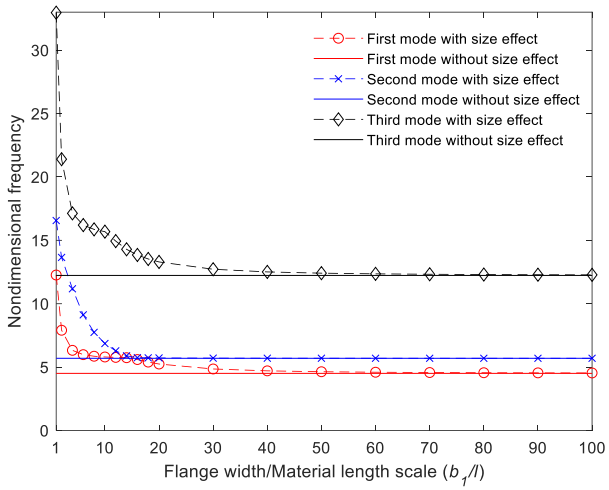

b) C-C

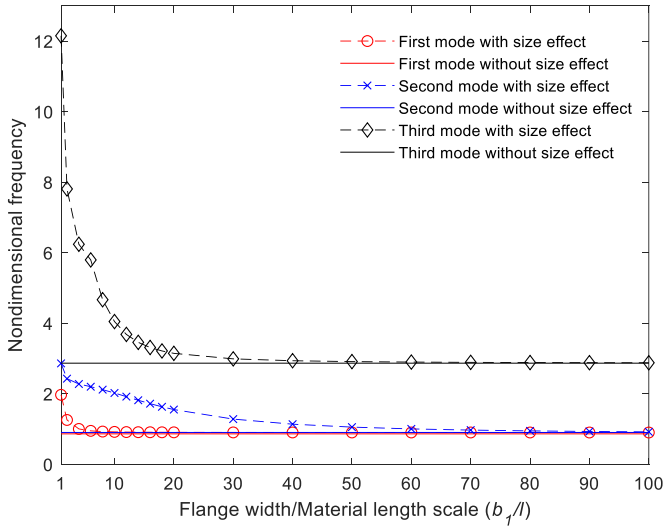

c) C-F

Figure 6-5: Effects of b_1/l on the first three natural frequencies of FG thin-walled C1-beams $\left(L/b_3 = 10,\ p = 1\right)$

Example 5: The size-dependent effect is investigated on the FG thin-walled I1- and I2-beams subjected to a concentrated load at mid-span and their mid-span displacements are

provided in Tables 6-11 and 6-12. The lower values demonstrate a stiffer beam, the microbeams again show an increase in stiffness compared to its macro beam counterpart. The lower the b_3 / l ratio is, the stiffer the microbeam becomes. As shown in Table 6-12, the mid-span displacement when $b_3 / l = 0$ is four to five times greater than when $b_3 / l = 1$. Fig. 6-9 further demonstrates the variation of the mid span displacement with different values of power index p and b_3 / l ratios.

Table 6-11: Size effects on the mid-span deflections of FG thin-walled I1-section microbeams under concentrated load at mid-span

BC	b_3 / l	$L / b_3 = 10$				$L / b_3 = 20$			
		p=0	1	2	5	p=0	1	2	5
S-	0	82.963	118.814	138.803	166.876	80.347	98.142	106.445	116.663
	1	23.664	33.889	39.590	47.599	22.620	27.298	29.354	31.773
	2	50.620	72.491	84.688	101.818	48.952	59.403	64.125	69.799
	4	71.483	102.372	119.597	143.787	69.231	84.371	91.351	99.879
C-	0	166.157	202.853	219.929	240.911	160.796	196.412	213.026	233.472
	1	47.307	57.068	61.350	66.380	45.262	54.622	58.738	63.579
	2	101.263	122.821	132.542	144.202	97.956	118.867	128.318	139.673
	4	143.087	174.283	188.641	206.135	138.546	168.838	182.814	199.870
C-	0	23.321	28.389	30.771	33.611	20.717	25.285	27.416	30.029
	1	6.889	8.299	8.915	9.633	5.908	7.126	7.671	8.290
	2	14.244	17.237	18.592	20.184	12.638	15.327	16.455	17.993
	4	20.045	24.371	26.899	28.627	17.848	21.739	24.020	25.721

Table 6-12: Size effects on the mid-span deflections of FG I2-section microbeams under concentrated load at mid-span

BC	b_3 / l	$L / b_3 = 10$				$L / b_3 = 20$			
		p=0	1	2	5	0	1	2	5
S-S	0	82.963	118.814	138.803	166.876	80.347	115.064	134.431	161.617
	1	23.664	33.889	39.590	47.599	22.620	32.393	37.843	45.497
	2	50.620	72.491	84.688	101.818	48.952	70.103	81.897	98.463
	4	71.483	102.372	119.597	143.787	69.232	99.152	115.827	139.259
C-F	0	166.157	237.953	277.989	334.219	160.796	230.276	269.020	323.436
	1	47.307	67.746	79.144	95.153	45.262	64.818	75.723	91.040
	2	101.263	145.017	169.416	203.684	97.956	140.281	163.883	197.033
	4	143.087	204.914	239.391	287.814	138.546	198.410	231.793	278.679
C-C	0	23.321	33.365	38.974	46.851	20.713	29.668	34.652	41.675
	1	6.889	9.866	11.525	13.857	5.907	8.462	9.884	11.882
	2	14.242	20.389	23.814	28.632	12.643	18.102	21.161	25.421
	4	20.066	28.614	33.572	40.320	17.851	25.553	29.860	35.902

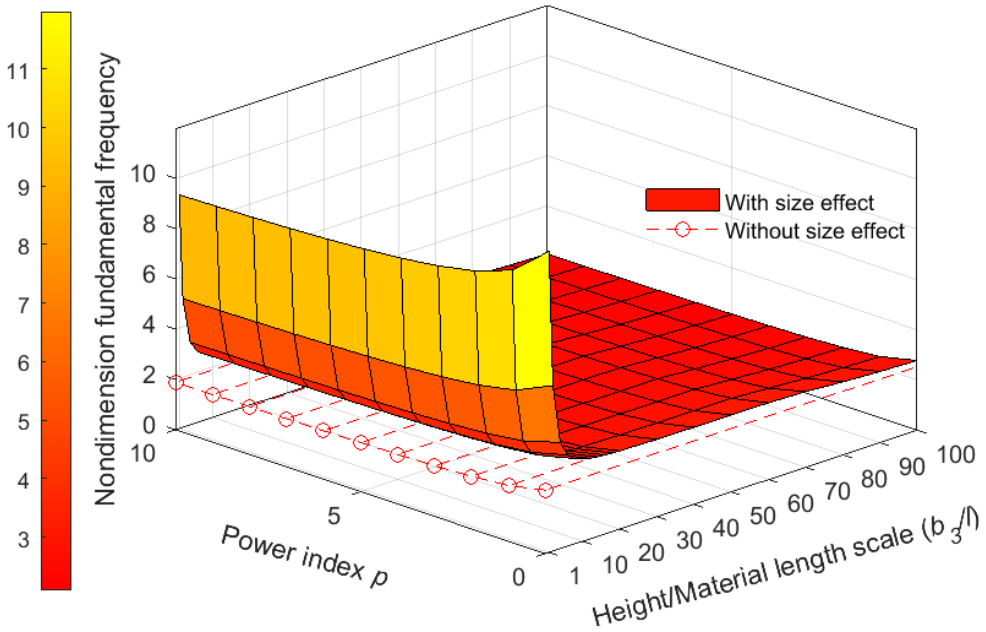
Nondimension fundamental frequency
With size effect
Without size effect
Power index p
Height/Material length scale (b 3/l)

a) S-S

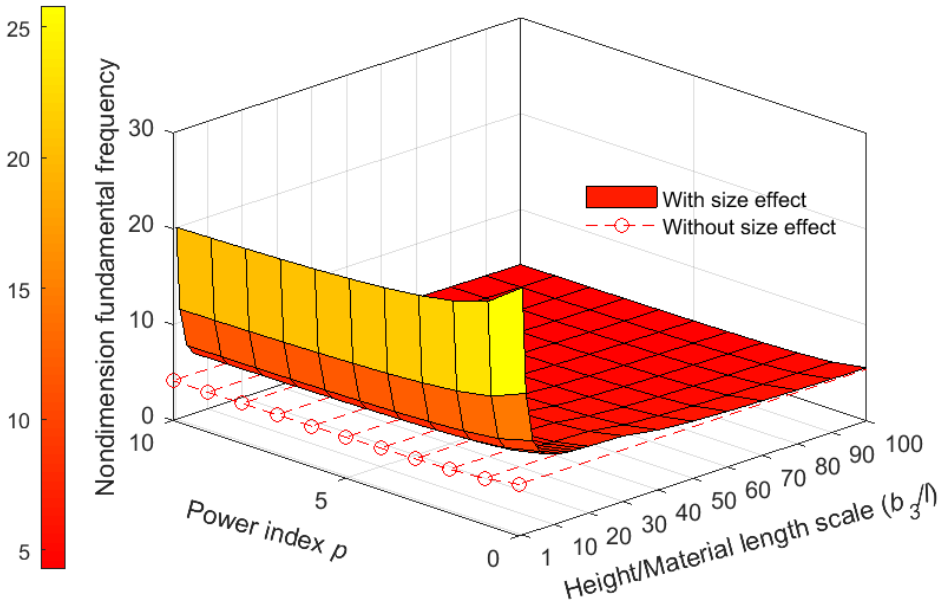
Nondimension fundamental frequency
With size effect
Without size effect
Power index p
Height/Material length scale (b 3/l)

b) C-C

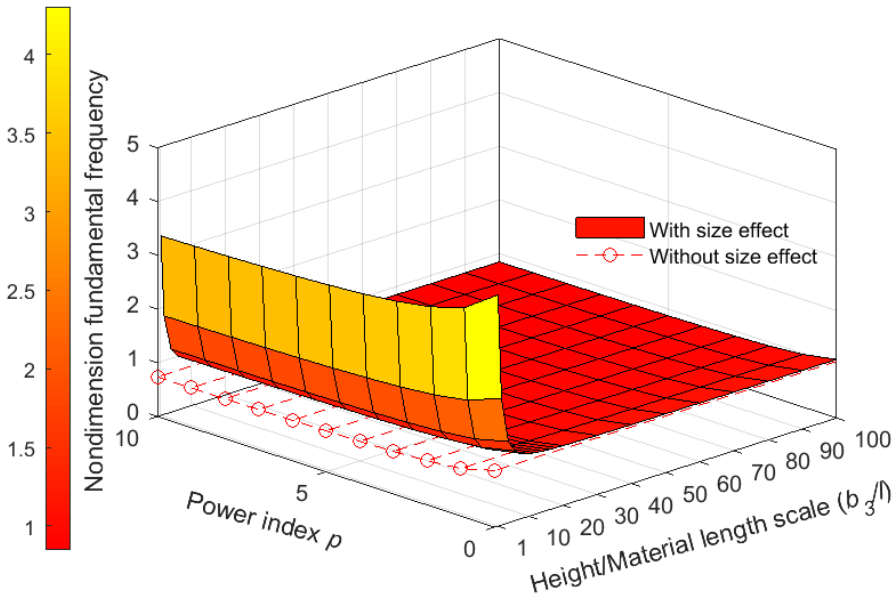

c) C-F

Figure 6-6: Effects of b_3/l and p on the fundamental frequency of FG sandwich thin-walled C2-beams $(L/b_3=10)$ under various boundary conditions

Example 6: Vibration analysis of the FG sandwich I1- and I2-microbeams is carried out. Tables 6-13 and 6-14 display the first four natural frequencies of simply-supported beams when $b_3/l=0,1,2,4$. At $p=0$, both sections are fully made of ceramic material and therefore, the results for both sections are identical. Nonetheless, across all values of p, the size-dependent effects on the microbeam are conspicuous as observed in previous examples. The beam becomes stiffer and thus, has higher dimensionless fundamental frequencies when the b_3/l ratio gets smaller. Besides, Fig. 6-8 shows the first two mode shapes of the micro- and macro-I1 S-S beams. Both the mode shapes of the macro I1-beam are torsion mode while those of micro I1-beam are bending mode. In Table 6-13 and 6-14, the frequencies in all modes of both I1- and I2- microbeam at $b_3/l=1$ are 5 to 12 times more than those of the

macrobeam at $b_3 / l = 0$. Thus, the microbeam is less likely to fail than the macrobeams made from the same FG material.

Table 6-13: Size effects on the lowest frequencies of FG thin-walled S-S I1-section microbeams ($L / b_3 = 10$)

b_3 / l	$\bar{\omega}$	p					
		0	0.5	1	2	5	10
0	$\bar{\omega}_1$	1.178	1.084	1.028	0.967	0.899	0.867
	$\bar{\omega}_2$	2.440	2.374	2.346	2.322	2.303	2.295
	$\bar{\omega}_3$	3.959	3.590	3.370	3.119	2.831	2.683
	$\bar{\omega}_4$	7.163	6.802	6.583	6.328	5.946	5.601
1	$\bar{\omega}_1$	11.728	11.211	10.919	10.602	10.255	10.086
	$\bar{\omega}_2$	13.429	12.808	12.450	12.052	11.605	11.382
	$\bar{\omega}_3$	45.203	43.201	42.074	40.847	39.503	38.848
	$\bar{\omega}_4$	49.542	47.269	45.966	44.522	42.906	42.103
2	$\bar{\omega}_1$	6.068	5.814	5.671	5.516	5.346	5.263
	$\bar{\omega}_2$	9.171	8.730	8.469	8.172	7.829	7.654
	$\bar{\omega}_3$	23.986	22.976	22.408	21.791	21.117	20.789
	$\bar{\omega}_4$	34.271	32.639	31.678	30.589	29.336	28.698
4	$\bar{\omega}_1$	3.326	3.210	3.145	3.075	2.999	2.962
	$\bar{\omega}_2$	7.716	7.334	7.104	6.838	6.524	6.362
	$\bar{\omega}_3$	13.232	12.768	12.508	12.227	11.922	11.774
	$\bar{\omega}_4$	28.860	27.445	26.596	25.618	24.471	23.878

Table 6-14: Size effects on the lowest frequencies of FG thin-walled S-S I2-section microbeams ($L/b_3 = 10$)

b_3/l	$\bar{\omega}$	p					
		0	0.5	1	2	5	10
0	$\bar{\omega}_1$	1.178	1.032	0.947	0.856	0.766	0.726
	$\bar{\omega}_2$	2.440	2.168	2.011	1.838	1.648	1.555
	$\bar{\omega}_3$	3.959	3.533	3.283	3.004	2.694	2.541
	$\bar{\omega}_4$	7.163	6.544	6.155	5.688	5.113	4.801
1	$\bar{\omega}_1$	11.728	10.715	10.078	9.314	8.372	7.861
	$\bar{\omega}_2$	13.429	12.270	11.540	10.665	9.586	9.002
	$\bar{\omega}_3$	45.203	41.301	38.844	35.900	32.267	30.300
	$\bar{\omega}_4$	49.542	45.266	42.573	39.346	35.365	33.209
2	$\bar{\omega}_1$	6.068	5.544	5.214	4.819	4.331	4.067
	$\bar{\omega}_2$	9.171	8.379	7.881	7.283	6.546	6.147
	$\bar{\omega}_3$	23.986	21.915	20.611	19.048	17.121	16.077
	$\bar{\omega}_4$	34.271	31.313	29.450	27.217	24.464	22.972
4	$\bar{\omega}_1$	3.326	3.038	2.857	2.641	2.373	2.229
	$\bar{\omega}_2$	7.716	7.050	6.631	6.128	5.508	5.172
	$\bar{\omega}_3$	13.232	12.089	11.369	10.507	9.444	8.868
	$\bar{\omega}_4$	28.860	26.369	24.800	22.920	20.601	19.345

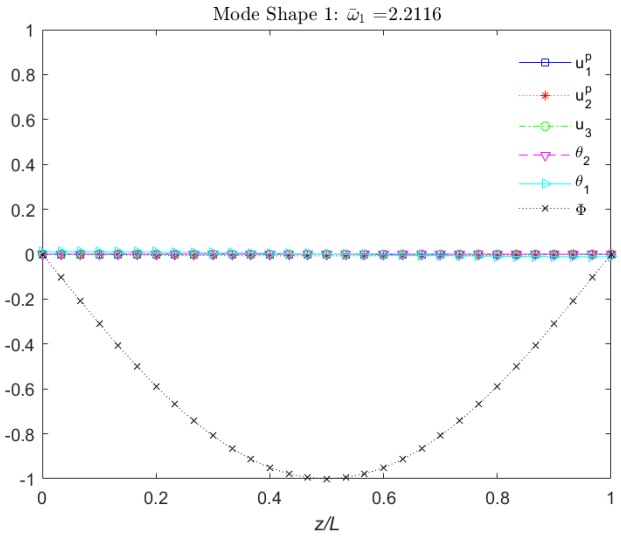

$l/b_3 = 0$

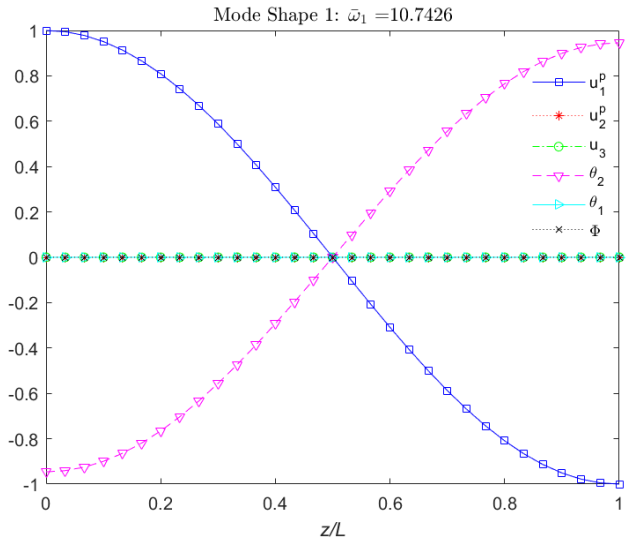

$l/b_3 = 1$

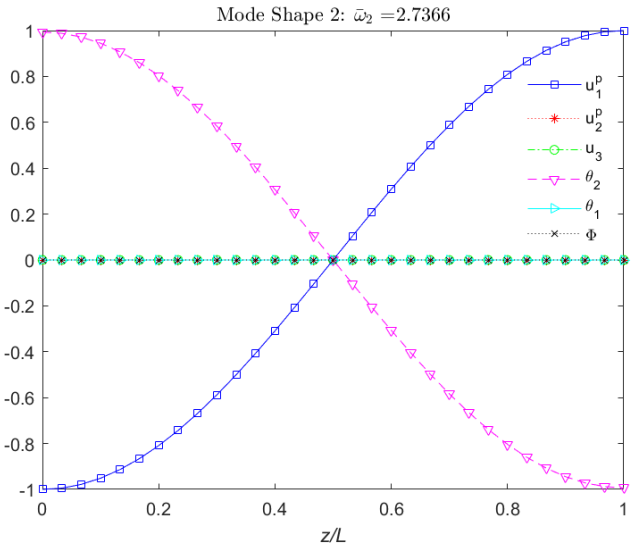

$l/b_3 = 0$

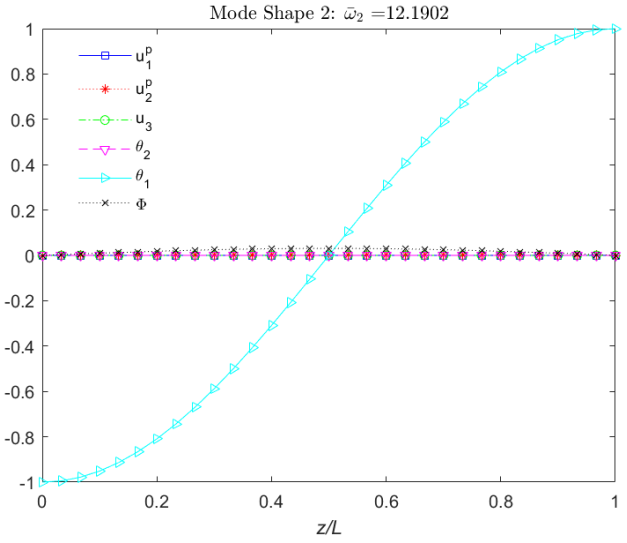

$l/b_3 = 1$

Figure 6-7: The first two mode shapes of FG thin-walled C2-section macro- and micro- beams (, , S-S boundary condition)

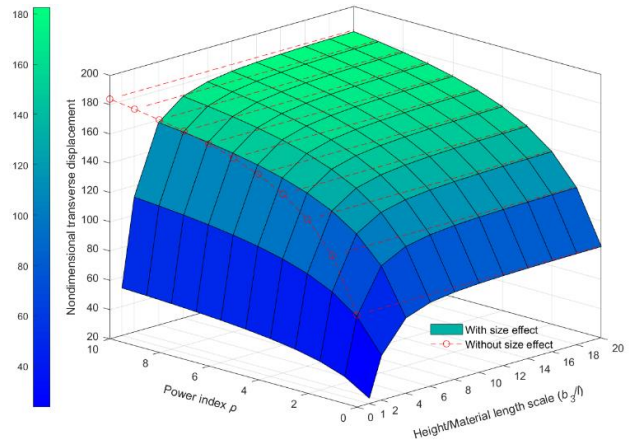

a) S-S

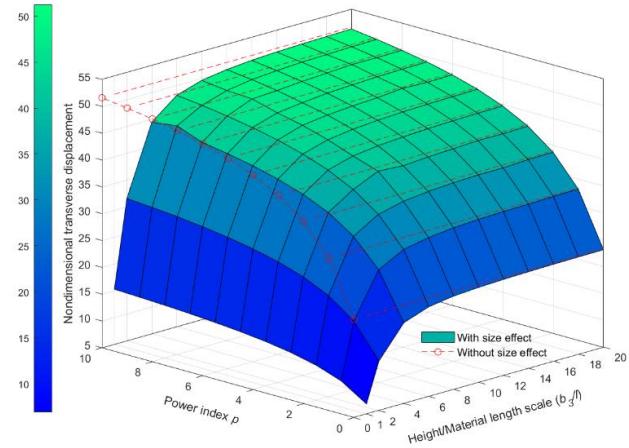

b) C-C

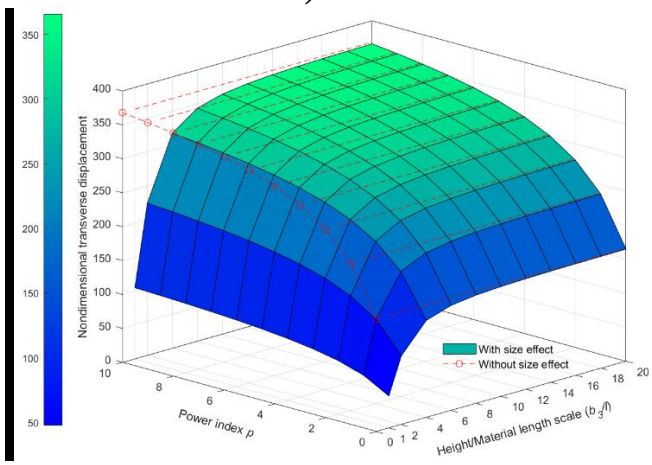

c) C-F

Figure 6-8: Effects of b_3 / l and p on the mid-span displacement of the FG sandwich thin-walled I2-beams $\left(L / b_3 = 10\right)$ under various boundary conditions

6.4. Conclusions

By using the first-order shear deformation theory and modified couple stress theory, this chapter studied for the first time the size-dependent behaviours of functionally graded sandwich thin-walled C and I-beams. The effects of boundary conditions, material distribution, beam length-to-height ratio and material length scale parameter were investigated. The following findings were drawn from the numerical results:

- The size-dependent effect made the FG thin-walled microbeams considerably stiffer, which in turn reduced the beam's bending transverse deflections and increased the beam's fundamental frequencies.
- The mid-span displacement of the C1 and I2 microbeams converged to the values of their macro-beam counterparts at $b_3 / l = 20$ under all three boundary conditions
- The fundamental frequency of the C1 and C2 microbeams converged to their macrobeam values quickly under C-F condition at $b_3 / l = 20$ but converged much slower under S-S and C-C condition at $b_3 / l = 100$

CHAPTER 7 : VIBRATION AND BUCKLING ANALYSIS OF POROUS METAL FOAM THIN-WALLED BEAMS WITH CLOSED SECTION

Extending the exploration of thin-walled beam behaviors to innovative material composition and closed cross-section, this chapter investigates the vibration and buckling analysis of porous metal foam thin-walled box beams. These beams exhibit a unique structural configuration with symmetrical and asymmetrical porosity distributions along their wall thickness, thereby altering their effective mechanical properties. The first-order shear deformable thin-walled beam theory is employed and the governing equations are derived using the Hamilton's principle. Numerical results are presented for porous metal foam thin-walled box beams under simply-supported, clamped-clamped and clamped-free boundary conditions. The effects of various porosity parameters, length-to-side and side-to-wall-thickness ratios on the beams' performance are also examined. A comprehensive comparison between the porous metal foam thin-walled box beams and their counterparts in the form of equivalent homogeneous and functionally graded thin-walled beams are presented. The findings contribute to the advancement of thin-walled beam theories and offer benchmarks for future studies in lightweight and high-performance structural applications.

7.1. Introduction

Previous Chapters have not performed the analysis on closed-section thin-walled beams (CSTWB). Henceforth, this Chapter fills in this void in this thesis. Compared to open-sectioned thin-walled beams, CSTWB possesses increased torsional rigidity, thanks to its closed shape. This is crucial in applications where resistance to twisting or torsional deformation is important. CSTWB also exhibit superior resistance to buckling compared to open-section beams. Choi and Kim [196] proposed a higher-order Vlasov's torsion theory that incorporates extra sectional deformation modes for thin-walled box beams. By using FTWBT, Ziane et al. [197] investigated the free vibration of FG thin-walled box beam.

Many other authors have investigated the FG thin-walled closed section beams but not porous metal foam (PMF) particularly.

Recently, the exceptional material attributes of PMF have increasingly enticed researchers to explore its characteristics and behaviors for various structures. Despite the growing number of recent researches in PMF beams with rectangle sections [198-202], there are no studies on the mechanical responses of PMF thin-walled beams. Only several earlier researches investigated static and dynamic responses of FG thin-walled beams with porosity. By using the FTWBT and Galerkin method, Ziane et al. [203] analysed the thermal effects on the stability of FG box beams with porosity and Farsadi [204] investigated the statics and dynamics of FG thin-walled rotating blades with porosity.

This Chapter aims to study vibration and buckling analysis of the PMF box beam using the FTWBT for the first time. Both symmetric and nonsymmetric porosity distributions via the thickness are considered. Governing equations are derived from the Hamilton's principle and are solved using the Ritz-type hybrid series solution. The effects of porosity configurations, boundary conditions, length-to-height ratio, height-to-wall-thickness ratio and cross-section shapes on the vibration and buckling analysis of PMF thin-walled box beams are evaluated. These insights can contribute to the future analysis and design considerations in multiple state-of-the-art engineering fields.

7.2. Theoretical formulation

This chapter considers a PMF thin-walled box beam with length L. For simplicity purpose, the following assumptions are made: the strains are small and the section contour does not deform in its own plane, the shear and warping shear strains are uniform over the section, local buckling and pre-buckling deformation are negligible.

7.2.1. Kinematics

The kinematics of the FTWBT at any points of the section can be derived from section 3.2.1 of Chapter 3 by setting $g = g_0 = 1, f = n$. These displacements are expressed by:

$$u(n,s,z) = u_P(z) - \left(y - nx_{,s} - y_P\right)\phi(z) \tag{7-1a}$$

$$v(n,s,z) = v_P(z) + \left(x + ny_{,s} - x_P\right)\phi(z) \tag{7-1b}$$

$$\begin{aligned} w(n,s,z) &= w_0(z) + \gamma_{xz}^{(0)}(z)\left(x + ny_{,s}\right) + \gamma_{yz}^{(0)}(z)\left(y - nx_{,s}\right) \\ &-\phi_{,z}(z)(F_\omega - nr_{,s}) - u_{P,z}(z)\left(x + ny_{,s}\right) - v_{P,z}\left(y - nx_{,s}\right) \end{aligned} \tag{7-1c}$$

where $F_\omega(s)$ is a warping function defined by:

$$F_\omega(s) = \int_{s_0}^{s}\left(r_n - \frac{2\Omega}{\beta}\right)(s)ds \tag{7-2}$$

where Ω is the area enclosed by the contour line of the beam and β is the cross-section perimeter.

7.2.2. Strains

The linear non-zero strains related to the displacements in Eq. (7-6) are given by:

$$\varepsilon_z(n,s,z) = \varepsilon_z^{(0)} + n\varepsilon_z^{(1)} \tag{7-3a}$$

$$\gamma_{sz}(n,s,z) = \gamma_{sz}^{(0)} + n\gamma_{sz}^{(1)} \tag{7-3b}$$

$$\gamma_{nz}(n,s,z) = \gamma_{nz}^{(0)} \tag{7-3c}$$

where

$$\varepsilon_z^{(0)}(s,z) = w_{,z}^{(0)} + \theta_{y,z}x + \theta_{x,z}y - \phi_{,zz}F_\omega \tag{7-4a}$$

$$\varepsilon_z^{(1)}(s,z) = \theta_{y,z}y_{,s} - \theta_{x,z}x_{,s} + \phi_{,zz}r_s \tag{7-4b}$$

$$\gamma_{sz}^{(0)}(s,z) = \gamma_{xz}^{(0)}x_{,s} + \gamma_{yz}^{(0)}y_{,s} \tag{7-4c}$$

$$\gamma_{sz}^{(1)}(s,z) = 2\phi_{,z} \tag{7-4d}$$

$$\gamma_{nz}^{(0)}(s,z) = \gamma_{xz}^{(0)} y_{,s} - \gamma_{yz}^{(0)} x_{,s} \tag{7-4e}$$

7.2.3. Stress

The stress-strain relation of the PMF thin-walled beams whose properties vary continuously in the thickness can be written as follows:

$$\begin{Bmatrix} \sigma_z \\ \sigma_{sz} \\ \sigma_{nz} \end{Bmatrix} = \begin{pmatrix} Q_{11} & 0 & 0 \\ 0 & Q_{66} & 0 \\ 0 & 0 & Q_{55} \end{pmatrix} \begin{Bmatrix} \varepsilon_z \\ \gamma_{sz} \\ \gamma_{nz} \end{Bmatrix} \tag{7-5}$$

where $Q_{11} = E(n)$, $Q_{66} = Q_{55} = \dfrac{E(n)}{2(1+\nu)}$; $E(n)$ is Young's modulus; ν is constant Poisson's ratio. In this study, two porosity patterns [51-53] of PMF thin-walled beams are considered as indicated in Fig. 7-2.

Symmetric pore distribution (Type A)

$$E(n) = E_{\max}\left(1 - e_0 \cos\left(\frac{\pi n}{h}\right)\right) \tag{7-6a}$$

$$\rho(n) = \rho_{\max}\left(1 - e_m \cos\left(\frac{\pi n}{h}\right)\right) \tag{7-6b}$$

Asymmetric pore distribution (Type B)

$$E(n) = E_{\max}\left[1 - e_0 \cos\left(\frac{\pi n}{2h} + \frac{\pi}{4}\right)\right] \tag{7-6a}$$

$$\rho(n) = \rho_{\max}\left[1 - e_m \cos\left(\frac{\pi n}{2h} + \frac{\pi}{4}\right)\right] \tag{7-6b}$$

where: $E_{\max}$ and $\rho_{\max}$ are the maximum values of Young's modulus and mass density, respectively; e_0 and $e_m = 1 - \sqrt{1 - e_0}$ are the porosity parameters; $\rho(n)$ is mass density of the PMF thin-walled beams.

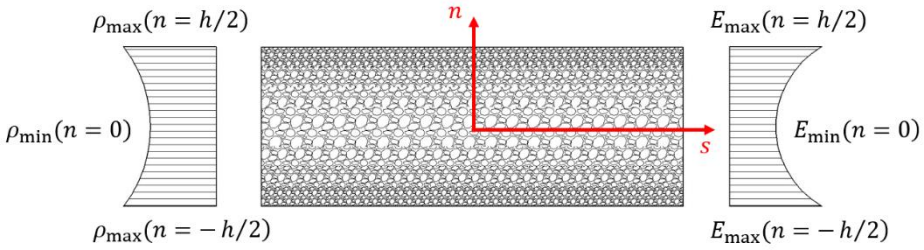

a) Symmetric pore distribution (Type A)

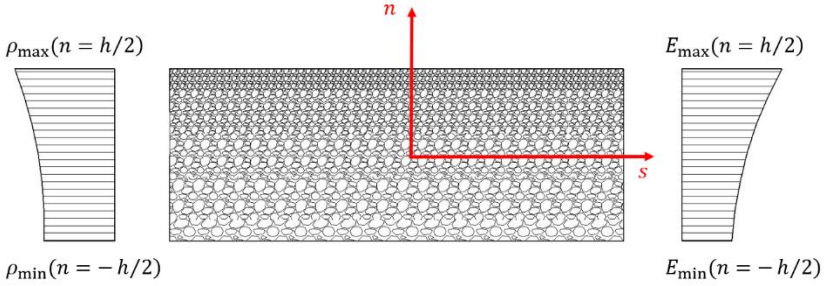

b) Asymmetric pore distribution (Type B)

Figure 7-1: Porous metal foam (PMF) material distribution in the wall thickness

7.2.4. Variational formulation and Solution

The variational formulation and solution in this Chapter is based on the FTWBT mentioned in Chapter II. The approximation functions for the Ritz-type solution is shown in Table 7-1. These functions are combined of exponential and admissible trigonometric functions to satisfy various boundary conditions.

Table 7-1: Shape functions and essential BCs of PMF thin-walled box beams

BC	$\varphi_j(x_3)$	$z=0$	$z=L$
S-S	$(z-L)\left(1-\frac{z}{L}\right)e^{\frac{-jz}{L}}$	$\xi=\eta=\phi=0$	$\xi=\eta=\phi=0$
C-F	$\left(\frac{z}{L}\right)^2 e^{\frac{-jz}{L}}$	$\xi=\eta=\phi=0$ $\xi_{,3}=\eta_{,3}=\phi_{,3}=0$ $\zeta=\psi_2=\psi_1=\psi_{\varpi}=0$	
C-C	$\left(\frac{z}{L}\right)^2\left(1-\frac{z}{L}\right)^2 e^{\frac{-jz}{L}}$	$\xi=\eta=\phi=0$ $\xi_{,3}=\eta_{,3}=\phi_{,3}=0$ $\zeta=\psi_2=\psi_1=\psi_{\varpi}=0$	$\xi=\eta=\phi=0$ $\xi_{,3}=\eta_{,3}=\phi_{,3}=0$ $\zeta=\psi_2=\psi_1=\psi_{\varpi}=0$

7.3. Numerical results

The present FTWBT beam model for the PMF box beams is compared and computed for different cases in this section. Porous alumina is chosen to be the material of the studied beams. The material has been widely used in the industry due to many advantages such as cost, environmental sustainability, and production time. Its properties in this chapter are assumed to be $E_{\max}=380GPa$, $v=0.3$, $\rho_{\max}=3800kgm^{-3}$. The following subsections investigate the impacts of porosity, boundary conditions and geometry on the buckling and vibration stability of the PMF thin-walled box beams. It is noted that when $e_0=0$, the PMF thin-walled box beam is isotropic, homogenous and pore-less.

7.3.1 Convergence study

By refering to the geometry symbols shown in Fig. 7-3, the convergence and accuracy of the present solution are studied for the sample thin-walled box beams with the following dimensions:

Buckling analysis: $h=h_1=h_2=h_3=h_4=0.005m$, $b_1=b_3=0.1m$, $b_2=b_4=0.2m$, $L=8\text{m}$.

Vibration analysis: $h=h_1=h_2=h_3=h_4=0.000762m$, $b_1=b_3=0.0136m-h$,

$b_2 = b_4 = 0.0242m - h$, $L = 0.762\text{m}$.

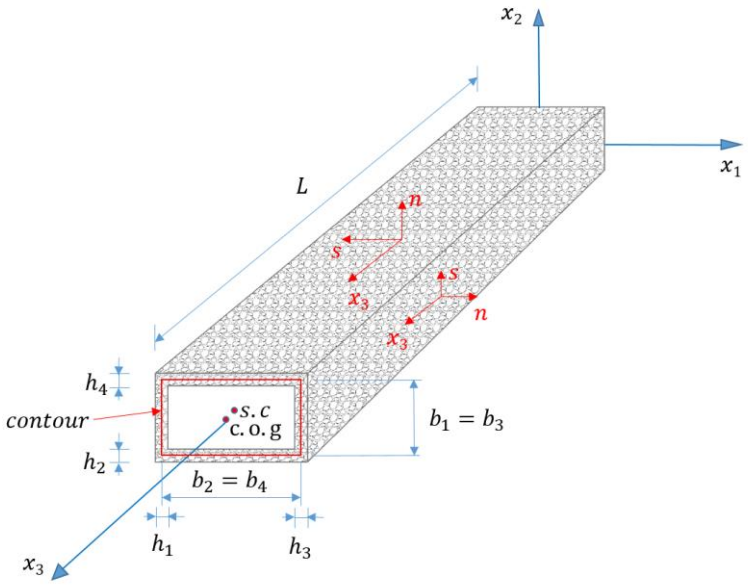

Figure 7-2: Geometry of PMF thin-walled box beams.

Table 7-2 shows the fundamental frequencies and the critical buckling loads of the PMF thin-walled box beams as the series number m increases. It can be seen that the present solution converges at series number $m = 8$ for all boundary conditions. For that reason, this series number is applied in the upcoming examples.

Table 7-2: Convergence of fundamental frequencies (*Hz*) and critical buckling load (*MN*) of the FGP thin-walled box beams

BCs	*m*					
	2	4	6	8	10	12
Critical buckling loads (*MN*)						
S-S	0.24018	0.23473	0.23307	0.23305	0.23305	0.23305
C-C	0.45929	0.45862	0.45851	0.45851	0.45851	0.45851
C-F	0.06162	0.05830	0.05830	0.05830	0.05830	0.05830
Fundamental frequencies (*Hz*)						
S-S	141.27	139.43	138.90	138.90	138.90	138.90
C-C	203.98	197.32	196.29	196.13	196.12	196.11
C-F	50.22	49.55	49.51	49.51	49.51	49.51

7.3.2 Verification study

Since there is no previous numerical data for the vibration and buckling analysis of the PMF thin-walled box beams, the present solutions are verified with those of Ziane et al. [197] and Lanc et al. [205] for metal-ceramic FG thin-walled box beams. The material properties used by Ziane et al. [197] are: $E_c = 380GPa, E_m = 70GPa$, $\rho_c = 3800kgm^{-3}, \rho_m = 2707kgm^{-3}$, $\nu = 0.3$. The material properties used by Lanc et al. [205] are: $E_c = 380GPa, E_m = 70GPa$, $\nu = 0.3$.

Example 1: The buckling responses of the present beam model align exceptionally with those computed by Lanc et al. [205] as shown in Tables 7-3 and 7-4. The solutions are computed with the different BCs (simply supported S-S, clamped-clamped C-C, clamped-free C-F) and, power-law indices p and types of FG material distribution. It is noted that while Lanc et al. [205] used the CTWBT, this chapter applies the FTWBT. Therefore, the buckling loads computed by the present model are expected to be lower than those of [205], which is shown in all cases. Nonetheless, the differences are only noticeable in S-S and C-C boundary conditions. This is due to the shear effects being only significant when the length-to-height ratio L/b_3 is low but the current beam's L/b_3 ratio equals 80 which is

relatively high. The buckling responses for the FG box beams with $L/b_3 = 10$ and $L/b_3 = 20$ are included in Tables 7-3 and 7-4 for future investigation of this shear effect.

Table 7-3: Verification the critical buckling loads ($10^6 N$) of the FG thin-walled box beams

BC	Mode	Reference	p					
			0	1	2	5	10	1000
$L/b_3 = 80$								
CF	Y	Present	0.08550	0.05162	0.04000	0.02809	0.02255	0.01583
	Y	Lanc [205]	0.08552	0.05163	0.04001	0.02810	0.02255	0.01583
	X	Present	0.24406	0.14551	0.11232	0.07886	0.06351	0.04516
	X	Lanc [205]	0.24420	0.14559	0.11239	0.07890	0.06355	0.04519
SS	Y	Present	0.34182	0.20637	0.15991	0.11231	0.09014	0.06327
	Y	Lanc [205]	0.34209	0.20654	0.16004	0.11240	0.09022	0.06332
	X	Present	0.97463	0.58105	0.44854	0.31490	0.25363	0.18036
	X	Lanc [205]	0.97683	0.58237	0.44956	0.31562	0.25421	0.18076
CC	Y	Present	1.36407	0.82351	0.63810	0.44815	0.35972	0.25248
	Y	Lanc [205]	1.36903	0.82655	0.64047	0.44982	0.36105	0.25340
	X	Present	3.87270	2.30870	1.78217	1.25117	1.00776	0.71664
	X	Lanc [205]	3.90921	2.33061	1.79912	1.26307	1.01732	0.72340
$L/b_3 = 20$								
CF	Y	Present	1.36407	0.82351	0.63810	0.44815	0.35972	0.25248
	X	Present	3.87270	2.30870	1.78217	1.25117	1.00776	0.71664
SS	Y	Present	5.40583	3.26299	2.52819	1.77558	1.42530	1.00060
	X	Present	15.09092	8.99483	6.94309	4.87435	3.92625	2.79256
CC	Y	Present	20.85207	12.57769	9.74325	6.84270	5.49386	3.85957
	X	Present	54.71422	32.59172	25.15278	17.65808	14.22589	10.12471
$L/b_3 = 10$								
CF	Y	Present	5.40583	3.26299	2.52818	1.77558	1.42530	1.00059
	X	Present	15.09092	8.99483	6.94309	4.87435	3.92625	2.79256
SS	Y	Present	20.85207	12.57770	9.74325	6.84270	5.49386	3.85957
	X	Present	54.71424	32.59172	25.15278	17.65808	14.22590	10.12471
CC	Y	Present	72.99406	43.92641	34.00344	23.87902	19.18438	13.51007
	X	Present	159.24272	94.70104	73.04994	51.28126	41.33262	29.46647

Table 7-4: Verification the critical buckling loads ($10^6 N$) of the FG thin-walled box beams (1-2-1 skin-core-skin ratio)

BC	Mode	Reference	0	1	2	5	10	1000
$L/b_3 = 80$								
CF	Y	Present	0.08550	0.06805	0.06224	0.05642	0.05378	0.05064
	Y	Lanc [205]	0.08552	0.06807	0.06225	0.05643	0.05379	0.05062
	X	Present	0.24406	0.19428	0.17769	0.16109	0.15355	0.14460
	X	Lanc [205]	0.24420	0.19439	0.17779	0.16119	0.15364	0.14458
SS	Y	Present	0.34182	0.27205	0.24880	0.22555	0.21499	0.20246
	Y	Lanc [205]	0.34209	0.27227	0.24900	0.22574	0.21517	0.20248
	X	Present	0.97463	0.77583	0.70957	0.64330	0.61319	0.57744
	X	Lanc [205]	0.97683	0.77758	0.71117	0.64476	0.61457	0.57835
CC	Y	Present	1.36407	1.08565	0.99287	0.90011	0.85795	0.80793
	Y	Lanc [205]	1.36903	1.08959	0.99648	0.90338	0.86107	0.81031
	X	Present	3.87270	3.08276	2.81946	2.55617	2.43650	2.29448
	X	Lanc [205]	3.90921	3.11182	2.84604	2.58027	2.45947	2.31451
$L/b_3 = 20$								
CF	Y	Present	1.36407	1.08565	0.99287	0.90011	0.85795	0.80793
	X	Present	3.87270	3.08276	2.81946	2.55617	2.43650	2.29448
SS	Y	Present	5.40583	4.30245	3.93476	3.56716	3.40010	3.20186
	X	Present	15.09092	12.01275	10.98674	9.96077	9.49444	8.94101
CC	Y	Present	20.85207	16.59609	15.17782	13.75985	13.11544	12.35078
	X	Present	54.71422	43.55403	39.83412	36.11434	34.42360	32.41701
$L/b_3 = 10$								
CF	Y	Present	5.40583	4.30245	3.93476	3.56716	3.40009	3.20186
	X	Present	15.09092	12.01275	10.98674	9.96077	9.49444	8.94100
SS	Y	Present	20.85207	16.59609	15.17782	13.75985	13.11545	12.35078

	X	Present	54.71424	43.55404	39.83414	36.11436	34.42361	32.41705
CC	Y	Present	72.99406	58.09715	53.13269	48.16917	45.91341	43.23662
	X	Present	159.24272	126.76267	115.93624	105.11024	100.18945	94.34946

Example 2: The free vibration of the present thin-walled and thick-walled box beam is examined. Table 7-5 shows excellent agreements between the present solutions with those from Ziane et al. [197] and Abaqus software [197] for all cases of $p = 0.2, p = 1, p = 10$ under various BCs (S-S, C-C, C-F). Even though FTWBT is used in both studies, , the formulation of the stress resultants displayed in Eq. (7-16) of this chapter is different from previous one [197]. The natural frequencies shown in [197] are for the bending modes in X and Y-direction which are equivalent to those in $x_1 -$ and $x_2 -$ directions of this Chapter.

Table 7-5: Verification of vibration analysis (rad / s) of the PMF thin-walled and thick-walled box beams

BC	Reference	p=0.2		p =1		p =10	
		Mode Y	Mode X	Mode Y	Mode X	Mode Y	Mode X
Thin-walled box beam							
CF	Present	324.84	510.28	285.79	446.86	203.40	317.90
	Ziane [197]	324.61	509.80	285.57	446.42	203.24	317.61
	Abaqus [197]	321.65	509.00	283.05	447.19	203.16	319.36
SS	Present	911.37	1430.56	801.81	1252.75	570.65	891.23
	Ziane [197]	909.98	1427.72	800.50	1250.22	569.72	889.43
	Abaqus [197]	913.20	1433.70	805.30	1261.20	574.16	898.29
CC	Present	2060.33	3221.20	1812.57	2820.71	1290.01	2006.70
	Ziane [197]	2044.51	3189.01	1797.73	2791.97	1279.39	1986.23
	Abaqus [197]	1998.40	3180.80	1752.90	2789.90	1256.40	1992.50
Thick-walled box beam							
CF	Present	243.02	477.86	223.50	422.91	160.59	301.28

	Ziane [197]	242.87	476.97	223.32	422.08	160.45	300.68
	Abaqus [197]	254.13	492.69	236.17	448.12	171.46	322.42
SS	Present	681.37	1335.44	626.59	1181.78	450.20	841.90
	Ziane [197]	680.53	1330.39	625.55	1176.97	449.41	838.44
	Abaqus [197]	709.67	1372.60	659.38	1248.00	478.70	897.87
CC	Present	1535.21	2958.56	1410.85	2616.54	1013.56	1863.88
	Ziane [197]	1525.49	2903.00	1398.94	2563.97	1004.50	1826.14
	Abaqus [197]	1584.90	3025.70	1469.40	2744.90	1067.40	1974.80

7.3.3 Parametric study

This section investigates the effects of porosity distribution (type A and B), porosity parameters, boundary conditions and geometryon the buckling and vibration responses of PMF thin-walled box beam. The PMF thin-walled box beams considered are made from porous alumina with the following properties: $E_{\max} = 380GPa$, $\rho_{\max} = 3800kgm^{-3}$, $\nu = 0.3$. Unless stated otherwise, the geometry of the beam in this parametric study section, as displayed in Fig.7-3, is $h = h_1 = h_2 = h_3 = h_4 = 0.005m$, $b_2 = b_4 = 2b_1 = 2b_3 = 0.2\,\mathrm{m}$. The percentage differences of the beams' responses between the porosity distribution type A and type B are computed as $\frac{response_{typeA} - response_{typeB}}{response_{typeA}} \times 100\%$.

Example 3: This example aims to investigate effects of porosity parameters and BCs on buckling and vibration of PMF thin-walled box beams. The length-to-height ratio L/b_3 equals to 10 or 80 for the buckling analysis, and equals to 10 for the vibration analysis. Table 7-6 and Fig.7-4 show the critical buckling loads (*MN*) while Table 7-7 and Fig.7-5 show the natural frequencies (*Hz*) of the PMF beams for various e_0 all three BCs (S-S, C-C, C-F). In Tables 7-6, when $L/\mathrm{b}_3 = 80$, the first buckling mode of the S-S and C-F beams is always x_2-mode but that of C-C beams is torsional mode. When $L/\mathrm{b}_3 = 10$, the buckling loads are much higher than when $L/\mathrm{b}_3 = 80$, but these loads also decreases as the porosity parameter

e_0 rises. Meanwhile, in case $L/\mathrm{b}_3 = 10$, Table 7-7 shows that the first vibration mode is always torsional mode and the torsional frequencies computed are significantly lower than those of bending modes. Considering Fig. 7-4 and 7-5, it can be seen from Eqs. (7-10) and (7-11) that the increasing porosity parameter e_0 leads to the decrement of the Young's modulus and the mass of porous beams. Consequently, as the e_0 increases from 0 to 0.7, the critical buckling loads decreases by up to 44%. However, there is a less drastic drop in natural frequencies since natural frequencies are inversely proportional to the square root of mass. The reduction in the beams' stiffness is offset by the lower beams' mass and therefore, when e_0 increases from 0 to 0.7, the natural frequencies for all bending modes decrease by 11.7%. Interestingly, apart from the torsional mode when the beam is under the C-C boundary condition, there is minimal difference across all values of e_0.

Table 7-6: Buckling loads (*MN*) of PMF thin-walled box beam with various values of porosity parameter e_0

BC	Mode	e_0						
		0.1	0.2	0.3	0.4	0.5	0.6	0.7
Type A, $L/b_3 = 80$								
S-S	x_2	0.3201	0.2983	0.2766	0.2548	0.2330	0.2113	0.1895
	x_1	0.9126	0.8505	0.7885	0.7265	0.6644	0.6024	0.5403
C-C	Min	0.5743	0.5512	0.5280	0.5048	0.4817	0.4585	0.4353
	x_2	1.3641	1.2773	1.1904	1.1036	1.0168	0.9300	0.8432
	x_1	3.8727	3.6262	3.3796	3.1331	2.8866	2.6400	2.3935
C-F	x_2	0.0855	0.0801	0.0746	0.0692	0.0637	0.0583	0.0529
	x_1	0.2441	0.2285	0.2130	0.1975	0.1819	0.1664	0.1508
Type B, $L/b_3 = 80$								
S-S	x_2	0.3206	0.2993	0.2781	0.2568	0.2356	0.2143	0.1931
	X	0.9131	0.8516	0.7900	0.7285	0.6669	0.6054	0.5439
C-C	Min	0.5405	0.5066	0.4728	0.4389	0.4051	0.3712	0.3373
	x_2	1.2793	1.1945	1.1096	1.0248	0.9400	0.8552	0.7704
	x_1	3.6282	3.3836	3.1391	2.8945	2.6500	2.4055	2.1609
C-F	x_2	0.0802	0.0749	0.0696	0.0642	0.0589	0.0536	0.0483
	x_1	0.2287	0.2132	0.1978	0.1824	0.1670	0.1516	0.1362
Type A, $L/b_3 = 10$								
SS	Min	1.7772	1.6709	1.5646	1.4583	1.3520	1.2457	1.1394
	x_2	19.5250	18.1979	16.8708	15.5437	14.2166	12.8895	11.5624
	x_1	51.2312	47.7481	44.2651	40.7820	37.2990	33.8159	30.3329
CC	Min	5.7006	5.3282	4.9559	4.5835	4.2111	3.8387	3.4664
	x_2	68.3483	63.7026	59.0568	54.4111	49.7653	45.1195	40.4738
	x_1	149.1054	138.9680	128.8307	118.6933	108.5559	98.4186	88.2812
CF	Min	0.7964	0.7566	0.7168	0.6770	0.6372	0.5974	0.5576
	x_2	5.0618	4.7177	4.3737	4.0297	3.6856	3.3416	2.9975
	x_1	14.1302	13.1696	12.2089	11.2482	10.2876	9.3269	8.3662

Table 7-7: Natural frequencies (*Hz*) of PMF box beam with various values of porosity parameter e_0 ($L/b_3 = 10$)

BC	Mode	e_0							
		0.0	0.1	0.2	0.3	0.4	0.5	0.6	0.7
Type A									
SS	Min	203.11	200.60	198.08	195.57	193.11	190.78	188.72	187.20
	x_2	670.41	659.59	648.46	637.05	625.43	613.72	602.23	591.60
	x_1	1072.96	1055.63	1037.81	1019.54	1000.93	982.18	963.77	946.73
CC	Min	412.80	406.62	400.31	393.89	387.42	381.00	374.85	369.41
	x_2	1398.49	1375.91	1352.70	1328.90	1304.65	1280.23	1256.25	1234.06
	x_1	2014.93	1982.39	1948.93	1914.62	1879.66	1844.45	1809.88	1777.88
CF	Min	92.39	91.58	90.79	90.04	89.36	88.78	88.40	88.34
	x_2	242.98	239.05	235.02	230.89	226.67	222.43	218.27	214.41
	x_1	399.37	392.92	386.29	379.49	372.56	365.58	358.73	352.39
Type B									
BC	Mode	e_0							
		0.0	0.1	0.2	0.3	0.4	0.5	0.6	0.7
SS	Min	203.11	199.95	196.70	193.38	190.02	186.65	183.37	180.38
	x_2	670.41	660.08	649.49	638.69	627.76	616.85	606.29	596.77
	x_1	1072.96	1055.88	1038.34	1020.39	1002.13	983.80	965.87	949.41
CC	Min	412.80	406.14	399.31	392.29	385.15	377.95	370.87	364.30
	x_2	1398.49	1376.78	1354.53	1331.81	1308.78	1285.76	1263.43	1243.21
	x_1	2014.93	1982.72	1949.62	1915.71	1881.21	1846.54	1812.59	1781.34
CF	Min	92.39	91.02	89.62	88.19	86.75	85.33	83.96	82.75
	x_2	242.98	239.24	235.41	231.50	227.54	223.60	219.78	216.35
	x_1	399.37	393.02	386.50	379.83	373.04	366.23	359.57	353.46

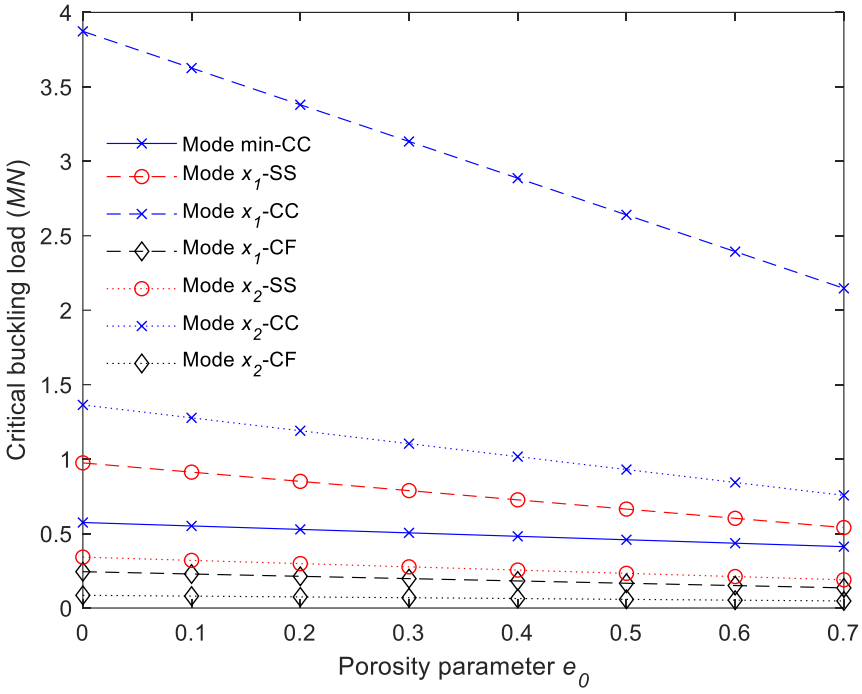

a) Buckling loads (MN) of type A

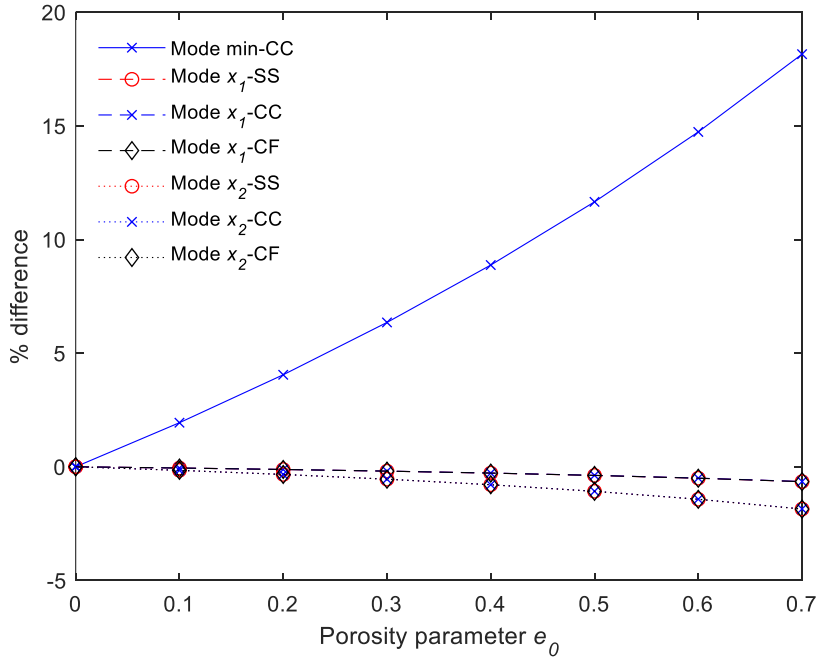

b) Percentage difference of buckling loads between types A and B

Figure 7-4: Buckling loads (MN) of PMF thin-walled box beams with respect to various values of porosity parameter e_0

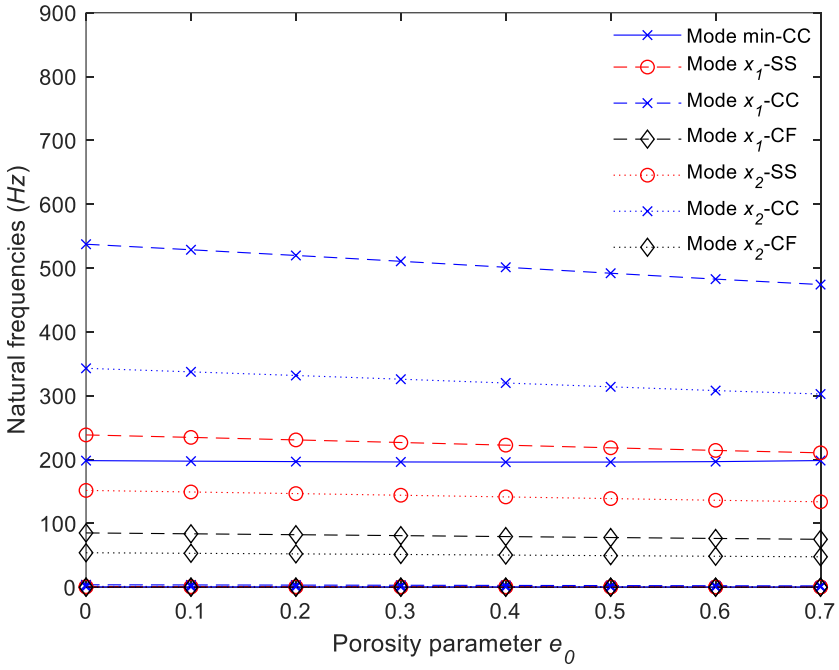

Figure 7-3: Natural frequencies of the type A PMF thin-walled box beams with respect to various values of porosity parameter

Example 4: The objective of this example is to consider the effect of length-to-height ratio L/b_3 on buckling and free vibration of PMF thin-walled box beams. The PMF thin-walled box beams with the aforementioned dimensions and $e_0 = 0.5$ is examined in this example. The beam's height is kept constant with $b_3 = 0.5b_2 = 0.1m$ and the wall thickness is $h = h_1 = h_2 = h_3 = h_4 = 0.005m$. While keeping the beam's height b_3 intact for both the buckling and vibration analysis, the length is varied for multiple L/b_3 ratios ranging from $L/b_3 = 10$ to $L/b_3 = 50$. Tables 7-8 and 7-9 show the critical buckling loads (*MN*) and the natural frequencies (*Hz*) of the studied PMF thin-walled beams. It is apparent that the short beams are much stiffer than the long ones which can be seen from both Tables, Figs. 7-6 and 7-7. The critical buckling loads and natural frequencies are subjected to exponential decay where the decay constant increases in the order of C-F<S-S<C-F boundary conditions. Comparing the porosity distribution types A and B, there is minimal difference of the critical

buckling loads and fundamental frequencies across all values of L/b_3. When $L/\mathrm{b}_3 > 35$, the critical buckling loads of the cantilevered type A and type B PMF box beams are identical. Moreover, Figs. 7-8 and 7-9 display the buckling and free vibration mode shapes of the type-A PMF box beams. The ascending order of the beams' responses are with reference to the torsional, and modes respectively. In Fig. 7-8 where the beam is under S-S boundary condition, the shapes of the beam's highest displacement variable is a half wave. Nonetheless, for cantilevered beams in Fig. 7-9 these shapes are a quarter wave.

Table 7-8: Buckling loads (*MN*) of PMF thin-walled box beams with various values of L/b_3 ($e_0 = 0.5$)

BC	Mode	L/b_3						
		10	20	30	40	50	60	70
Type A								
S-S	Min	1.35198	0.63720	0.50483	0.45851	0.43706	0.41405	0.30431
	x_2	14.21660	3.68563	1.64936	0.93001	0.59587	0.41405	0.30431
	x_1	37.29898	10.28758	4.66139	2.64005	1.69502	1.17914	0.86721
C-C	Min	4.21110	1.35198	0.82252	0.63720	0.55143	0.50483	0.47674
	x_2	49.76530	14.21660	6.48998	3.68563	2.36932	1.64935	1.21355
	x_1	108.55587	37.29896	17.81220	10.28758	6.66666	4.66139	3.43892
C-F	Min	0.63720	0.45851	0.41405	0.23305	0.14919	0.10362	0.07614
	x_2	3.68563	0.93001	0.41405	0.23305	0.14919	0.10362	0.07614
	x_1	10.28758	2.64005	1.17914	0.66441	0.42556	0.29566	0.21728
Type B								
S-S	Min	1.29757	0.58356	0.45134	0.40506	0.38364	0.37201	0.30760
	x_2	14.36292	3.72498	1.66709	0.94003	0.60230	0.41852	0.30760
	x_1	37.42319	10.32539	4.67886	2.65001	1.70144	1.18361	0.87051
C-C	Min	4.15358	1.29757	0.76868	0.58356	0.49788	0.45134	0.42328
	x_2	50.21296	14.36292	6.55861	3.72498	2.39473	1.66709	1.22661
	x_1	108.81873	37.42322	17.87596	10.32539	6.69147	4.67886	3.45186
C-F	Min	0.58356	0.40506	0.37201	0.23556	0.15080	0.10474	0.07696
	x_2	3.72498	0.94003	0.41852	0.23556	0.15080	0.10474	0.07696
	x_1	10.32539	2.65001	1.18361	0.66694	0.42718	0.29678	0.21810

Table 7-9: Natural frequencies (*Hz*) of PMF thin-walled box beams with various values of

L / b_3 ($e_0 = 0.5$)Tub

BC	Mode	L / b_3						
		10	15	20	25	30	35	40
Type A								
SS	Min	190.78	99.24	65.52	48.76	38.88	32.39	27.79
	x_2	613.72	277.71	157.23	100.94	70.21	51.64	39.56
	x_1	982.18	457.05	261.64	168.86	117.81	86.80	66.58
CC	Min	381.00	178.83	107.55	74.11	55.59	44.12	36.44
	x_2	1280.23	604.67	348.17	225.35	157.47	116.13	89.14
	x_1	1844.45	936.03	557.45	367.28	259.33	192.50	148.39
CF	Min	88.78	50.48	34.68	26.21	20.99	17.47	14.11
	x_2	222.43	99.72	56.27	36.06	25.06	18.42	14.11
	x_1	365.58	166.35	94.38	60.65	42.21	31.05	23.80
Type B								
SS	Min	186.65	95.80	62.61	46.27	36.71	30.48	26.09
	x_2	616.85	279.17	158.07	101.47	70.59	51.91	39.77
	x_1	983.80	457.86	262.11	169.17	118.03	86.96	66.71
CC	Min	377.95	176.29	105.29	72.08	53.74	42.43	34.89
	x_2	1285.76	607.60	349.94	226.52	158.30	116.75	89.61
	x_1	1846.54	937.39	558.35	367.91	259.78	182.06	148.66
CF	Min	85.33	48.09	32.89	24.78	19.80	16.45	14.06
	x_2	223.60	100.25	56.57	36.26	25.20	18.52	14.19
	x_1	366.23	166.66	94.56	60.76	42.29	31.11	23.84

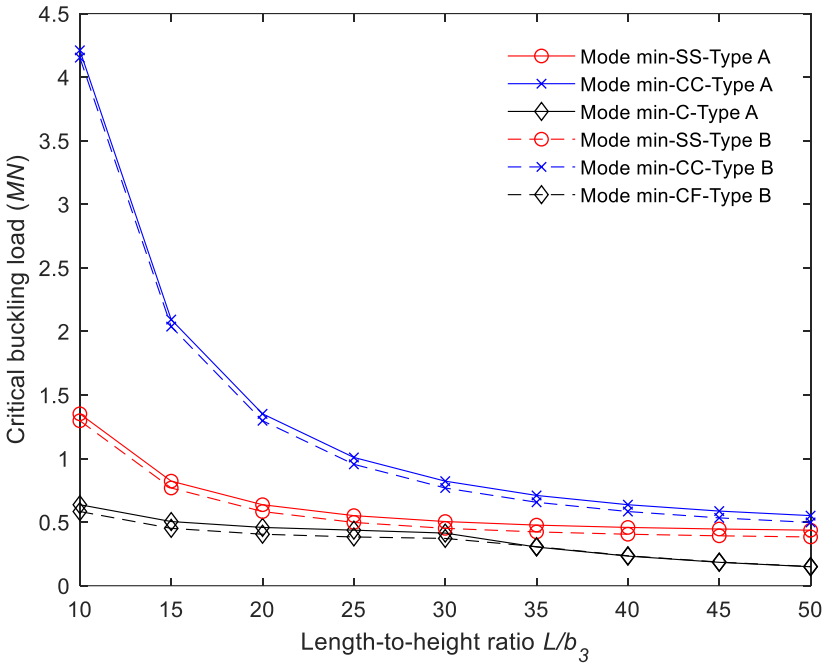

Figure 7-6: Critical buckling loads (*MN*) of FGP type A and B box beams with various values of L/b_3

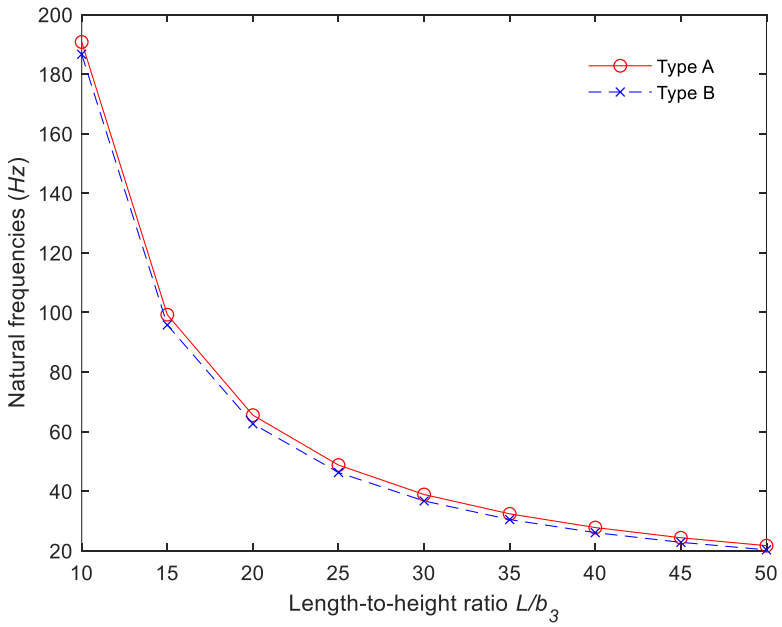

Figure 7-5: Natural frequencies of PMF thin-walled box beams with respect to L/b_3 ($e_0 = 0.5$, S-S boundary condition)

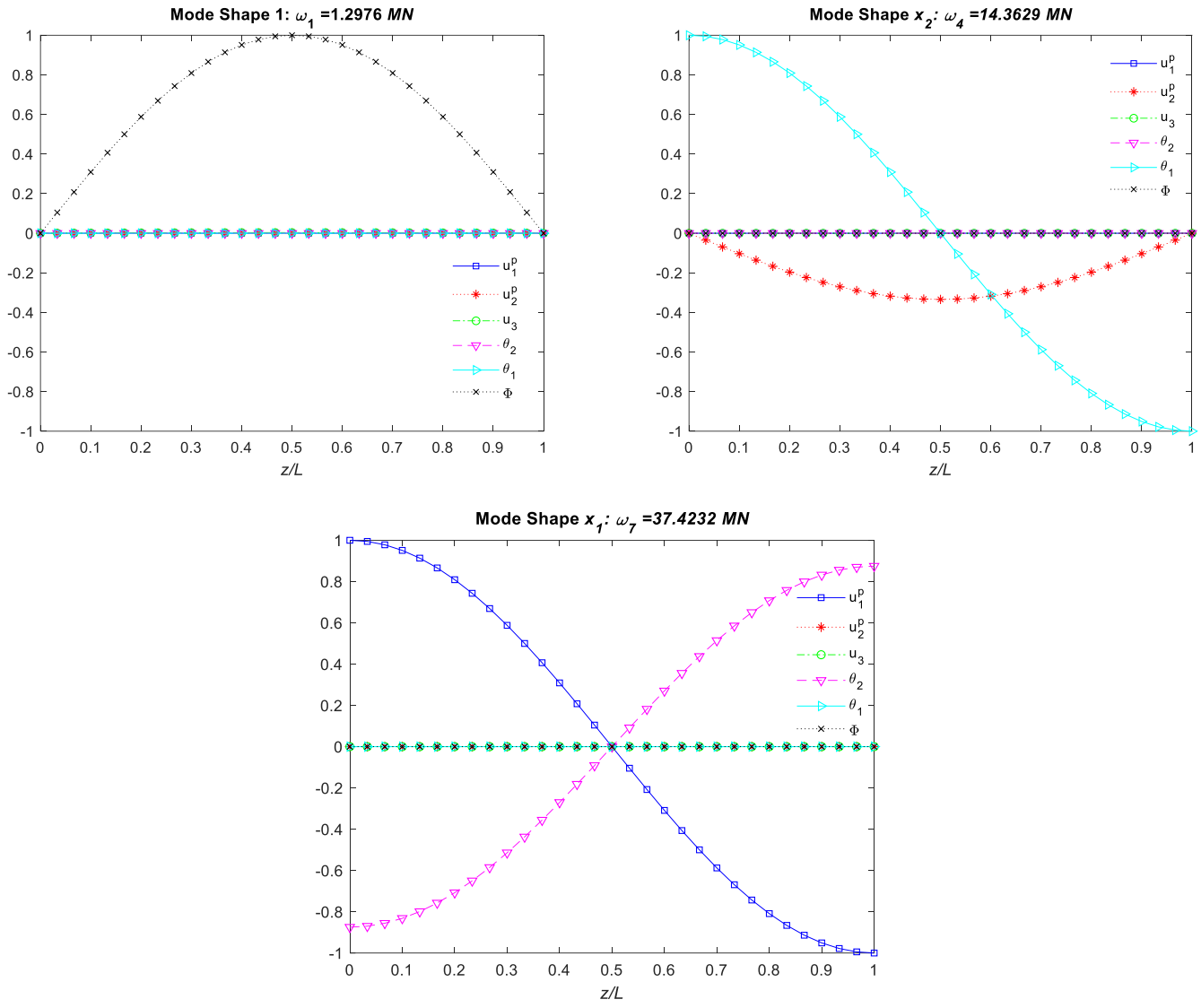

Figure 7-7: Buckling mode shapes of type-B PMF thin-walled box beams with $e_0 = 0.5$, S-S boundary condition and $L/b_3 = 10$

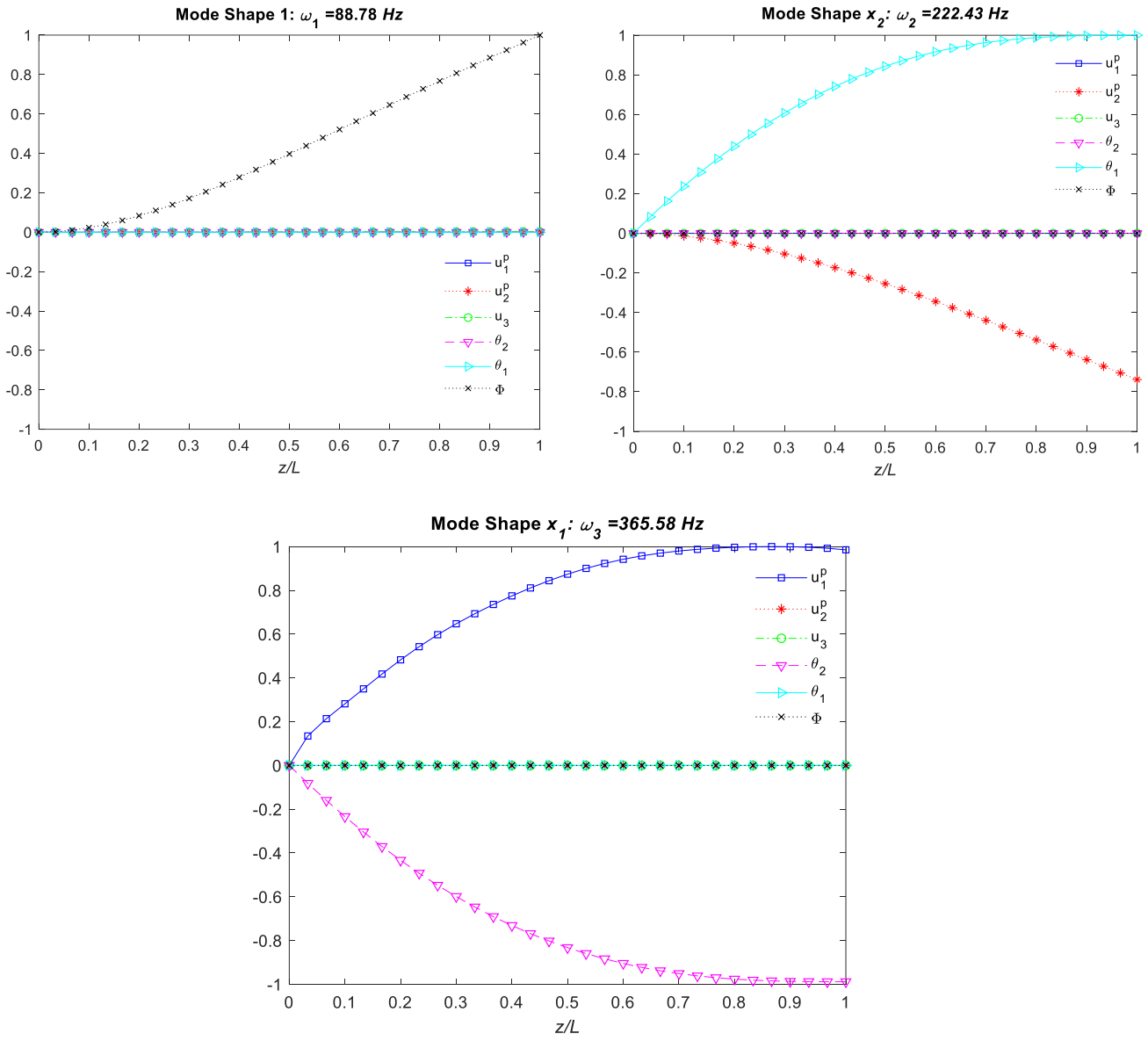

Figure 7-8: Free vibration mode shapes of type-A PMF thin-walled box beams with $e_0 = 0.5$, C-F boundary condition and $L/b_3 = 10$

Example 5: This example is to examine the effect of height-to-thickness ratio on buckling and vibration responses of PMF thin-walled box beams. In this example, the PMF thin-walled box beams with $e_0 = 0.5$, are considered. The thickness of the beam walls is fixed at $h = h_1 = h_2 = h_3 = h_4 = 0.005m$ for both the buckling analysis and for the vibration analysis. Tables 7-10, 7-11 and Figs. 7-10, 7-11 demonstrate the variation of the critical buckling loads and natural frequencies as the beams' height b_3 increase by the factor of $b_3 / h = 5$ to 50. The buckling loads in bending mode x_1 and x_2 become larger as the b_3 / h ratio increase in all boundary condition cases. However, the lowest critical buckling loads dip slightly from $b_3 / h = 5$ to 25 before rising slowly up until $b_3 / h = 50$ in the S-S and C-C boundary condition cases. This trend is opposite to that of the C-F case where the lowest critical buckling loads increase from $b_3 / h = 5$ to 15 but gradually drop afterwards. On the other hand, the natural frequencies experience an exponential decay as the height-to-thickness ratio rises. Comparing the responses of beams with type A and type B porosity distributions, Fig. 7-11b shows little discrepancy when the beams are in mode x_1 and x_2. The differences are only significant in the cases of the lowest mode. Under the C-C boundary condition, the beam's lowest mode is torsional mode for all b_3 / h ratios and the highest percentage difference is 6%. The sudden change of the "mode min" plots for SS and CF boundary condition at $b_3 / h = 10$ and $b_3 / h = 15$ respectively are due to the fact that at these thresholds, the type-A PMF beams' lowest mode transitions from x_2-bending mode to torsion mode, while the type-B PMF beams' lowest mode remains torsional.

Table 7-10: Buckling loads (*MN*) of PMF thin-walled box beams with various values of b_3 / h ($L / \mathrm{b}_3 = 20$, $e_0 = 0.5$)

BC	Mode	b_3 / h							
		5	10	15	20	25	30	35	40
Type A									
S-S	Min	0.9331	0.9186	0.7114	0.6372	0.6163	0.6221	0.6432	0.6737
	x_2	0.9331	1.8475	2.7660	3.6856	4.6056	5.5258	6.4462	7.3666
	x_1	2.5775	5.1460	7.7166	10.2876	12.8588	15.4301	18.0015	20.5729
C-C	Min	1.8503	1.2829	1.2502	1.3520	1.5077	1.6905	1.8886	2.0964
	x_2	3.5977	7.1257	10.6692	14.2166	17.7655	21.3152	24.8654	28.4158
	x_1	9.3431	18.6568	27.9771	37.2990	46.6215	55.9444	65.2674	74.5906
C-F	Min	0.2355	0.4662	0.5767	0.4585	0.3935	0.3550	0.3318	0.3181
	x_2	0.2355	0.4662	0.6980	0.9300	1.1622	1.3943	1.6266	1.8588
	x_1	0.6615	1.3206	1.9803	2.6400	3.2999	3.9597	4.6196	5.2795
Type B									
S-S	Min	0.9712	0.8115	0.6399	0.5836	0.5734	0.5863	0.6125	0.6469
	x_2	0.9712	1.8864	2.8053	3.7250	4.6451	5.5653	6.4857	7.4061
	x_1	2.6147	5.1836	7.7543	10.3254	12.8967	15.4680	18.0394	20.6108
C-C	Min	1.6336	1.1742	1.1776	1.2976	1.4642	1.6542	1.8575	2.0692
	x_2	3.7389	7.2704	10.8150	14.3629	17.9122	21.4621	25.0124	28.5629
	x_1	9.4651	18.7803	28.1011	37.4232	46.7459	56.0688	65.3919	74.7151
C-F	Min	0.2452	0.4761	0.5055	0.4051	0.3507	0.3194	0.3013	0.2913
	x_2	0.2452	0.4761	0.7080	0.9400	1.1722	1.4044	1.6366	1.8689
	x_1	0.6713	1.3305	1.9902	2.6500	3.3099	3.9697	4.6296	5.2895

Table 7-11: Natural frequencies (*Hz*) of PMF thin-walled box beams with various values of b_3 / h ($L / b_3 = 20$, $e_0 = 0.5$)

BC	Mode	b_3 / h							
		5	10	15	20	25	30	35	40
Type A									
SS	Min	632.89	222.50	106.58	65.52	46.11	35.24	28.43	23.82
	x_2	632.89	314.86	209.71	157.23	125.77	104.80	89.82	78.59
	x_1	1047.67	523.38	348.87	261.64	209.30	174.42	149.50	130.81
CC	Min	969.31	292.53	158.61	107.55	81.43	65.66	55.11	47.55
	x_2	1401.05	697.18	464.37	348.17	278.50	232.06	198.90	174.03
	x_1	2231.92	1115.11	743.30	557.45	445.95	371.62	318.53	278.71
CF	Min	226.50	112.68	57.41	34.68	23.71	17.53	13.67	11.09
	x_2	226.50	112.68	75.05	56.27	45.01	37.50	32.14	28.12
	x_1	377.94	188.80	125.85	94.38	75.50	62.92	53.93	47.19
Type B									
SS	Min	645.64	208.55	100.90	62.61	44.42	34.18	27.73	23.32
	x_2	645.64	318.15	211.19	158.07	126.30	105.17	90.10	78.80
	x_1	1055.15	525.28	349.71	262.11	209.61	174.63	149.66	130.93
CC	Min	908.45	279.63	153.83	105.29	80.19	64.92	54.63	47.22
	x_2	1427.96	704.13	467.49	349.94	279.63	232.85	199.48	174.48
	x_1	2246.02	1118.69	744.90	558.35	446.53	372.02	318.82	278.94
CF	Min	231.10	112.43	54.21	32.89	22.57	16.74	13.10	10.67
	x_2	231.10	113.87	75.58	56.57	45.20	37.64	32.24	28.20
	x_1	380.70	189.50	126.16	94.56	75.62	63.00	53.99	47.23

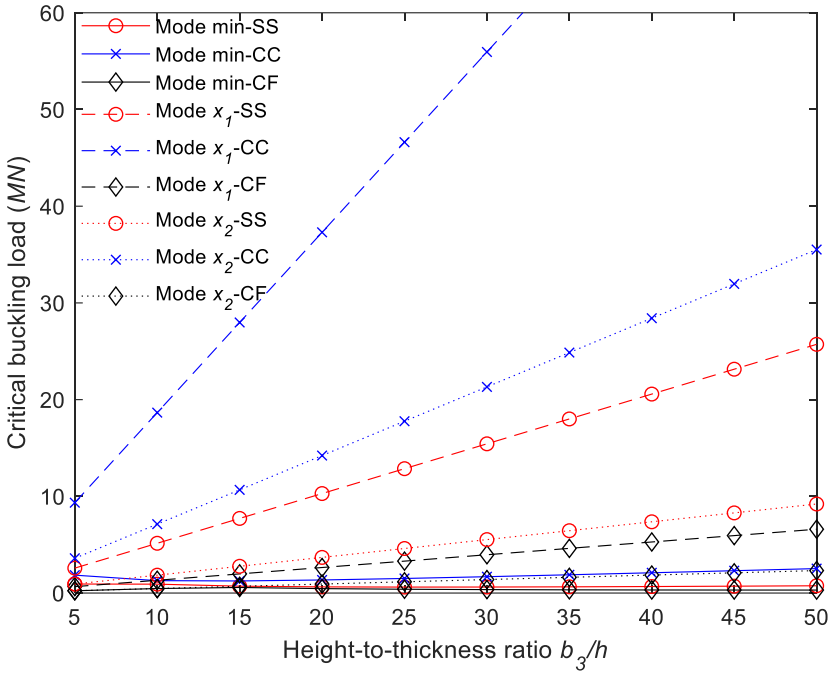

Figure 7-9: Buckling loads (*MN*) of type-A PMF thin-walled box beams with respect to various values of b_3 / h

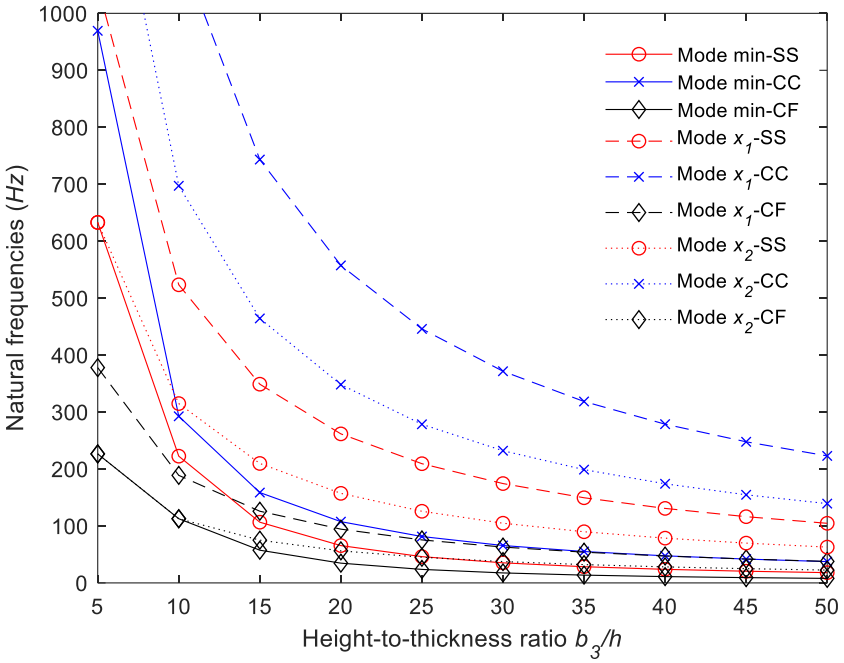

a) Natural frequencies (Hz) of type A

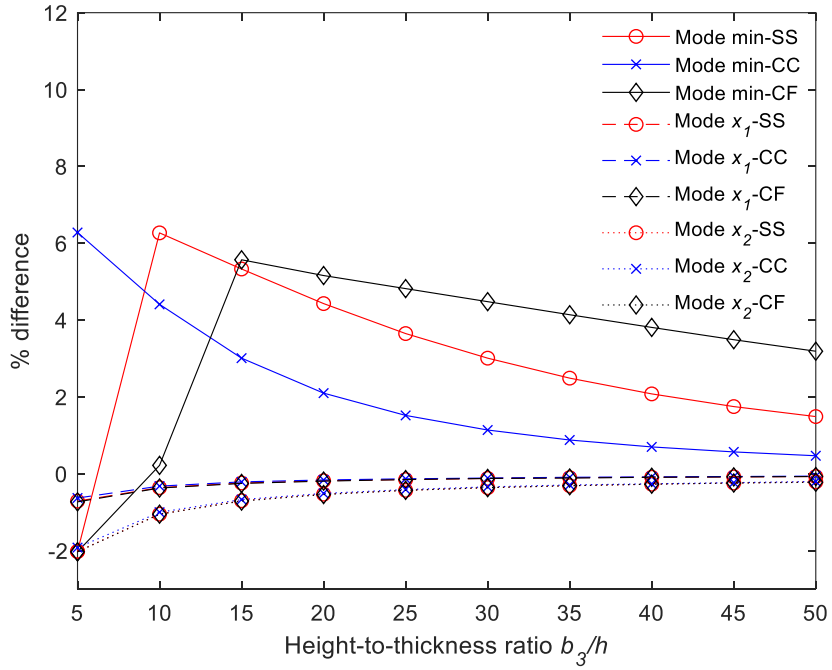

b) Percentage difference of natural frequencies between types A and B

Figure 7-10: Natural frequencies (*Hz*) of PMF thin-walled box beams with respect to various values of b_3 / h

7.4. Conclusion

The first-order-shear-deformable thin-walled beam model for the buckling and vibration analysis of porous metal foam thin-walled box beam is proposed in this Chapter. The Hamilton's principles and hybrid series solution have been used to solve for the beams' responses. Both the symmetric (Type A) and nonsymmetric (Type B) porosity distributions are examined. In additions, the beams are studied by varying the following parameters: boundary conditions, porosity parameter, length-to-height ratio, height-to-thickness ratio and width-to-height ratio. From the analysis, the ensuing conclusions are drawn:

- The increasing porosity parameter e_0 reduces both the critical buckling loads and natural frequencies of the porous beams but the effects are more significant in the buckling responses. The difference between type A and type B porous beams with respect to e_0 is only noticeable in the lowest mode in C-C boundary condition.
- The increasing length-to-height ratio L/b_3 drastically reduce the critical buckling loads and natural frequencies especially when the L/b_3 goes from 10 to 30. At certain values of , the lowest mode of the PMF box beam changes from the torsional mode to the bending mode under S-S and C-F boundary conditions
- The increasing height-to-thickness ratio b_3/h raises the critical buckling loads in bending mode significantly but does not quite affect the lowest mode .
- The increasing height-to-thickness ratio b_3/h lowers the natural frequencies of all modes in the way of a negative exponential relationship.

CHAPTER 8 : CONCLUSION AND FUTURE DIRECTIONS

8.1. Conclusion

In conclusion, this thesis has delved into the comprehensive study of thin-walled beams, emphasizing their widespread applications in diverse engineering domains such as civil, aerospace, and automobile engineering due to their notable advantages in load-carrying capacity and lightweight properties. The investigation primarily focused on understanding the structural responses of thin-walled beams with different cross-section shapes, addressing the static, buckling and dynamic responses to mechanical and thermal loads. This thesis has made several novel contributions to the field of thin-walled composite beam analysis, advancing both theoretical modeling and computational methodologies. The research objectives outlined in the first chapter have been systematically addressed, leading to significant advancements in the computational modeling and analysis of composite thin-walled beams.

For static analysis, it developed a robust framework for accurately predicting beam deflection and buckling stability under varied thermal and mechanical loading conditions. The vibration analysis extended this understanding by investigating fundamental frequencies and mode shapes, with a particular focus on torsional modes in open-section beams. Building on classical models such as Vlasov's theory and first-order shear deformable thin-walled beam theory, the thesis introduced a general higher-order shear deformable thin-walled beam theory. This new model demonstrates superior predictive capability, especially for thin-walled beams with low length-to-depth ratios, addressing limitations in existing theories. A robust MATLAB-based computational framework was successfully developed and validated, demonstrating the effectiveness of higher-order shear deformation theory in capturing the complex mechanical behavior of thin-walled beam structures. The influence of material heterogeneity was also thoroughly investigated, revealing its critical role in structural performance.

A significant contribution of this work lies in its stochastic analysis framework, which incorporates material property randomness to account for real-world uncertainties. The

integration of probabilistic methods provided a comprehensive approach to quantifying uncertainties in material properties, geometric imperfections, and loading conditions. The development of a novel beam solver, utilizing hybrid series-type approximation functions combined with Polynomial Chaos Expansion (PCE) and Artificial Neural Networks (ANNs), represents a major innovation. The solver achieves highly efficient evaluations of stochastic responses, requiring only 256 training samples to produce accurate results comparable to Monte Carlo simulations with over 10^6 samples. This efficiency underscores its practical utility, offering a computationally viable alternative for uncertainty quantification in thin-walled composite beams.

Furthermore, the thesis also carried out the size-dependent effects analysis, replacing classical continuum mechanics with the modified couple stress theory. The study of size-dependent effects in micro-beams contributed valuable insights into scale-dependent behavior, enhancing the understanding of microscale structural applications. Numerical results elucidated the influences of material distribution, span-to-height ratio, and material length scale parameters on the bending and vibration behaviors of microbeams under various boundary conditions. The micro-beam exhibits much stiffer behaviours compared to its macro- counterpart. In addition, the thermal buckling analysis offered a deeper perspective on the stability of composite thin-walled beams under various thermal loading scenarios

All theoretical and numerical models developed in this research were rigorously validated against analytical, numerical, and experimental benchmarks, ensuring their reliability and computational efficiency. This thesis not only enhances the theoretical foundation for thin-walled beam modeling but also establishes benchmark results and computational tools for future research. By emphasizing accuracy, efficiency, and practical applicability, the findings have broad implications for the scientific and engineering communities, setting a new standard for the analysis and design of thin-walled composite structures.

8.2. Future directions

The thesis plans the following directions for the future researches:

- The thermal and hygro analysis of closed-section thin-walled beams with arbitary cross section shapes
- The incorporation of isogeometric method to replace the Ritz solution in this thesis
- The effects of geometrical nonlinearity on thin-walled beams
- The effects of other loading conditions (moving loads, impact loads) on thin-walled beams
- The Karhunen-Loeve expansion for the stochastic analysis of thin-walled beams
- Artificial neural network's hyperparameter optimisation

APPENDIX

Third-order multivariate Hermite basis function Ω_i for the Polynomial chaos expansion (PCE) in case the size of the input vector $\mathbf{q}$ is 6 (contains 6 random input variables)

Index i	Ω_i	Index i	Ω_i	Index i	Ω_i
1	1	29	$q_1^3 - 3q_1$	57	$q_2 q_3 q_5$
2	q_1	30	$q_2(q_1^2 - 1)$	58	$q_2 q_3 q_6$
3	q_2	31	$q_3(q_1^2 - 1)$	59	$q_2(q_4^2 - 1)$
4	q_3	32	$q_4(q_1^2 - 1)$	60	$q_2 q_4 q_5$
5	q_4	33	$q_5(q_1^2 - 1)$	61	$q_2 q_4 q_6$
6	q_5	34	$q_6(q_1^2 - 1)$	62	$q_2(q_5^2 - 1)$
7	q_6	35	$q_1(q_2^2 - 1)$	63	$q_2 q_5 q_6$
8	$q_1^2 - 1$	36	$q_1 q_2 q_3$	64	$q_2(q_6^2 - 1)$
9	$q_1 q_2$	37	$q_1 q_2 q_4$	65	$q_3^3 - 3q_3$
10	$q_1 q_3$	38	$q_1 q_2 q_5$	66	$q_4(q_3^2 - 1)$
11	$q_1 q_4$	39	$q_1 q_2 q_6$	67	$q_5(q_3^2 - 1)$
12	$q_1 q_5$	40	$q_1(q_3^2 - 1)$	68	$q_6(q_3^2 - 1)$
13	$q_1 q_6$	41	$q_1 q_3 q_4$	69	$q_3(q_4^2 - 1)$
14	$q_2^2 - 1$	42	$q_1 q_3 q_5$	70	$q_3 q_4 q_5$
15	$q_2 q_3$	43	$q_1 q_3 q_6$	71	$q_3 q_4 q_6$
16	$q_2 q_4$	44	$q_1(q_4^2 - 1)$	72	$q_3(q_5^2 - 1)$
17	$q_2 q_5$	45	$q_1 q_4 q_5$	73	$q_3 q_5 q_6$
18	$q_2 q_6$	46	$q_1 q_4 q_6$	74	$q_3(q_6^2 - 1)$
19	$q_3^2 - 1$	47	$q_1(q_5^2 - 1)$	75	$q_4^3 - 3q_4$

20	q_3q_4	48	$q_1q_5q_6$	76	$q_5(q_4^{\,2}-1)$
21	q_3q_5	49	$q_1(q_6^{\,2}-1)$	77	$q_6(q_4^{\,2}-1)$
22	q_3q_6	50	$q_2^{\,3}-3q_2$	78	$q_4(q_5^{\,2}-1)$
23	$q_4^{\,2}-1$	51	$q_3(q_2^{\,2}-1)$	79	$q_4q_5q_6$
24	q_4q_5	52	$q_4(q_2^{\,2}-1)$	80	$q_4(q_6^{\,2}-1)$
25	q_4q_6	53	$q_5(q_2^{\,2}-1)$	81	$q_5^{\,3}-3q_5$
26	$q_5^{\,2}-1$	54	$q_6(q_2^{\,2}-1)$	82	$q_6(q_5^{\,2}-1)$
27	q_5q_6	55	$q_2(q_3^{\,2}-1)$	83	$q_5(q_6^{\,2}-1)$
28	$q_6^{\,2}-1$	56	$q_2q_3q_4$	84	$q_6^{\,3}-3q_6$

REFERENCES

1. MathWorks, *MATLAB Neural Network Training (nntraintool)*. 2020
2. Choi, Y.Y.K.G.-W.J.S., *Analysis of Thin-Walled Beams*. Solid Mechanics and Its Applications. 2023: Springer Singapore.
3. Jansons, V. Kulakov, A. Aniskevich, and Lagzdiņš, *Structural Composites − From Aerospace To Civil Engineering Applications.* Innovations and Technologies News, 2012. **17**: p. 3-12
4. Mohammadi, M., M. Rajabi, and M. Ghadiri, *Functionally graded materials (FGMs): A review of classifications, fabrication methods and their applications.* Processing and Application of Ceramics, 2021. **15**: p. 319-343.10.2298/PAC2104319M
5. Young, R.J. and M. Liu, *The microstructure of a graphene-reinforced tennis racquet.* Journal of Materials Science, 2016. **51**(8): p. 3861-3867.10.1007/s10853-015-9705-6
6. Bui, X.B., P.H. Ngo, and T.K. Nguyen, *A unified third-order shear deformation theory for static analysis of laminated composite beams.* Journal of Technical Education Science, 2019(55): p. 87-93
7. Bui, X.B., T.K. Nguyen, Q.C. Le, and T.T.P. Nguyen. *A novel two-variable model for bending analysis of laminated composite beams*. in *2020 5th International Conference on Green Technology and Sustainable Development (GTSD)*. 2020.
8. Bui, X.-B., A.-C. Nguyen, N.-D. Nguyen, T.-T. Do, and T.-K. Nguyen, *Buckling analysis of laminated composite thin-walled I-beam under mechanical and thermal loads.* Vietnam Journal of Mechanics, 2023. **45**(1): p. 75-90.https://doi.org/10.15625/0866-7136/17956
9. Bui, X.-B., T.-K. Nguyen, T.T.-P. Nguyen, and V.-T. Nguyen. *Stochastic Vibration Responses of Laminated Composite Beams Based on a Quasi-3D Theory*. in *ICSCEA 2021*. 2023. Singapore: Springer Nature Singapore.
10. Bui, X.-B., T.-K. Nguyen, N.-D. Nguyen, and T.P. Vo, *A general higher-order shear deformation theory for buckling and free vibration analysis of laminated*

thin-walled composite I-beams. Composite Structures, 2022. **295**: p. 115775.https://doi.org/10.1016/j.compstruct.2022.115775

11. Bui, X.-B., T.-K. Nguyen, and P.T.T. Nguyen, *Stochastic vibration and buckling analysis of functionally graded sandwich thin-walled beams.* Mechanics Based Design of Structures and Machines, 2023: p. 1-23.https://doi.org/10.1080/15397734.2023.2165101
12. Bui, X.-B., T.-K. Nguyen, A. Karamanli, and T.P. Vo, *Size-dependent behaviours of functionally graded sandwich thin-walled beams based on the modified couple stress theory.* Aerospace Science and Technology, 2023. **142**: p. 108664.https://doi.org/10.1016/j.ast.2023.108664
13. Bui, X.-B., P.T.T. Nguyen, and T.-K. Nguyen, *Spectral projection and linear regression approaches for stochastic flexural and vibration analysis of laminated composite beams.* Archive of Applied Mechanics, 2024.https://doi.org/10.1007/s00419-024-02565-x
14. Carrera, E., G. Giunta, and M. Petrolo, *Beam structures: classical and advanced theories*. 2011, Chichester, United Kingdom: John Wiley and Sons.
15. Timoshenko, S., *Theory of Elasticity*. 1934: McGraw-Hill.
16. Franza, A., S. Acikgoz, and M.J. DeJong, *Timoshenko beam models for the coupled analysis of building response to tunnelling.* Tunnelling and Underground Space Technology, 2020. **96**: p. 103160.https://doi.org/10.1016/j.tust.2019.103160
17. Guiyun, X.I.A. and Z. Qingyuan, *TIMOSHENKO BEAM THEORY AND ITS APPLICATIONS.* MECHANICS IN ENGINEERING, 2015. **37**(3): p. 302-316.10.6052/1000-0879-14-080
18. Wang, C.M., S. Kitipornchai, C.W. Lim, and M. Eisenberger, *Beam Bending Solutions Based on Nonlocal Timoshenko Beam Theory*. Journal of Engineering Mechanics, 2008. **134**(6): p. 475-481.10.1061/(ASCE)0733-9399(2008)134:6(475)
19. Kadoli, R., K. Akhtar, and N. Ganesan, *Static analysis of functionally graded beams using higher order shear deformation theory.* Applied Mathematical Modelling, 2008. **32**(12): p. 2509-2525.https://doi.org/10.1016/j.apm.2007.09.015

20. Ferreira, A.J.M., C.M.C. Roque, and P.A.L.S. Martins, *Radial basis functions and higher-order shear deformation theories in the analysis of laminated composite beams and plates.* Composite Structures, 2004. **66**(1): p. 287-293.https://doi.org/10.1016/j.compstruct.2004.04.050
21. Subramanian, P., *Dynamic analysis of laminated composite beams using higher order theories and finite elements.* Composite Structures, 2006. **73**(3): p. 342-353.https://doi.org/10.1016/j.compstruct.2005.02.002
22. Shao, D., S. Hu, Q. Wang, and F. Pang, *Free vibration of refined higher-order shear deformation composite laminated beams with general boundary conditions.* Composites Part B: Engineering, 2017. **108**: p. 75-90
23. Vo, T.P., H.-T. Thai, T.-K. Nguyen, F. Inam, and J. Lee, *A quasi-3D theory for vibration and buckling of functionally graded sandwich beams.* Composite Structures, 2015. **119**: p. 1-12.https://doi.org/10.1016/j.compstruct.2014.08.006
24. Nguyen, T.-K., T.P. Vo, and H.-T. Thai, *Static and free vibration of axially loaded functionally graded beams based on the first-order shear deformation theory.* Composites Part B: Engineering, 2013. **55**: p. 147-157.https://doi.org/10.1016/j.compositesb.2013.06.011
25. Nguyen, T.-K., T.P. Vo, B.-D. Nguyen, and J. Lee, *An analytical solution for buckling and vibration analysis of functionally graded sandwich beams using a quasi-3D shear deformation theory.* Composite Structures, 2016. **156**: p. 238-252.https://doi.org/10.1016/j.compstruct.2015.11.074
26. Hahn, H.T. and S.W. Tsai, *Introduction to Composite Materials*. 1980: Taylor & Francis.
27. Sayyad, A.S. and Y.M. Ghugal, *Bending, buckling and free vibration of laminated composite and sandwich beams: A critical review of literature.* Composite Structures, 2017. **171**: p. 486-504.https://doi.org/10.1016/j.compstruct.2017.03.053
28. Thostenson, E.T., Z. Ren, and T.-W. Chou, *Advances in the science and technology of carbon nanotubes and their composites: a review.* Composites science and technology, 2001. **61**(13): p. 1899-1912

29. Gay, D., S.V. Hoa, and S.W. Tsai, *Composite Materials: Design and Applications*. 2002: CRC Press.
30. Librescu, L. and O. Song, *Thin-walled composite beams: theory and application*. Vol. 131. 2005: Springer Science & Business Media.
31. Vo, T.P., H.-T. Thai, T.-K. Nguyen, A. Maheri, and J. Lee, *Finite element model for vibration and buckling of functionally graded sandwich beams based on a refined shear deformation theory.* Engineering Structures, 2014. **64**: p. 12-22.https://doi.org/10.1016/j.engstruct.2014.01.029
32. Nguyen, T.-K., N.-D. Nguyen, T.P. Vo, and H.-T. Thai, *Trigonometric-series solution for analysis of laminated composite beams.* Composite Structures, 2017. **160**: p. 142-151.https://doi.org/10.1016/j.compstruct.2016.10.033
33. Lee, J., *Flexural analysis of thin-walled composite beams using shear-deformable beam theory.* Composite Structures, 2005. **70**(2): p. 212-222
34. Lee, J. and S.-E. Kim, *Flexural–torsional buckling of thin-walled I-section composites.* Computers & Structures, 2001. **79**(10): p. 987-995.https://doi.org/10.1016/S0045-7949(00)00195-4
35. Lee, J., S.E. Kim, and K. Hong, *Lateral buckling of I-section composite beams.* Engineering Structures, 2002. **24**(7): p. 955-964.https://doi.org/10.1016/S0141-0296(02)00016-0
36. Lee, J. and S.-h. Lee, *Flexural–torsional behavior of thin-walled composite beams.* Thin-Walled Structures, 2004. **42**(9): p. 1293-1305.https://doi.org/10.1016/j.tws.2004.03.015
37. Ghane, M., A.R. Saidi, and R. Bahaadini, *Vibration of fluid-conveying nanotubes subjected to magnetic field based on the thin-walled Timoshenko beam theory.* Applied Mathematical Modelling, 2020. **80**: p. 65-83.https://doi.org/10.1016/j.apm.2019.11.034
38. Xie, Y., J. Lei, S. Guo, S. Han, J. Ruan, and Y. He, *Size-dependent vibration of multi-scale sandwich micro-beams: An experimental study and theoretical analysis.*

Thin-Walled Structures, 2022. **175**: p. 109115.https://doi.org/10.1016/j.tws.2022.109115

39. Nguyen, N.-D., T.-K. Nguyen, H.-T. Thai, and T.P. Vo, *A Ritz type solution with exponential trial functions for laminated composite beams based on the modified couple stress theory.* Composite Structures, 2018. **191**: p. 154-167.https://doi.org/10.1016/j.compstruct.2018.02.025
40. Roudbari, M.A., T.D. Jorshari, C. Lü, R. Ansari, A.Z. Kouzani, and M. Amabili, *A review of size-dependent continuum mechanics models for micro- and nano-structures.* Thin-Walled Structures, 2022. **170**: p. 108562.https://doi.org/10.1016/j.tws.2021.108562
41. Trinh, M.-C. and H. Jun, *Stochastic vibration analysis of functionally graded beams using artificial neural networks.* Structural Engineering and Mechanics, 2021. **78**(5): p. 529-543
42. Trinh, M.-C., S.-N. Nguyen, H. Jun, and T. Nguyen-Thoi, *Stochastic buckling quantification of laminated composite plates using cell-based smoothed finite elements.* Thin-Walled Structures, 2021. **163**: p. 107674
43. Sharma, H., S. Mukherjee, and R. Ganguli, *Stochastic strain and stress computation of a higher-order sandwich beam using hybrid stochastic time domain spectral element method.* Mechanics of Advanced Materials and Structures, 2022. **29**(4): p. 525-538
44. Thuan, N. and T. Hien, *Stochastic perturbation-based finite element for free vibration of functionally graded beams with an uncertain elastic modulus.* Mechanics of Composite Materials, 2020. **56**: p. 485-496
45. Shen, Z., S. Hao, and H. Li, *Comparison of various thin-walled composite beam models for thermally induced vibrations of spacecraft boom.* Composite Structures, 2023. **320**: p. 117163
46. Simonetti, S.K., G. Turkalj, and D. Lanc, *Thermal buckling analysis of thin-walled closed section FG beam-type structures.* Thin-walled structures, 2022. **181**: p. 110075

47. Nguyen, T.-K., B.-D. Nguyen, T.P. Vo, and H.-T. Thai, *Hygro-thermal effects on vibration and thermal buckling behaviours of functionally graded beams.* Composite Structures, 2017. **176**: p. 1050-1060.https://doi.org/10.1016/j.compstruct.2017.06.036
48. Liviu Librescu, O.S., *Thin-Walled Composite Beams*. Solid Mechanics and Its Applications. 2006: Springer Dordrecht.
49. Vlasov, V.Z., *Thin-walled elastic beams*. 1961, Published for the National Science Foundation, Washington, D.C., by the Israel Program for Scientific Translations Jerusalem: Jerusalem
50. Reddy, J.N., *Mechanics of Laminated Composite Plates and Shells*. 2nd Edition ed. 2003, Boca Raton: CRC Press.
51. Gao, K., R. Li, and J. Yang, *Dynamic characteristics of functionally graded porous beams with interval material properties.* Engineering Structures, 2019. **197**: p. 109441
52. Fang, W., T. Yu, and T.Q. Bui, *Analysis of thick porous beams by a quasi-3D theory and isogeometric analysis.* Composite Structures, 2019. **221**: p. 110890
53. Chen, D., J. Yang, and S. Kitipornchai, *Elastic buckling and static bending of shear deformable functionally graded porous beam.* Composite Structures, 2015. **133**: p. 54-61
54. Szabados, T., *An elementary introduction to the Wiener process and stochastic integrals.* Studia Scientiarum Mathematicarum Hungarica, 2010. **31**
55. Andrews, G.E. and R. Askey. *Classical orthogonal polynomials*. in *Polynômes Orthogonaux et Applications*. 1985. Berlin, Heidelberg: Springer Berlin Heidelberg.
56. Shen, D., H. Wu, B. Xia, and D. Gan, *Polynomial Chaos Expansion for Parametric Problems in Engineering Systems: A Review.* IEEE Systems Journal, 2020. **14**(3): p. 4500-4514.10.1109/JSYST.2019.2957664

57. Hadigol, M. and A. Doostan, *Least squares polynomial chaos expansion: A review of sampling strategies.* Computer Methods in Applied Mechanics and Engineering, 2018. **332**: p. 382-407.https://doi.org/10.1016/j.cma.2017.12.019
58. Lüthen, N., S. Marelli, and B. Sudret, *Sparse Polynomial Chaos Expansions: Literature Survey and Benchmark.* SIAM/ASA Journal on Uncertainty Quantification, 2021. **9**(2): p. 593-649.10.1137/20M1315774
59. Susac, F., E.F. Beznea, and N. Baroiu. *Artificial neural network applied to prediction of buckling behavior of the thin walled box*. in *Advanced Engineering Forum*. 2017. Trans Tech Publ.
60. Jeon, J., J. Kim, J.J. Lee, D. Shin, and Y.Y. Kim, *Development of deep learning-based joint elements for thin-walled beam structures.* Computers & Structures, 2022. **260**: p. 106714
61. Torregrosa, A., A. Gil, P. Quintero, and A. Cremades, *A reduced order model based on artificial neural networks for nonlinear aeroelastic phenomena and application to composite material beams.* Composite Structures, 2022. **295**: p. 115845
62. Zenkour, A.M. and H.D. El-Shahrany, *Control of a laminated composite plate resting on Pasternak's foundations using magnetostrictive layers.* Archive of Applied Mechanics, 2020. **90**(9): p. 1943-1959.10.1007/s00419-020-01705-3
63. Aydogdu, M., *Vibration analysis of cross-ply laminated beams with general boundary conditions by Ritz method.* International Journal of Mechanical Sciences, 2005. **47**(11): p. 1740-1755.https://doi.org/10.1016/j.ijmecsci.2005.06.010
64. Daneshjou, K., A. Nouri, and R. Talebitooti, *Sound transmission through laminated composite cylindrical shells using analytical model.* Archive of Applied Mechanics, 2007. **77**(6): p. 363-379.10.1007/s00419-006-0096-7
65. Kant, T., S.R. Marur, and G.S. Rao, *Analytical solution to the dynamic analysis of laminated beams using higher order refined theory.* Composite Structures, 1997. **40**(1): p. 1-9.https://doi.org/10.1016/S0263-8223(97)00133-5
66. Karama, M., K.S. Afaq, and S. Mistou, *Mechanical behaviour of laminated composite beam by the new multi-layered laminated composite structures model*

with transverse shear stress continuity. International Journal of Solids and Structures, 2003. **40**(6): p. 1525-1546.https://doi.org/10.1016/S0020-7683(02)00647-9

67. Khdeir, A.A. and J.N. Reddy, *Free vibration of cross-ply laminated beams with arbitrary boundary conditions.* International Journal of Engineering Science, 1994. **32**(12): p. 1971-1980.https://doi.org/10.1016/0020-7225(94)90093-0
68. Ebrahimi, F. and M.F. Ahari, *Magnetostriction-assisted active control of the multi-layered nanoplates: effect of the porous functionally graded facesheets on the system's behavior.* Engineering with Computers, 2023. **39**(1): p. 269-283.10.1007/s00366-021-01539-9
69. Dhore, N., L. Khalsa, and V. Varghese, *Hygrothermoelastic analysis of non-simple nano-beam induced by ramp-type heating.* Archive of Applied Mechanics, 2023.10.1007/s00419-023-02444-x
70. Chen, W. and X. Li, *A new modified couple stress theory for anisotropic elasticity and microscale laminated Kirchhoff plate model.* Archive of Applied Mechanics, 2014. **84**(3): p. 323-341.10.1007/s00419-013-0802-1
71. Vo, T.P. and J. Lee, *Geometrical nonlinear analysis of thin-walled composite beams using finite element method based on first order shear deformation theory.* Archive of Applied Mechanics, 2011. **81**(4): p. 419-435.10.1007/s00419-010-0407-x
72. Adam, C., D. Ladurner, and T. Furtmüller, *Moderately large deflection of slightly curved layered beams with interlayer slip.* Archive of Applied Mechanics, 2022. **92**(5): p. 1431-1450.10.1007/s00419-022-02119-z
73. Zhang, Y., L. Zhang, and S. Zhang, *Exact series solutions of composite beams with rotationally restrained boundary conditions: static analysis.* Archive of Applied Mechanics, 2022. **92**(12): p. 3999-4015.10.1007/s00419-022-02277-0
74. Ebrahimi, F. and S.H.S. Hosseini, *Nonlinear vibration and dynamic instability analysis nanobeams under thermo-magneto-mechanical loads: a parametric*

excitation study. Engineering with Computers, 2021. **37**(1): p. 395-408.10.1007/s00366-019-00830-0

75. Ebrahimi, F., M. karimiasl, and V. Mahesh, *Chaotic dynamics and forced harmonic vibration analysis of magneto-electro-viscoelastic multiscale composite nanobeam.* Engineering with Computers, 2021. **37**(2): p. 937-950.10.1007/s00366-019-00865-3
76. Selvamani, R., R. Loganathan, and F. Ebrahimi, *Nonlocal State-Space Strain Gradient Approach to the Vibration of Piezoelectric Functionally Graded Nanobeam.* Engineering Transactions; Vol 70, No 4 (2022), 2022
77. Selvamani, R., J. Rexy, and F. Ebrahimi, *Vibration Analysis of a Magneto Thermo Electrical Nano Fiber Reinforced with Graphene Oxide Powder Under Refined Beam Model.* Journal of Solid Mechanics, 2021. **13**(1): p. 80-94.10.22034/jsm.2020.1895052.1557
78. Ellali, M., M. Bouazza, and K. Amara, *Thermal buckling of a sandwich beam attached with piezoelectric layers via the shear deformation theory.* Archive of Applied Mechanics, 2022. **92**(3): p. 657-665.10.1007/s00419-021-02094-x
79. Jun, L., B. Yuchen, and H. Peng, *A dynamic stiffness method for analysis of thermal effect on vibration and buckling of a laminated composite beam.* Archive of Applied Mechanics, 2017. **87**(8): p. 1295-1315.10.1007/s00419-017-1250-0
80. Liu, L., W. Yang, Y. Chai, and G. Zhai, *Vibration and thermal buckling analyses of multi-span composite lattice sandwich beams.* Archive of Applied Mechanics, 2021. **91**(6): p. 2601-2616.10.1007/s00419-021-01908-2
81. Beheshti-Aval, S.B. and M. Lezgy-Nazargah, *A coupled refined high-order global-local theory and finite element model for static electromechanical response of smart multilayered/sandwich beams.* Archive of Applied Mechanics, 2012. **82**(12): p. 1709-1752.10.1007/s00419-012-0621-9
82. Vo, T.P., H.-T. Thai, and F. Inam, *Axial-flexural coupled vibration and buckling of composite beams using sinusoidal shear deformation theory.* Archive of Applied Mechanics, 2013. **83**(4): p. 605-622.10.1007/s00419-012-0707-4

83. Vo, T.P. and H.-T. Thai, *Static behavior of composite beams using various refined shear deformation theories.* Composite Structures, 2012. **94**(8): p. 2513-2522.https://doi.org/10.1016/j.compstruct.2012.02.010
84. Rakočević, M. and S. Popović, *Bending analysis of simply supported rectangular laminated composite plates using a new computation method based on analytical solution of layerwise theory.* Archive of Applied Mechanics, 2018. **88**(5): p. 671-689.10.1007/s00419-017-1334-x
85. Gao, Y., H. Zhang, W. Yang, and D. He, *A new bending model for composite laminated shells based on the refined zigzag theory.* Archive of Applied Mechanics, 2022. **92**(10): p. 2899-2915.10.1007/s00419-022-02210-5
86. Nguyen, N.-D., T.-K. Nguyen, T.P. Vo, and H.-T. Thai, *Ritz-Based Analytical Solutions for Bending, Buckling and Vibration Behavior of Laminated Composite Beams.* International Journal of Structural Stability and Dynamics, 2018. **18**(11): p. 1850130.10.1142/s0219455418501304
87. Schuëller, G.I., *Developments in stochastic structural mechanics.* Archive of Applied Mechanics, 2006. **75**(10): p. 755-773.10.1007/s00419-006-0067-z
88. Liu, X., L. Jiang, P. Xiang, W. Zhou, Z. Lai, and Y. Feng, *Stochastic finite element method based on point estimate and Karhunen–Loéve expansion.* Archive of Applied Mechanics, 2021. **91**(4): p. 1257-1271.10.1007/s00419-020-01819-8
89. Batou, A. and C. Soize, *Stochastic modeling and identification of an uncertain computational dynamical model with random fields properties and model uncertainties.* Archive of Applied Mechanics, 2013. **83**(6): p. 831-848.10.1007/s00419-012-0720-7
90. Füssl, J., G. Kandler, and J. Eberhardsteiner, *Application of stochastic finite element approaches to wood-based products.* Archive of Applied Mechanics, 2016. **86**(1): p. 89-110.10.1007/s00419-015-1112-6
91. Wang, L., Y. Liu, Y. Xie, and B. Chen, *Impact load identification of composite laminated cylindrical shell with stochastic characteristic.* Archive of Applied Mechanics, 2022. **92**(4): p. 1397-1411.10.1007/s00419-022-02116-2

92. Stefanou, G., *The stochastic finite element method: Past, present and future.* Computer Methods in Applied Mechanics and Engineering, 2009. **198**(9): p. 1031-1051.https://doi.org/10.1016/j.cma.2008.11.007
93. Rahman, S. and B.N. Rao, *A perturbation method for stochastic meshless analysis in elastostatics.* International Journal for Numerical Methods in Engineering, 2001. **50**(8): p. 1969-1991.https://doi.org/10.1002/nme.106
94. Sahoo, R., N. Grover, and B.N. Singh, *Random vibration response of composite–sandwich laminates.* Archive of Applied Mechanics, 2021. **91**(9): p. 3755-3771.10.1007/s00419-021-01976-4
95. Li, H.-s., Z.-z. Lü, and Z.-f. Yue, *Support vector machine for structural reliability analysis.* Applied Mathematics and Mechanics, 2006. **27**(10): p. 1295-1303.10.1007/s10483-006-1001-z
96. Peng, X., D. Li, H. Wu, Z. Liu, J. Li, S. Jiang, and J. Tan, *Uncertainty analysis of composite laminated plate with data-driven polynomial chaos expansion method under insufficient input data of uncertain parameters.* Composite Structures, 2019. **209**: p. 625-633.https://doi.org/10.1016/j.compstruct.2018.11.015
97. Nguyen, H.X., T. Duy Hien, J. Lee, and H. Nguyen-Xuan, *Stochastic buckling behaviour of laminated composite structures with uncertain material properties.* Aerospace Science and Technology, 2017. **66**: p. 274-283.https://doi.org/10.1016/j.ast.2017.01.028
98. Elishakoff, I. and E. Archaud, *Modified Monte Carlo method for buckling analysis of nonlinear imperfect structures.* Archive of Applied Mechanics, 2013. **83**(9): p. 1327-1339.10.1007/s00419-013-0749-2
99. da S, C.R.Á. and R.M.F. Squarcio, *The Neumann–Monte Carlo methodology applied to the quantification of uncertainty in the problem stochastic bending of the Levinson–Bickford beam.* Archive of Applied Mechanics, 2023. **93**(5): p. 2009-2024.10.1007/s00419-023-02369-5
100. Naskar, S., T. Mukhopadhyay, S. Sriramula, and S. Adhikari, *Stochastic natural frequency analysis of damaged thin-walled laminated composite beams with*

uncertainty in micromechanical properties. Composite Structures, 2017. **160**: p. 312-334.https://doi.org/10.1016/j.compstruct.2016.10.035

101. Li, J., X. Tian, Z. Han, and Y. Narita, *Stochastic thermal buckling analysis of laminated plates using perturbation technique.* Composite Structures, 2016. **139**: p. 1-12.https://doi.org/10.1016/j.compstruct.2015.11.076
102. Onkar, A.K., C.S. Upadhyay, and D. Yadav, *Stochastic Finite Element Buckling Analysis of Laminated Plates With Circular Cutout Under Uniaxial Compression.* Journal of Applied Mechanics, 2006. **74**(4): p. 798-809.10.1115/1.2711230
103. Verma, V.K. and B.N. Singh, T*hermal buckling of laminated composite plates with random geometric and material properties.* International Journal of Structural Stability and Dynamics, 2009. **09**(02): p. 187-211.10.1142/s0219455409002990
104. Chandra, S., K. Sepahvand, V.A. Matsagar, and S. Marburg, *Stochastic dynamic analysis of composite plate with random temperature increment.* Composite Structures, 2019. **226**: p. 111159.https://doi.org/10.1016/j.compstruct.2019.111159
105. Chakraborty, S., B. Mandal, R. Chowdhury, and A. Chakrabarti, *Stochastic free vibration analysis of laminated composite plates using polynomial correlated function expansion.* Composite Structures, 2016. **135**: p. 236-249.https://doi.org/10.1016/j.compstruct.2015.09.044
106. Bhattacharyya, B., *On the use of sparse Bayesian learning-based polynomial chaos expansion for global reliability sensitivity analysis.* Journal of Computational and Applied Mathematics, 2023. **420**: p. 114819.https://doi.org/10.1016/j.cam.2022.114819
107. Nguyen, T.-K., N.-D. Nguyen, T. Vo, and T. Thai, *Trigonometric-series solution for analysis of laminated composite beams.* Composite Structures, 2016. **160**.10.1016/j.compstruct.2016.10.033
108. Dalbey, K., M.S. Eldred, G. Geraci, J.D. Jakeman, K.A. Maupin, J.A. Monschke, D.T. Seidl, L.P. Swiler, A. Tran, F. Menhorn, and X. Zeng, *Dakota A Multilevel Parallel Object-Oriented Framework for Design Optimization Parameter Estimation Uncertainty Quantification and Sensitivity Analysis: Version 6.12*

Theory Manual. 2020, ; Sandia National Lab. (SNL-NM), Albuquerque, NM (United States). p. Medium: ED; Size: 128 p.

109. Sobol, I.M., *Sensitivity Estimates for Nonlinear Mathematical Models.* Mathematical Modelling and Computational Experiments, 1993

110. Saltelli, A., P. Annoni, I. Azzini, F. Campolongo, M. Ratto, and S. Tarantola, *Variance based sensitivity analysis of model output. Design and estimator for the total sensitivity index.* Computer Physics Communications, 2010. **181**(2): p. 259-270.https://doi.org/10.1016/j.cpc.2009.09.018

111. Saltelli, A., M. Ratto, S. Tarantola, and F. Campolongo, *Update 1 of: Sensitivity Analysis for Chemical Models.* Chemical Reviews, 2012. **112**(5): p. PR1-PR21.10.1021/cr200301u

112. Sudret, B., *Global sensitivity analysis using polynomial chaos expansions.* Reliability Engineering & System Safety, 2008. **93**(7): p. 964-979.https://doi.org/10.1016/j.ress.2007.04.002

113. Nguyen, N.-D., T.-K. Nguyen, T.-N. Nguyen, and H.-T. Thai, *New Ritz-solution shape functions for analysis of thermo-mechanical buckling and vibration of laminated composite beams.* Composite Structures, 2018. **184**: p. 452-460.https://doi.org/10.1016/j.compstruct.2017.10.003

114. Khdeir, A.A. and J.N. Reddy, *An exact solution for the bending of thin and thick cross-ply laminated beams.* Composite Structures, 1997. **37(**2): p. 195-203.https://doi.org/10.1016/S0263-8223(97)80012-8

115. Piovan, M.T., J.M. Ramirez, and R. Sampaio, *Dynamics of thin-walled composite beams: Analysis of parametric uncertainties.* Composite Structures, 2013. **105**: p. 14-28

116. Bauld, N.R. and T. Lih-Shyng, *A Vlasov theory for fiber-reinforced beams with thin-walled open cross sections.* International Journal of Solids and Structures, 1984. **20**(3): p. 277-297.https://doi.org/10.1016/0020-7683(84)90039-8

117. Pandey, M.D., M.Z. Kabir, and A.N. Sherbourne, *Flexural-torsional stability of thin-walled composite I-section beams.* Composites Engineering, 1995. **5**(3): p. 321-342.https://doi.org/10.1016/0961-9526(94)00101-E
118. Lee, J. and S.-E. Kim, *Free vibration of thin-walled composite beams with I-shaped cross-sections.* Composite Structures, 2002. **55**(2): p. 205-215.https://doi.org/10.1016/S0263-8223(01)00150-7
119. Latalski, J. and D. Zulli, *Generalized Beam Theory for Thin-Walled Beams with Curvilinear Open Cross-Sections.* Applied Sciences, 2020. **10**(21): p. 7802
120. Yu, W., D. Hodges, V. Volovoi, and E. Fuchs, *A generalized Vlasov theory of composite beams.* Thin-Walled Structures, 2005. **43**: p. 1493-1511.10.1016/j.tws.2005.02.003
121. Maddur, S.S. and S.K. Chaturvedi, *Laminated composite open profile sections: non-uniform torsion of I-sections.* Composite Structures, 2000. **50**(2): p. 159-169.https://doi.org/10.1016/S0263-8223(00)00093-3
122. Maddur, S.S. and S.K. Chaturvedi, *Laminated composite open profile sections: first order shear deformation theory.* Composite Structures, 1999. **45**(2): p. 105-114.https://doi.org/10.1016/S0263-8223(99)00005-7
123. Qin, Z. and L. Librescu, *On a shear-deformable theory of anisotropic thin-walled beams: further contribution and validations.* Composite Structures, 2002. **56**(4): p. 345-358.https://doi.org/10.1016/S0263-8223(02)00019-3
124. Vo, T.P. and J. Lee, *Flexural–torsional coupled vibration and buckling of thin-walled open section composite beams using shear-deformable beam theory.* International Journal of Mechanical Sciences, 2009. **51**(9): p. 631-641.https://doi.org/10.1016/j.ijmecsci.2009.05.001
125. Lee, J., *Center of gravity and shear center of thin-walled open-section composite beams.* Composite Structures, 2001. **52**(2): p. 255-260.https://doi.org/10.1016/S0263-8223(00)00177-X

126. Jung, S. and J.-Y. Lee, *Closed-form analysis of thin-walled composite I-beams considering non-classical effects.* Composite Structures, 2003. **60**: p. 9-17.10.1016/S0263-8223(02)00318-5
127. Kim, N.-I. and D.K. Shin, *Coupled deflection analysis of thin-walled Timoshenko laminated composite beams.* Computational Mechanics, 2008. **43**(4): p. 493.10.1007/s00466-008-0324-9
128. Wu, L. and M. Mohareb, *Finite element formulation for shear deformable thin-walled beams.* Canadian Journal of Civil Engineering, 2011. **38**(4): p. 383-392.10.1139/l11-007
129. Carrera, E., F. Miglioretti, and M. Petrolo, *Accuracy of refined finite elements for laminated plate analysis.* Composite Structures, 2011. **93**(5): p. 1311-1327.10.1016/j.compstruct.2010.11.007
130. Fazzolari, F.A. and E. Carrera, *Refined hierarchical kinematics quasi-3D Ritz models for free vibration analysis of doubly curved FGM shells and sandwich shells with FGM core.* Journal of Sound and Vibration, 2014. **333**(5): p. 1485-1508.https://doi.org/10.1016/j.jsv.2013.10.030
131. Carrera, E., *Transverse Normal Stress Effects in Multilayered Plates.* Journal of Applied Mechanics, 1999. **66**(4): p. 1004-1012.10.1115/1.2791769
132. Robaldo, A., E. Carrera, and A. Benjeddou, *A Unified Formulation for finite element analysis of piezoelectric plates.* Computers & Structures - COMPUT STRUCT, 2006. **84**: p. 1494-1505.10.1016/j.compstruc.2006.01.029
133. Cinefra, M., E. Carrera, S. Brischetto, and S. Belouettar, *ThermoMechanical Analysis Of Functionally Graded Shells.* Journal of Thermal Stresses - J THERMAL STRESSES, 2010. **33**: p. 942-963.10.1080/01495739.2010.482379
134. Fazzolari, F. and E. Carrera, *Thermal Stability of FGM Sandwich Plates Under Various Through-the-Thickness Temperature Distributions.* Journal of Thermal Stresses, 2014. **37**: p. 1449–1481.10.1080/01495739.2014.937251
135. Pagani, A., E. Carrera, M. Boscolo, and J.R. Banerjee, *Refined dynamic stiffness elements applied to free vibration analysis of generally laminated composite beams*

with arbitrary boundary conditions. Composite Structures, 2014. **110**: p. 305-316.https://doi.org/10.1016/j.compstruct.2013.12.010

136. Carrera, E. and B. Kröplin, *ZIGZAG AND INTERLAMINAR EQUILIBRIA EFFECTS IN LARGE-DEFLECTION AND POSTBUCKLING ANALYSIS OF MULTILAYERED PLATES.* Mechanics of Composite Materials and Structures, 1997. **4**(1): p. 69-94.10.1080/10759419708945875
137. Khalili, S.M.R., M. Botshekanan Dehkordi, E. Carrera, and M. Shariyat, *Non-linear dynamic analysis of a sandwich beam with pseudoelastic SMA hybrid composite faces based on higher order finite element theory.* Composite Structures, 2013. **96**: p. 243-255.https://doi.org/10.1016/j.compstruct.2012.08.020
138. Carrera, E., A. Pagani, and M. Petrolo, *Classical, Refined, and Component-Wise Analysis of Reinforced-Shell Wing Structures.* AIAA Journal, 2013. **51**(5): p. 1255-1268.10.2514/1.J052331
139. Pagani, A., A.G. de Miguel, M. Petrolo, and E. Carrera, *Analysis of laminated beams via Unified Formulation and Legendre polynomial expansions.* Composite Structures, 2016. **156**.10.1016/j.compstruct.2016.01.095
140. Carrera, E., M. Petrolo, and E. Zappino, *Performance of CUF Approach to Analyze the Structural Behavior of Slender Bodies.* Journal of Structural Engineering, 2012. **138**: p. 285-297.10.1061/(ASCE)ST.1943-541X.0000402
141. Carrera, E., M. Boscolo, and A. Robaldo, *Hierarchic Multilayered Plate Elements for Coupled Multifield Problems of Piezoelectric Adaptive Structures: Formulation and Numerical Assessment.* Archives of Computational Methods in Engineering, 2007. **14**(4): p. 383-430.10.1007/s11831-007-9012-8
142. Carrera, E., M. Filippi, and E. Zappino, *Free vibration analysis of rotating composite blades via Carrera Unified Formulation.* Composite Structures, 2013. **106**: p. 317-325.10.1016/j.compstruct.2013.05.055
143. Carrera, E., *Temperature Profile Influence on Layered Plates Response Considering Classical and Advanced Theories.* Aiaa Journal - AIAA J, 2002. **40**: p. 1885-1896.10.2514/2.1868

144. Chandiramani, N.K., L. Librescu, and C.D. Shete, *On the free-vibration of rotating composite beams using a higher-order shear formulation.* Aerospace Science and Technology, 2002. **6**(8): p. 545-561.https://doi.org/10.1016/S1270-9638(02)01195-1

145. Bhaskar, K. and L. Librescu, *A geometrically non-linear theory for laminated anisotropic thin-walled beams.* International Journal of Engineering Science, 1995. **33**(9): p. 1331-1344

146. Megson, T.H.G., *Aircraft Structures for Engineering Students*. Seventh Edition ed. 2021, United Kingdom: Butterworth-Heinemann. 649.

147. Nguyen, N.-D., T.-K. Nguyen, T. Vo, N. Thiện Nhân, and S. Lee, *Vibration and buckling behaviours of thin-walled composite and functionally graded sandwich I-beams.* Composites Part B: Engineering, 2019. **166**.10.1016/j.compositesb.2019.02.033

148. CortÍNez, V.H. and M.T. Piovan, *VIBRATION AND BUCKLING OF COMPOSITE THIN-WALLED BEAMS WITH SHEAR DEFORMABILITY.* Journal of Sound and Vibration, 2002. **258**(4): p. 701-723.https://doi.org/10.1006/jsvi.2002.5146

149. Piovan, M.T. and V.H. Cortínez, *Mechanics of shear deformable thin-walled beams made of composite materials.* Thin-Walled Structures, 2007. **45**(1): p. 37-62.https://doi.org/10.1016/j.tws.2006.12.001

150. Kim, N.-I., D. Shin, and Y.S. Park, *Dynamic stiffness matrix of thin-walled composite I-beam with symmetric and arbitrary laminations.* Journal of Sound and Vibration, 2008. **318**: p. 364-388.10.1016/j.jsv.2008.04.006

151. Kim, N.-I. and J. Lee, *Exact solutions for stability and free vibration of thin-walled Timoshenko laminated beams under variable forces.* Archive of Applied Mechanics, 2014. **84**(12): p. 1785-1809.10.1007/s00419-014-0886-2

152. Kim, N.-I., D. Shin, and M.-Y. Kim, *Flexural–torsional buckling loads for spatially coupled stability analysis of thin-walled composite columns.* Advances in Engineering Software, 2008. **39**: p. 949-961.10.1016/j.advengsoft.2008.03.001

153. Trinh, L.C., T.P. Vo, H.-T. Thai, and T.-K. Nguyen, *An analytical method for the vibration and buckling of functionally graded beams under mechanical and thermal loads.* Composites Part B: Engineering, 2016. **100**: p. 152-163.https://doi.org/10.1016/j.compositesb.2016.06.067
154. Li, X., Y.H. Li, and Y. Qin, *Free vibration characteristics of a spinning composite thin-walled beam under hygrothermal environment.* International Journal of Mechanical Sciences, 2016. **119**: p. 253-265.https://doi.org/10.1016/j.ijmecsci.2016.10.028
155. Sun, Y. and S. Li, *Thermal buckling and post-buckling of FGM Timoshenko beams on nonlinear elastic foundation.* Journal of Thermal Stresses, 2016. **39**: p. 11-26.10.1080/01495739.2015.1120627
156. Pantousa, D., *Numerical study on thermal buckling of empty thin-walled steel tanks under multiple pool-fire scenarios.* Thin-Walled Structures, 2018. **131**: p. 577-594.https://doi.org/10.1016/j.tws.2018.07.025
157. Jagtap, K.R., A. Lal, and B.N. Singh, *Stochastic nonlinear bending response of functionally graded material plate with random system properties in thermal environment.* International Journal of Mechanics and Materials in Design, 2012. **8**(2): p. 149-167.10.1007/s10999-012-9183-9
158. Borges, R.A., L.F.F. Rodovalho, T.d.P. Sales, and D.A. Rade, *Stochastic eigenfrequency and buckling analyses of plates subjected to random temperature distributions.* Mechanical Systems and Signal Processing, 2021. **147**: p. 107088.https://doi.org/10.1016/j.ymssp.2020.107088
159. Kumar, R.R., T. Mukhopadhyay, K.M. Pandey, and S. Dey, *Stochastic buckling analysis of sandwich plates: The importance of higher order modes.* International Journal of Mechanical Sciences, 2019. **152**: p. 630-643.https://doi.org/10.1016/j.ijmecsci.2018.12.016
160. Umesh, K. and R. Ganguli, *Material Uncertainty Effect on Vibration Control of Smart Composite Plate Using Polynomial Chaos Expansion.* Mechanics of

Advanced Materials and Structures, 2013. **20**(7): p. 580-591.10.1080/15376494.2011.643279

161. Sasikumar, P., A. Venketeswaran, R. Suresh, and S. Gupta, *A data driven polynomial chaos based approach for stochastic analysis of CFRP laminated composite plates.* Composite Structures, 2015. **125**: p. 212-227.https://doi.org/10.1016/j.compstruct.2015.02.010
162. Shaker, A., W. Abdelrahman, M. Tawfik, and E.A. Sadek, *Stochastic finite element analysis of the free vibration of laminated composite plates.* Computational Mechanics, 2008. **41**: p. 493-501.10.1007/s00466-007-0205-7
163. Parhi, A. and B.N. Singh, *Stochastic Response of Laminated Composite Shell Panel in Hygrothermal Environment.* Mechanics Based Design of Structures and Machines, 2014. **42**(4): p. 454-482.10.1080/15397734.2014.888006
164. Guo, H., X. Zhuang, and T. Rabczuk, *A Deep Collocation Method for the Bending Analysis of Kirchhoff Plate.* Computers, Materials \& Continua, 2019. **59**(2).10.32604/cmc.2019.06660
165. Samaniego, E., C. Anitescu, S. Goswami, V.M. Nguyen-Thanh, H. Guo, K. Hamdia, X. Zhuang, and T. Rabczuk, *An energy approach to the solution of partial differential equations in computational mechanics via machine learning: Concepts, implementation and applications.* Computer Methods in Applied Mechanics and Engineering, 2020. **362**: p. 112790.https://doi.org/10.1016/j.cma.2019.112790
166. Zhuang, X., H. Guo, N. Alajlan, H. Zhu, and T. Rabczuk, *Deep autoencoder based energy method for the bending, vibration, and buckling analysis of Kirchhoff plates with transfer learning.* European Journal of Mechanics - A/Solids, 2021. **87**: p. 104225.https://doi.org/10.1016/j.euromechsol.2021.104225
167. Tran, V.-T., T.-K. Nguyen, H. Nguyen-Xuan, and M. Abdel Wahab, *Vibration and buckling optimization of functionally graded porous microplates using BCMO-ANN algorithm.* Thin-Walled Structures, 2023. **182**: p. 110267.https://doi.org/10.1016/j.tws.2022.110267

168. Tsokanas, N., T. Simpson, R. Pastorino, E. Chatzi, and B. Stojadinović, *Model order reduction for real-time hybrid simulation: Comparing polynomial chaos expansion and neural network methods.* Mechanism and Machine Theory, 2022. **178**: p. 105072.https://doi.org/10.1016/j.mechmachtheory.2022.105072
169. Jakeman, J.D., M. Perego, and W.M. Severa, *Neural Networks as Surrogates of Nonlinear High-Dimensional Parameter-to-Prediction Maps*. 2018: United States.10.2172/1481639
170. Tran, V.-T., T.-K. Nguyen, P.T.T. Nguyen, and T.P. Vo, *Stochastic vibration and buckling analysis of functionally graded microplates with a unified higher-order shear deformation theory.* Thin-Walled Structures, 2022. **177**: p. 109473.https://doi.org/10.1016/j.tws.2022.109473
171. Xiu, D. and G.E. Karniadakis, *The Wiener--Askey Polynomial Chaos for Stochastic Differential Equations.* SIAM Journal on Scientific Computing, 2002. **24**(2): p. 619-644.10.1137/s1064827501387826
172. Colombi, P. and C. Poggi, *An experimental, analytical and numerical study of the static behavior of steel beams reinforced by pultruded CFRP strips.* Composites Part B: Engineering, 2006. **37**(1): p. 64-73.https://doi.org/10.1016/j.compositesb.2005.03.002
173. Nguyen, N.D. and T.K. Nguyen. *Ritz Solution for Static Analysis of Thin-Walled Laminated Composite I-beams Based on First-Order Beam Theory*. in *2020 5th International Conference on Green Technology and Sustainable Development (GTSD)*. 2020.
174. Mahamood, R.M. and E.T. Akinlabi, *Types of Functionally Graded Materials and Their Areas of Application*, in *Functionally Graded Materials*, R.M. Mahamood and E.T. Akinlabi, Editors. 2017, Springer International Publishing: Cham. p. 9-21.
175. Miteva, A. and A. Bouzekova-Penkova, *Some aerospace applications of functionally graded materials.* Aerospace Research in Bulgaria, 2021. **33**.https://doi.org/10.3897/arb.v33.e14

176. Osiander, R., M.A.G. Darrin, and J.L. Champion, *MEMS and microstructures in aerospace applications*. 2018: CRC press.
177. Yang, F., A.C.M. Chong, D.C.C. Lam, and P. Tong, *Couple stress based strain gradient theory for elasticity.* International Journal of Solids and Structures, 2002. **39**(10): p. 2731-2743.https://doi.org/10.1016/S0020-7683(02)00152-X
178. Fang, J., J. Gu, and H. Wang, *Size-dependent three-dimensional free vibration of rotating functionally graded microbeams based on a modified couple stress theory.* International Journal of Mechanical Sciences, 2018. **136**: p. 188-199.https://doi.org/10.1016/j.ijmecsci.2017.12.028
179. Ke, L.-L. and Y.-S. Wang, *Size effect on dynamic stability of functionally graded microbeams based on a modified couple stress theory.* Composite Structures, 2011. **93**(2): p. 342-350.https://doi.org/10.1016/j.compstruct.2010.09.008
180. Şimşek, M. and J.N. Reddy, *Bending and vibration of functionally graded microbeams using a new higher order beam theory and the modified couple stress theory.* International Journal of Engineering Science, 2013. **64**: p. 37-53.https://doi.org/10.1016/j.ijengsci.2012.12.002
181. Thai, H.-T., T.P. Vo, T.-K. Nguyen, and J. Lee, *Size-dependent behavior of functionally graded sandwich microbeams based on the modified couple stress theory.* Composite Structures, 2015. **123**: p. 337-349.https://doi.org/10.1016/j.compstruct.2014.11.065
182. Fan, F., Y. Xu, S. Sahmani, and B. Safaei, *Modified couple stress-based geometrically nonlinear oscillations of porous functionally graded microplates using NURBS-based isogeometric approach.* Computer Methods in Applied Mechanics and Engineering, 2020. **372**: p. 113400.https://doi.org/10.1016/j.cma.2020.113400
183. Farzam, A. and B. Hassani, *Isogeometric analysis of in-plane functionally graded porous microplates using modified couple stress theory.* Aerospace Science and Technology, 2019. **91**: p. 508-524.https://doi.org/10.1016/j.ast.2019.05.012

184. Kim, J., K. Żur, and J.N. Reddy, *Bending, free vibration, and buckling of modified couples stress-based functionally graded porous micro-plates.* Composite Structures, 2018. **209**.10.1016/j.compstruct.2018.11.023
185. Liu, H. and Q. Zhang, *Nonlinear dynamics of two-directional functionally graded microbeam with geometrical imperfection using unified shear deformable beam theory.* Applied Mathematical Modelling, 2021. **98**: p. 783-800.https://doi.org/10.1016/j.apm.2021.05.029
186. Chen, X., Y. Lu, and Y. Li, *Free vibration, buckling and dynamic stability of bi-directional FG microbeam with a variable length scale parameter embedded in elastic medium.* Applied Mathematical Modelling, 2019. **67**: p. 430-448.https://doi.org/10.1016/j.apm.2018.11.004
187. Ebrahimi, F. and F. Mahmoodi, *A modified couple stress theory for buckling analysis of higher order inhomogeneous microbeams with porosities.* Proceedings of the Institution of Mechanical Engineers, Part C: Journal of Mechanical Engineering Science, 2019. **233**(8): p. 2855-2866.10.1177/0954406218791642
188. Soltani, M. and F. Atoufi, *Non-local finite element formulation for stability analysis of thin-walled nanobeams with varying I-section.* Acta Mechanica, 2022. **233**(2): p. 789-811.10.1007/s00707-021-03126-x
189. Soltani, M., F. Atoufi, F. Mohri, R. Dimitri, and F. Tornabene, *Nonlocal elasticity theory for lateral stability analysis of tapered thin-walled nanobeams with axially varying materials.* Thin-Walled Structures, 2021. **159**: p. 107268.https://doi.org/10.1016/j.tws.2020.107268
190. Soltani, M., A. Soltani, and O. Civalek, *Interaction of the lateral buckling strength with the axial load for FG micro-sized I-section beam–columns.* Thin-Walled Structures, 2022. **179**: p. 109616.https://doi.org/10.1016/j.tws.2022.109616
191. Lam, D.C.C., F. Yang, A.C.M. Chong, J. Wang, and P. Tong, *Experiments and theory in strain gradient elasticity.* Journal of the Mechanics and Physics of Solids, 2003. **51**(8): p. 1477-1508.https://doi.org/10.1016/S0022-5096(03)00053-X

192. Nguyen, N.-D., T.-K. Nguyen, T.P. Vo, and L.B. Nguyen, *Bending, buckling and free vibration behaviors of thin-walled functionally graded sandwich and composite channel-section beams.* Mechanics Based Design of Structures and Machines, 2020: p. 1-29.10.1080/15397734.2020.1859385
193. Nguyen, T.-T., N.-I. Kim, and J. Lee, *Free vibration of thin-walled functionally graded open-section beams.* Composites Part B: Engineering, 2016. **95**: p. 105-116
194. Kim, N.-I. and J. Lee, *Flexural-torsional analysis of functionally graded sandwich I-beams considering shear effects.* Composites Part B: Engineering, 2017. **108**: p. 436-450.https://doi.org/10.1016/j.compositesb.2016.09.092
195. Nguyen, N.-D., T.P. Vo, and T.-K. Nguyen, *An improved shear deformable theory for bending and buckling response of thin-walled FG sandwich I-beams resting on the elastic foundation.* Composite Structures, 2020. **254**: p. 112823.https://doi.org/10.1016/j.compstruct.2020.112823
196. Choi, S. and Y.Y. Kim, *Higher-order Vlasov torsion theory for thin-walled box beams.* International Journal of Mechanical Sciences, 2021. **195**: p. 106231.https://doi.org/10.1016/j.ijmecsci.2020.106231
197. Ziane, N., S.A. Meftah, H.A. Belhadj, A. Tounsi, and E.A.A. Bedia, *Free vibration analysis of thin and thick-walled FGM box beams.* International Journal of Mechanical Sciences, 2013. **66**: p. 273-282.https://doi.org/10.1016/j.ijmecsci.2012.12.001
198. Chen, D., J. Yang, and S. Kitipornchai, *Free and forced vibrations of shear deformable functionally graded porous beams.* International Journal of Mechanical Sciences, 2016. **108-109**: p. 14-22.https://doi.org/10.1016/j.ijmecsci.2016.01.025
199. Keleshteri, M.M. and J. Jelovica, *Nonlinear vibration analysis of bidirectional porous beams.* Engineering with Computers, 2022. **38**(6): p. 5033-5049.10.1007/s00366-021-01553-x
200. Tang, H., L. Li, and Y. Hu, *Buckling analysis of two-directionally porous beam.* Aerospace Science and Technology, 2018. **78**: p. 471-479.https://doi.org/10.1016/j.ast.2018.04.045

201. Nguyen, N.-D., T.-N. Nguyen, T.-K. Nguyen, and T.P. Vo, *A new two-variable shear deformation theory for bending, free vibration and buckling analysis of functionally graded porous beams.* Composite Structures, 2022. **282**: p. 115095
202. Nguyen, N.-D., T.-N. Nguyen, T.-K. Nguyen, and T.P. Vo. *A Legendre-Ritz solution for bending, buckling and free vibration behaviours of porous beams resting on the elastic foundation*. in *Structures*. 2023. Elsevier.
203. Ziane, N., S.A. Meftah, G. Ruta, and A. Tounsi, *Thermal effects on the instabilities of porous FGM box beams.* Engineering Structures, 2017. **134**: p. 150-158.https://doi.org/10.1016/j.engstruct.2016.12.039
204. Farsadi, T., *Variable thickness thin-walled rotating blades made of functionally graded porous materials.* Proceedings of the Institution of Mechanical Engineers, Part C: Journal of Mechanical Engineering Science, 2022. **236**(14): p. 7674-7689.10.1177/09544062221080654
205. Lanc, D., T.P. Vo, G. Turkalj, and J. Lee, *Buckling analysis of thin-walled functionally graded sandwich box beams.* Thin-Walled Structures, 2015. **86**: p. 148-156.https://doi.org/10.1016/j.tws.2014.10.006